

**GEOFORSCHUNGSZENTRUM POTSDAM**  
STIFTUNG DES ÖFFENTLICHEN RECHTS

---

# Scientific Technical Report

ISSN 1610-0956

Active Intraplate Faulting in the Forearc of North Central Chile  
(30°-31° S)  
Implications from Neotectonic Field Studies, GPS Data, and Elastic  
Dislocation Modeling

Dissertation zur Erlangung des Doktorgrades  
im Fachbereich Geowissenschaften  
an der Freien Universität Berlin

**vorgelegt von:**  
Bertram Heinze

**begutachtet durch:**  
Prof. O. Oncken<sup>1</sup>  
Prof. Ch. Reigber<sup>2</sup>

04. März 2003

<sup>1</sup>Freie Universität Berlin

<sup>2</sup>Universität Potsdam



## Kurzfassung

Im kontinentalen Forearc Nord-Zentral Chiles ( $30^{\circ}$ - $31^{\circ}$  S) ist eine hohe Konzentration von plattenrandparallelen Störungen zu beobachten. Neotektonische Felduntersuchungen zeigen, daß die Mehrzahl dieser Störungen Sedimente der Plio-Pleistozänen Schichtenfolgen verwerfen. Die Verwerfung der Plio-Pleistozänen Ablagerungen deutet an, dass die kontinentale Kruste aktiven Deformationsprozessen ausgesetzt ist. Die E-W Deformation des Forearc seit dem Plio-/Pleistozän kann auf der Grundlage neotektonischer und bilanzierter Profile, sowie anhand von Dislokationsmodellen abgeschätzt werden. Mit Hilfe satellitengestützter Messungen des horizontalen Deformationsfeldes auf der Basis von GPS-Netzen (SAGA) wird versucht, die rezente Intraplattendeformation des Forearc zu quantifizieren. Aufgrund periodisch wiederkehrender Starkbebenereignisse entlang der Plattengrenze wird vermutet, dass die krustale Deformation entscheidend von den Deformationsprozessen innerhalb der Subduktionszone beeinflusst wird.

Der kontinentale Forearc zwischen  $30^{\circ}$ - $31^{\circ}$  südlicher Breite setzt sich aus einer stark herausgehobenen Küstenkordillere im Westen und einem mit känozoischen Sedimenten gefüllten Becken im Osten zusammen. Diese strukturellen Einheiten werden durch eine 60 km lange und ca.  $65^{\circ}$  nach Osten einfallende Störung, der *Puerto Aldea Fault*, voneinander getrennt. Darüber hinaus wird das känozoische Becken intern durch zahlreiche N-S streichende und vorwiegend nach Osten einfallende Störungen deformiert. Zahlreiche Geländebefunde und die Ergebnisse der elastischen Dislokationsmodellierung erklären die beschriebene Deformation entlang dieser Intraplattenstörungen mit Hilfe koseismischer Relaxationsbewegungen in krustalen Tiefen von 10 – 20 km. Vertikale Versatzbeträge von 2 – 5 m geben Hinweise auf quartäre Beben, die aufgrund ihrer Magnitude ( $M_w 7$ ) mit grosser Wahrscheinlichkeit die Kruste durchschlagen haben. Eine Vielzahl geomorphologischer Aspekte, z.B. gehobene marine Terrassen und Abrasionsplattformen, stark hervortretende Störungsmorphologien, Hangrutsche, (Thermal-)Quellaustritte in unmittelbarer Umgebung von Störungsbahnen und ein in weiten Teilen tektonisch kontrolliertes natürliches Drainagesystem lassen die Schlussfolgerung zu, dass die beobachtete Intraplattendeformation im Arbeitsgebiet rezent aktiv ist. Seit dem Einsetzen des jüngsten Deformationsregimes, zur Zeit des Plio-Pleistozäns, wanderte die Zone der grössten Intraplattendeformation von Osten nach Westen und befindet sich heute ca. 40 – 45 km landeinwärts der Küstenlinie. Geomorphologische Untersuchungen an jungen Verwerfungsabstürzen (fault scarps) in diesem Gebiet ergeben jung- Pleistozäne-Holozäne Störungsalter (10 – 84 ka BP).

Die Ergebnisse der Störungsflächenanalyse zeigen, dass während des Plio-/Pleistozäns das Arbeitsgebiet einer dominanten ENE-WSW gerichteten Extension und einer untergeordneten NNW-SSE orientierten Kontraktion unterworfen war. Die Auswertung der kinematischen Daten mit Hilfe der Störungsflächenanalyse weist darauf hin, dass beide Deformationstypen gleichzeitig wirksam waren. Die Grössenordnung der E-W Dehnung, abgeleitet aus der neotektonischen Analyse und der krustalen Bilanzierung des 25 km breiten Forearcs, liegt bei 0.6-3.3%, bezogen auf die letzten 1.2 – 6.5 Ma. Resultierende Deformationsraten variieren zwischen  $0.001 - 0.028 \mu \text{ strain a}^{-1}$ . Aus dem Residualfeld der GPS-Geschwindigkeiten können fast identische Extensionsrichtungen (ENE-WSW) und Kontraktionsrichtungen (NNW-SSE) abgeleitet werden, wie aus der Störungsflächenanalyse. Die aus GPS-Messungen abgeleiteten E-W Dehnungsraten erreichen  $0.038 \pm 0.018 \mu \text{ strain a}^{-1}$ . Unter Berücksichtigung der geodätischen Dehnungsraten und der Annahme der Konservierung des

geodätischen Moments entlang der Puerto Aldea Fault ergeben sich Wiederkehrperioden von 500-1500 Jahren für Erdbeben der Stärke  $M_w 7$  an dieser Störung.

Mit Hilfe eines einfachen Dislokationsmodells der Subduktionszone können vertikale und horizontale Versatzbeträge, die aufgrund starker Subduktionsbeben im kontinentalen Forearc auftreten, abgeschätzt werden. Am Beispiel des Illapel Bebens von 1943 ( $M_w 8.2$ ) wird gezeigt, dass die Küstenkordillere um bis zu 0.4 m herausgehoben wird, während der Bereich des känozoischen Beckens eine geringere Heraushebung oder sogar Absenkung erfährt. Der horizontale Versatzbetrag erreicht in den äussersten Küstenbereichen bis zu 0.8 m in wsw Bewegungsrichtung. Die durch Subduktionsbeben auf den kontinentalen Forearc umgelagerte Deformation erzeugt, ähnlich den aus der neotektonischen Strukturanalyse und den GPS-Residualgeschwindigkeiten abgeleiteten Dehnungshauptachsen, E-W gerichtete Dehnung und N-S gerichtete Kontraktion im Arbeitsgebiet. Die zusätzliche Beanspruchung der Intraplattenstörungen durch die Umlagerung von Deformation und Spannung im Zusammenhang mit starken Subduktionsbeben verringert die Wiederkehrperiode für Intraplattenbeben der Stärke ( $M_w 7$ ) um 40 – 100 Jahre.

Die Ergebnisse dieser Studie zeigen, dass die im kontinentalen Forearc beobachtete Deformation in engem Zusammenhang mit grundlegenden tektonischen Prozessen entlang der Plattengrenze steht. Unter Hinzuziehung der Ergebnisse vorangegangener Autoren wird deutlich, dass die hier beschriebene Intraplattendeformation über das Arbeitsgebiet hinaus an verschiedenen Schlüsselstellen mit vergleichbarer struktureller Ausprägung (z.B. Mejillones, Caldera und Arauco Halbinseln) in ähnlicher Form zu beobachten ist. Die offensichtliche Gültigkeit der beschriebenen Forearc-Deformation über sich ändernde plattentektonische Rahmenbedingungen hinweg gibt Anlass zu der Vermutung, dass singuläre Prozesse, wie z.B. das Abtauchen ozeanischer Rücken oder die Verschluckung mächtiger Sedimentpakete als alleinige Ursache für die Hebungsprozesse entlang der chilenischen Küste in Frage gestellt werden müssen. Stattdessen ist der Abstand der Küstenlinie zum Tiefseegraben, bzw. die Lage des kontinentalen Forearc in Bezug auf die seismisch gekoppelten Bereiche der Subduktionszone als entscheidendes Kriterium in diesem Zusammenhang heranzuziehen. Ein übergreifendes Erklärungsmodell bietet das Zusammenspiel von grabenwärtiger Migration des südamerikanischen Kontinents mit aufwärtsgerichteter Translation und basaler Erosion des kontinentalen Forearc entlang der Plattengrenze. Eine Translation des Forearc könnte zu dessen Heraushebung und zur Ausbildung der nach Osten einfallenden Intraplattenstörungen führen, während die basale Erosion den Kontinentalhang übersteilen und zu dessen Kollaps zwingen würde. Vorausgesetzt, diese Prozesse stünden im Gleichgewicht zur grabenwärtigen Migration des südamerikanischen Kontinents, käme es zur Herausbildung eines dynamischen Systems, das langfristig eine Konsumierung des kontinentalen Forearc zur Folge hätte.

## Abstract

The continental forearc of North Central Chile (30°-31° S) is characterized by the overall abundance of trench-parallel crustal faults. Neotectonic field studies show that most of these faults ruptured the Plio-Pleistocene sedimentary cover. The displacement of Plio-Pleistocene sediments indicates that the continental crust along this stretch of the Chilean coast is subject to active deformation processes. The E-W deformation in the forearc during Plio-Pleistocene times is approximated based on neotectonic and balanced profiles, and by simple dislocation models. By means of space-geodetic measurements of the horizontal displacement field (SAGA-Network), I attempted to quantify the present-day intraplate deformation rates within the forearc. As a result of periodically reoccurring megathrust events along the plate interface, it is assumed that the observed crustal deformation is largely controlled by deformation processes within the subduction zone.

The continental forearc between 30°-31° S latitude mainly consists of the Coastal Cordillera in the west and a basin filled with Cenozoic deposits in the central and eastern part, separated by the prominent Puerto Aldea Fault. In addition, the Cenozoic Basin is internally dissected by numerous N-S striking, predominantly 65° E-dipping intraplate normal faults of up to 60 km length. Abundant field evidence and results from elastic dislocation modeling show that deformation along these intraplate faults is associated with coseismic rupture at crustal depth (10 – 20 km). Vertical offsets within the Plio-Pleistocene sedimentary cover reach up to 2 – 5 m, implying that earthquakes of magnitude  $M_w$  7.0 ruptured the study area during the recent geologic past. Numerous geomorphic aspects, i.e. uplifted marine terraces and abrasion platforms, pronounced range-front faults, the occurrence of fresh surface scarps, landslides, thermal springs in association with fault traces, and a tectonically controlled drainage pattern together suggest that intraplate deformation is active throughout the study area. Since the onset of the most recent deformation regime, at the earliest during Plio-Pleistocene times, the intraplate deformation front shifted eastward, away from the coastline. The most recent deformation of the land surface is observed 40 – 45 km inland from the coast. This is supported through studies of degraded fault scarps in this part of the working area, which reveal Late Pleistocene-Holocene faulting ages (10 – 84 ka BP).

The fault-slip data analysis shows that the study area is subject to ENE-WSW extension and NNW-SSE contraction. Cross-cutting relationships between fault-slip data and fault/Riedel-shear plane relationships suggest that both deformations occurred simultaneously during Plio-Pleistocene times. The amount of E-W extension as inferred from neotectonic analysis and crustal balancing of the 25 km wide forearc zone approximates 0.6-3.3% for the last 1.2 – 6.5 Ma. Resulting strain rates range between 0.001 – 0.028  $\mu$  strain  $a^{-1}$ . GPS residual velocities reveal almost identical extension directions (ENE-WSW) and also indicate trench-parallel shortening (NNW-SSE), counterintuitively to the plate-convergent setting. The GPS-derived E-W strain rates for North-Central Chile range between  $0.038 \pm 0.018 \mu$  strain  $a^{-1}$ . Invoking conservation of the geodetic strain rates along the Puerto Aldea Fault, recurrence times in the order of 500 – 1500 years for  $M_w$  7 intraplate earthquakes are estimated for this fault.

Applying a simple dislocation model of the plate interface, the vertical and horizontal displacement of the continental forearc due to large subduction earthquakes can be approximated. For the 1943 Illapel  $M_w$  8.2 event, up to 0.4 m of uplift are obtained for the Coastal Cordillera, while the

Cenozoic Basin is subject to less pronounced uplift or subsidence. The horizontal displacement reaches up to 0.8 m of west-southwestward motion in the outermost portions of the continental forearc. This produces E-W extensional and N-S contractional strains along the N-S striking intraplate faults, which largely corresponds to principal strain directions that can be inferred from neotectonic field investigations and GPS residual velocity fields. The redistribution of coseismic strains due to interplate earthquakes causes additional loading of intraplate faults, which reduces the estimated recurrence times for  $M_w 7$  earthquakes by 40 – 100 years.

The results of this study strongly suggest that the deformation observed in the continental forearc is closely associated with general tectonic processes active along the plate interface. Taking into account the results of previous authors who studied forearc tectonics, it becomes very clear that the deformation observed in the study area coincides well with that of several structurally similar regions (Mejillones, Caldera, and Arauco peninsulas) in the Chilean forearc. Because the forearc deformation described here seems to be universally valid regardless of the particular plate-tectonic setting, it has to be reconsidered if individual processes such as oceanic ridge subduction or the subduction of large sediment packages represent the only possible causes for strong uplift of marine terraces along the Chilean coasts. Instead, the distance between the coastline and the trench or the position of the continental forearc with respect to the coupled portions of the plate interface appear to be far more important criteria. A unifying model for the understanding of the deformation processes along the Nazca-South America plate boundary is provided by *trenchward migration* of the SA continent in association with *updip translation* and *basal erosion* of the continental forearc. Updip translation could result in the emergence of the continental forearc and the formation of E-dipping intraplate faults, while the basal erosion would lead to an oversteepening of the continental slope and to its subsequent collapse. Provided these processes equilibrate with the trenchward migration of the South American continent, a *dynamic equilibrium* would eventually be established, which would in the long term cause a consumption or tectonic erosion of the overriding plate.

# Contents

<b>1</b>	<b>Introduction</b>	<b>1</b>
1.1	Aims of study . . . . .	2
1.2	Conceptual Framework . . . . .	3
<b>2</b>	<b>Geodynamic and Neotectonic Setting</b>	<b>5</b>
2.1	Nazca-South America Plate Convergence . . . . .	5
2.1.1	The Subduction Interface . . . . .	6
2.1.2	Interaction between Interplate and Intraplate Deformation . . . . .	7
2.2	Neotectonics in the Central and Southern Andes – State of Research . . . . .	8
2.2.1	The Forearc . . . . .	8
2.2.2	The Backarc . . . . .	11
2.2.3	Coastal Uplift Phenomena . . . . .	11
2.3	Geological Setting of the Study Area . . . . .	13
2.3.1	Morphostructural Units and Stratigraphy . . . . .	13
2.3.2	Marine Terraces and Wave-cut Platforms . . . . .	19
2.3.3	Large Historical Subduction Earthquakes . . . . .	22
2.3.4	Present-day Crustal Seismicity . . . . .	23
2.4	Climatic Evolution of North Central Chile . . . . .	23
<b>3</b>	<b>Methods</b>	<b>25</b>
3.1	Neotectonic Field Studies . . . . .	25
3.1.1	Remote Sensing Analysis . . . . .	25
3.1.2	Macroscopic Fault Documentation . . . . .	26
3.2	Paleokinematic Analysis . . . . .	26
3.2.1	Data Acquisition . . . . .	27
3.2.2	Fault-slip Data Analysis . . . . .	27
3.3	Tectonic Geomorphology . . . . .	31
3.3.1	Range-front Geometry . . . . .	31
3.3.2	Drainage Network Analysis . . . . .	32
3.3.3	Fault-scarp Degradation . . . . .	32
3.4	Fault Construction and Restoration . . . . .	34
3.5	Dislocation Modeling . . . . .	35
3.5.1	Theory . . . . .	35

3.5.2	Modeling Intraplate Fault Geometries . . . . .	36
3.5.3	Modeling Strain Redistribution . . . . .	37
3.6	GPS Residual Velocities . . . . .	38
3.6.1	Geodetic Strain Rates and Differential Motion . . . . .	39
<b>4</b>	<b>Results</b>	<b>41</b>
4.1	Neotectonic Field Observations . . . . .	41
4.1.1	Intraplate Deformation . . . . .	41
4.2	Fault-Slip Data Analysis . . . . .	53
4.2.1	Fault Plane Distribution . . . . .	53
4.2.2	Fault Slip Data Distribution . . . . .	54
4.2.3	Fault Plane Solutions . . . . .	55
4.2.4	Deformation of the Cenozoic Basin . . . . .	59
4.3	Tectonic Geomorphology . . . . .	59
4.3.1	Range Front Geometry . . . . .	59
4.3.2	Fault-scarp Degradation . . . . .	61
4.3.3	Drainage Network Analysis . . . . .	64
4.4	Geologic Strains/Strain Rates . . . . .	66
4.4.1	E-W Neotectonic Cross-sections – Recent Topography . . . . .	66
4.4.2	E-W Balanced Cross-section – Basement Geometry . . . . .	70
4.5	Elastic Half-Space Modeling . . . . .	72
4.5.1	Intraplate Fault Geometries . . . . .	72
4.5.2	Forearc Deformation due to Large Subduction Earthquakes . . . . .	74
4.5.3	Strain Redistribution due to Large Subduction Earthquakes . . . . .	78
4.6	Space Geodetic Observations . . . . .	80
4.6.1	GPS Strain Rates and Differential Motions . . . . .	80
4.6.2	Recurrence Intervals for Intraplate Earthquakes . . . . .	84
<b>5</b>	<b>Discussion</b>	<b>86</b>
5.1	Active Intraplate Faulting . . . . .	86
5.2	Fault-Slip Data Analysis . . . . .	88
5.3	Intraplate Fault Geometries and Plio-Pleistocene Strain Rates . . . . .	91
5.4	Recurrence Times for Significant Intraplate Earthquakes . . . . .	97
5.5	Implications for the Nazca-SA Plate Boundary . . . . .	98
<b>6</b>	<b>Conclusions</b>	<b>100</b>
	<b>References</b>	<b>102</b>
	<b>Appendix</b>	<b>112</b>
	<b>Acknowledgements</b>	<b>126</b>
	<b>Curriculum Vitae</b>	<b>127</b>

# 1 Introduction

The Andean forearc of Chile is frequently affected by large shallow subduction earthquakes. These events occur along the interface between the subducting Nazca and the overriding South America (SA) plates and are therefore referred to as interplate events. During earthquake faulting, seismic energy is released by elastic waves inducing second order interplate as well as intraplate (within the crust) deformation and loading or unloading of adjacent intraplate faults. Intraplate earthquakes - though in general much smaller in magnitude than subduction earthquakes - may cause high deformation intensities due to their shallow focal depths (5 – 15 km) and possible small distance to housing and property [Ewing 1990]. In turn, Intraplate deformation rates are very small and therefore hardly detectable by terrestrial means like triangulation networks. The advent of modern space geodetic techniques (GPS) made it possible to approximate these rather small intraplate deformations with sufficient accuracy. However the GPS data need to be associated with existing geologic features in order to validate the observations.

This study provides a detailed analysis of the long term geologic deformation record and correlates these with the present day deformation rates inferred from GPS data in an area well known for its rapidly deforming crusts - the Nazca-SA plate boundary. In order to quantify the long-term deformation rates in the overriding continental crust a series of neotectonic field investigations was carried out in the forearc of North Central Chile - "Norte Chico"- during 1999-2001. Roughly 240 geologic outcrops and topographic features were studied in the field. Apparent fault traces were detected from remote sensing data and ca. 1500 fault-slip data sets were collected along intraplate fault planes and analyzed for their principal strain axes. Topographic profiles crossing potential surface ruptures or fault scarps were measured in the field and applied to diffusion equations in order to estimate the age of scarplike landforms. Fault planes within the Cenozoic sedimentary record were carefully examined for proofs of instantaneous fault behavior and active deformation. Subsequently the geological results were correlated with results from GPS residual velocities and results from elastic half space modeling and possible recurrence intervals for intraplate earthquakes were estimated. The study area is located in the Chilean forearc between 30°-31° S latitude. It is characterized by a strongly uplifted Paleozoic basement complex in the west - the Coastal Cordillera - and a Cenozoic basin in the east [Bohnhorst 1967]. The Coastal Cordillera is deeply incised by extensive marine abrasion platforms on different levels of elevation along its western shores [Paskoff 1970]. The Cenozoic basin is separated from the Coastal Cordillera by a prominent E-dipping range-front fault, the Puerto Aldea Fault (PAF). The northern part of the Cenozoic basin is covered by Mid-Miocene-Pleistocene marine terraces whereas the central and southern parts are characterized by Plio-Pleistocene fluvial terraces and alluvial fan

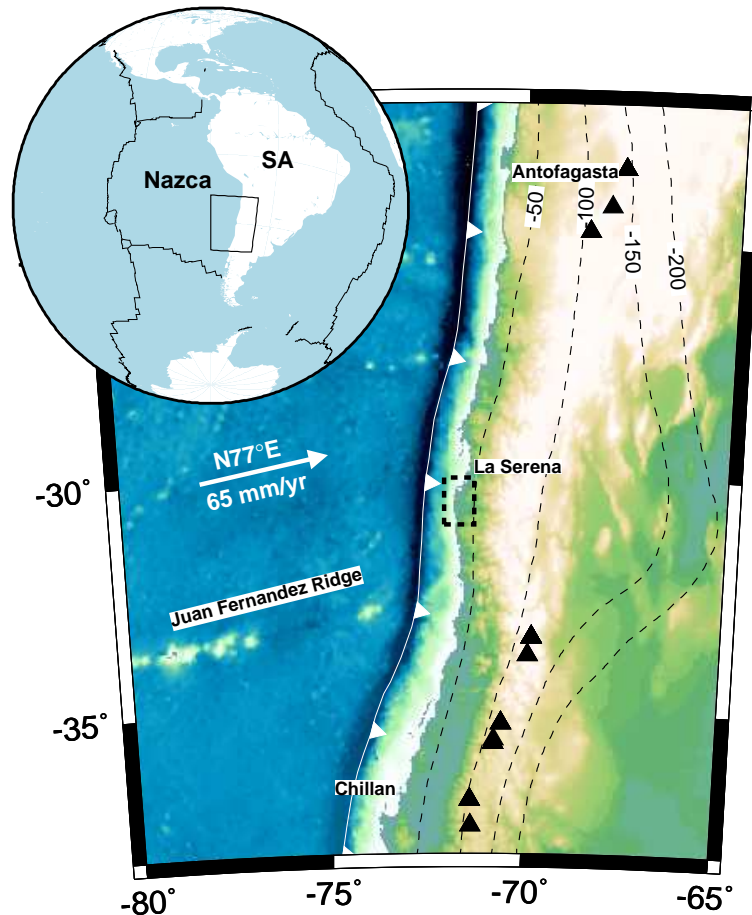


Figure 1.1: Geodynamic setting of North Central Chile and location of the study area (dashed frame). White arrow delineates the present-day plate convergence direction [Angermann et al. 1996] and convergence rate. Topographic relief from Smith & Sandwell [1997]. The line with white triangles shows the trace of the Peru-Chile Trench. The black triangles represent Quaternary volcanoes. The dashed contour lines show the depth of the Subducting Nazca plate under the SA continent in km [Cahill and Isacks 1992; Creager et al. 1995].

deposits. Parallel to the PAF, the entire study area is dissected by numerous NS-striking intraplate normal faults that clearly ruptured the sedimentary cover of the Cenozoic basin during the recent geologic past.

## 1.1 Aims of study

The thesis presents results from geological field investigations conducted in North Central Chile (“Norte Chico”), where abundant relics of intraplate normal faulting were detected. The objective of this study is to characterize the recent forearc deformation, quantify deformation rates by means of neotectonic field observations, elastic half space modeling and fault construction and restoration, and compare these results to recent deformation rates obtained through space geodetic techniques (GPS). Based on these data, recurrence intervals for large intraplate events within the Chilean forearc were approximated. In addition, historical subduction related earthquake faulting is tested for its ability in

reducing or enhancing deformation along the studied faults. Finally, the results obtained in the study area are placed into the framework of the Central and Southern Andean plate convergent margin and related to similar forearc settings as observed along the Chilean coast.

The key questions to be answered for a better understanding of the deformational processes in the Chilean forearc are as follows:

1. What are the characteristic fault patterns and geometries of intraplate faults in the forearc between 30°-31° S?
2. What are the orientations of the principal deformation axes inferred from fault-slip data, how do these change in space and time and of what type is the most recent deformation?
3. Is the observed deformation related to instantaneous fault behavior and is this type of deformation likely to have occurred during the Holocene and/or historical times?
4. Do principal strain rates and principal strain axes orientations inferred from fault-slip data and elastic half space modeling match the results obtained from GPS residual velocities?
5. What are the possible causes for the massive uplift of the Coastal Cordillera observed in the study area?
6. What are possible recurrence times for intraplate earthquakes and where does future intraplate faulting most likely occur in the study area?
7. How is the study area structurally related to other regions along the Central and Southern Andean forearc and how representative is the deformation, observed in the study area, for the Nazca-SA plate boundary as a whole?

## 1.2 Conceptual Framework

Within the framework of this thesis a multidisciplinary approach was chosen in order to address the aforementioned questions. This study applies various results from the fields of *neotectonics*, *structural geology*, *elastic half-space modeling* and *geodesy* in order to better constrain the geologically derived deformation rates and to create a sufficient overview on the issue of intraplate deformation in a plate convergent forearc setting. In the following the contributions of the particular approaches are pointed out briefly:

- **Neotectonics:** Identification of active crustal faults and coseismic deformation by field observation (paleoseismology); Determination of principal strain directions (fault-slip data analysis); Quantification of deformation rates (tectono-geomorphology)
- **Structural Geology:** Constraining fault parameters by fault construction and restoration on a type example (balanced profile)
- **Elastic Half-space Modeling:** Setting further constraints to intraplate fault geometries at depth (modeling fault related topographies); Approximating short-term crustal strain rates caused by large interplate earthquakes (strain redistribution)

- **Geodesy:** Approximating long-term intraplate deformation rates in the forearc (GPS residuals); Estimation of recurrence times for characteristic  $M_w 7$  intraplate normal faulting events (differential motion)

As part of the conceptual framework the area between Tongoy ( $30.25^\circ\text{S}$ ) and Quebrada Teniente ( $31.00^\circ\text{S}$ ) was chosen because of its widespread prevalence of Cenozoic sedimentary rocks and the abundance of crustal faults. In addition, the predominantly semi arid climate of North Central Chile favors both, the creation and the preservation of neotectonic outcrops. General scarcity of precipitation prevents the geologic units from significant physical and biochemical erosion, whereas sporadic heavy rainfall and seasonal snowmelt runoff from the High Andes cause the rivers and creeks to incise steeply into their beds, leaving excellent outcrop conditions.

## 2 Geodynamic and Neotectonic Setting

### 2.1 Nazca-South America Plate Convergence

The convergent plate boundary between the Nazca and South America (SA) plates stretches over 5000 km from Colombia to southern Chile (Fig. 1.1). Its southern boundary is outlined by an active spreading center, the Chile Rise, which forms a triple junction at its intersection with the Nazca-SA plate boundary near 46° S latitude. At the triple junction the oceanic lithosphere is very young (0-5 Ma) but increases in age gradually towards the north. Between 30°-31° S the presently subducted oceanic crust has an age of 43 – 55 Ma [Gutscher et al. 2000]. In North Central Chile, the Nazca plate subducts beneath the SA continent at a present-day convergence rate of  $\sim 65 \text{ mm yr}^{-1}$  and an azimuth of N77° E [Angermann et al. 1999]. This results in a present-day convergence obliquity of  $\sim 20^\circ$  (Fig. 2.1).

The oceanic plate begins to flex downward into the subduction zone about 50 km west of the trench axis, dissecting the oceanic crust into numerous horst and graben structures which trend 8° diagonal to the trench. The fault scarps separating the horsts and grabens are locally up to 800 m high but generally do not exceed 500 m near the trench axis [von Huene et al. 1999]. The trench of North-Central Chile is almost devoid of sediments in its northern parts but fills rapidly towards the south after crossing the so called *dry diagonal*, which separates the arid north of Chile from the more humid south. The topographic expression of the downgoing slab is that of a sawtooth pattern (Fig. 2.2) which is assumed to be responsible for subduction erosion processes taking place at the base of the continental plate. Subduction erosion provides a mechanism which causes mass deficit due to material transported down dip into the *subduction channel*, destabilization, and gravitational collapse of the slope. The continental slope itself is characterized by similar horst and graben structures as in the oceanic crust, outlined by east- or west-dipping normal faults subparallel to the trench. The estimated long-term continental slope retreat amounts to  $1 - 2 \text{ km Ma}^{-1}$  [von Huene et al. 1999].

The Andean subduction zone is also characterized by major along-strike variations related to significant changes of the slab geometry. These changes are observed in the depth range between 100 – 200 km (Fig. 1.1), where the oceanic crust continues as a subhorizontal slab under the Andean orogen. This phenomenon was first identified as *flat slab subduction* by Barazangi and Isacks [1976]. The Central Chile flat slab segment is located between 28°- 33° S. It is inferred from earthquake locations and focal mechanism solutions of the geometry of the Wadati-Benioff zone. A sharp flexure in the downgoing slab near 33° S latitude changes the subduction angle from nearly horizontal to almost 30° [Cahill and Isacks 1992]. The development of flat slab subduction is commonly attributed to inhomogeneities in composition and bathymetry of the oceanic plate, such as aseismic ridges [Gutscher

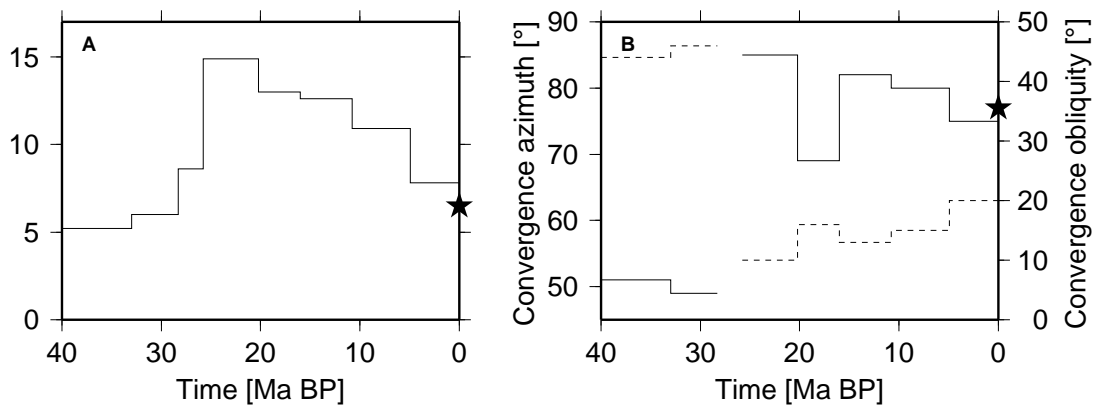


Figure 2.1: Mean convergence rate, azimuth and obliquity between the Nazca and SA plates at 30° S for the last 40 Ma, modified after Somoza [1998]; A – Mean convergence rate; Star denotes present-day convergence rate of  $6.5 \text{ cm a}^{-1}$  according to Angermann [1999]; B – Solid line indicates Convergence azimuth; Solid star indicates azimuth of N77° E as presented in Fig. 1.1; Dashed line shows convergence obliquity for N5° E striking trenchline.

et al. 2000]. In North Central Chile the Juan Fernandez Ridge is presently subducted beneath the SA continent [von Huene et al. 1997; Flueh et al. 1998; Yanez et al. 2001]. In addition, it has been noted that the extinction of Quaternary volcanism is closely related to the development of flat slab segments in space and time.

### 2.1.1 The Subduction Interface

According to bathymetric profiles by Schweller et al. [1981] the Peru-Chile Trench between 30°-31° S latitude is located 90 km offshore. The strike of the trench is approximately N-S. According to the Andean Elastic Dislocation Model (AEDM) presented by Khazaradze et al. [1999], the plate interface dips east with 16°- 23°. The subduction interface is subdivided into three zones [Oleskevich et al. 1999]: (a) The aseismic zone above the 100°C isotherm or between 2 – 10 km depth, which corresponds to the dehydration of stable sliding smectite clays to illite-chlorite. Further down-dip follows the fully coupled zone (b) where stick-slip behavior prevails. Stick-slip is the overall responsible mechanism for the generation of earthquakes in the subduction zone. The down-dip extension of this zone is limited either by the 350°C isotherm [Hyndman and Wang 1993] or by the 40 km depth level (Fig. 2.2). The latter applies if temperatures of 350°C or higher are reached at depth greater than 40 km [Tichelaar and Ruff 1993]. The depth level of the 350°C isotherm roughly corresponds to the intersection of the thrust interface with the continental forearc Moho at ~40 km depth (Fig. 2.2). Around this point the transition zone (c) marks the change from stick-slip to thermally activated stable sliding behavior of crustal rocks [Oleskevich et al. 1999]. Within the transition zone, slip during large subduction earthquakes gradually tapers out, which is described as a 50% coupling compared to the fully coupled zone, where 100% coupling is assumed [Klotz et al. 2000]. In general, the horizontal distance from the trench to the coastline is ~110 km (Fig. 2.2). In the study area (30°-31° S) the horizontal distance between the Peru-Chile Trench and the coastline is only 65 – 70 km. The up-dip edge of the seismogenic zone (100% coupling) begins ~20 km east of the trench and ends just below

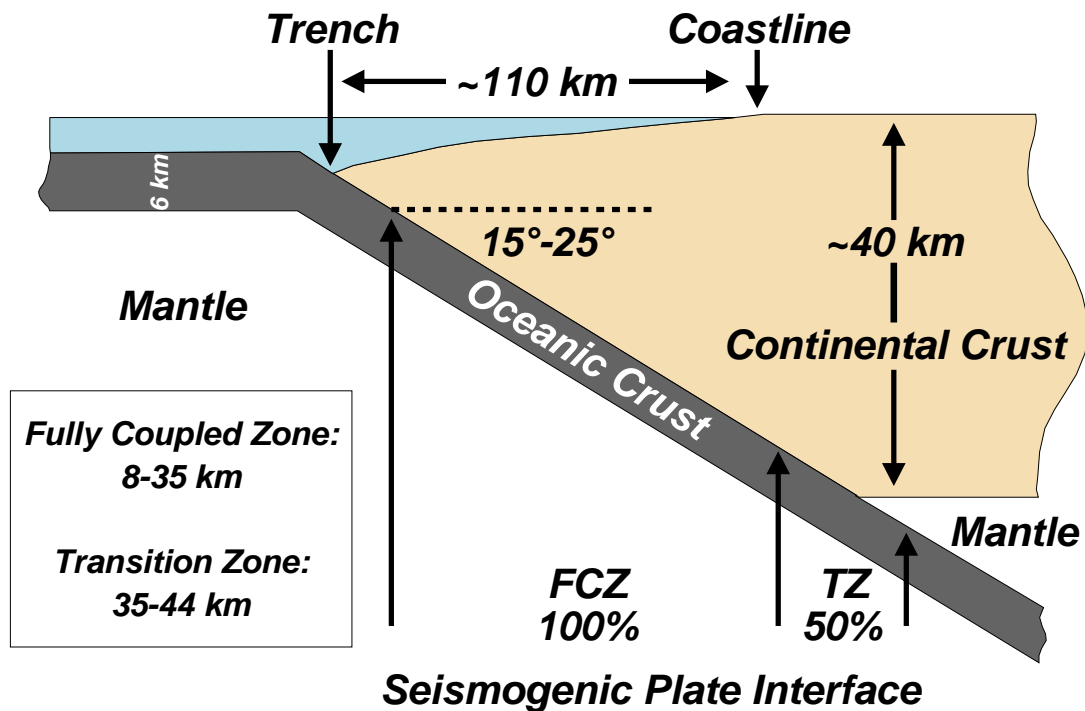


Figure 2.2: Generalized cross-section through the Nazca-SA plate margin, modified after Ruff and Tichelaar [1996]. FCZ – Fully Coupled Zone; TZ – Transition Zone.

the present-day coastline. In general, the position of the down-dip edge of the transition zone roughly falls in place with the coastline [Ruff and Tichelaar 1996]. According to the AEDM [Khazaradze et al. 1999], in the study area the down-dip edge of the transition zone is located  $\sim 50$  km landward from the coastline. Given the  $16\text{-}23^\circ$  dip angle of the plate interface as stated above, the depth range for the fully coupled parts of the interface is limited to 8 – 35 km depth, while the transition zone is constraint to 35 – 48 km depth (Fig. 2.2).

### 2.1.2 Interaction between Interplate and Intraplate Deformation

The subduction interface between the oceanic slab and the continental crust is generally locked. Due to the locking of the interface the plate convergence causes the accumulation of strains in the subduction zone. In turn, the build-up of strains in the subduction zone causes the deformation of the overriding continental crust. Assuming an elastic behavior of the continental crust [Okada 1985], a great deal of the deformation is predestined to be reversed. The reversal of elastic deformation is accomplished by periodically occurring large subduction earthquakes. These earthquakes predominantly occur when the locking forces (*shear strength*) of the plate interface are overcome by the *shear strains* acting along the subduction zone. The alternation between strain accumulation and strain release along the subduction interface is commonly referred to as the *seismic cycle* [Fedotov 1968].

The seismic cycle itself is subdivided into three stages - the *interseismic* strain accumulation between two earthquakes, the *coseismic* strain release during the actual earthquake rupture process and the *postseismic* relaxation phase, which gradually decays back to the interseismic state. For very

large earthquakes (e.g. 1960 Valdivia  $M_L$ 9.5) this phase can last for several decades as observed from GPS residual velocities between 38°-42° S [Khazaradze and Klotz 2002]. However, the same authors report a much shorter postseismic phase for the 1995 Antofagasta  $M_w$ 8.0 event. Here the postseismic effects were only detected for 2-3 years after the earthquake. Because the Chilean forearc is frequently struck by large interplate earthquakes, coseismic energy is released by elastic waves, inducing second-order interplate as well as intraplate deformation and loading or unloading of adjacent active faults in the neighboring crusts. Eventually these loading processes lead to the activation of intraplate faults in the continental crust. The reactivation of the *Salar del Carmen* fault during the 1995 Antofagasta event provides convincing evidence for this phenomenon (Gonzalez, 2002 pers. comm.). Hence, the interaction between the subducting and the overriding plates possibly provides the driving mechanism for the deformation processes within the continental forearc of the South American continent [Klotz et al. 2001].

## 2.2 Neotectonics in the Central and Southern Andes – State of Research

### 2.2.1 The Forearc

The first observations of crustal deformation along the Nazca-SA plate boundary to be published were the cruise reports of Charles Darwin [1891], who attributed coastal uplift phenomena to the combined effects of small coseismic episodes and episodes of "insensibly slow rise". Darwin witnessed the Concepción earthquake of 1835 and later gave a detailed description of the geologic effects on Quiriquina Island which was uplifted as a whole by roughly 2.5 m after the event. "*The Palaeozoic basement rocks of the island were shattered at the surface, large north-south fissures opened up and great masses of rock broke away from the cliffs*" [Lomnitz 1970].

Brief outlines of Quaternary tectonics along the continental margin of Chile were later presented by Segerstrom [1964] and Paskoff [1977] who described the forearc as to be characterized by overall extension along normal faults that limit uplifted, downwarped and tilted blocks. Katz [1971] stressed the fact that counterintuitive to the overall compressive regime of plate convergence "*the tectonic style in the overriding crust is extensional rather than contractional, affecting an area of up to 300 km landward from the trench*". The Atacama Fault zone (AFZ) was one of the first crustal structures in the Chilean forearc to be studied by means of neotectonics. An example of Quaternary surface rupture along the AFZ was published by Brügger [1950], who first described a scarp near Antofagasta (23.5°S), a few meters high and several kilometers long, that cuts an alluvial fan built up during the Pleistocene along the eastern limits of the Coastal Cordillera. Okada [1971] found a fault scarp at the western limits of the Salar Grande (21°S) disrupting talus cones and Segerstrom [1965] reports a 40 – 50 m offset within early Quaternary strata on a NNE-striking, E-dipping normal fault crossing the lower course of Río Copiapó (27.3°S). Geomorphological studies in the *El Salado Valley* near *Chañaral* (26° S) strongly suggest that the AFZ accommodates at least part of the uplift of the Coastal Cordillera by normal faulting along its major fault traces up to the present date [Riquelme et al. 2003].

Recent neotectonic studies focused on the inversion of principal stress/strain axes from fault-slip data, the recording of crustal seismicity, the determination of average uplift rates of the coastal zones and the study of coseismic effects related to large earthquakes in the subduction zone. The forearc of

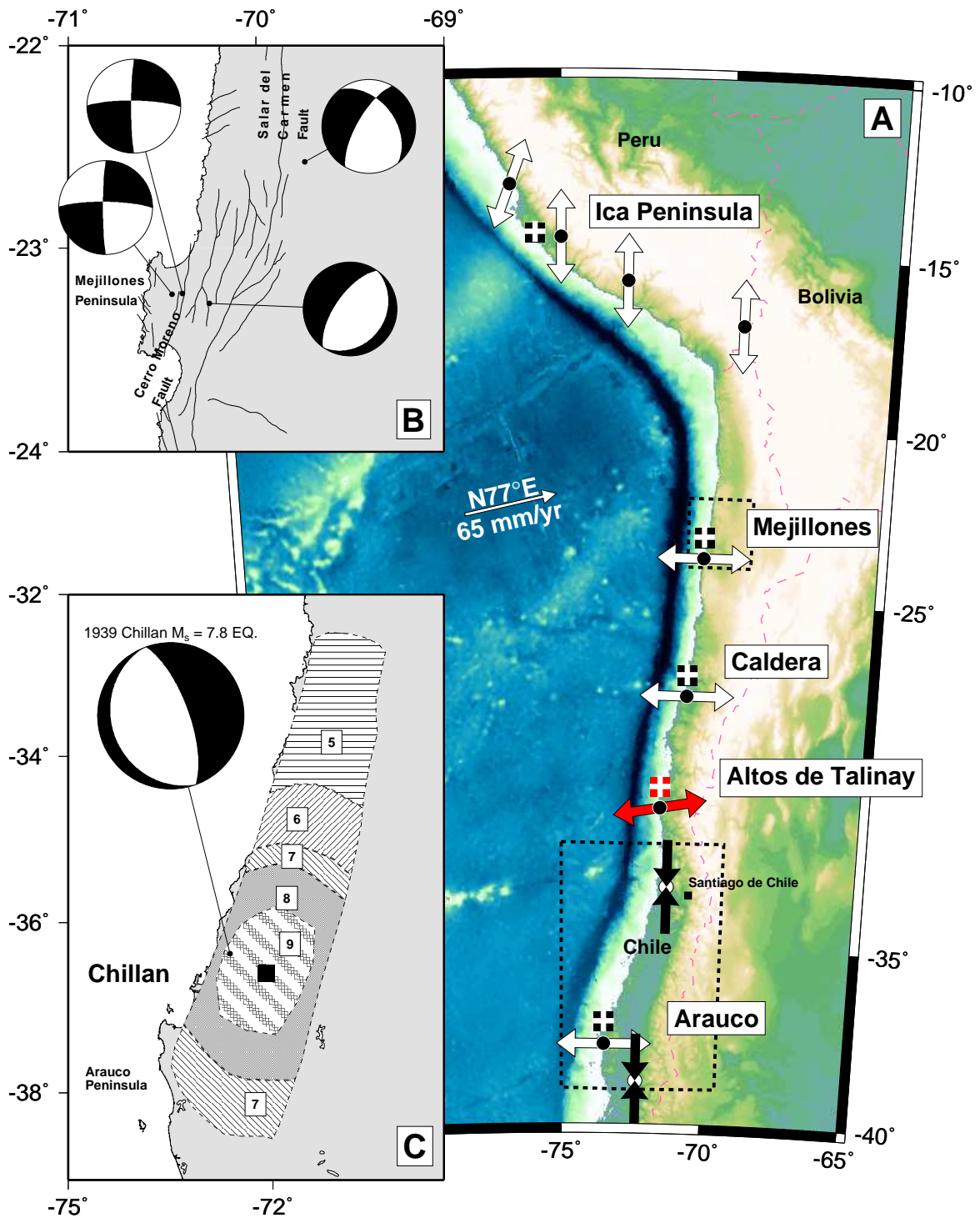


Figure 2.3: Neotectonic deformation patterns and crustal seismicity in the Central and Southern Andean forearc, compiled from various authors (A: [Lavenue et al. 1999], B: [Comte et al. 1992]; C: [Beck et al. 1998]); A – Deformation inferred from fault-slip data; White arrows indicate zones of predominant extension; Black arrows show regions of overall contraction; Plus signs indicate strongly uplifted regions of the Coastal Cordillera; Gray arrow denotes deformation presented in this study; Seafloor and continental topography as in Fig. 1.1; B – Crustal seismicity < 30 km depth near Antofagasta, Northern Chile; C – Focal mechanism and intensity map (MMI) for the 1939 Chillan  $M_s 7.8$  crustal(?) event.

northern Chile between 20°-24° S latitude is dominated by NS-striking normal faults displaying vertical offsets of up to 300 m. In some parts the E-W extension rate reaches 1-1.5% or 500 – 1000 m over a width of 70 km since the beginning of the Neogene [Pelz 2000]. Based on observations along N-S striking crustal normal faults on Mejillones Peninsula and near Antofagasta (23°-24° S) (Fig. 2.3 A) Armijo and Thiele [1990], Delouis [1998] and Marquardt [2000] show that the predominant deformation regime in the forearc is E-W extension. Observed slip vectors and surface displacements along these faults generally indicate normal and/or left-lateral strike slip. Further south near Caldera (27° S; Fig. 2.3 A) a NNE-SSW trending normal fault scarp with a vertical offset of up to 4 m is observed. The age of the displaced marine sediments is constrained to < 125 ka [Marquardt and Lavenu 1999]. Lavenu and Cembrano [1999] studied Quaternary brittle deformation in the forearc and intraarc zones between 33°- 46° S latitude (Fig. 2.3 A). They found trench parallel (N-S to NNE-SSW) compression ( $s_1$ ) in the forearc zone and transpressional deformation with  $s_1$  oriented NE-SW in the intraarc zone. On Arauco peninsula, which is located in the outer forearc, E-W extension was observed. Eight years after the great 1960 Valdivia earthquake ( $M_w = 9.5$ ) Plafker and Savage [1970] resurveyed a triangulation network set up in the 1950s by the Instituto Geografico Militar de Chile between 38°-41° S latitude. Their data reveal significant E-W extensional strains (25 – 50  $\mu$  strain) and slightly lower N-S compressional strains in the forearc. According to these authors the deformations have to be attributed to the coseismic and postseismic effects of the Valdivia earthquake.

Crustal seismicity (< 30 km) was recorded in Northern Chile between 22.5°-24.5° S. Focal mechanisms show pure normal faulting or normal faulting with a left-lateral component along NE-SW striking intraplate normal faults (Fig. 2.3 B). In addition, focal mechanisms inferred from two crustal earthquakes located near the Cerro Moreno fault on Mejillones Peninsula show left-lateral strike-slip motion along N-S striking fault planes [Comte et al. 1992]. In Central and Southern Chile, Fuenzalida [1993] showed that shallow earthquakes with hypocenters < 30 km are abundant and eventually induce coseismic surface rupture (e.g.  $M_s$  6.8 on Sept. 4<sup>th</sup>, 1958). The majority of the earthquakes occur at depths greater than 10 km; however, related focal mechanisms are mainly inconsistent with principal stress directions inferred from fault-slip data [Lavenu and Cembrano 1999, and ref. therein]. An exception forms the February 24<sup>th</sup>, 1989 event located in the intraarc zone southeast of Temuco [Dziewonski et al. 1990], which shows NE-SW compression. Near La Serena (30°S), a moderate - strong intraplate crustal earthquake was recorded in 1969 [ISC 2001]. The magnitudes reported for this event range from  $M_s$  5.5 to 6.1. The earthquake was felt in the city of La Serena with an intensity of IV (MMI), about 75 km north of the hypocenter location.

The most devastating earthquake during the 20th century in Chile occurred in 1939 near the city of Chillan (Fig. 2.3 C). According to focal mechanism solutions [Beck et al. 1998], this earthquake is termed an intraplate event that either occurred within the upper crust at  $\sim$  10 km depth or within the subducting slab at 80 – 100 km depth. However, the long duration of this event and the large area of high intensities (MMI = VIII-IX, see Fig. 2.3) compared to its size ( $M_s$  7.8) suggests that the earthquake might have occurred at shallow crustal depth rather than within the subducting slab. In addition, the strike (N320°-350° E) and the dip (60°- 80° E) of the fault plane, as inferred from waveform analysis [Beck et al. 1998], largely corresponds to the strikes and dips reported by many authors for crustal faulting geometries in the Chilean forearc.

### 2.2.2 The Backarc

Though not the subject of this thesis the general style of crustal deformation in the *Andean backarc* shall be presented here briefly. The most important morphostructural units in the backarc adjacent to the study area ( $27^{\circ}$ - $33.5^{\circ}$  S) are the *Subandean fold and thrust belt* and the *Sierras Pampeanas* in NW Argentina. In contrast to the forearc deformation, as stated above, the backarc is governed by ENE-WSW to NE-SW shortening, along NW-SE striking and northeast verging thrust planes in the Subandean fold and thrust belt. The Frontal Cordillera of NW Argentina exhibits significantly higher frequencies of crustal seismicity than the neighboring backarc segments, implying a higher ratio of intraplate deformation. A possible cause for this increase of crustal seismicity is the existence of a flat-slab segment in this part of the subduction zone [Cahill and Isacks 1992; Ramos et al. 1996; Kley et al. 1999; Heredia et al. 2002]. Flat slab segments develop due to the buoyancy of thickened oceanic crust of moderate to young age being subducted beneath the SA continent. Interestingly, the present day location of the subducted Juan Fernandez Ridge as predicted by Yanez et al [2001] is exactly beneath the Sierras Pampeanas. Gutscher [2000] finds a 3-5 times greater seismic energy release above flat slab segments than above adjacent steep slab segments based on statistic analysis of earthquakes at  $< 70$  km depth and 250 – 800 km horizontal distance from the trench.

The geological setting of the Subandean fold and thrust belt between  $30.5^{\circ}$ - $31.35^{\circ}$  S is characterized by polycyclic tectonics along east verging structures. The Palaeozoic basement shows characteristic thin-skinned tectonics, while Mesozoic sediments from the Andean orogenic cycle indicate remarkable amounts of extension followed by a Tertiary compressional tectonic regime [Heredia et al. 2002]. Late Cenozoic deformation styles in the backarc of NW-Argentina (Qbd. del Toro) were inferred from stratigraphical, chronological and fault kinematic data by Marrett and Strecker [2000]. They find a NW-SE compressional regime initiated in Late Miocene times and lasting for about 1 Ma. Between Late Miocene and 4.17 Ma BP this regime was replaced by NE-SW directed contraction resulting in NW-SE striking thrust faults. The NE-SW contraction continues to be the observed present-day deformation style in NW Argentina. The fluctuations in the orientation of intraplate deformation directions during the Late Cenozoic are explained with changes in the absolute motion of the SA plate with respect to the hotspot reference frame. The geologically derived shortening in the Subandean fold and thrust belt at  $30^{\circ}$  S latitude amounts to 95 km during the last 10 – 50 Ma [Allmendinger et al. 1990]. The resulting backarc shortening rate is  $0.63 - 0.95 \text{ cm a}^{-1}$ , which accounts for no more than 10-15% of the geodetically inferred Nazca-SA plate convergence rate of  $\sim 6.5 \text{ cm a}^{-1}$  [Angermann et al. 1999].

### 2.2.3 Coastal Uplift Phenomena

The Chilean forearc provinces are characterized by strongly uplifted marine terraces and abrasion platforms. In addition, dune formation and sand-barred estuaries of major rivers indicate ongoing coastal uplift along the Chilean coast. Quaternary uplift rates calculated by several authors [Hsu et al. 1989; Atwater et al. 1992a; Leonard and Wehmler 1992; Ota and Paskoff 1993; Ota et al. 1995; Ortlieb et al. 1996b] vary between  $0.1 - 0.8 \text{ m ka}^{-1}$ . The higher uplift rates ( $> 0.4 \text{ m ka}^{-1}$ ) usually account for frontal forearc positions with greater proximity to the trenchline, e.g. the Altos de Talinay.

<b>Author</b>	<b>Area</b>	<b>Method</b>	<b>Uplift rate</b> [ $m\ ka^{-1}$ ]
Hsu (1989)	Peru, Nazca Ridge	Mollusk aminostratigraphy	0.1-0.5
Leonard (1992)	Herradura Bay Coquimbo Bay	Mollusk aminostratigraphy	0.08-0.15
Ota (1993)	Tongoy Bay Altos de Talinay	Radiocarbon Terrace correlation	0.1-0.3 0.4-0.5
Pelz (2000)	North Chile	Numerical modeling	0.084
Adam, Lohrmann (2002)	erosive plate margin	analogue sandbox modeling (regional/localized uplift)	0.47-0.75

Table 2.1: Coastal uplift rates [ $m\ ka^{-1}$ ] for determined by various authors for selected sites in Chile and southern Peru. Values from Tongoy Bay and Altos de Talinay directly refer to the study area. Data for Herradura and Coquimbo Bay were obtained 50 km north of the study area.

The lower uplift rates are typically observed in segments of the forearc that are more distant from the trenchline. Occasionally, zones of faster and slower emergence are observed in immediate vicinity to each other, as is the case for a number of peninsulas along the southern Peruvian and Chilean coasts, e.g. Ica, Mejillones, Altos de Talinay, and Arauco (see Fig. 2.3 A). The Coastal Cordilleras of these regions typically consist of strongly uplifted basement complexes, which in turn are bordered by Cenozoic basins on their landward flanks. Despite the fact that both structural units show evidence of substantial uplift, the uplift rates observed in the Coastal Cordillera are significantly higher than those inferred for the marine terraces topping the Cenozoic basins. In addition, several authors [Leonard et al. 1988; Hsu et al. 1989] found that periods of substantial uplift must have alternated with times of subsidence and terrace reoccupation in the Cenozoic basins.

It is not yet understood what are the driving mechanisms for the uplift in the forearc. Coseismic and postseismic uplift and or subsidence were frequently observed as an immediate response to the rupture of the seismogenic interface during large subduction earthquakes [e.g. Darwin 1846; Ortlieb et al. 1996a]. The subduction of aseismic ridges as proposed by Machare [1992] provides a possible mechanism for rapid uplift. A third source for the elevation of coastal areas is the interaction between tectonic erosion and subsequent underplating of basally eroded material in the subduction interface. This process has been studied using analogue sandbox models [Adam and Kukowski 1999]. Uplift rates inferred from analogue sandbox modeling range from  $0.47 - 0.75\ m\ ka^{-1}$ .

## 2.3 Geological Setting of the Study Area

### 2.3.1 Morphostructural Units and Stratigraphy

The study area stretches over 85 km in N-S direction between *Bahia Tongoy* and *Quebrada del Teniente* (30.25°-31° S) covering an E-W width of ~45 km between the shoreline and the Precordillera. The dominant morphostructural units are the *Coastal Cordillera (CC)* in the west, namely the *Altos de Talinay*, the *Cenozoic Basin (CB)* in the north-central and central parts, and the mountain blocks in the north-eastern and south-eastern parts, hereafter referred to as the *Cretaceous Arc (CA)* in Fig. 2.4).

The *Coastal Cordillera* is 300 – 750 m high with its highest peak, the *Cerro Talinay*, located 10 km southeast of the *Río Limarí* estuary. Its western shores are dominated by 2.5 – 5 km wide wave-cut platforms at elevations of 100 – 200 m. Internally, the Coastal Cordillera is dissected by N-S striking, east- or west-dipping normal faults. In many places the topography is characterized by oversteepened hillslopes, indicating recent crustal faulting activity. The Cenozoic basin is separated from the Coastal Cordillera by the NNW-SSE striking, 60 km long *Puerto Aldea Fault (PAF)*, an east dipping normal fault named after a village in the southwestern corner of Tongoy Bay. Along the PAF the same basement rocks that are forming the Coastal Cordillera are subducted to depths of 600 m b.s.l. (see contour lines in Fig. 2.4).

The *Cenozoic Basin* is characterized by the formation of a broad marine terrace, the *Great Plain* [Paskoff 1970], which extends from the southern shores of Tongoy Bay deeply into the continental forearc, covering an area of ~ 500 km<sup>2</sup>. The Great Plain gently (~ 0.2°) dips towards the northwest. It represents a single planation surface spanning various lithological units, i.e. marine sediments in the north and fluvial deposits in the center and the south. Towards the center of the study area, the marine deposits gradually interfinger with the fluvial sediments. Despite the lithological changes within the terrace deposits, the planation surface continues unperturbed towards the south and the east, indicating that both the marine and the continental successions were leveled subsequent to their formation. The only perturbations within the Great Plain are formed by the numerous N-S striking fault traces (see also Fig. 4.1), indicating that faulting activity occurred after the formation of the Great Plain. The northern and central parts of the Great Plain is incised by broad, 50 – 100 m deep, U-shaped valleys hosting the major rivers of the study area. The largest river, *Río Limarí*, intersects the Coastal Cordillera perpendicular to its strike, leaving a spectacular gorge of 600 m depth and 20 km length. The incision of the valley into the relatively resistant basement rocks of the Altos de Talinay is likely to have occurred simultaneously to their uplift. This observation allows for the interpretation of the *Río Limarí* gorge as an *antecedent valley*. Other examples for antecedent valleys crossing the Coastal ranges are known from Northern Chile, e.g. the *Quebrada Camarones* at 19° S [Paskoff 1996].

The *Cretaceous Arc* reaches elevations of up to 1350 m a.s.l.. The hillslopes are gently curved and erode radially. In the central part the *Limarí* river eroded most of the Cretaceous Arc leaving a gap which was refilled with fluvial deposits reaching up to 200 m in thickness (Fig. 2.6). No major structural elements can be detected throughout its ranges apart from a N-S striking fault 1 km east of the city of Ovalle. However, 65 km east of the study area a normal fault of regional scale was mapped by several authors [Bohnhorst 1967; Paskoff 1970]. This fault separates the Precordillera

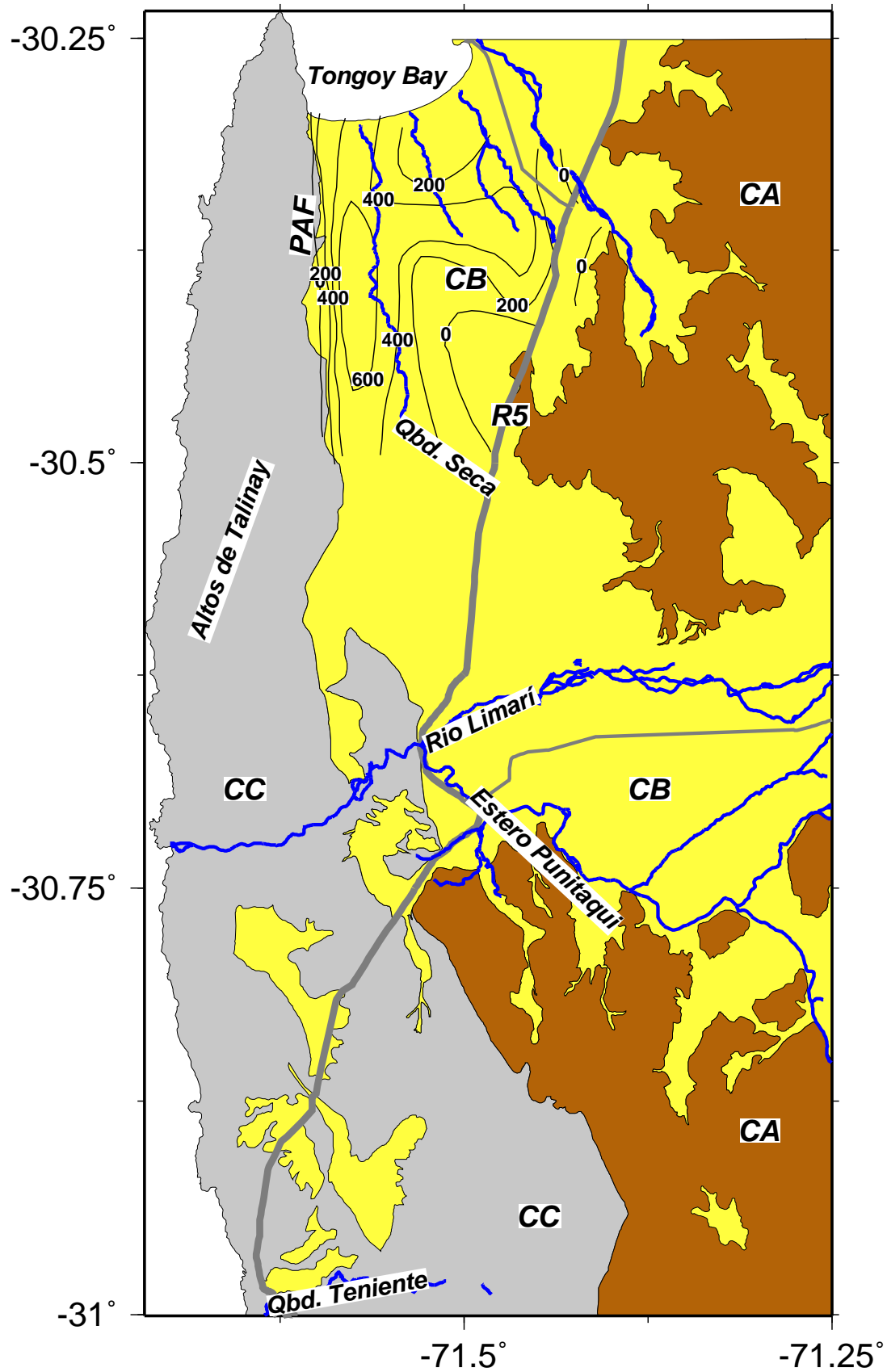


Figure 2.4: Morphostructural units and major rivers in the study area; CA – Cretaceous Arc; CB – Cenozoic Basin; CC – Coastal Cordillera; PAF – Puerto Aldea Fault; R5 – Pan American Highway; Contours – Depth of basement [m b.s.l.] adopted from [Paskoff 1970].

from the High Andes over a length of  $> 300$  km. The coastline of the Altos de Talinay region protrudes significantly towards the west when compared to adjacent coastal areas. This westward shift is in the order of  $20 - 30$  km and remarkably reduces the distance between the Coastal Cordillera and the Peru-Chile Trench. Due to its protruding nature, the coastline is much stronger exposed to coastal erosion processes. This exposure leads to the formation of typical *lee shores* as can be observed at its northern tip. Interestingly, similar observations with respect to the coastal morphology and structural geology can be made at Mejillones Peninsula ( $23^{\circ}$ - $23.5^{\circ}$  S) and Caldera ( $27^{\circ}$  S) in the north, and Arauco Peninsula ( $37^{\circ}$ - $37.5^{\circ}$  S) in the south. The positions of these regions along the Chilean forearc are indicated in Fig. 2.3.

### 2.3.1.1 The Coastal Cordillera

The Coastal Cordillera predominantly consists of Precambrian to late Paleozoic metamorphic rocks and Mesozoic plutons and dikes [Bohnhorst 1967]. Near *Punta Lengua de Vaca* and 6 km south of *Ensenada Mar Gruesa* Bohnhorst [1967] determined Lower Triassic ages ( $219 \pm 20$  Ma BP &  $223 \pm 25$  Ma BP) for granodiorites and granites (Fig. 2.5). Granites near *Peña Blanca* revealed Upper Carboniferous-Lower Permian ages ( $276 \pm 30$  Ma BP). The Jurassic granites and granodiorites are relatively well constrained to  $134 \pm 10$  Ma BP based on K/Ar ages [Gana 1991]. According to Irwin [1988], the Coastal Cordillera between  $30.85^{\circ}$ - $31^{\circ}$  S is composed of highly metamorphosed ultra-basic and basic extrusives, cherts, arkoses, and conglomerates which have been subject to polyphase metamorphism. He distinguishes three deformation phases:

1. The first deformation phase took place between  $220 - 200$  Ma BP and produced compositional layering and amphibolite-facies metamorphism. The metamorphism was accompanied by the intrusion of an extensive igneous complex composed of fine-grained gabbro and monzogranite.
2. A second phase between  $163 - 140$  Ma BP can be inferred from K/Ar and Rb/Sr ages. This phase is characterized by the formation of *reverse faults and tight recumbent folds* and was accompanied by the emplacement of large quartz diorite and gabbro plutons.
3. In a third stage between  $140 - 126$  Ma BP *upright, open to tight folds* with N-S striking and steeply E-dipping axial planes developed.

In addition, three generations of dikes, from Jurassic to Mid-Cretaceous age can be distinguished. The Jurassic dikes are near vertical and trend either N-S or E-W while the Cretaceous dikes are oriented E-W, perpendicular to the Peru-Chile trench. The formation of dikes can also be subdivided into three stages - (1) Diabasic dikes of Jurassic age or older. (2) Jurassic - Early Cretaceous alkaline - sub-alkaline dikes and (3) Mid-Cretaceous *ocoites*. The intrusions of calc-alkaline dikes fall within the period of  $160 - 170$  Ma BP, while the alkaline and andesitic dikes intruded around  $145 - 120$  Ma BP, respectively. The intrusion of the Cretaceous dikes took place during the early stages of the eastward shift of the magmatic arc during Mid-Jurassic to Cretaceous times [Farrar et al. 1970].

The presence of alkaline magmas is commonly associated with intraarc or backarc extension [Allen 1986]. This suggests that the study area might have shifted over time from a position much

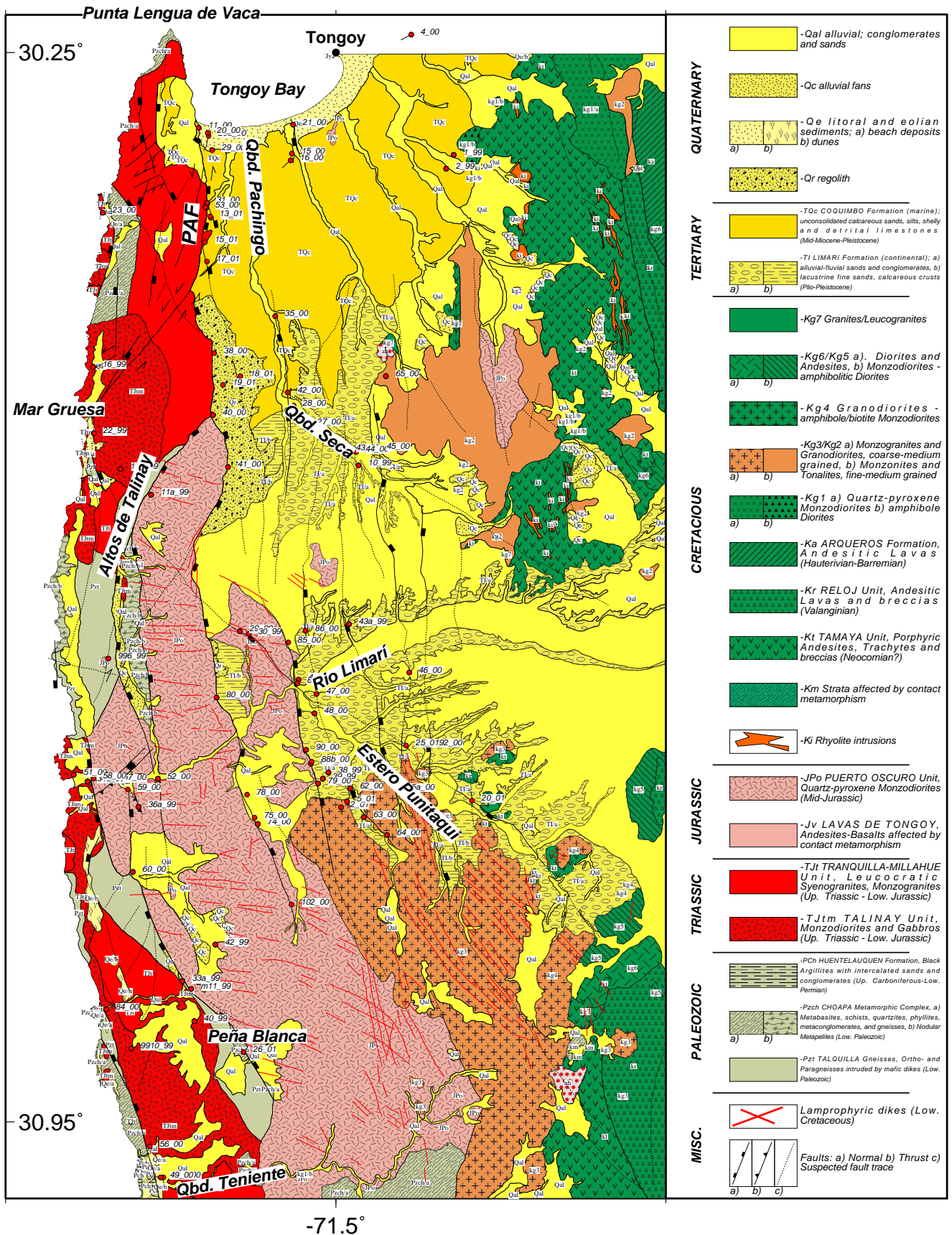


Figure 2.5: Geological map of the study area modified after Gana [1991] and Bohnhorst [1967]. Fault traces are compiled from geological maps and field investigations. Numbers show locations of outcrops as presented in Figs. 4.13 A-C and in Appx. A.1; PAF – Puerto Aldea Fault.

farther inland from the coastline (i.e. backarc position) towards the present location in the forearc. This shift of the position relative to the trenchline would agree with modern concepts of tectonic erosion along the Nazca-SA plate boundary [von Huene et al. 1999]. However, the proposal of a constant trenchward migration and erosion of the continent stated above is contrasted by Hervé [1974] and Forsythe [1982] who consider the coastal region of Central Chile a *Paleozoic forearc province* [Irwin et al. 1988]. This interpretation is based on the occurrence of Late Paleozoic blueschist containing mélanges and high-grade metamorphic rocks along the coast of Central Chile [Irwin et al. 1988] and implies that the forearc remained stable for hundreds of millions of years. Ramos [1988], however, concluded that due to an important period of continental accretion the Paleozoic subduction zone between 30°- 33° S shifted westward over a distance of ~ 300 km. This finding corresponds well with the observations of blueschist metamorphic rocks of Late Paleozoic age along the present-day coastline of the study area but opposes the idea of a long-term stable continental margin.

### 2.3.1.2 The Cenozoic Basin

The Cenozoic basin extends over the north-central and central parts of the study area (Fig. 2.4), reaching a depth of 600 m just below the N-S striking valley of *Quebrada Pachingo* [Paskoff 1970]. Along its western margin the Cenozoic basin borders on the Coastal Cordillera. The sharp lithological contact is related to normal faulting activity along the range-front fault (PAF). In contrast to this, the eastern border with the Cretaceous Arc forms a smooth embayment, which is related to erosion and peneplain formation rather than faulting controlled behavior.

The dominating sedimentary sequence in the Cenozoic basin is the Mid-Miocene to Pleistocene *Coquimbo Formation*, which was first described by Darwin [1846]. It occupies the entire sector between the shoreline of Tongoy Bay and the confluence of *Qbd. Seca* with *Qbd. Pachingo* Fig. 2.5. Outside the study area it fringes the coastline as far north as La Serena. The Coquimbo Formation consists of loosely consolidated calcareous sands and conglomerates, shelly limestones and strongly cemented mussel beds [Paskoff 1970; Martinez 1979; Martinez and Perez 1980; Gana 1991]. Detrital carbonates with sandy matrix and coarse, strongly cemented shell horizons represent shallow marine conditions and beach-ridge environments. In some places, e.g. along the western flank of *Qbd. Pachingo* or south of *El Tangué*, up to 4 m thick layers of diatomite occur. Martinez [1980] analyzed assemblages of siliceous microfossils from these diatomites at the location of *El Rincón*. He concludes that the Coquimbo Formation must be of Mid-Miocene age. The diatomites can be correlated with lithological units found near Caldera (27° S) and Mejillones Peninsula (23°-23.5° S). Based on investigations on foraminiferal assemblages from the same outcrop, Martinez [1979] discovered a 7 – 8 Ma lasting hiatus between the Coquimbo Formation and the overlying sediments of the Plio-Pleistocene transgression. He distinguishes Miocene infralittoral warm water faunas (26°C) out of the Coquimbo formation from cold water faunas out of the overlying Pleistocene rocks. The lithological units are separated by an angular unconformity. Based on the analysis of foraminiferal assemblages, the Miocene terraces of Tongoy and Puerto Aldea can further be synchronized with the *Navidad Formation* on Arauco peninsula (37°-37.5° S).

South of 30.35° S latitude the Coquimbo Formation gradually interfingers with its continental equivalent the Plio-Pleistocene *Limarí Formation* [Bohnhorst 1967; Gana 1991] (Fig. 2.5). The Limarí Formation predominantly consists of fluvial-alluvial deposits. The fluvial deposits are composed

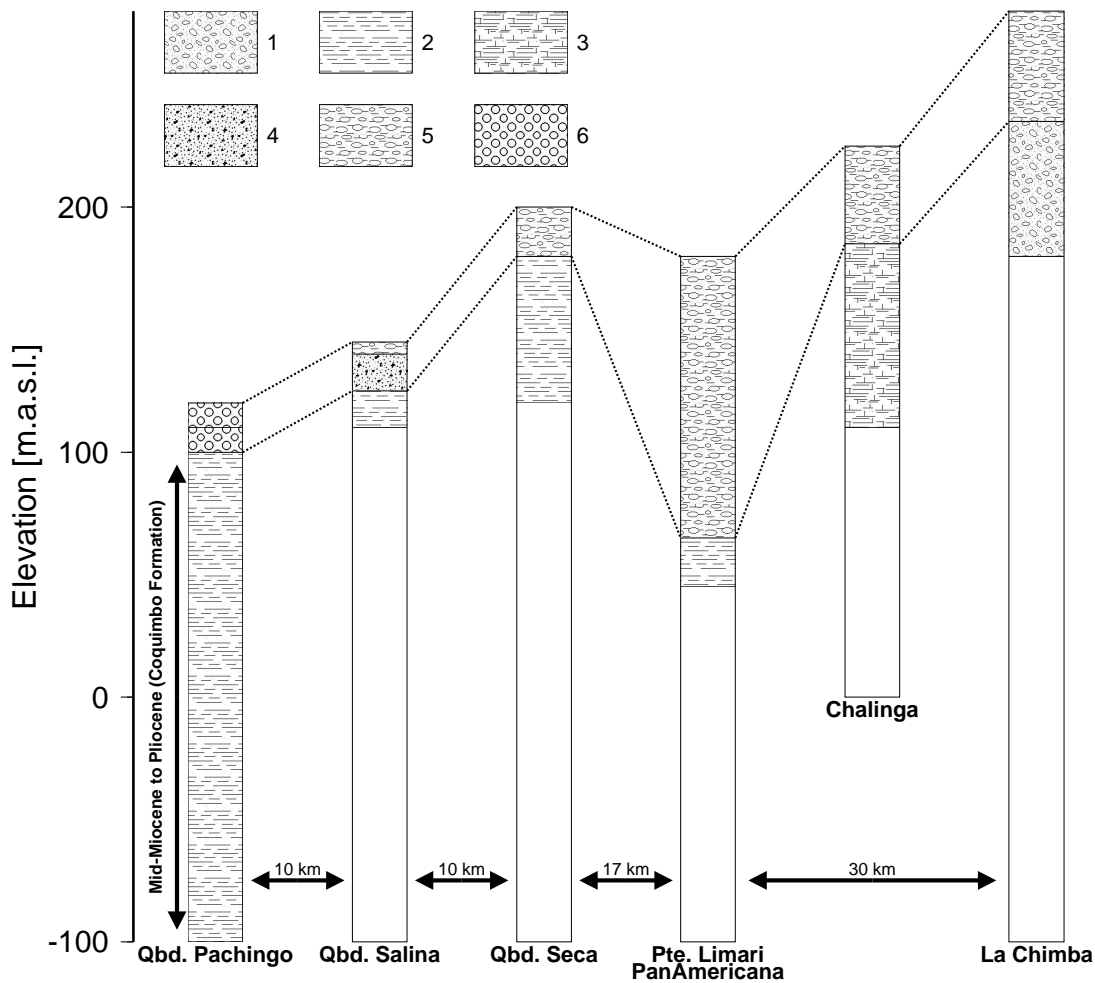


Figure 2.6: Stratigraphic section through the Cenozoic basin deposits and lateral correlation [Paskoff 1970] modified after [Gana 1991] ; 1 – Lower Pliocene continental gravel (Limarí Formation), 2 – Mid-Miocene to Pleistocene marine deposits (Coquimbo Formation), 3 – Plio-Pleistocene lacustrine sediments (Limarí Formation), 4 – Lower Quaternary continental deposits (?), 5 – (Plio)-Pleistocene fluvial conglomerates (Limarí Formation), 6 – Lower Quaternary beach deposits (Serena I terrace), Qbd. – Quebrada Profile of El Rincón with Stratigraphic information from Martinez and Paskoff.

of loosely cemented, coarse grained conglomerates with well-rounded components of cobble-boulder size. The conglomerates are frequently intercalated with lenticular sandbodies of 10 – 50 m length. The maximum thickness of the Limarí formation is found at *Puente Limarí* (Fig. 2.6), where the Limarí river intersects with the range front of the Coastal Cordillera. The southern limits of the Limarí Formation are formed by a NW-SE trending line connecting the villages of Termas Socos, Chalinga and the city of Punitaqui. In places the fluvial deposits are replaced by lacustrine sediments. The lacustrine deposits are restricted to areas of 10 – 15 km<sup>2</sup> and are typically localized on the downthrown sides of eastward dipping intraplate normal faults. They consist of calcareous muds and fine sands [Gana 1991]. Calcareous crusts are commonly found in these sediments. However, their occurrence is also closely associated with the localization of major fault traces throughout the entire Cenozoic basin.

Near the coastline of Tongoy Bay a white calcareous rock called *losa* [Bohnhorst 1967] covers the Coquimbo and partly the Limarí Formation. The *losa* deposits contain abundant fossils which are *undoubtedly of Pleistocene age* [Bohnhorst 1967, and ref. therein]. They are attributed to the Plio-Pleistocene transgression which formed an extensive, gently seaward dipping planation surface (The Great Plain) spanning the northern and central parts of the study area. This surface remains unperturbed by the intercalation of the Coquimbo and Limarí Formations and is only intersected by U-shaped valleys and eventually offset by surface ruptures along N-S striking intraplate faults. The *losa* deposits can easily be detected from aerial views and Landsat TM scenes (Fig. 2.7). They form numerous concentric lineaments that run parallel to the present-day shoreline of Tongoy Bay, each of which possibly represents an individual stage of the Post-Plio-Pleistocene regression. The same *losa* deposits can be observed on Mejillones peninsula (Wilke, 2001 pers. comm.), where radiometric datings of these fossils reveal ages of  $\sim 400$  ka at elevations of  $\sim 150$  m a.s.l. [Gonzalez et al. 2002]. The Coquimbo and Limarí Formations are overlain by Pleistocene alluvial fans along their western margins. The alluvial deposits consist of poorly sorted and moderately rounded rock debris which is referred to as *regolith* by Gana [1991]. The occurrence of hardgrounds within the alluvial fans, suggests a periodical activation of debris flow along the range front, possibly due to climatic changes and recurrent faulting of the PAF.

### 2.3.2 Marine Terraces and Wave-cut Platforms

Around Tongoy Bay and Coquimbo Bay area, a low marine terrace at less than 7 m above present sea level was recognized as early as the middle of the 19<sup>th</sup> century [Darwin 1846; Domeyko 1848; Brüggén 1929]. Already these authors attributed the formation of terraces to recent tectonic uplift of the Chilean coast. Later, Herm & Paskoff [1967] presented a first classification for the marine sediments south of Tongoy Bay. They distinguished four stages of terrace formation. The highest terraces are formed by the **Serena I & II** levels between 40 – 130 m a.s.l.. The lower two terraces, named **Herradura I & II**, fringe the modern coastline at elevations between 5 – 35 m a.s.l. (Tab. 2.2). Below the Herradura II level a Holocene terrace with several paleo beach ridges is developed. Radiocarbon datings of mollusc shells from these beach deposits and Indian shell middens show Holocene ages (2400 – 6000 a BP) [Paskoff 1973; Ota and Paskoff 1993].

Ota [1995] studied the uplift of the Altos de Talinay region, which is characterized by 6 – 8 km wide wave-cut or abrasion platforms on different levels of altitude. He subdivided the abrasion platforms into four stages from *Talinay I-IV* and tried to synchronize these with the terrace levels outlined by Herm & Paskoff [1967]. According to this correlation, the Talinay I level corresponds to the highest marine terrace found in the Cenozoic basin (Serena I), while the Talinay IV level corresponds to the lowermost marine terrace around Tongoy Bay (Herradura II) (see also Tab. 2.2). It is obvious that the uplift rates for the Altos de Talinay region are significantly higher compared to the uplift rates for the neighboring Cenozoic basin. In the Cenozoic basin the oldest terrace level (Serena I) reaches a maximum elevation of 80 – 120 m a.s.l. while the corresponding Talinay I terrace reaches elevations of 200 – 400 m a.s.l. in the northern and southern part, and 675 m a.s.l. in the central part of the study area.

<b>Classifications of Terraces and Abrasion Platforms in the Study Area</b>				
Herm (1967)	HERRADURA II	HERRADURA I	SERENA II	SERENA I
Height [m a.s.l.]	7-15	20-35	40-75	80-120
Ota (1995)	TALINAY IV	TALINAY III	TALINAY II	TALINAY I
Height [m a.s.l.]	20-30	35-50	100-140	200/675/400
Age [ka BP]	125	300	$\geq 330$	$\gg 330$

Table 2.2: Nomenclature and approximated ages for terraces and abrasion platforms in the study area. Herm's [1967] nomenclature applies to terraces found in the Cenozoic basin south of Tongoy Bay. Ota's [1995] classification validates for abrasion platforms in the Coastal Cordillera (Altos de Talinay) between 30.25°-31.00° S. For TALINAY I heights are given as N/C/S with N = North; C = Center & S = South.

Substantial dating of marine terraces was conducted by Radtke [1987]. He primarily applied AMS-<sup>14</sup>C (Accelerated Mass Spectrometer) and ESR (Electron Spin Resonance) dating techniques to mollusc shells. The samples collected along a NW-SE trending profile covering all four stages of terrace formation, reveal ages between 80 – 472 ka BP for the terraces between sea level and 100 – 120 m elevation. There is no clear trend towards older ages away from the coast. This effect is probably related to subsequent terrace reoccupation during sea level highstands, as was observed by Hsu [1989], who used Amino acid enantiomeric ratio data from 200 molluscs collected along the Peruvian and Chilean coasts. Hsu inferred typical uplift rates of 0.1 – 0.2 m ka<sup>-1</sup> for coastal stretches which are associated with normal steep subduction but found uplift rates of up to 0.5 m ka<sup>-1</sup> for terraces that lie immediately above flat slab regions, e.g. the Central Andean flat slab caused by the subduction of the aseismic Nazca Ridge. Leonard [1992] used aminostratigraphy from molluscs for the determination of uplift rates at Coquimbo Bay, approximately 50 km north of the study area. The uplift rates range between less than 0.1 m ka<sup>-1</sup> to no more than 0.2 m ka<sup>-1</sup>. He thinks that the slow uplift rates are the major cause for the successive reoccupation of terraces. The inferred uplift rates are not sufficient to isolate an earlier abrasion platform from subsequent glacioeustatic sea level highstands [Leonard and Wehmiller 1992]. Based on eight radiocarbon dated shell samples, Ota [1993] reports uplift rates ranging from 0.2 – 0.3 m ka<sup>-1</sup>, in the region south of Tongoy Bay. For the Altos de Talinay region he concludes that uplift rates have to be as fast as 0.5 m ka<sup>-1</sup>.

Uplift rates similar to those obtain in and near the study area can be observed farther north and south along the Chilean coast. Ortlieb [1996b] reveals uplift rates of 0.24 m ka<sup>-1</sup> for the last 330 ka, in the Hornitos area (23° S) slightly north of Mejillones peninsula. Marquardt et al. [1999] calculates 0.2 – 0.4 m ka<sup>-1</sup> vertical motion for marine terraces in the Caldera area (27° S). A net Late Holocene emergence of maximum 0.63 – 0.67 m ka<sup>-1</sup>, despite earthquake induced submergence, was observed by [Atwater et al. 1992b] near Maullin and Carelmapu (41.6°-41.7° S). These rates were obtained along coastal stretches that are located at similar distances from the Peru-Chile trench (100 – 110 km) as is the study area. In contrast, Mocha Island (38.5° S) which is located closer to the trenchline (< 60 km), exhibits uplift rates in the order of 6.3 m ka<sup>-1</sup> during the Holocene.

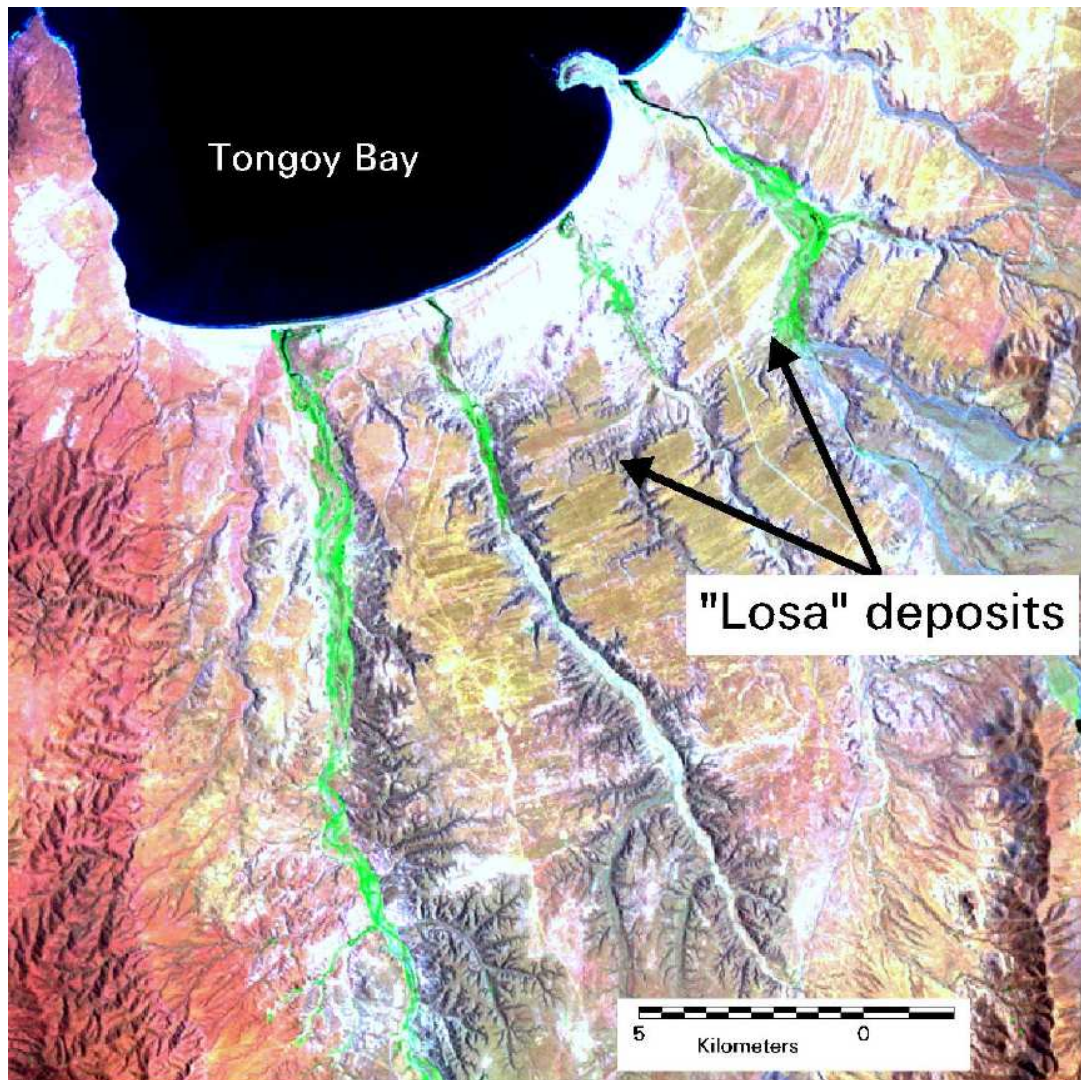
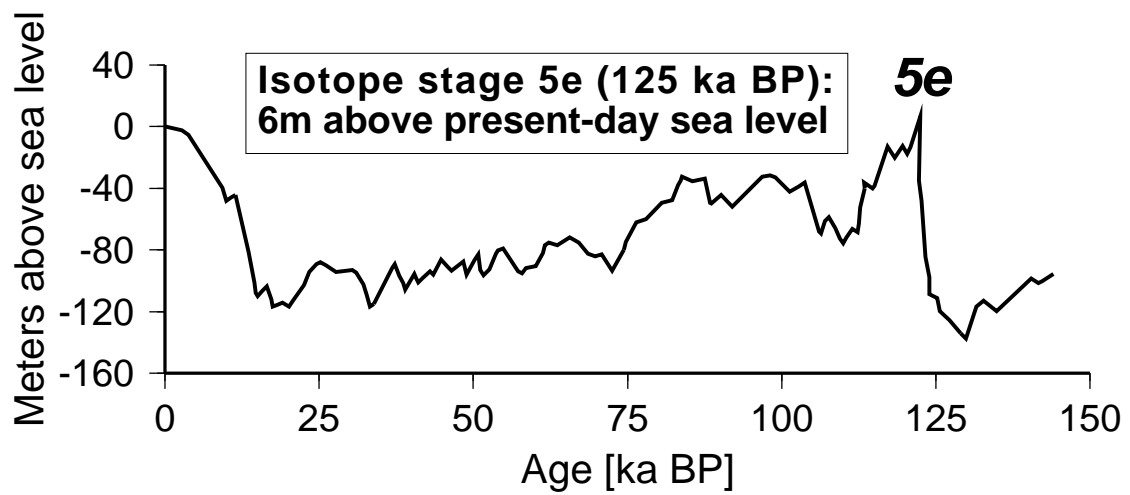


Figure 2.7: Sea level changes since the Late Pleistocene transgression (Isotope stage: 5e) and corresponding *losa* deposits [Jordan 1929; Bohnhorst 1967] south of Tongoy Bay. Circular fringes of *losa* deposits probably outline individual regression cycles since 125 ka BP (Wilke, 2001 pers. comm.).

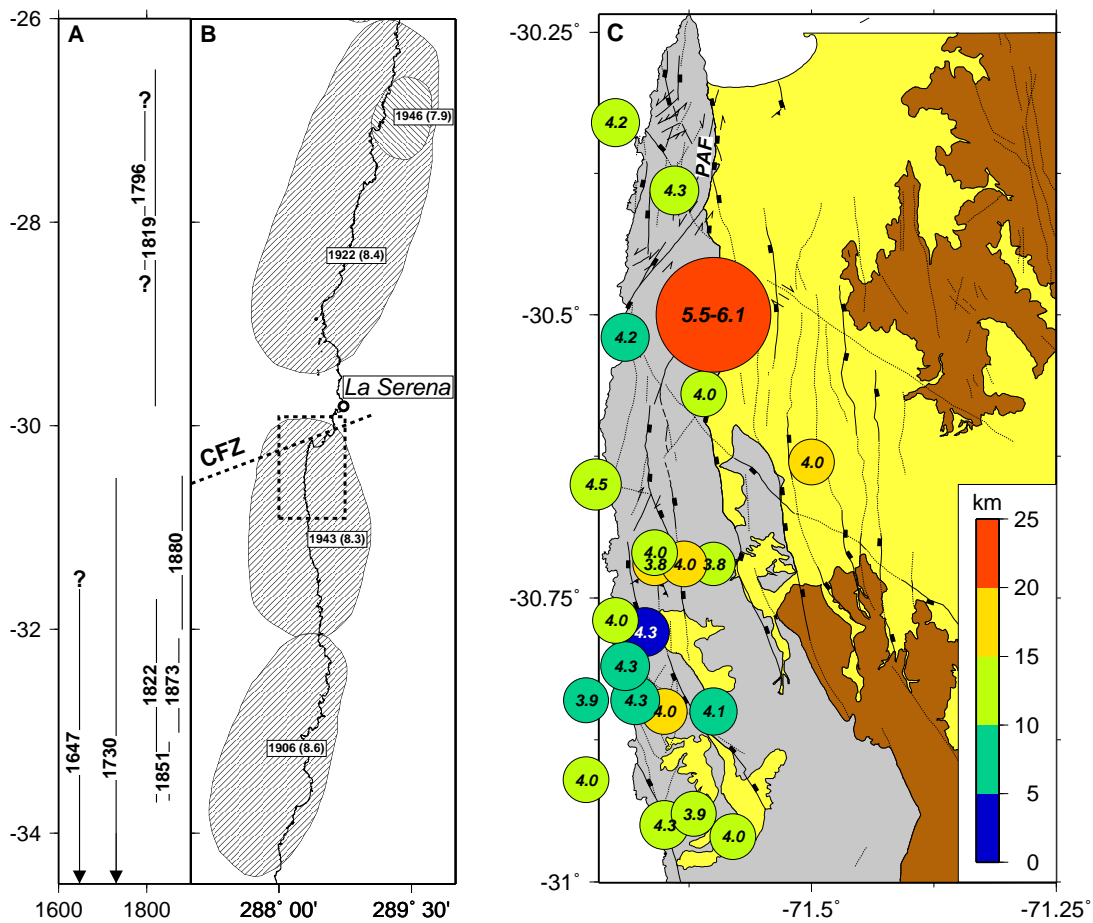


Figure 2.8: Large historical subduction earthquakes between  $26^{\circ}$ - $34^{\circ}$  S latitude and present-day crustal seismicity in between  $30^{\circ}$ - $31^{\circ}$  S. A – Rupture lengths for large historical subduction earthquakes from  $17^{th}$ - $19^{th}$  century [Beck et al. 1998]; B – rupture zones for large  $20^{th}$  century subduction earthquakes [Kelleher 1972], dashed frame – study area. CFZ – Challenger Fracture Zone; C – Present-day crustal seismicity; Hypocenter locations, depth (see scale) and magnitudes ( $M_s$ ) for crustal events during 1969 [ISC 2001] and 1990-2001 [NEIC 2001]; PAF – Puerto Aldea Fault.

### 2.3.3 Large Historical Subduction Earthquakes

According to historic earthquake catalogues [USGS 2001] large subduction events have struck the segment of the subduction zone between  $30^{\circ}$ - $32^{\circ}$  S latitude repeatedly during the last 350 years (Fig. 2.8). The main events occurred on May  $13^{th}$ , 1647 ( $M_w = 8.5$ ), on July  $8^{th}$ , 1730 ( $M_w = 8.7$ ), August  $15^{th}$ , 1880 ( $M_w = 7.7$ ), and April  $6^{th}$ , 1943 ( $M_w = 8.23$ ) [Beck et al. 1998].

The most recent megathrust event within the latitudes of the study area was the April  $6^{th}$ , 1943 Illapel earthquake. It originated at  $30.98^{\circ}$ S/ $71.27^{\circ}$ W, possibly rupturing the entire  $\sim 240$  km long segment of the subduction interface between  $30^{\circ}$ - $32.2^{\circ}$  S latitude. The northern boundary of the after-shock zone roughly coincides with the intersection of the Challenger Fracture Zone (CFZ; Fig. 2.8 B) with the overriding SA plate [Tichelaar and Ruff 1991]. The seismic moment released during the 1943 Illapel event was as high as  $6 \times 10^{20} - 25 \times 10^{20}$  Nm. The focal depth of the Illapel earth-

quake was approximated at 10 – 35 km [Pacheco and Sykes 1992; Beck et al. 1998]. The May 13<sup>th</sup>, 1647 and the July 8<sup>th</sup>, 1730 megathrusts were assumed to be even larger. Presumably these earthquakes originated further southwest and propagated northward into the study area [Beck et al. 1998] (Fig. 2.8 A). Based on these data recurrence intervals for large subduction earthquakes in this segment of the Peru-Chile Trench were estimated to range between 63 – 150 years [Kelleher 1972].

### 2.3.4 Present-day Crustal Seismicity

In contrast to the aforementioned Interplate megathrust events, intraplate earthquakes, rupturing the continental forearc, are scarcely recorded. However, a moderate - strong intraplate crustal event occurred in 1969 [ISC 2001]. Its hypocenter is located near the fault trace of the PAF in the center of the study area (Fig. 2.8 C). The magnitudes reported for this event range from  $M_s$ 5.5-6.1. The earthquake was felt with an intensity of IV (MMI) 75 km to the north in the town of La Serena. In addition to this, 21 events with magnitudes ranging from  $M_s$ 3.8-4.3 could be related to the upper crust during the last decade [NEIC 2001]. A local seismic network, which was set up between November 1999 and March 2000, recorded 314 events with hypocenters falling within the study area. However, only 7 out of these could be attributed to the continental crust. Their magnitudes are very low ( $M_s$ 0.5-1.5) so that they could easily refer to mine blasts in local gold mines rather than intraplate earthquakes (Monfret, 2002 pers. comm.).

## 2.4 Climatic Evolution of North Central Chile

North Central Chile (27°-33° S) at present exhibits a semiarid climate. It represents the transition zone between the hyperarid North and the humid South of Chile, which is commonly referred to as the *Dry Diagonal*. The amount of precipitation is controlled by atmospheric perturbations associated with the belt of westerly wind circulation [Veit 1996]. Annual average rainfall ranges from 15 – 400 mm a<sup>-1</sup> [Veit 1993b]. However, climatic changes during the Late Quaternary were detected by several authors based on geomorphological, palynological, and pedological studies [Veit 1993a; Veit 1993b; Veit 1995; Veit 1996; Lamy et al. 1998; Lamy et al. 1999] and archeological investigations [Lynch 1990]. Cyclic variations between comparatively arid climates and more humid conditions with seasonal precipitation repeatedly occurred through the Late Quaternary (10 – 120 ka BP). The effect of these climatic variations were found as far north as 27.5° S [Lamy et al. 1998], at the southern rim of the present-day Atacama desert. The driving mechanism for periodic climate variations in North Central Chile is the latitudinal shift of the southern westerlies [Veit 1996].

Veit [1993a] subdivides the climatic evolution of the Norte Chico since the Last Glacial Temperature Minimum (LGTM; 19,000 a BP) into 5 phases (Tab. 2.3). The most important period of soil formation took place during the Late Glacial period. The activation of alluvial fans during Upper Pleistocene and Early to Mid-Holocene times provides a necessary time constraint throughout the study area. The alluvial fans are commonly found along the eastern flank of the Coastal Cordillera [Gana 1991] and represent the uppermost layers in several paleoseismological outcrops. In addition, the late glacial soils are faulted by Late Quaternary surface ruptures at several outcrops in the study area. The present semiarid conditions developed only 3000 years ago [Veit 1993a], which supported

Phase	Climate		Morphologic & Pedologic Characteristics	Age
I	dry-cold, rains	heavy	alluvial fan activity, cover sediments	Late Pleistocene to LGTM
II	wet-cold, vegetation cover	dense	soil formation (Luvisol)	Late Glacial
III	dry-warm, rains	heavy	alluvial fan activity, cover sediments, soil erosion	Early to Mid-Holocene
IV	dry-warm		dune accumulation near the coast	Mid-Holocene
V	semiarid-warm		weak soil formation, increasing human influence	Upper Holocene

Table 2.3: Main climatic, morphologic, and pedologic phases in the Andean forearc between 27°-33°S latitude adopted from Veit [1993a]; LGTM – Last Glacial Temperature Minimum.

the formation of mediterranean-type red soils. Soil formation mainly takes place during the wet winters through leaching of clays and carbonates and the release of iron which imparts a red colour to the soil. Leaching is slight during the dry summers but evaporation is high, so there is often a build-up of a carbonate horizons in the soil. Hence, calcrete formation or caliche horizons are frequently found throughout the study area.

## 3 Methods

### 3.1 Neotectonic Field Studies

Following the concept of correlating the kinematics of the most recent geologic past with GPS derived present-day deformation rates in the continental forearc, the neotectonic field studies were conducted under the premise of locating intraplate faults throughout the study area primarily within the youngest lithological units.

#### 3.1.1 Remote Sensing Analysis

The localization of fault traces in the field was aided by the geological map (1:100 000; [Gana 1991]), remote sensing data such as aerial views ( $\sim$ 1:70 000; [IGM 1955]) and a Landsat 5 TM scene (path: 001; row: 081; acq.-date: 07.02.1987). Within the limits of the study area, the Landsat TM image and the geological map were referenced to six topographic maps (1:50 000 [IGM 1968]) using proper Geographic Information System software (ERDAS/Imagine, ARC/Info). A Digital Elevation Model (DEM) was constructed selecting 50 m contour intervals from the topographic maps. For the interpretation of the aerial views a portable stereoscope was applied. All imagery data were scrutinized carefully for indicators of faults or fault related structures as there are:

- Offset geologic features (i.e. magmatic dikes)
- Lithological contrasts (i.e. basement rocks vs. sediments)
- Topographic features (i.e. "flat irons")
- Deranged drainage patterns (i.e. offset drainages)
- Photolineaments

By these means numerous sites of interest all over the study area were determined. Where possible, the selected locations were visited in the field and checked for presence of fault related features. Based on the complementing information from the aforementioned sources (geological map, remote sensing data and field observations) a very detailed fault network could be established for the study area.

Category	Stratigraphy	Feature	Slip Surface
A	Neogene- Quaternary	fault plane	thin clay gouge or fresh lithological contrast
B	Paleozoic- Cretaceous	fault plane	thick clay gouge or remineralized gouge material
C	Paleozoic- Cretaceous	shear plane or cleavage	plain rock surface (no gouge material)
D	Neogene- Quaternary	topographic escarpment	shear planes in adjacent units

Table 3.1: Classification of outcrops in the study area depending on approximate ages of lithologies according to the geological map [Gana 1991], observed structural features and the type of considered slip surface.

### 3.1.2 Macroscopic Fault Documentation

In first place the studied geologic outcrops were subdivided into four major groups (A-D) depending on their lithological content. The differentiation was necessary in order to detect changes of the deformation pattern in space and time. The basic criteria applied for the subdivision into groups are listed in Tab. 3.1. For all outcrops that were attributed to group A the macroscopic analysis focused on the identification of indicators for *active* deformation and *coseismic* rupture. In order to decide whether a fault formed due to coseismic rupture rather than *aseismic* creep the outcrop was checked for the following macroscopic indicators, all of which suggest instantaneous faulting:

- Crushed cobbles in the fault plane
- Colluvial wedges on the hanging wall
- Fault scarps on the surface

Vertical offsets of geologic units in outcrops of group A or significant topographic features as in group D were determined using a simple 25 m tape measure or a geodetic total station (Geodimeter). If possible, each fault was checked for its continuation into the overlying rocks in order to better constrain the timing of deformation. The presence of fresh *clay gouges* exhibiting a low degree of remineralization, and of *springs* in the immediate vicinity of the outcrop were taken as indicators for recent, active faulting. In a last step the fault traces within the outcrop were laid open in order to obtain fault-slip data as described in the following section.

## 3.2 Paleokinematic Analysis

Faulting is the brittle response of rocks to tectonic stresses. The geometrical properties of faults and their movements are thought to be controlled by the nature of the active stresses [Orife et al.

Plane (dip azimuth/dip)	Striation (trend/plunge)	Sense of Slip (+/-)	Quality (1-5)	Comments (type/offset/relative age)
90/69	78/68	-	1	cm/> 4.2/a
59/60	52/60	-	3	tm/> 4.2/no
71/78	140/59	-	2	is/> 4.2/no

Table 3.2: Three exemplary fault-slip data sets as recorded during field studies. The quality signal was modified to range from 1-5 as compared to the method described by Meschede [1994]; The most frequent slickenside kinematic indicators recorded in the field according to Petit [1987] and Doblas [1998] are: cm – *crescentic markings*; tm – *trailed material*; is – *trains of inclined planar structures*; a-d – denote relative age from youngest (a) to oldest (d); no – no relative age constraint available.

2002]. Anderson [1951] and Angelier [1989; Angelier 1994] realized that if faults are governed by stresses, the orientation information collected from faults in the field could be used to characterize the paleostress tensor. This process has become known as *stress inversion*.

### 3.2.1 Data Acquisition

Within the framework of this study the fault-slip data were obtained according to the methods described by Meschede [1994]. A single fault-slip data set consists of a slip surface/striation data pair, information about the sense of slip (normal/reverse), and a quality signal. In addition to this, the type of the observed kinematic indicator is specified according to the methods described by Petit [1987] and Doblas [1998]. In case of multiple generations of slickenlines on the same fault plane, it was attempted to assign relative ages to the different deformations based on cross-cutting relationships between distinct lineations, where these are unambiguous. If present, offsets were measured and added to the fault-slip data set. An example for a field record of three fault-slip data sets is presented in Tab. 3.2.

### 3.2.2 Fault-slip Data Analysis

The reconstruction of paleo-kinematics is based on Bott's [1959] assumption that slip on a fault, represented by slickenside kinematic indicators, also records the direction of maximum shear stress on its surface. Following this concept, a strain tensor can be determined from homogeneous populations of fault-slip data and, given the coaxiality of principal stresses and strains, the contraction (P) and extension (T) axes [Marrett and Peacock 1999] of the strain tensor can be regarded as stress tensor with P corresponding to  $\sigma_1$  and T corresponding to  $\sigma_3$ . The obtained P-T solutions only represent the incremental deformation on a local scale (outcrop). For a regional kinematic solution, a homogeneous (isotropic) rock mass, coaxial deformation and no mechanical interference of adjacent slip surfaces must ideally be given [Marrett and Allmendinger 1990; Twiss and Unruh 1998].

### 3.2.2.1 Fault-slip Data Separation

In order to obtain homogeneous populations of fault-slip data and to approximate their corresponding P-T axes, the field records need to be properly separated. The handling of fault-slip data is easily performed by a number of freely available software packages: CHECK, TURNER, NDA [Sperner et al. 1993] and KINEMAT [Michel 1994]. Using these software packages the separation is conducted as an iterative procedure involving three main steps (Fig. 3.1).

In a first step CHECK determines the acute angle  $\alpha$  between the fault plane and the striae in order to check if the measured striation lies within the fault plane. For  $\alpha \leq 20^\circ$  the striae are rotated into the fault plane whereas data sets with  $\alpha > 20^\circ$  are discarded. In a next step the angle between the fault plane and  $\sigma_1$  is determined. According to the Mohr Coulomb Fracture criterion this angle is called  $\Theta$ . Experimentally derived values for  $\Theta$  range between  $17^\circ$ - $40^\circ$  [Jaeger and Cook 1979]. KINEMAT evaluates the clustering characteristics for  $\sigma_1$  and  $\sigma_3$  in both, the *constrictional* case (axial contraction) and the *tensional* case (axial extension) on the basis of an eigenvalue analysis [Michel 1993; Michel 1994]. Data sets that strongly deviate from a tight clustering for the contraction and/or extension axes either contain superimposed fault-plane populations or overemphasize one of the fault-plane populations. In both cases  $\Theta$  results in either very high ( $89^\circ$ ) or very low ( $1^\circ$ ) values. For superimposed fault-plane populations this means that the data need to be further separated. This can be done by visualization of the data in a stereo plot with the help of the program TURNER, applying a randomly chosen value for  $\Theta$ . For overemphasized fault-plane populations, the data set is strictly speaking not applicable to this procedure. However, overemphasis of one fault-plane population generally occurs where young lithological units were subject to brittle faulting near the surface. In this case macroscopic observations like the clear offset of a marker horizon usually provide enough information for the correct interpretation of fault-slip data instead.

Once a single or several clearly distinguishable fault-slip data populations were identified in one outcrop, the determination of the principal stress/strain axes was accomplished in a third step. Here the method of Turner [1953] is applied, which was initially designed to derive P- and T-axes of shear planes in calcite e-twin lamellae [Sperner et al. 1993]. In its application for fault-slip data analysis (see software TURNER & NDA) theoretical P- and T-axes are calculated for each data set. The resulting contraction (P) and extension (T) axes are lying in a plane given by the shear plane normal and the slickenline [Sperner et al. 1993]. In order to calculate the P-T axes orientations with TURNER the angle of the contraction axis with the fault plane ( $\Theta$ ) has to be specified manually. Principally it is possible to accept the angle  $\Theta$  that results from the eigenvalue analysis (KINEMAT) during the procedure of data separation. However, due to the fact that many outcrops show only singular slip surfaces in unconsolidated sediments, overemphasis of individual fault-plane populations is frequently observed and no realistic values for  $\Theta$  can be obtained. For these data sets an angle  $\Theta = 30^\circ$  was attributed, which is a well tested general estimate for newly formed fractures based on experimental studies [Sperner and Ratschbacher 1996]. With given  $\Theta$  TURNER calculates the orientations of the  $\sigma_1$ - and  $\sigma_3$ -axes for each fault-slip data pair. The vector mean for each axis is calculated and plotted as P- and T-axis, respectively (Fig. 3.1). The intermediate B-axis is inferred as being oriented perpendicular to both, the P- and T-axis. The resolving P-T-B-axes triples represent the principle axes of the reduced stress tensor at each outcrop (see Appx. A.1-A.13 for solutions at individual outcrops).

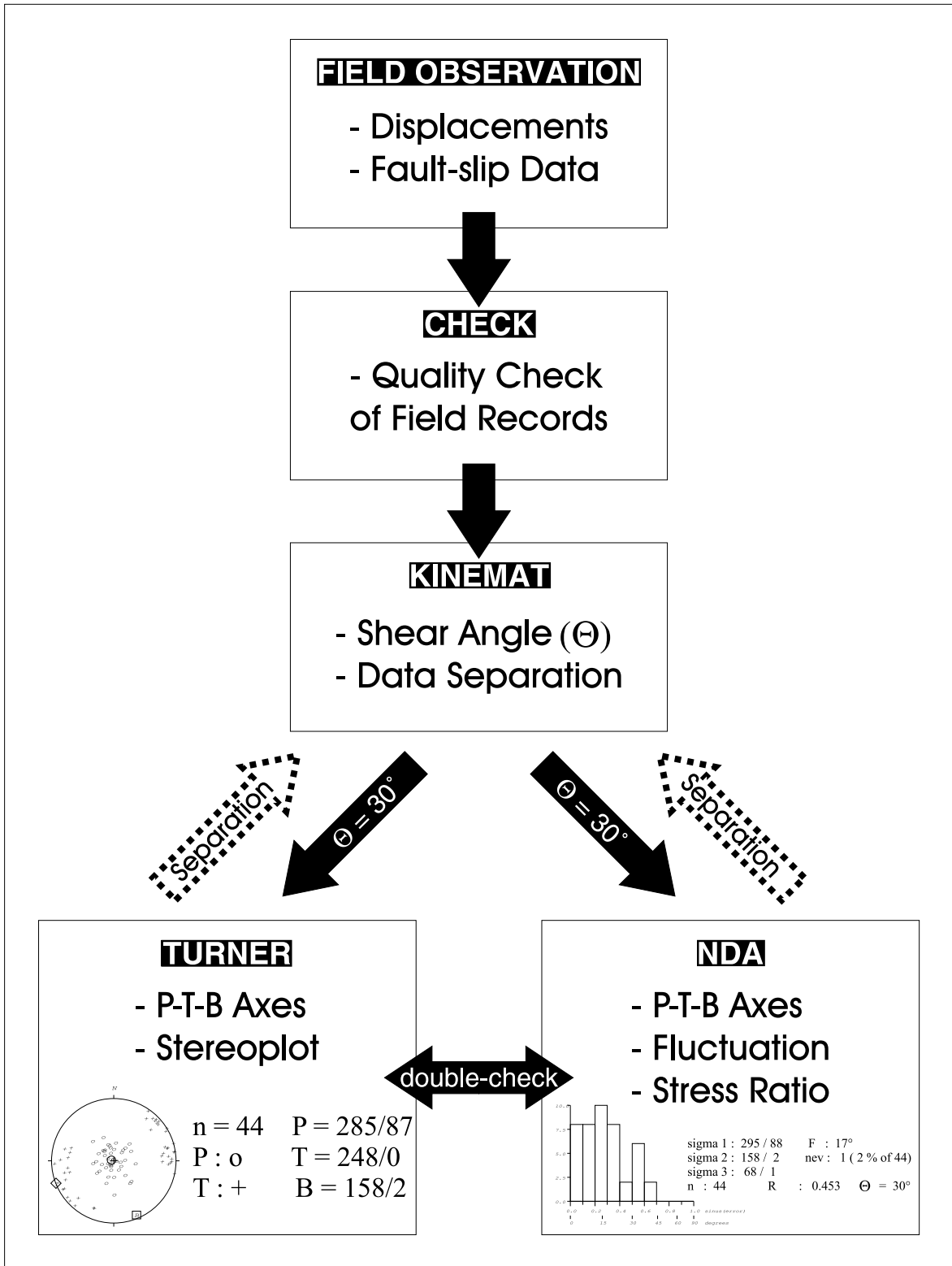


Figure 3.1: Flow chart showing the order of data acquisition and separation. P – Contraction axis; T – Extension axis; B – intermediate axis; F – Fluctuation; R – stress ratio or strain factor; n – Number of data sets.

In order to double-check the results obtained from the above described method, the separated fault-plane populations were subject to the *Numerical Dynamic Analysis* (NDA). This method is an extension to the P-T-axis analysis based on Spang [1972]. The P-T-axes orientations are calculated for each fault-slip data set equivalent to TURNER. A stress/strain tensor is determined for each fault-slip data set assuming an arbitrary shear stress magnitude of 1 along each fault plane and a coincidence of  $\sigma_1$  with P and  $\sigma_3$  with T. The summation of the stress tensors of each individual fault-slip data set and the division by its number (n) yields the bulk stress tensor [Sperner et al. 1993]. The orientations and relative values of the principal stresses are derived from eigenvector analysis of the bulk stress tensor. This information is then used in order to calculate the *stress ratio* or *strain factor*  $R$  (3.1). According to Etchecopar [1981]  $R$  is the ratio of magnitudes of the principal axes of the bulk stress tensor:

$$R = \frac{(\sigma_2 - \sigma_3)}{(\sigma_1 - \sigma_3)} \quad (3.1)$$

Additionally the *fluctuation*  $F$  [°] is calculated for each fault-plane population. This value describes the mean angular deviation of the measured slip direction from the orientation of the calculated maximum shear stress. Ideally  $F$  is close to zero but values of up to 25° are tolerable with respect to comparability of these results with those obtained with TURNER. Only when  $F$  is bigger than 25° significant discrepancies between the principal axes orientations obtained by TURNER and NDA are observed. For fault-plane populations that represent pure normal, thrust or strike-slip faulting regimes  $R$  is close to 0.5. fault-slip data sets that exhibit a transpressive or transtensive component trend towards values near 0.25 or 0.75 respectively. However, a thoroughly separated fault-slip data set will never yield values for  $R$  significantly above or below 0.5. Consequently the fault-slip data separation may result in the identification of multiple deformation regimes where only a transtensive or transpressive regime is actually present. Therefore the separated fault-plane populations need to be checked for possible correlations, e.g. if the P-axes of different populations gather on a great circle or if the T-axes of these populations cluster in the same octants in an equal area, lower hemisphere stereogram. If this is the case one could easily conclude that transtensions prevails rather than a sequence of distinct normal and strike-slip faulting regimes.

In case of true multiple fault-slip data populations on one fault plane a further distinction based on the relative age criterion (Tab. 3.2) is needed. Ideally the cross-cutting relationships between different slickenlines as observed in the field serve as the main criterion. However, cross-cutting relationships are extremely difficult to obtain and often reveal ambiguous results when the observations are repeated on the same or adjacent slip surface in one outcrop. Therefore no weight is put on the relative age constraints that were scarcely obtained in the field. Instead it is attempted to identify possible changes in the deformation regime by classifying outcrops depending on their lithologic ages (Tab. 3.1).

### 3.3 Tectonic Geomorphology

#### 3.3.1 Range-front Geometry

On the basis of georeferenced imagery data and topographic maps the *range-front sinuosity* and the *valley depth/valley width ratio* can be determined. The range-front sinuosity is the length of the mountain-piedmont junction (erosional curvature) divided by the straight length of the front (linear distance of endpoints) [Bull 1984]. The valley depth/valley width ratio is the valley-floor width divided by the mean height of the adjacent watershed divides. It is measured 500 m upstream from the apparent mountain-piedmont junction. Combined with morphologic information about the *piedmont* and *mountain-block* landforms the uplift velocities can be estimated in an order of magnitude fashion. Bull and McFadden [1977] and Bull [1984; 1987] use several quantitative measures in order to describe range-front tectonic geomorphology and to define five classes in arid and semi-arid climates given in Tab. 3.3.

For the study area the range-front sinuosity and the valley depth/valley width ratio is determined on the basis of georeferenced topographic maps [1:50 000 IGM 1968]. In order to avoid smoothing effects by averaging over long distances the range-front sinuosity is calculated for the full length or fractions of the PAF. Valley depth/valley width ratios are determined along the same fault and plotted along its strike for each individual measurement in order to detect relative changes in range-front faulting activity (Fig. 4.14).

Classes of relative activity	Piedmont landforms	Mountain-block landforms	Range-front sinuosity	Valley depth/valley width ratio	Inferred uplift rate [m/ka]
1-Maximal	Unentrenched alluvial fan	V-shaped valley in bedrock, U-shaped valley in alluvium or soft bedrock			1.0-5.0
2-Rapid	Entrenched alluvial fan	V-shaped valley	1.1–1.3	0.06-0.53 mean (0.15)	0.5
3-Slow	Entrenched alluvial fan	U-shaped valley	1.6–2.3	0.2-3.5 mean (1.5)	0.05
4-Minimal	Entrenched alluvial fan	Embayed mountain front	$\geq 2.5$	0.4-3.8 mean (1.7-2.5)	0.005
5-Inactive	Dissected pediment	Pediment embayment	2.6-4.0	0.9-39.4 mean (7.4)	$\leq 0.005$

Table 3.3: Classification of relative tectonic activity of normal fault-block mountain fronts [adapted from McCalpin 1996]. Uplift rates in semiarid climates only; in subhumid or humid areas rates may be several times larger for each class.

### 3.3.2 Drainage Network Analysis

The arrangement and organization of stream courses is generally referred to as the *drainage network* or *drainage pattern*. The drainage pattern is strongly influenced by the underlying geological structures. *Anastomotic* drainage shows a division of a river into several channels, and develops on nearly horizontal, coarse sediments. *Annular* or *radial* drainage shows streams radiating out from a center with the tributaries arranged along a series of nested arcs. Annular drainage develops on domes, particularly where belts of resistant rock are separated by belts of weaker rock. *Centripetal* drainage shows a movement into a center created by a crater or depression. *Dendritic* drainage shows a branching network similar to that of a tree, and is most commonly found on horizontally bedded or crystalline rocks where the geology is uniform and unaffected by recent faulting. *Parallel* drainage develops on slopes of moderate angle. *Rectangular* drainage shows tributaries running at right angles to each other and occurs on rocks which have intersecting, rectangular joints and faults.

The drainage network was digitized from six georeferenced topographic maps (1:50 000) using Arc/Info. Each individual segment was assigned to one of three classes (full rivers, seasonal rivers, dry stream valleys). Each class is given a class-number similar to Strahler's [1952] *stream ordering*. Based on these data, a weighted analysis of the drainage network is conducted. The stream segments are subdivided according to 72 arbitrarily chosen subareas of  $\sim 8 \times 8$  km side length. For each individual subarea the azimuths are calculated and grouped into  $30^\circ$  bins. The results are plotted as rose diagrams showing the relative length of accumulated segments per bin and the absolute number of applied segments per subarea (Fig. 4.17).

### 3.3.3 Fault-scarp Degradation

Displacement of the land surface along a fault during an earthquake produces a scarp with a steep face (the free face) commonly sloping between  $50^\circ$ – $90^\circ$ . Debris spalling off the free face accumulates on a sloping surface below at about the angle of repose ( $\sim 35^\circ$ ). Erosion and sedimentation begin to produce a more gently sloping wedge of alluvium at the base of the scarp. Eventually the free face disappears, rounding of the crest begins, and fluvial processes become dominant on the scarp. Thus, the slope of the scarp is decreased, and the profile is further modified [Bucknam and Anderson 1979]. This is generally true for transport-limited slopes, where transport occurs more slowly than weathering. The evolution of a transport-limited slope can be evaluated quantitatively by assuming that sediment transport is a diffusion process [Pinter 1996]. In order to apply a diffusion equation, the dominant erosional process must be creep, which is the slow movement of sediment as a result of gravity. However, landslides, debris flows, or even bioturbated hillslope transport along slopes with steep angles are not adequately modeled by the diffusion equation. In this study the morphology of scarplike landforms was determined with a laser-optic theodolite (Geodimeter). At each site three profiles were shot perpendicular to the strike of the scarp. Data were recorded with a horizontal and vertical accuracy of 0.1 m.

For the case of small topographic scarps in non-dissecting, weakly consolidated materials, erosion of the footwall crest can be taken to be the anti-symmetric equivalent of deposition on the hanging wall side. The anti-symmetry criteria holds true for two physical assumptions: (a) the mass is conserved

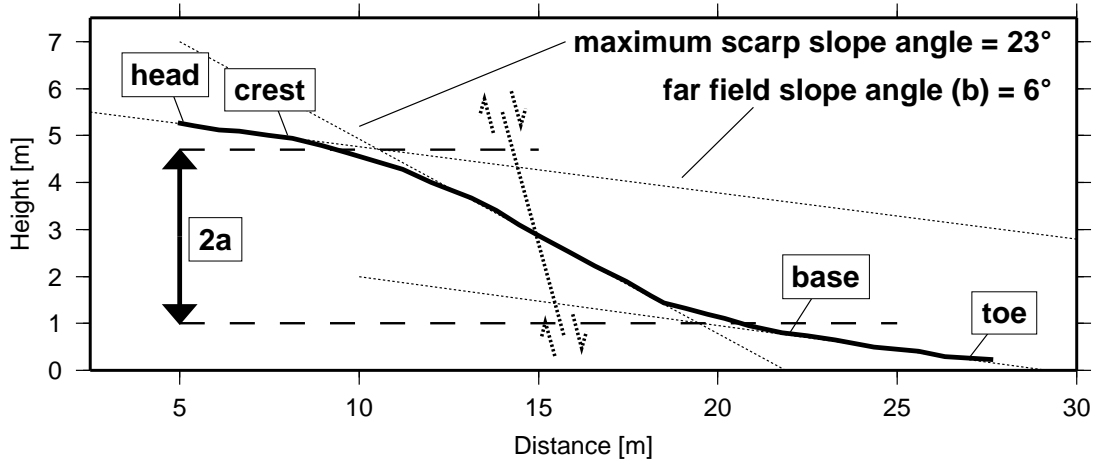


Figure 3.2: Geometry and terminology of a simple fault scarp. Profile constructed by the method of Bucknam and Anderson [1979]; The fault geometry and sense of slip is indicated by arrows, The lines connecting *head* and *crest* or *base* and *toe* respectively represent the far-field slope angle. Their intersections with the the maximum slope angle define the upper and lower vertical limits (offset);  $a$  is defined as half the vertical offset.

on a local scale and no channelized flow occurs (non-dissecting criteria), (b) the erosional diffusivity is not too different from the depositional diffusivity (weakly consolidated criteria). This allows for the assumption of a constant mass diffusivity  $\kappa [m^2 ka^{-1}]$  [Hanks 2000]. It is further assumed that mass is transported downslope at a rate directly proportional to the local slope. If this rate and the boundary conditions of the problem remain invariant with time, a one-dimensional homogeneous diffusion equation can easily be applied to describe the process of scarp degradation.

$$\frac{\partial u}{\partial t} - \kappa \frac{\partial^2 u}{\partial x^2} = 0 \quad (3.2)$$

Equation (3.2) states that the rate of change of elevation ( $\partial u/\partial t$ ) is proportional to its curvature ( $\partial^2 u/\partial x^2$ ). If the topography is concave down, as is the case with the crest of the scarp-like landforms,  $u$  will decrease with time ( $t$ ). Since the base of a scarp is concave up,  $u$  will increase with time ( $t$ ). In order to describe a simple fault-scarp imposed upon a flat surface with a preexisting slope ( $b$ ) evolving morphologically over time, equation (3.3) delivers an elementary solution [Hanks 2000],

$$u(x, t) = a \operatorname{erf}\left(\frac{x}{2\sqrt{\kappa t}}\right) + bx \quad (3.3)$$

where  $a$  is half the vertical offset between the crest and the base of the scarp Fig. 3.2,  $b$  is the far field slope angle and  $x$  is the cross-strike spatial dimension. Equation 3.3 is valid for an initially vertical scarp face. Given a detailed topographic profile, and the far field slope angle from field observations a best-fit model is calculated by varying  $\kappa t$  the *morphologic age*. The best-fit model is defined as the one that yields the least root mean square error between the observation and the model. In a last step the morphologic age ( $\kappa t$ ) of the best-fit model is divided by the mass diffusivity constant ( $\kappa$ ) that is applicable for the specific region. Ideally the mass diffusivity constant is established on the basis of local radiometric datings. In this study, due to the absence of dated fault-scarps, the mass diffusivity constant was chosen based on similarities of materials and climatic aspects with other study

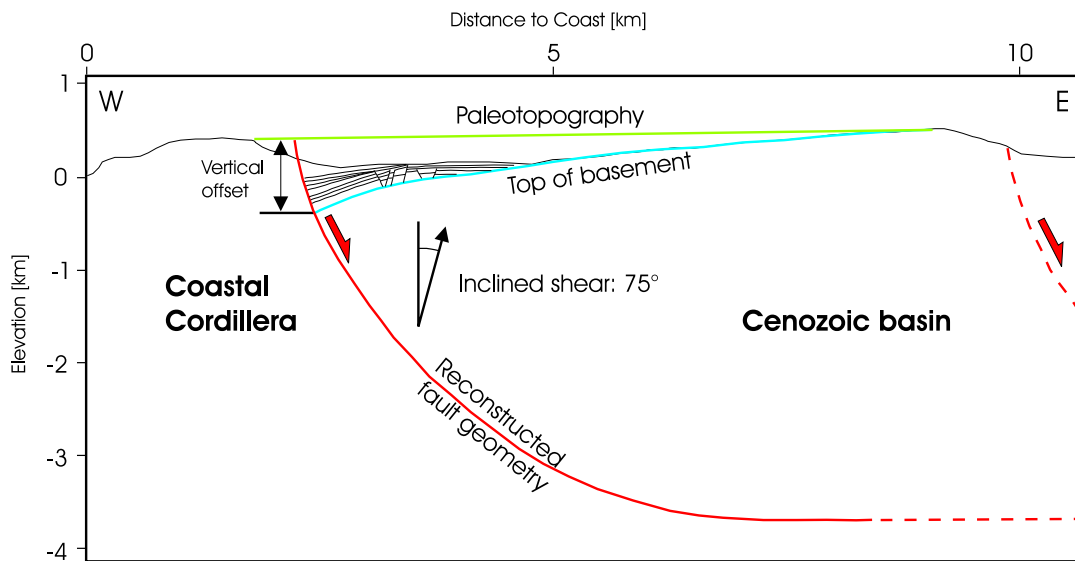


Figure 3.3: Construction of fault geometry applying the inclined shear method described by White et al. [1986]. Shear angle ( $75^\circ$ ) corresponds to dip of antithetic faults in the sediments of the hanging wall block. The top of the basement is restored to the presumed paleotopography. Figure modified after Pelz [2000].

areas (i.e. Western United States; [Hanks 1984; Arrowsmith et al. 1996]). The results represent age estimates for the formation of the scarp-like landforms, which have to be seen as *order of magnitude* approaches rather than as absolute ages.

### 3.4 Fault Construction and Restoration

Geologic cross sections are commonly applied to estimate the shortening and/or extension over a specific area. In this procedure the determination of the fault geometries and the conservation of the area during restoration plays a vital role for the yield of realistic results. The theory of *balancing geological cross-sections* [Dahlstrom 1969; Hossack 1979] provides the necessary tools and algorithms for the *construction of faults* and *restoration of paleotopographies* under conservation of area and/or volume. The most common algorithm used to balance cross-sections that describe internally complex structures of several kilometers width like half-grabens [Pelz 2000], is the *inclined shear* method described by White et al. [1986]. The inclined shear algorithm is implemented in the software package 2D-Move (Midland Valley Exploration Ltd.).

If the geometry of a fault bend fold is known from geological and/or geophysical observations (bedding slope, borehole logs, seismic records etc.), the fault geometry at depth can be constructed from these data using the inclined shear module of 2D-Move. The basic assumption is that the geometry of the fold in the hanging wall is directly and exclusively influenced by the geometry of the fault and the movement along its plane. Consequently the warped units must represent fault-bend folds, whose geometry can be inverted to obtain the geometry of the fault at depth. In order to do this, the input data is converted to a simple 2D cross-section for which the best fault geometry is constructed using the inclined shear module. Various shear angles are tested for their potential to create realistic

fault geometries. The shear angle is representative for the internal deformation of the hanging wall block [Pelz 2000]. It is commonly thought to be subparallel to antithetic minor faults in the deformed hanging wall beds, if such features are abundant. The construction of fault geometries is repeated for different elevations to which the deformed bed shall further be restored. The accuracy to which the *Top of Basement* geometry on the hanging wall side can be obtained plays a crucial part for the results of the restoration process itself. In this study, the top of the basement was inferred from an isoline plot (Fig. 4.21 A) based on reflection seismic data [Meinardus 1961; Rocroi 1964] as presented in Paskoff [1970]. For simplicity, the *regional* or paleotopography to which the top of the basement will be restored is assumed to be horizontal. The hanging wall block is then restored using the constructed fault geometry until its top matches the position of the regional on the undeformed footwall side. The shear angle for the restoration process should be chosen in accordance with the angle used for the construction of the fault geometry. Once the reconstruction is completed, the heave denotes the horizontal displacement needed to balance the cross-section and provides a measure for the shortening or extension along the profile.

### 3.5 Dislocation Modeling

In geosciences elastic dislocation modeling is, among other prospects of this method, commonly applied to infer subsurface fault geometries from observed surface displacements. In its application to study subsurface fault geometries, elastic dislocation theory considers the earth a homogeneous isotropic elastic half-space with no stress applied to the free surface [Larsen et al. 1992].

#### 3.5.1 Theory

The theory was first developed by Steketee [1958] and Chinnery [1961] but due to the rather complex analytical solutions to the first formulations describing the displacement field of a dislocation source, it was simplified for special cases of dislocation or fault geometry [Savage and Hastie 1966; Mansinha and Smylie 1967]. General expressions of the displacement field for rectangular strike-slip and dip-slip faults have been computed by Mansinha and Smylie [1971] and Okada [1985]. These expressions support that arbitrary slip directions could be designed by the superposition of strike-slip and dip-slip dislocations. The assumption of an isotropic homogeneous half-space represents the simplest source configuration. This rather simple approach is mainly used for its usefulness as a first-order approximation. Since the source model by itself is *inherently nonunique* with respect to the generated displacement field, and the quality of crustal movement data is generally scarce, it is meaningless to compare the field observations with the predictions of a too sophisticated earth model [Okada 1985]. The fact that an elastic half-space is applied as an earth model requires certain assumptions coming along with the elastic theory. *Elastic deformation* is a temporary deformation, from which material recovers, caused by an applied stress, such that on release of the stress the body reverts to its former, unstrained condition (Fig. 3.4). In purely elastic materials such deformation is generally described by a linear stress-strain relationship ( $\tau \sim \varepsilon$ ). In rocks, ideal elastic strain is combined with viscous components. The *elastic rebound theory* holds that accumulated potential energy, stored as *elastic strains*, is released by faulting, i.e. during earthquake rupture processes. Zones adjacent to the fault

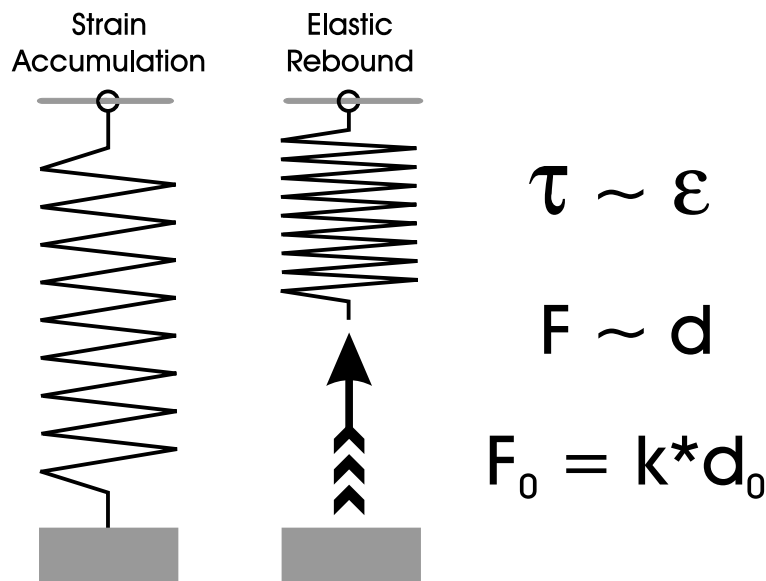


Figure 3.4: Strain accumulation and elastic rebound in elastic dislocation theory. Helical spring represents elastic behavior;  $\tau$  – Stress ;  $\varepsilon$  – Strain;  $F$  – Force;  $d$  – displacement;  $k$  – Spring constant.

plane *rebound elastically*, leaving them relatively unstrained (Fig. 3.4). In the case of natural (locked) fault planes this means that elastic strains are accumulating until the shear stresses acting on the fault plane overcome the peak shear strength of the fault plane. The peak shear strength is the highest stress sustainable just prior to complete failure of a rock under load. After this, stress cannot be maintained and faulting usually occurs by displacement along a rupture plane.

### 3.5.2 Modeling Intraplate Fault Geometries

If the aforementioned rupture process becomes the size of a moderate to large crustal (intraplate) earthquake it would commonly leave a topographic signal on the surface — a fault-scarp. The geometry of the fault-scarp is directly related to the subsurface geometry of the rupture plane. Thus, modeling the surface displacement yields information about the faulting parameters at depth. The modeling of surface deformations is strongly aided by the software package DISL [Larsen and Reilinger 1992; Larsen et al. 1992]. The program calculates surface deformations based on a simple dislocation source model in an elastic half-space (Fig. 3.5). The necessary input parameters are: *fault type* (strike slip or dip slip), *slip* along the fault, *length*, *down-dip width*, *location*, and *azimuth* of the fault.

In this study the topographic signal of the Coastal Cordillera is interpreted as accumulated displacement due to repeated crustal faulting. The topography is inverted for seismic slip along a fault plane adjusting three parameters, the *width* of the fault, the amount of *slip*, and the fault *dip*, until a best-fit model between the topographic profile and the dislocation curve is obtained. Though the best-fit model is nonunique within certain limits, the results provide a good approximation of the subsurface fault geometries. The dislocation model presented in this study does not account for erosional processes and postseismic (viscoelastic) relaxation effects.

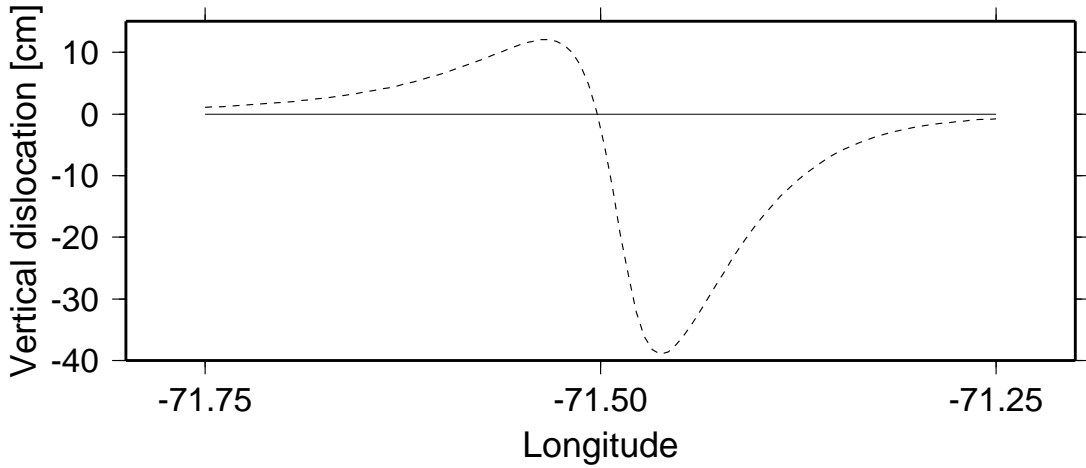


Figure 3.5: Vertical displacement for a moderate sized ( $M_w = 6.5$ ) crustal earthquake on a N-S striking normal fault. The plot is centered over the top of the fault at depth. The fault depth ranges between 3 – 9 km. The solid line represents the undisturbed surface previous to the rupture process. The dashed line shows the warped surface subsequent to faulting. Faulting parameters: *length* 30 km, *width* = 10 km, *slip* = 100 cm, *dip* =  $65^\circ$ , *length* = 30 km.

### 3.5.3 Modeling Strain Redistribution

Large interplate earthquakes originating at the lower boundary of the subduction zone have the potential to impose additional strains on preexisting intraplate faults. In order to quantify the amount of redistributed strains, a simple dislocation model is applied with the subduction interface as a source zone. The slab geometry is approximated according to the best-fit solution of the *Andean Elastic Dislocation Model* (AEDM) [Khazaradze et al. 1999]. Apparent trench azimuths are derived from the global seafloor topography data set [Smith and Sandwell 1997]. The rupture width and the subsurface rupture length are approximated by applying scaling laws [Kanamori and Anderson 1975; Wells and Coppersmith 1994] to seismic catalogue data [NEIC 2001], taking advantage of the near identical relationship between seismic moment ( $M_o$ ), surface magnitude ( $M_s$ ) and body wave magnitude ( $m_b$ ). The downdip edge of the subduction interface is specified according to results from Tichelaar [1991]. The slip is partitioned into a dip-slip and a strike-slip component, taking into account the oblique convergence direction, the trench azimuth, and the dip of the interface.

$$\mathbf{C} = \mathbf{A} \times \mathbf{B}; \quad \mathbf{A} = \begin{bmatrix} \cos\alpha & \sin\alpha & 0 \\ -\sin\alpha & \cos\alpha & 0 \\ 0 & 0 & 0 \end{bmatrix}; \quad \mathbf{B} = \begin{bmatrix} \cos\beta & 0 & -\sin\beta \\ 0 & 1 & 0 \\ \sin\beta & 0 & \cos\beta \end{bmatrix} \quad (3.4)$$

Redistributed strains are estimated using the software DISN [Larsen and Reilinger 1992; Larsen et al. 1992] which applies dislocation theory to an elastic half-space. Results are given as a strain tensor ( $T_{ij}$  [ $\mu\text{strain}$ ]) in a cartesian coordinate system ( $x = \text{east}$ ,  $y = \text{north}$ ,  $z = \text{positive up}$ ; Fig. 3.6). In order to rotate the strain tensor from the cartesian coordinate system into the observed fault-plane orientation, a  $3 \times 3$  rotation matrix  $\mathbf{C}$  (Eq. 3.4) is applied, with  $\mathbf{A}$  representing the rotation around the  $z$ -axis and  $\mathbf{B}$  the rotation around the  $y$ -axis, respectively (Fig. 3.6). From the rotated strain tensor the shear strain components parallel to the fault plane are determined. Given the fault dimensions

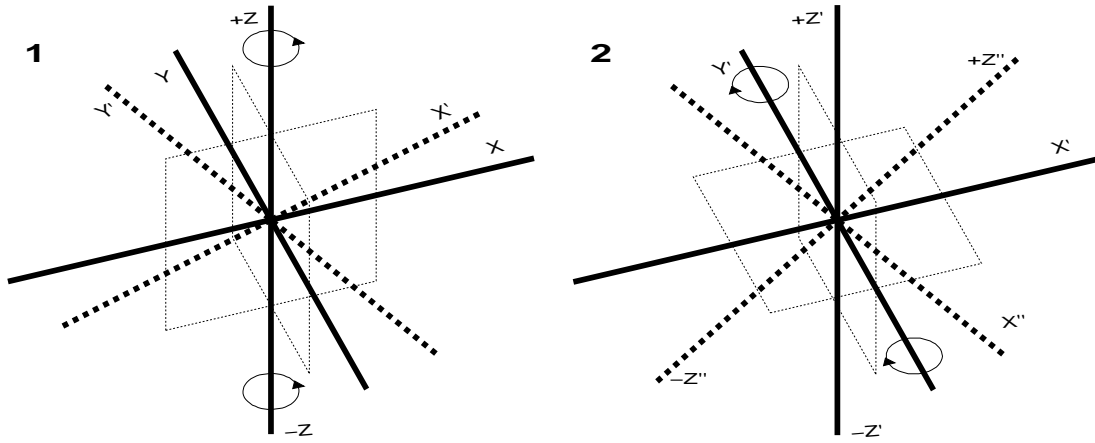


Figure 3.6: Rotation of the strain tensor ( $T_{ij}$ ). In a first step (1) the z-axis is rotated around until  $y'$  parallel to the strike of the fault plane. In a second step (2) the  $y'$ -axis is rotated until  $x''$  parallels the dip of the fault plane.

(length, width), the resulting shear strain components can be converted into strike slip and dip slip along the fault, respectively. Finally, the relationship between strike slip and dip slip defines the resulting (oblique) slip and the associated rake within the model fault plane. Using Kostrov's [1974] formulation, where  $\mu$  = shear modulus ( $3 \times 10^{10}$  Pa),  $A$  = area, and  $u$  = slip, the amount of seismic moment redistributed along intraplate faults during large subduction earthquakes can finally be estimated:

$$M_o = \mu A u \quad (3.5)$$

Based on the applied intraplate fault geometries and the inferred rake theoretical fault-plane solutions (focal mechanisms) can be constructed. The purpose of displaying the induced deformation rates as focal mechanisms is to improve compatibility between the results from fault-slip data analysis and dislocation modeling on a visual basis. The resolving focal mechanisms do not represent recent seismicity or predictions for future earthquakes (Fig. 4.27).

### 3.6 GPS Residual Velocities

Within the framework of this thesis a set of space geodetic observations (GPS) is applied in order to correlate present-day deformation rates with the results obtained from neotectonic field studies. The GPS observations derive from a network comprising 230 sites in Chile and western Argentina, which was established by the GeoForschungsZentrum Potsdam (GFZ Potsdam) in the context of the SAGA (South American Geodynamic Activities) Project [Klotz et al. 1999]. Since 1993 the network was re-observed in a two year cycle. Due to fixed monuments that enable an exact relocation of the GPS-antennas during follow-up campaigns, an accuracy of  $2 - 4 \text{ mm a}^{-1}$  for the determination of horizontal displacements is achieved. The GPS observation data was processed using the EPOS (Earth Parameter and Orbit System) software package [Angermann et al. 1997] and referenced to the ITRF-97 reference frame [Khazaradze and Klotz 2002]. All site velocities were defined relative to

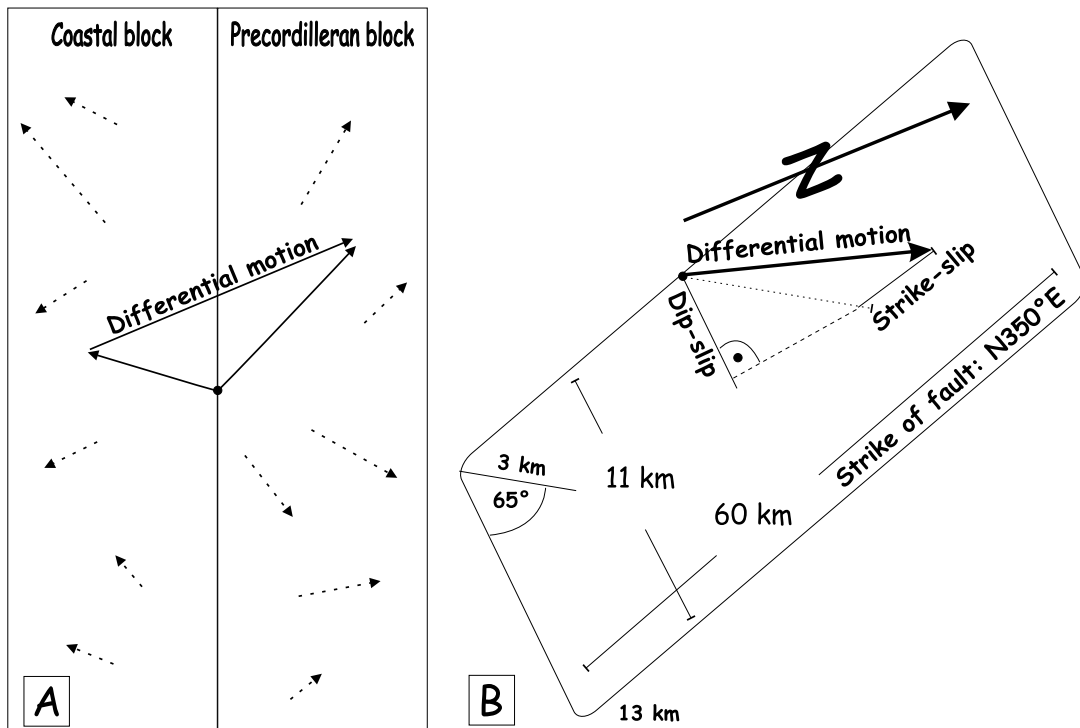


Figure 3.7: Determination of GPS residual differential motion and resolving moment/moment rates along intraplate normal faults. A – GPS residual velocity fields for Coastal and Precordilleran blocks (dashed arrows), averaged block and resulting differential motions (black arrows); B – Conversion of differential motion into strike-slip and dip-slip components.

stable South America by means of estimating a best-fitting Euler vector for the South America plate. In order to properly interpret the tectonic significance of the observed velocities, a 3D model of the seismogenic interface between the subducting Nazca and the overriding South America plates was constructed. Based on this geometry an elastic dislocation model predicting the amount of interseismic deformation at the given observation points was established. In the following, this model will be referred to as the *Andean Elastic Dislocation Model* (AEDM) [Khazaradze and Klotz 2002]. Subtracting the best-fit model solution from the GPS observation data resolves a *residual velocity field*, which is assumed to represent the intraplate deformation of the overriding South America plate. Due to the fact that the GPS technology allows for the determination of absolute displacement vectors, rigid body motions (rotations and translations) as well as internal deformations (strains) can be determined for the velocity fields. The basic theory for the calculation of strains and rigid body motions is provided by Khazaradze [1999 and ref. therein].

### 3.6.1 Geodetic Strain Rates and Differential Motion

For the purpose of this study a subset containing 15 sites located in North Central Chile was selected from the GPS network. The selected stations are aligned in two subparallel N-S trending rows representing the Coastal Block and in the Precordilleran Block, respectively (Fig. 3.7 A). Since this study focuses on horizontal deformation rates, the vertical components are ignored. Thus only the north-

ward (positive N) and eastward (positive E) velocities were taken from the residual velocity field in order to approximate deformation rates for the study area. There are two ways to analyze the residual velocity field:

1. Calculation of the two-dimensional strain tensor at the center of the considered area
2. Calculation of the differential motion between two rigid blocks

The principal horizontal strain rates (1) are calculated using the computer code “strain\_m“ written by Wang [1998]. The program is based on formulations presented in Khazaradze [1999]. The program converts site positions into a geocentric (x,y,z) coordinate system, assuming a spherical earth. A local two-dimensional coordinate system (x = east and y = north) is established in the plane perpendicular to the center vector of the network, with the center of the network taken as its origin. The strain calculation is based on the assumption that the estimated velocity at each site remains constant throughout the observation period of 2 – 3 years. The resulting strain rates represent an average strain field over the entire net. The differential motion (2) between the Coastal and the Precordilleran Blocks is calculated based on the assumption that both represent individual rigid blocks. If this is the case, the N-S and E-W components for each block can be averaged individually and the differential motion is resolved by subtracting the mean vectors from one another (Fig. 3.7 A).

In order to estimate the interseismic geodetic moment rate imposed on existing crustal faults separating the Coastal and the Precordilleran Block, the differential motion is applied to a model fault geometry which best represents the intraplate fault geometry observed in the field and modeled with the help of simple dislocation models. Considering the strike and dip of the intraplate fault, and the azimuth of the horizontal differential motion, a dip-slip and strike-slip component within the fault plane is calculated (Fig. 3.7 B). Based on these slip components the length and the rake of the resulting slip vector within the fault plane is obtained. Given the fault dimensions and the shear modulus ( $3 \times 10^{10}$  Pa) the resulting slip rate can be applied to Kostrov's [1974] formulation (3.5) in order to obtain the moment imposed on the considered intraplate fault geometry.

## 4 Results

### 4.1 Neotectonic Field Observations

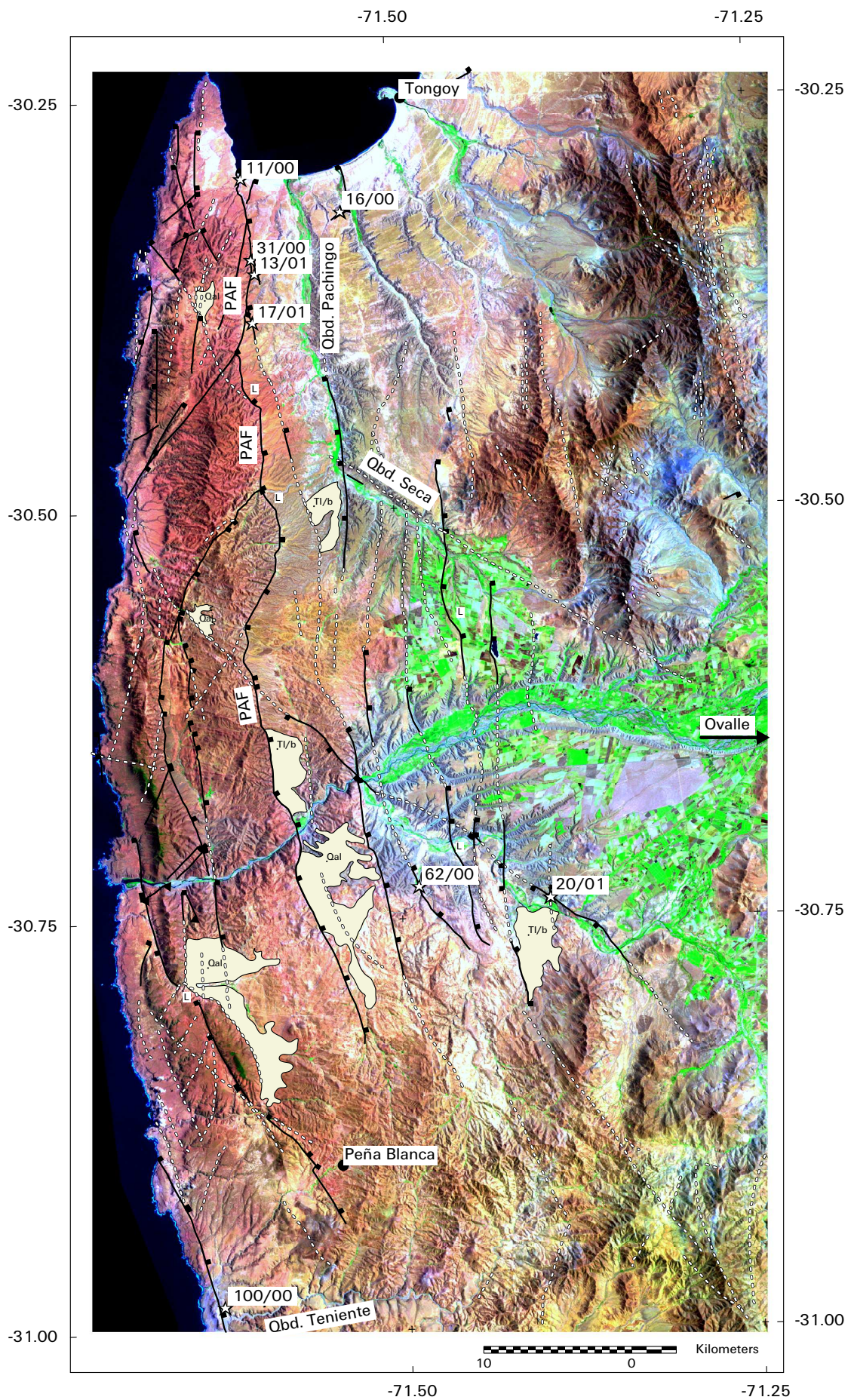
This section presents the major findings resulting from neotectonic field studies and remote sensing analysis. Proofs for intraplate faulting were collected from satellite imagery data (Landsat TM), aerial views and through field observations. Later these were complemented with the information provided by the geological map [Gana 1991]. A selection of excellent outcrops showing the most recent type of deformation will be presented in greater detail.

#### 4.1.1 Intraplate Deformation

The resulting *intraplate fault pattern* is shown in Fig. 4.1. The predominant type of intraplate faults detected from remote sensing data and observed in the field are N-S to NNW-SSE striking normal faults. The most important intraplate feature is the *Puerto Aldea Fault* (PAF), which is easily mapped as photolineament over a distance of  $\sim 60$  km between the southern tip of Tongoy Bay and the village of Peña Blanca. The majority of N-S striking faults dips towards the east, while only a few faults within the Coastal Cordillera and the Cenozoic basin dip towards the west. According to the geological map and field observations such as offset drainages (see Fig. 4.5), a left-lateral component is observed along these faults. A number of micro-basins, filled with Plio-Pleistocene lacustrine sediments or Quaternary alluvial deposits ("TI/b" or "Qal" in Fig. 4.1), are juxtaposed to the N-S striking faults. The western borders of these micro-basins are rectilinear while the eastern margins are strongly embayed. This indicates normal faulting activity along the western borders, with depressions forming on the hanging wall side of the faults. In addition the traces of the N-S striking faults frequently exhibit *left-stepping extensional jogs* ("L" in Fig. 4.1), which support the observation of left-lateral strike slip along the PAF. In the south of the study area most of the prominent N-S striking intraplate faults gradually taper out. The satellite image shows that this part of the study area is extremely fragmented, without any predominant structural lineation.

---

Figure 4.1: (See next page) Intraplate fault pattern compiled from remote sensing information (Landsat TM scene, aerial views), field observations and geological map [Gana 1991]. Boxed line – proper intraplate normal faults; Line with triangles – reverse faults; Dashed line – apparent or hidden faults; L – left-stepping jog; Polygons – Plio-Pleistocene lacustrine (TI/b) or Quaternary alluvial (Qal) micro-basins [Gana 1991]; Stars – locations of Figs. 4.2-4.10.



The Coastal Cordillera exhibits two clearly NE-SW striking SE-dipping normal faults. These faults are truncated by the N-S trending range-front fault (PAF), suggesting that the latter postdates the formation of the NE-SW trending features. In addition, two NW-SE striking lineaments cross the Cenozoic basin. They appear as clear lineaments due to their strong topographic expression. Oversteepened hillslopes and apparent topographic offsets mark their trace in the field, but very rarely fault planes are exposed. These features are interpreted as hidden or proposed intraplate faults. It is not clear whether these predate or postdate the N-S striking intraplate faults. However, the NW-SE striking faults show two clear examples of multiply, right-laterally offset stream channels. The offset streams are located near the junction of Qbd. Pachingo with Qbd. Seca and steeply incise a loosely consolidated Plio-Pleistocene river terrace.

Only three examples for reverse faulting of marker horizons were found in the field. One outcrop is located within the Plio-Quaternary sedimentary record (Fig. 4.10). It is located near the southern margin of Tongoy Bay with a fault plane striking NE-SW and dipping towards the southeast. Another NE-SW striking and SE-dipping thrust plane is found near the Río Limarí estuary within the Paleozoic rocks of the Coastal Cordillera. One kilometer southeast of this point, the only reverse fault striking perpendicular to the shortening direction of the plate convergence is found. However, the displaced lithological units at this site are considerably older compared to the other locations and thus may not represent the most recent type of deformation.

The careful interpretation of the fault pattern reveals an overall E-W oriented extensional character of the study area. The E-W extension affects the most recent lithological units and leaves a strong signal in the topography. The formation of micro-basins on top of the Cenozoic basin all over the study area indicates ongoing tectonic activity. In addition, the left-lateral motion along the N-S striking faults and the right-lateral deformation along NW-SE striking faults complement each other in a way that both indicate a paleostress regime with the principal compressional forces acting subparallel to the trench.

### **Extensional and Strike-slip Faulting**

In the following, seven outstanding examples of extensional and strike-slip faulting observed throughout the study area are presented in greater detail in order to demonstrate the abundance of paleoseismological features in this part of the Chilean forearc. Four outcrops were found along the northern segment of the PAF (11/00, 31/00, 13/01 & 17/01). These four sites provide evidence for crustal faulting activity of Plio-Pleistocene soft rocks along the present range front separating the Coastal Cordillera from the Cenozoic basin.

About 1 km south of the village of Puerto Aldea in the SW corner of Tongoy Bay the outcrop of *El Rincón; 11/00* is located (Fig. 4.2). At this site a sequence of marine terraces from the Mid-Miocene *Coquimbo Formation* [Martinez 1979; Martinez and Perez 1980; Gana 1991] are tilted towards the west. The tilt of the marine terraces implies that a tectonic rollover structure is situated at depth. The dip of the bedding planes averages 30° [Paskoff 1970]. Approximately 1.3 – 1.4 km east of *El Rincón* the terraces come to rest again in subhorizontal position. Sediments of the Plio-Pleistocene transgression discordantly overlay the tilted Mid-Miocene strata. The Plio-Pleistocene sediments themselves are overlain by Quaternary alluvial deposits.

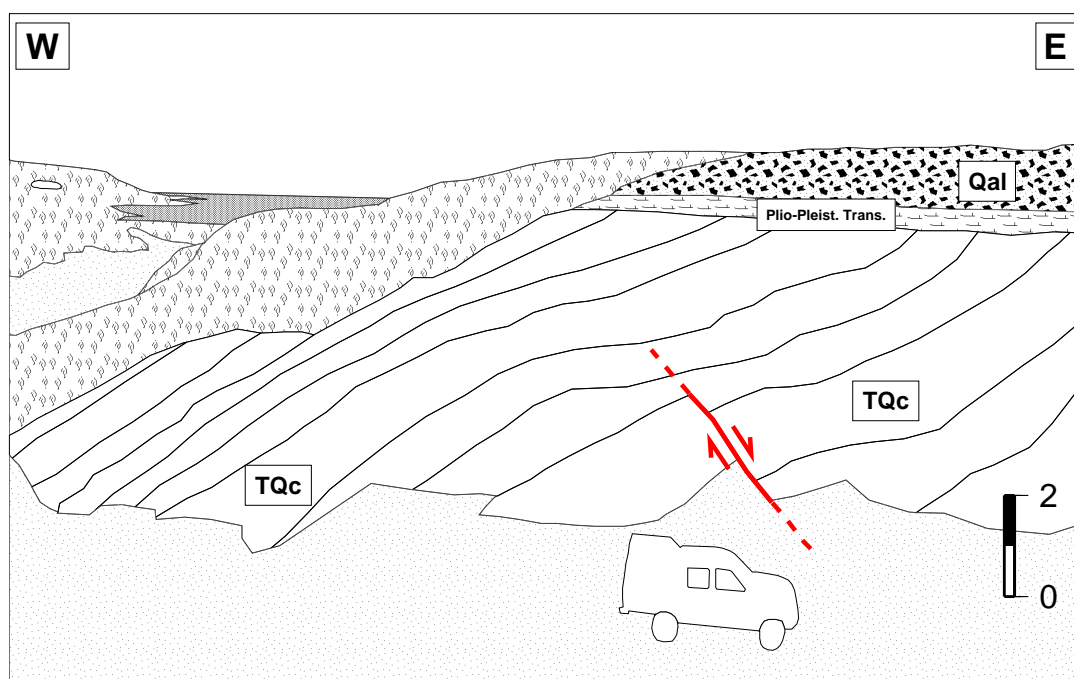


Figure 4.2: Site 11/00. Tilted terraces of Middle-Upper Miocene Coquimbo Formation (TQc) with secondary fault plane. Bedding planes dip with  $30^\circ$  towards the main fault trace of the Puerto Aldea Fault located west outside the frame. Plio-Pleistocene transgression discordantly overlays Coquimbo Formation; Qal – Quaternary alluvial; Thick line (continuous/dashed) - secondary fault plane.

Fault-slip data were collected along secondary fault planes within the sequence of tilted terraces and from the contact between the Coquimbo Formation and the Paleozoic. The observed vertical offsets range from 0.1 – 0.5 m on the secondary fault planes. However the total inferred vertical displacement amounts to 570 – 675 m as suggested by the wavelength of the rollover structure and from geophysical records [Meinardus 1961; Rocroi 1964]. The dominant dip direction of fault planes in this outcrop is ENE. The dip angle is  $60\text{--}65^\circ$ . In total 33 fault-slip data sets from distinct oblique dip-slip or strike-slip kinematic indicators were obtained. Together with the macroscopic inventory of the outcrop and the geomorphology of the nearby range front, this suggests predominantly extensional faulting with a left-lateral component. The extension axis resulting from the fault-slip data analysis trends SW-NE (trend/plunge =  $238^\circ/7^\circ$ ; see 11/00 in Appx. A.4). The maximum shortening direction for the strike-slip motion is oriented NNW-SSE. Fibre growth and the formation of riedel shear planes is observed on fracture planes along the contact between the Paleozoic basement and the marine terraces. The growth direction of the fibres as much as the riedel shear planes indicate dip-slip motion at this site.

Following the strike of the Puerto Aldea fault  $\sim 5$  km towards the south, a  $75^\circ$  E-dipping normal fault offsetting Plio-Pleistocene alluvial and fluvial strata of the Limarí Formation is found Fig. 4.3. The outcrop (31/00) is located in a steeply incised creek valley. A 2 m thick fluvial horizon consisting of relatively well sorted and well rounded cobbles (diameter: 1 – 50 cm) is vertically offset by 5.2 m. Where the fault plane intersects with the fluvial horizon numerous *crushed cobbles* were found. On the splitting planes of the crushed cobbles kinematic indicators can be observed. Overlying the fluvial

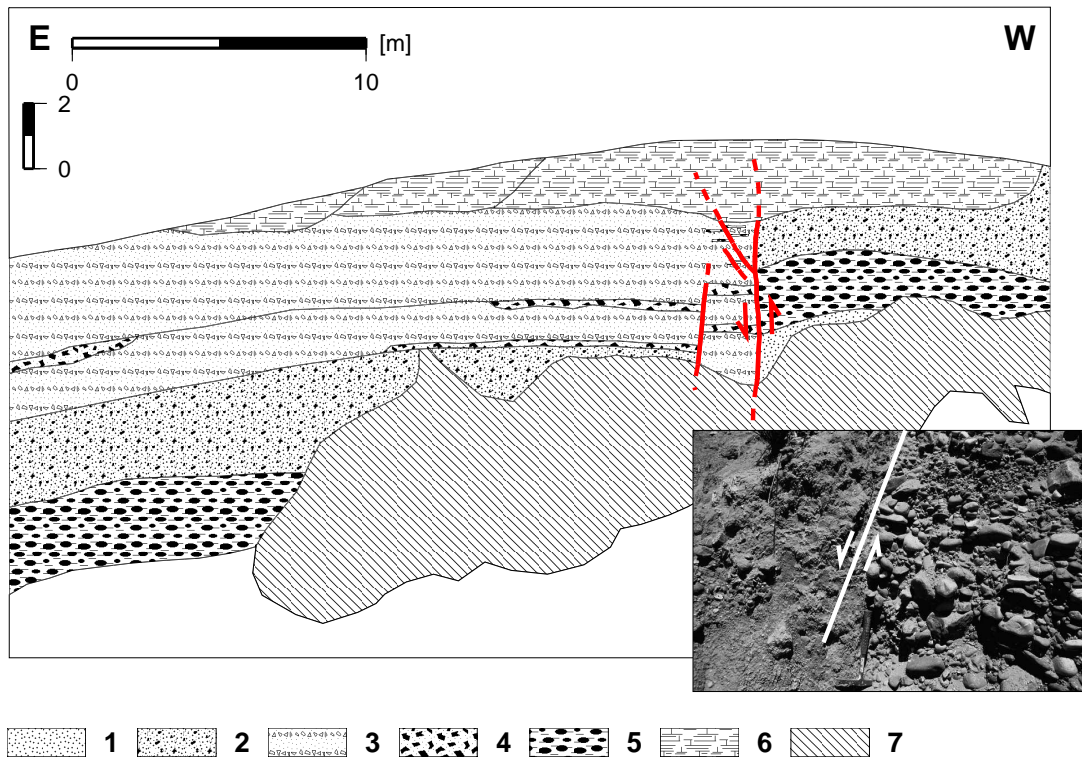


Figure 4.3: Site 31/00. Puerto Aldea fault 4 km S of El Rincón. Vertical offset of 5.2 m within Limarí Formation. Inset shows crushed cobbles in the fault plane. 1- Sand, 2 - Sand with up to 30% components of cm - dm size, 3 - Alluvial (silty sandy) with soil formation, 4 - Alluvial layer (poorly rounded cobbles), 5 - Fluvial layer with crushed cobbles at intersection with fault plane (> 75% well rounded cobbles), 6 - Alluvial (sandy-silty) with caliche formation, 7 - talus deposits, Thick line (continuous/dashed) - fault plane.

horizon follow sandy-silty sediments, intercalated by several 0.1 – 0.5 m thick alluvial debris layers and paleosols. Within the alluvial debris minor normal offsets in the order of 0.5 m were observed. Near the surface a secondary thrust dipping towards the major fault plane produces a vertical offset of 0.25 m. Despite the large displacement along the main fault-trace no fault-scarp was observed at the surface. However, the silty-sandy caliche horizon on top of the outcrop displays a strong cleavage on the hanging wall side, close to the projection of the major fault plane into the overlying beds. About 24 fault-slip data sets showing distinct dip-slip and strike-slip slickenside kinematic indicators were obtained. The dip-slip lineations have an oblique component and the strike-slip indicators show sinistral movement. The extension axes resulting from both, the normal faulting and strike-slip kinematic indicators, are oriented SW-NE ( $237^{\circ}/0^{\circ}$ ; see 31/00 in Appx. A.5). The shortening direction inferred from the strike-slip kinematic indicators is oriented (NW-SE).

The next site (*13/01*) is located 1 km farther south along the Puerto Aldea fault (Fig. 4.4). Here, Plio-Pleistocene sediments (Limarí Formation) are offset by 4.0 – 4.7 m vertically. The central sequence is a 4 – 5 m thick reddish-brown clayey silt which contains two 0.1 – 0.2 m thick caliche bearing marker horizons that are offset by the fault. The uppermost unit of this outcrop consists of well to moderately rounded cobbles with diameters ranging from 1 – 25 cm in size. Its fluvial char-

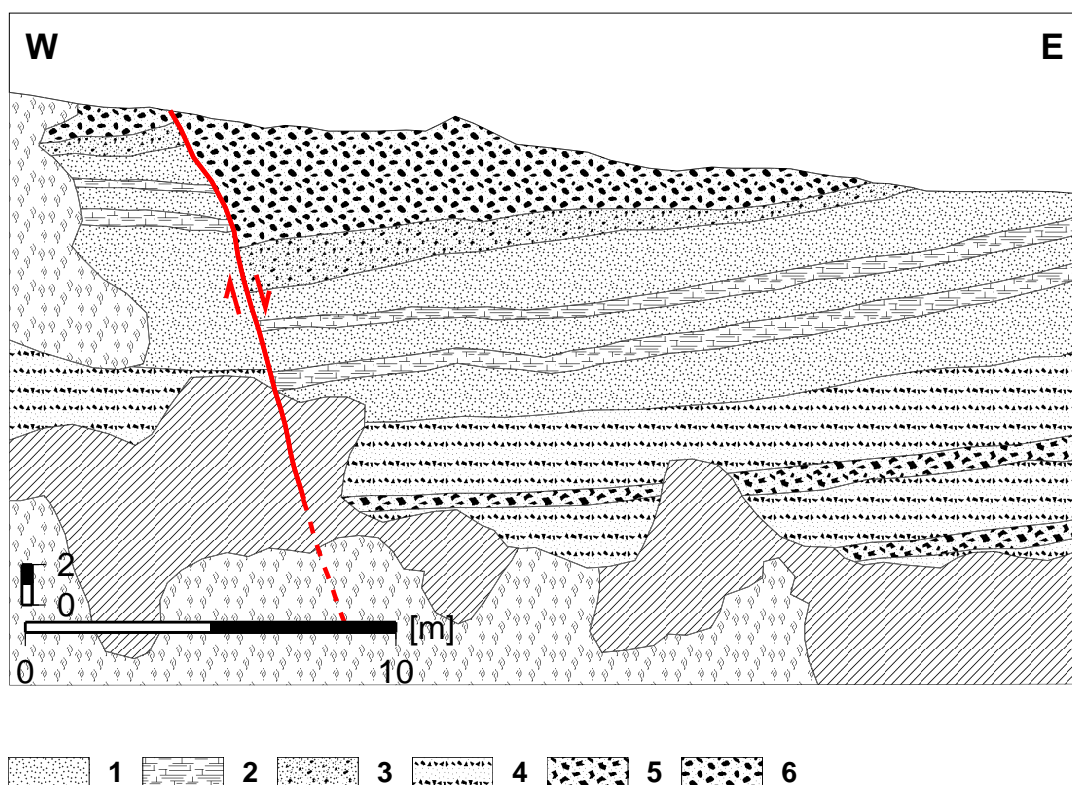


Figure 4.4: Site 13/01. Puerto Aldea fault 5 km S of El Rincón. Plio-Pleistocene Limarí Formation offset by 4.0 – 4.7 m 1- Clayey silt with soil formation in the capping beds, 2 - Clayey silt with caliche formation (white bands), 3 - Silty sand with up to 10% components of mm - cm size (moderately rounded), 4 - Sand (fine-coarse grained, grey-green), 5 - Alluvial layer (poorly rounded cobbles), 6 - Fluvial layer with crushed cobbles at intersection with fault plane (> 75% well rounded cobbles), Thick line (continuous/dashed) - known/presumed fault plane.

acter compares well to the main 2 m thick fluvial horizon in Fig. 4.3. The lower boundary of this unit is offset along the fault by about 4.7 m vertically. In the fault plane several *crushed cobbles* were identified. Slickenside kinematic indicators for both, oblique normal and strike-slip deformation were found on the gouge material of the fault plane or on crushed cobbles. The macroscopic structural inventory and the obtained fault-slip data reveal significant WSW-ENE normal faulting activity at this site ( $247^{\circ}/1^{\circ}$ ; Appx. A.12). The strike-slip shortening direction is NW-SE.

All outcrops shown in Figs. 4.2-4.4 have in common that distinct normal and strike-slip kinematic indicators are present on well developed clay gouges. Topographic fault-scarps, which are typically linked with normal faulting near the surface, were not found. Most likely they have been eroded over time. The strike-slip component however, leaves a strong signal in the topography (Fig. 4.5). Numerous stream channels are left-laterally offset along the northernmost segment of the PAF. The individual horizontal displacements measured in range from 75 – 250 m. The topographic signal of the strike-slip deformation is still present while potential fault-scarps connected to normal faulting are already eroded. This suggests that the strike-slip activity postdates the dip-slip motion along these faults. However, both types of deformation were inferred from slickenside kinematic indicators

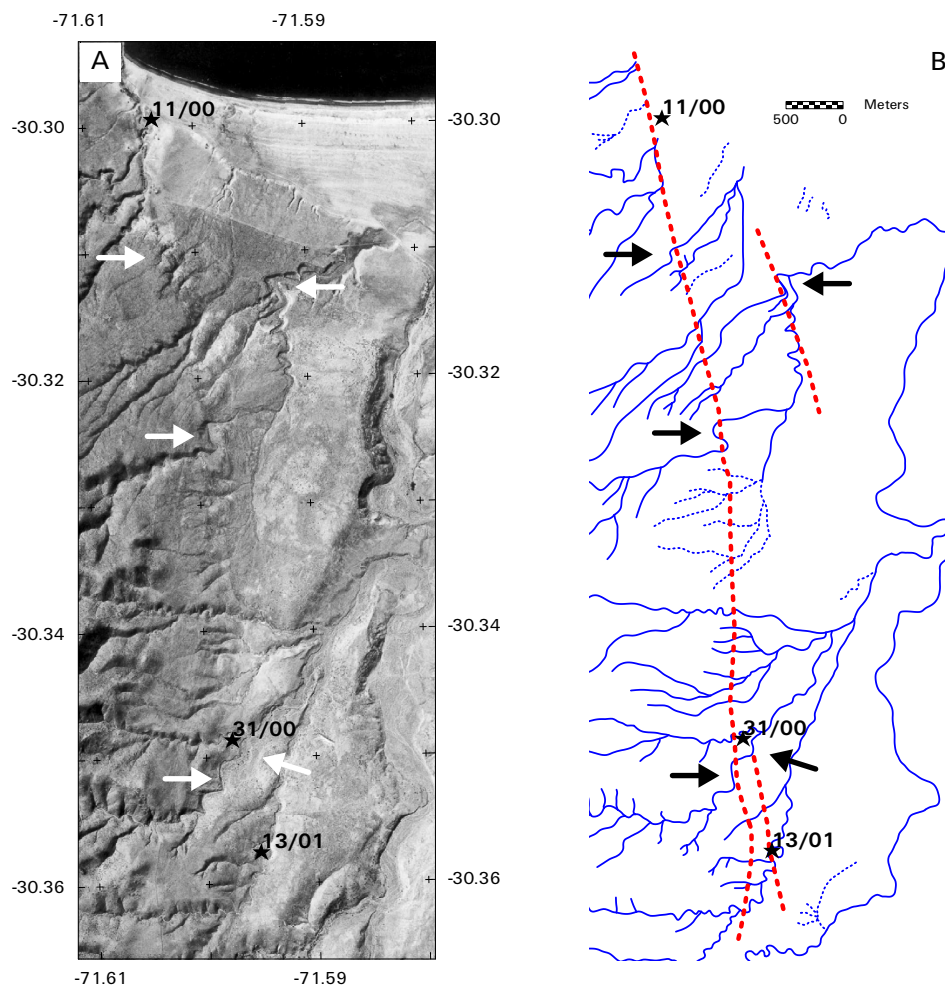


Figure 4.5: The *Puerto Aldea Fault* south of Tongoy Bay; A – Aerial view showing left-laterally offset stream channels (white arrows) and locations of Figs. 4.2-4.4; B – Sketch map of the drainage network in A; Dashed line – *Puerto Aldea Fault* and secondary strands; Arrows depict left-laterally offset stream channels.

on fault planes truncating the Plio-Pleistocene *Limarí Formation*. Thus both deformations occurred during the recent geologic past and have to be regarded as simultaneous rather than successive events.

The outcrop *17/01* (Fig. 4.6) is located ~ 3 km south of site *13/01*. It is dominated by a *colluvial wedge* that reaches 2.1 m in thickness near the fault plane and rapidly tapers out to the east away from the fault. It consists of a grey, sandy matrix and contains up to 50% components. The components are badly - moderately rounded metamorphic rock fragments of 0.01 – 1 m in size, assembled in complete disorder. The uppermost 0.5 m of this unit change towards brown colors and show a *hardground* on top, suggesting exposure to subaerial conditions and a beginning soil formation. At the base of the colluvial wedge follows a paleosol which is truncated by the colluvium. There are no signs of a fault-scarp at the surface. The alluvial horizon covering the outcrop remains unfaulted. It was not possible to trace the fault plane into the subjacent beds but the lithological contrast between the pre-

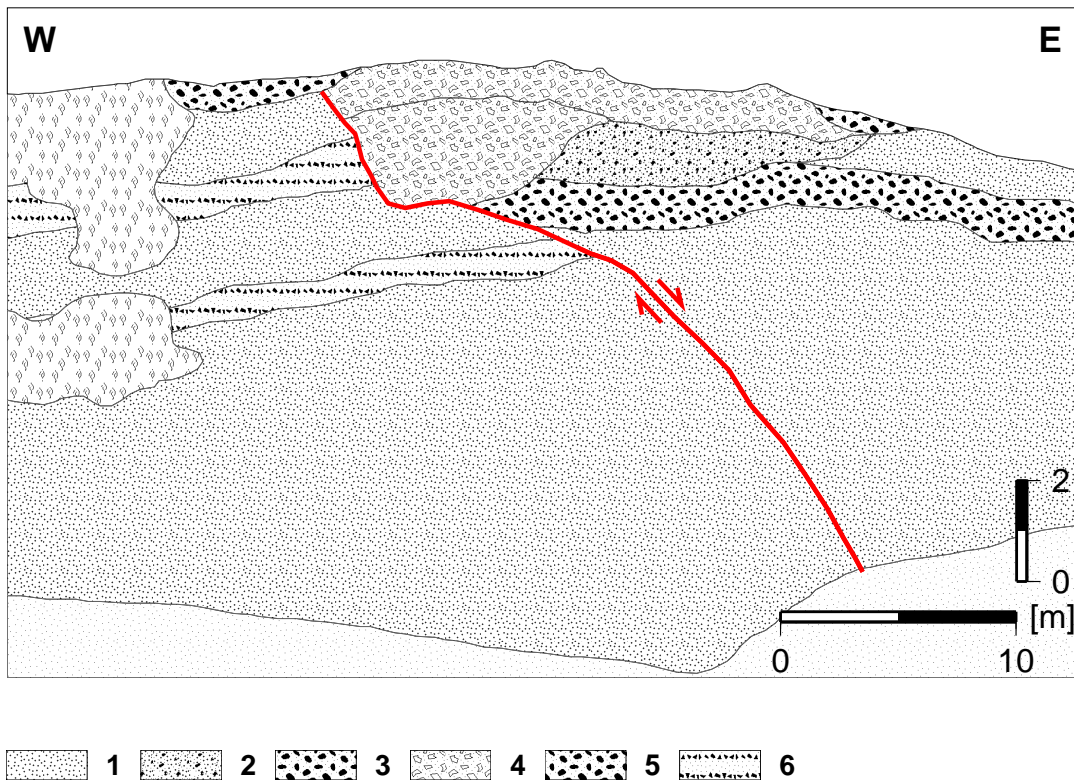


Figure 4.6: Site 17/01. Puerto Aldea fault 8 km S of El Rincón. *Colluvial wedge* of 2.1 m thickness leaning against footwall scarp. The colluvium consists of a grey sandy matrix with up 50% badly - moderately rounded components of 0.001 – 1 m size. 1 - Clayey silt (red-brown) < 10% components, 2 - Silty sand (red-brown) < 10% components with soil formation, 3 - Sandy matrix (dark red- black) > 75% components of cm-dm size (badly-well rounded), 4 - Colluvium (grey-brown) with > 50% components of cm - m scale (badly - moderately rounded); upper section represents hardground, 5 - Alluvial (sandy-silty) with > 75% components of cm - dm size (badly-moderately rounded), caliche coatings, Thick line - fault plane.

sumed footwall- and hanging wall sides indicates a fault contact. The vertical offset is 2.1 – 2.7 m. The bedding planes on both sides of the fault-trace are clearly tilted towards the west, suggesting that larger scale deformation occurred further west along the nearby range-front fault. This interpretation is strengthened by the finding of a spring in the river terrace only 150 m west of this point. Fault-slip data at this site are scarce and resulting principal strain directions have to be treated with care. From three fault-slip data sets a roughly WSW-ENE extension direction ( $246^{\circ}/20^{\circ}$ ; see 17/01 in Appx. A.12) can be inferred. Fault-slip data was mainly collected from *crushed cobbles* at the contact between the colluvial wedge and the fault plane.

Site 62/00 is located in the very center of the study area near the village of *Termas Socos* (Fig. 4.1), a few hundred meters east of the Pan American Highway (PanAm). A near vertical fault plane truncates the free face of the  $\sim 8$  m high outcrop into two halves (Fig. 4.7). A mega-conglomerate containing boulders in the order of 0.1 – 1 m dominates the western side while coarse sands interbedded with alluvial horizons prevail on the eastern side. The fault dips steeply ( $70^{\circ}$ - $80^{\circ}$ ) to the east and exhibits a clay-gouge with clear subhorizontal striations. *Crushed cobbles* are found in the fault plane,

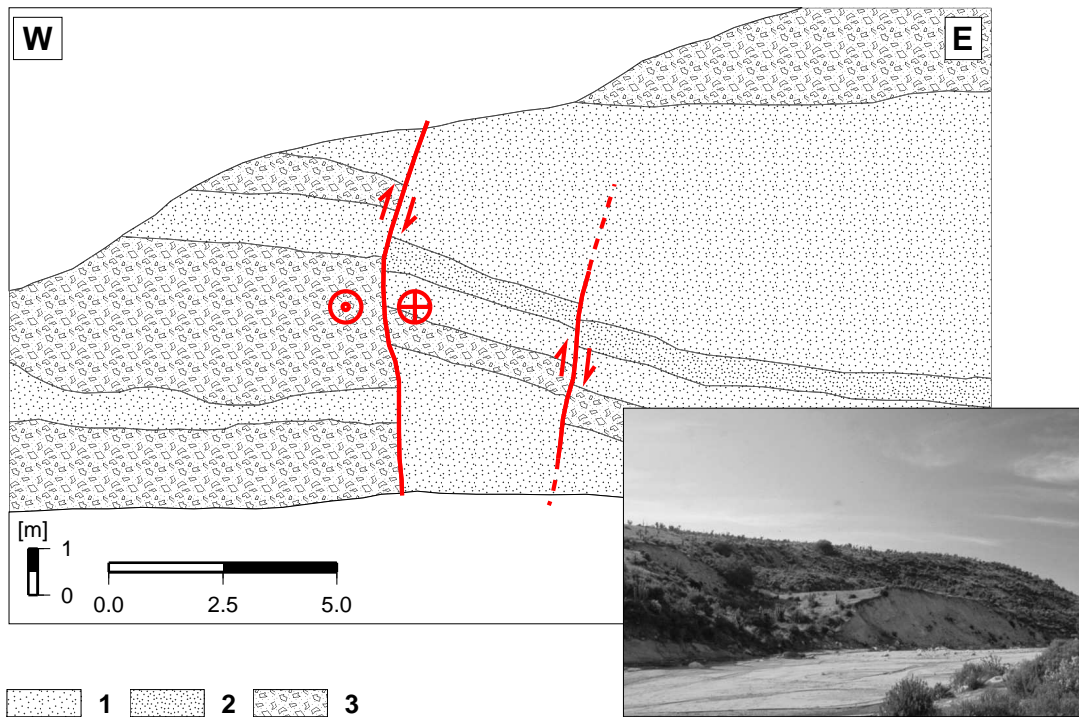


Figure 4.7: Site 62/00. Terrace riser at Termas Socos near the Pan American Highway. Left lateral strike-slip and E-W normal faulting on 70-80° E-dipping fault planes (Apparent W-dip in sketch due to cross bearing effects of steep fault planes in the outcrop). Clay gouges with broad striations. Lithological contrast approximately 8 m high. Normal faulting offset along secondary fault plane is  $\sim 0.65$  m. Inset shows nearby *landslide*; 1 – Gray medium - coarse sand with  $< 10\%$  components (0.1 – 1 cm); 2 – Red-brown sandy silt; 3 – Alluvial horizon (mega-conglomerate) with  $> 50\%$  badly rounded components (0.1 – 1 m).

suggesting instantaneous fault rupture. An offset of (0.65 m) along a secondary E-dipping fault plane indicates normal faulting only 2 m east of the main fault-trace. About 300 m north of this site a *thermal spring*, presently exploited by a health resort, is located right on top of the prolongation of the fault-trace. The water is  $\sim 28^\circ$  hot and rich in iodine, bromine, magnesium and soda. In the southern continuation a fresh landslide is observed (see inset of Fig. 4.7), suggesting recent strong ground motion in this region, possibly related to activation of the nearby fault. In total 14 fault-slip data sets were obtained, showing predominantly left-lateral strike slip along the fault. Only three dip-slip kinematic indicators were found on secondary fault planes. The resolving shortening direction is oriented SE-NW, while the extension direction trends WSW-ESE. A composite solution of both, the strike-slip and dip-slip motion would yield left-oblique transtensional deformation at this site (see 62/00 in Appx. A.8).

The outcrop 100/00 is located in the southernmost section of the study area near Qbd. Teniente ( $30.98^\circ$  S; Fig. 4.8). Here, thanks to the reconstructions of the PanAm, a  $\sim 500$  m long road-cut exposes extensional and strike-slip faulting of Quaternary conglomerates and sands. The whole outcrop is dissected into numerous *horst and graben* structures which are flanked by two strike-slip faults at the eastern and western ends, respectively. The strike-slip faults are easily recognizable through

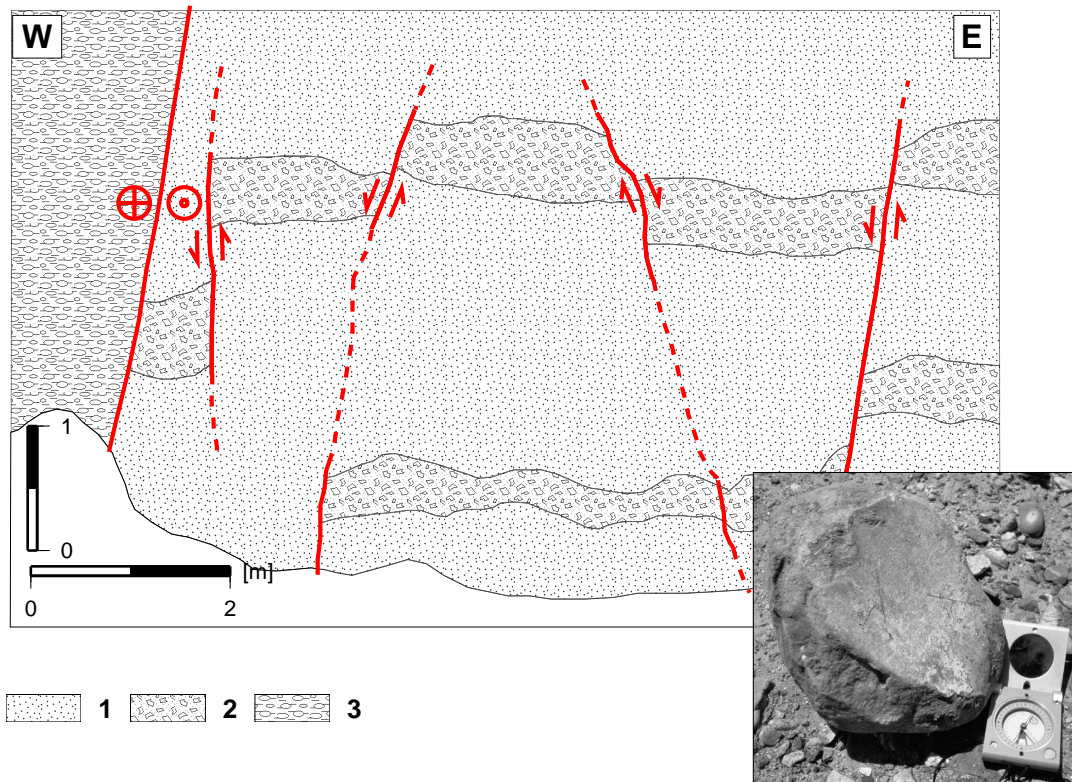


Figure 4.8: Site 100/00 near Qbd. Teniente ( $30.98^{\circ}$  S). *Horst and Graben* structures in Plio-Pleistocene Alluvial/Fluvial deposits. Inset shows *Crushed Cobble*; 1 – medium - coarse sand with < 5% components. Components are 0.5 – 5 cm in size; 2 – Alluvial/Fluvial horizons with up to 75% components in same matrix as 1. Components (1 – 50 cm) are badly rounded, fluvial components (0.5 – 5 cm) are moderately - well rounded; 3 – Conglomerate in coarse sandy matrix with well rounded, elongated cobbles (diameter: 1 – 50 cm).

lithological contacts that persist from the top to the bottom of the free face, covering a vertical distance of 10 – 30 m. A representative fraction of the observed deformation is shown in Fig. 4.8. The conglomerates consist of  $\sim 60\%$  sandy matrix with well rounded slightly elongated cobbles of cm-dm in size. They form a sharp contrast to the juxtaposed coarse sands that are interbedded with  $\sim 1$  m thick alluvial and fluvial horizons (Fig. 4.8). These horizons are truncated in a horst and graben like fashion and thus provide excellent markers for the deformation at this site. The measured vertical offsets vary between 0.5 – 0.9 m. The adjacent lithological contrast represents a strike-slip fault with a dextral component. This fault can be traced over  $\sim 30$  m vertically and thus suggests the accommodation of much larger amounts of deformation as can be inferred from the offsets observed in the fluvial/alluvial horizons (Fig. 4.8).

In addition, the occurrence of two *seasonal springs* in the immediate vicinity of the fault-trace indicates that the subsurface continuations of the major faults are open connected features. Numerous *crushed cobbles* were found in this outcrop (see inset in Fig. 4.8). Their splitting planes are neatly aligned with the fault planes, suggesting instantaneous fault rupture rather than creep as the prevailing deformation process. At the western border of this outcrop and to the south, inside the Qbd. Teniente, the eastern range front of the Coastal Cordillera is well exposed forming an impressive  $65^{\circ}$  E-dipping

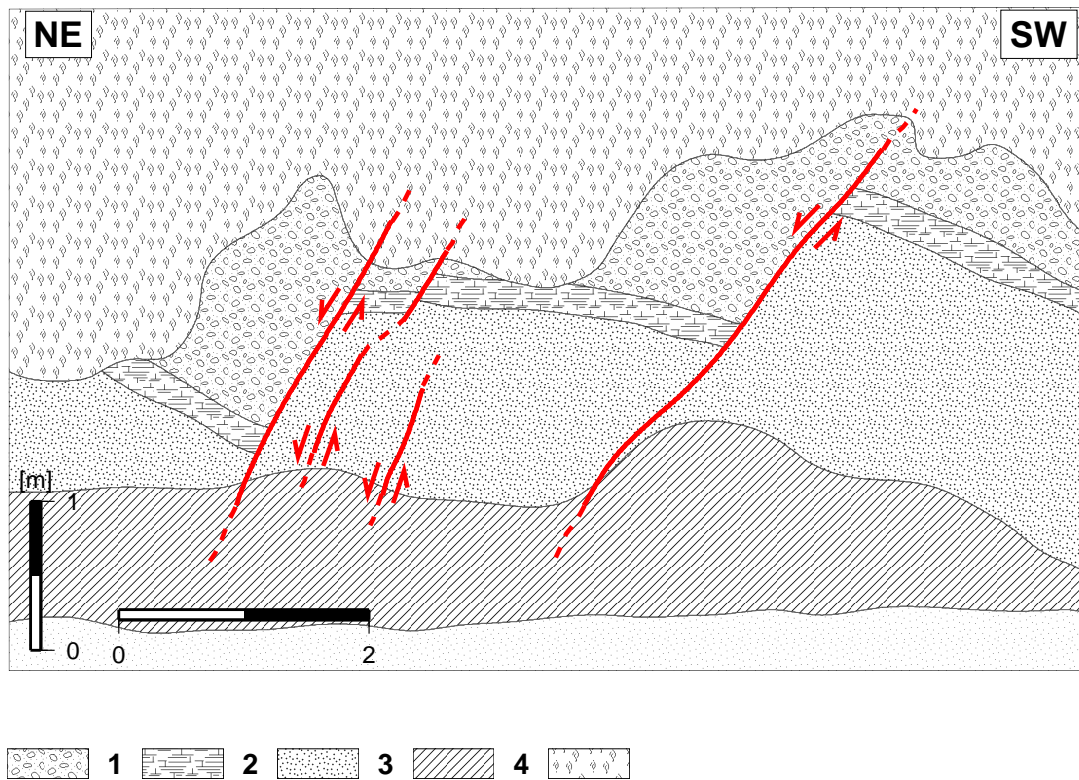


Figure 4.9: Site 20/01. Road-cut near the village of Chalinga. Vertical displacements on 65-80° E-dipping normal fault planes amount to 2.2 – 2.6 m; 1 – Gray-white medium sand with > 50% components (0.5 – 10 cm). Crushed cobbles with striations in the fault plane; 2 – Caliche bearing clayey silt, 3 – Layers of Silty fine - medium sands. Colors: red-brown (top), gray-green (middle), and yellow-brown (bottom); 4 – Talus deposits; 5 – Vegetation.

plane extending from the river bed to approximately  $\sim 200$  m in altitude. While the range front dips towards the east, the slip surfaces within the outcrop predominantly dip to the west, probably representing antithetic secondary features related to the deformation along range-front fault itself.

Site 20/01 is a road-cut near the village of Chalinga (Fig. 4.9). A set of 65-80° E-dipping normal faults is observed. Two offsets of 1.1 – 1.3 m were measured using a caliche bearing layer as marker horizon. The surrounding topography is characterized by numerous scarplike landforms that could be related to the observed fault plane. The tilting of the bedding planes in combination with the strong signal from the adjacent topography suggests that displacements with greater magnitudes are hidden east of this point. A nearby rollover structure also indicates displacements in the order of tens of meters. These observations from the eastern central part of the study area, show that significant normal faulting is not restricted to the frontal edge of the continental forearc but remains the dominant type of deformation at least as far as 30 km landward from the coast. In addition, morphological scarps are more frequently detected in the topography farther away from the actual coastline. This suggests that intraplate faulting activity is more recent landward from the eastern range front of the Coastal Cordillera. The apparent landward shift of crustal deformation imposes a higher seismic hazard on the communities further inland (i.e. Ovalle) than the more frequent subduction earthquakes do alone.

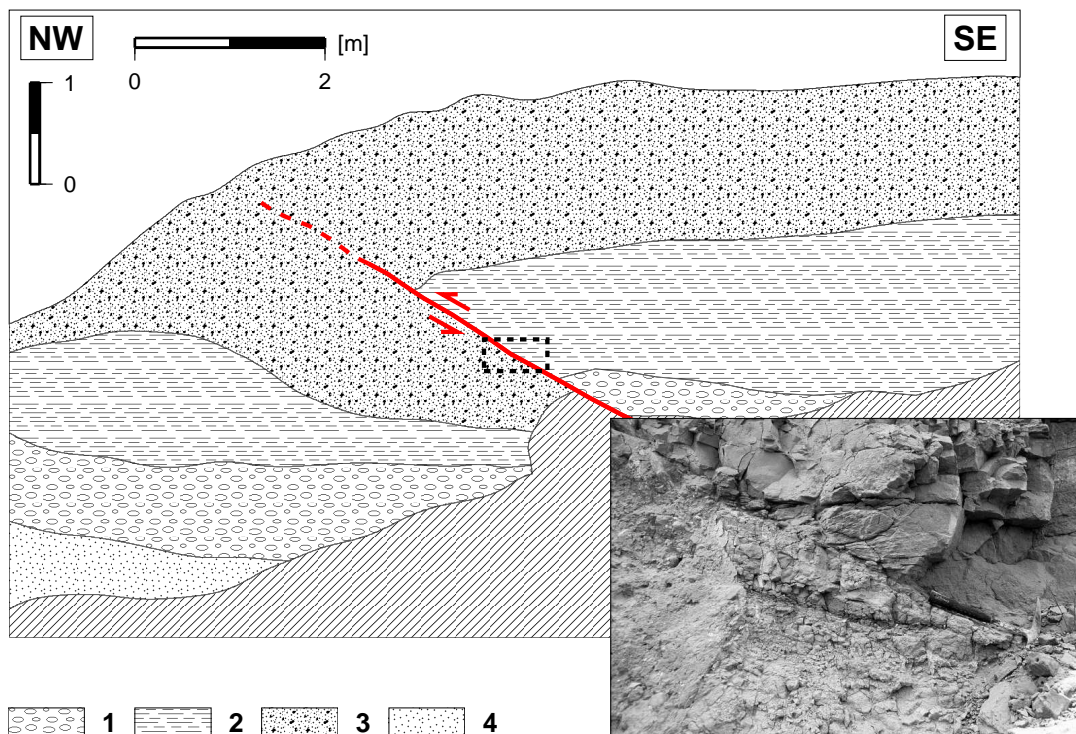


Figure 4.10: Site 16/01. Road-cut near the village of El Tangué. The figure shows reverse faulting in Plio-Pleistocene fluvial sediments (Limarí Formation). The vertical displacement is 0.8 – 1.2 m. Inset shows broadly developed *riedel shear planes* dipping towards the fault plane. 1 – Fluvial layer with sandy matrix and > 50% well rounded and elongated components (1 – 10 cm); 2 – Clayey silt, finely laminated; 3 – Reddish-brown clayey-silty sand with ~ 20% moderately rounded components (1 – 25 cm); 4 – Sand.

### Reverse Faulting

Reverse faulting is rarely observed all over the study area. Within the sediments of the Cenozoic basin only one single outcrop with a low angle thrust fault was found in a road-cut near *El Tangué* (Fig. 4.10). The observed vertical displacement at this site (16/00) is 0.8 – 1.2 m on both sides of the road. The slip surface consists of a well developed clay gouge that truncates a > 1 m thick fluvial conglomerate. The conglomerate consists of a coarse sandy matrix with > 50% components. The components are well rounded and elongated pebbles of 1 – 10 cm in size. The overlying finely laminated clayey silt is partly smeared into the fault zone. In direct contact with the fault the clayey material shows pronounced *riedel shear planes* (see inset Fig. 4.10). The orientations of the riedel shear planes clearly suggest reverse faulting along the fault. Since the fault plane verges towards the slope of the local topography it is possible that the offset represents a landslide rather than a crustal faulting event. The shortening direction inferred from 4 fault-slip data sets is oriented SE-NW. A lateral continuation of this fault is not clearly identified, neither as photolineament on aerial views nor as geomorphic feature in the field.

## 4.2 Fault-Slip Data Analysis

In order to investigate the paleokinematics of the study area ca. 1500 fault-slip data sets from 84 outcrops were collected in the field and analyzed according to the methods described in Chapter 3.2.2. Many fault planes exhibit two or more distinct slickenlines on the same slip surface. Fault planes within the Paleozoic basement rocks display up to four cross cutting lineations, while fault planes in the Cenozoic strata predominantly show no more than two superimposed sets of fault striae on the same surface.

### 4.2.1 Fault Plane Distribution

The dip azimuths of 1000 individual fault planes derived from  $\sim 1500$  fault-slip data sets are plotted in Fig. 4.11. Approximately  $2/3$  out of all fault planes dip towards ENE-NE directions. The average dip angle is  $63.8^\circ \pm 14.9^\circ$ . The average dip azimuth of faults is  $83.6^\circ \pm 5.1^\circ$ . The preferred trend of dip azimuths corresponds well with the intraplate fault pattern presented in Fig. 4.1. The aforementioned recognition of multiple slickenlines on identical slip surfaces leads to a large discrepancy between the total of fault-slip data sets (1513) and the number of fault planes (1000), as demonstrated in Fig. 4.11. The misfit between these numbers simply shows that roughly  $1/3$  of all fault planes underwent multiple stages of deformation. The strongest maximum in Fig. 4.11 B covers a range of  $5^\circ$ - $25^\circ$  between azimuths  $55^\circ$  and  $80^\circ$ . The spread in the data corresponds to the field observation, that despite natural undulations of dip azimuths and minor measurement errors, many outcrops within the Cenozoic

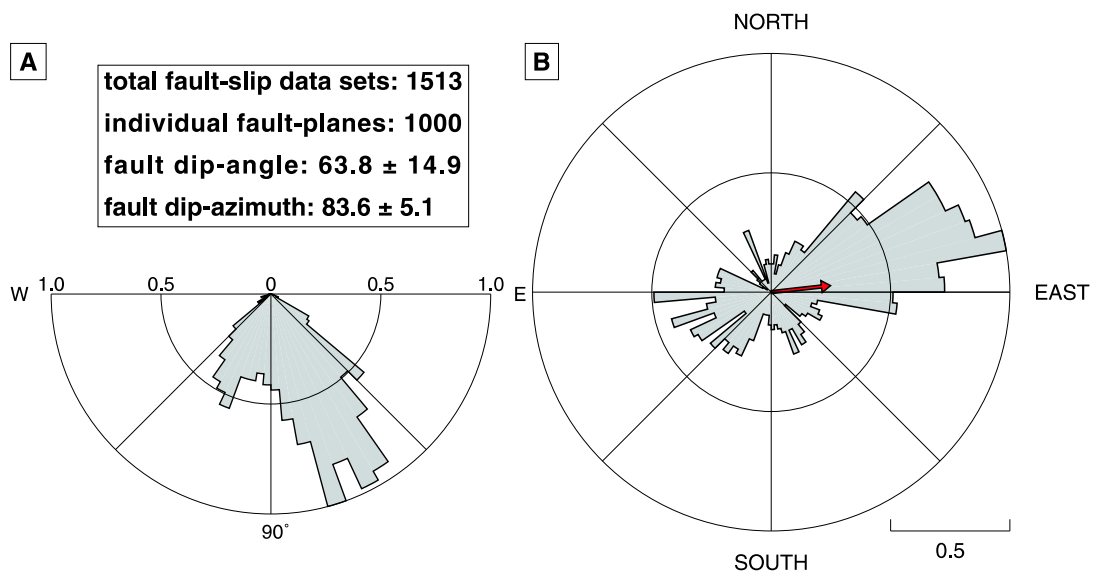


Figure 4.11: Equal length rose diagrams showing dip angle (A) and dip azimuth (B) of 1000 fault planes measured in the study area. Data is grouped in  $5^\circ$  bins. A – Dip-angles of fault striae separated into E-dip and W-dip. Faults revealing azimuths between  $0^\circ$ - $180^\circ$  were interpreted as E-dipping planes, faults revealing azimuths between  $180^\circ$ - $360^\circ$  were interpreted as W-dipping planes. Average dip angle for E- and W-dipping planes is:  $63.8^\circ \pm 14.9^\circ$ ; B – Fault-plane azimuths were treated as polar data in order to emphasize preferred dip-directions, Highest peak for all data ranges from  $70^\circ$ - $75^\circ$  E, average indicated by arrow:  $83.6^\circ \pm 5.1^\circ$ ; (For discussion see text).

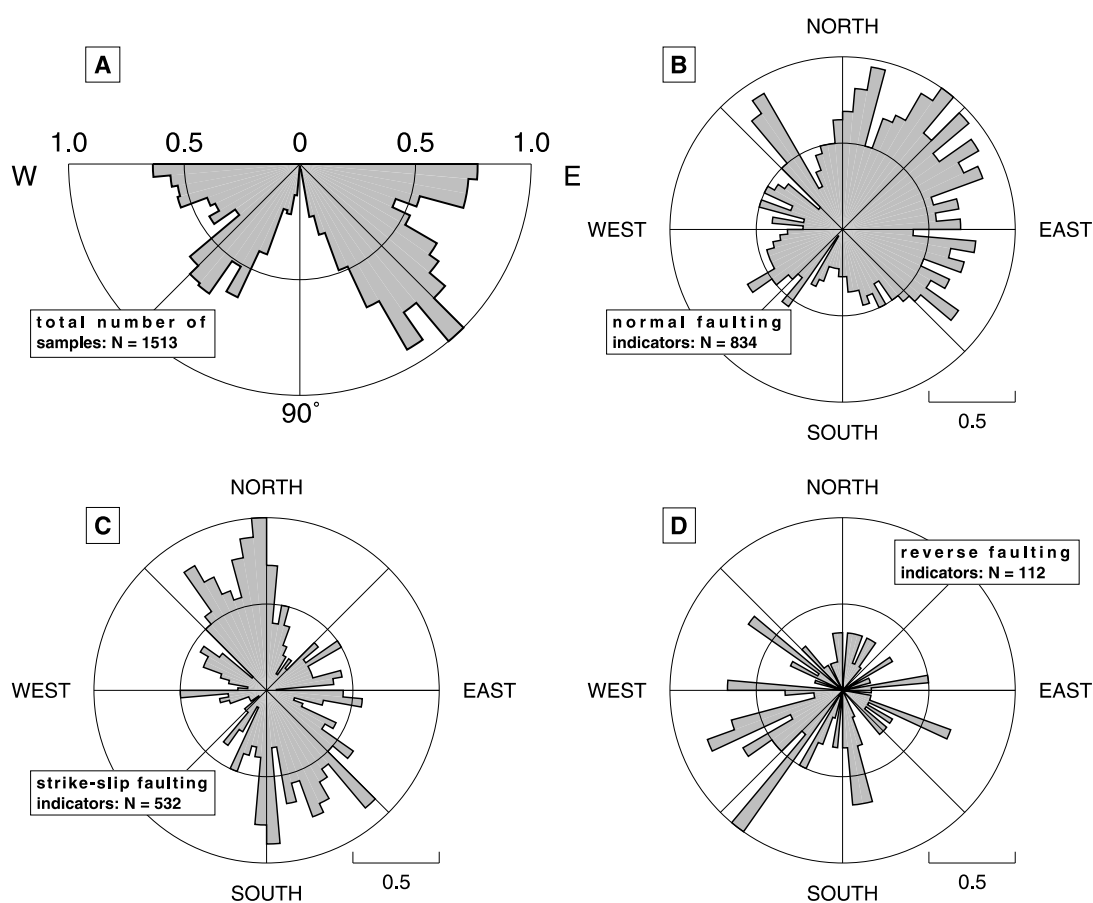


Figure 4.12: Equal length rose diagrams showing plunges (A) and trends of slickenlines grouped as normal, strike-slip or reverse faulting indicators (B-D). Data is grouped in 5° bins. A – Plunge of all fault striae; B – Trend of normal faulting indicators, ( $48.0^{\circ} \pm 6.8^{\circ}$ ); C – Trend of strike-slip faulting indicators, ( $157.7^{\circ} \pm 6.2^{\circ}$ ); D – Trend of reverse faulting indicators, ( $225.6^{\circ} \pm 17.9^{\circ}$ ).

Basin exhibit distinct cross-cutting relationships between fault planes. The cross-cutting relationship is most frequently observed between NNE and NE striking slip surfaces and probably reflects a fault plane/riedel-shear plane ( $R_1$ ) relationship. Synthetic riedel shear-planes commonly truncate the fault plane at angles of 10°-15°, leaving an arcuate trace with the concave side pointing towards the slip direction of the missing block [Petit 1987; Meschede 1994]. An extraordinarily well preserved example of synthetic riedel shear-planes is given in Fig. 4.10. At map scale, the cross-cutting relationship finds expression as left-lateral extensional jogs. The latter can be observed along several NNW-SSE striking fault-traces (see Fig. 4.1).

#### 4.2.2 Fault Slip Data Distribution

The spatial distribution of 1513 fault-slip data obtained in the study area is plotted in Fig. 4.12. A clear distinction between the plunges of strike-slip (0°-20°) and dip-slip (40°-60°) kinematic indicators on either side of the rose diagram can be observed in Fig. 4.12 A. The most prominent peak in this diagram dips towards the east and plunges between 45°-60°. This shows that the predominant

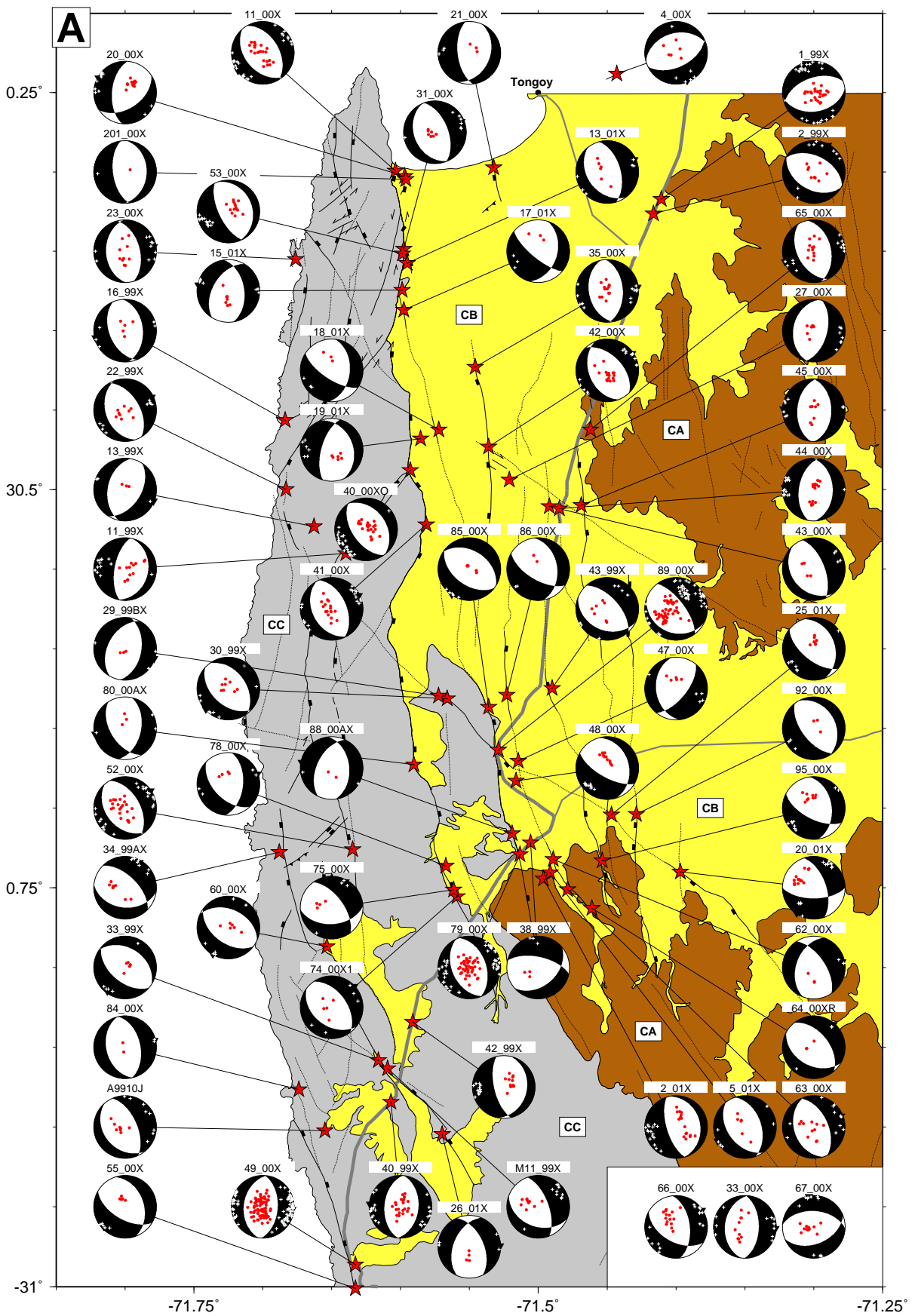
deformation in the study area occurs due to dip-slip motion along E-dipping fault planes. However, the plunge of the lineations is slightly shallower than the average dip of the faults. This leaves a discrepancy of  $5^{\circ}$ - $20^{\circ}$  between the average dip angle of fault planes ( $\sim 65^{\circ}$ ) and the preferred plunge of the slickenlines ( $45^{\circ}$ - $60^{\circ}$ ) and indicates that oblique dip slip rather than pure dip slip dominates the normal faulting process in the study area. This observation holds true for the westward dipping slickenlines as well and is strongly supported by field evidence. In total 834 slickenlines ( $> 50\%$ ) were attributed to normal faulting activity. Fig. 4.12 B shows that most of the normal faulting slickenlines trend towards the NE and SE quadrants of the rose diagram. Despite a significant scatter over the NE and SE quadrants the data distribution has a preferred trend averaging at  $48.0^{\circ} \pm 6.8^{\circ}$  azimuth. In correspondence with the aforementioned misfit between the dip angle of fault planes and the plunge of lineations, a discrepancy of  $10^{\circ}$ - $30^{\circ}$  between the average dip azimuth of fault planes ( $\sim 65^{\circ}$ ) and the preferred trend of the normal faulting lineations ( $48.0^{\circ} \pm 6.8^{\circ}$ ) is observed. Due to the broad scatter of lineations, the misfit is less pronounced but a clear tendency towards left-oblique dip slip is still detectable for this group of data. Approximately 1/3 of all slickenlines were attributed to strike-slip deformations. Fig. 4.12 C shows the trend of 532 strike-slip lineations. Here, the average trend azimuth of  $157.7^{\circ} \pm 6.2^{\circ}$  is flanked by two clear maxima at around  $0^{\circ}$ - $355^{\circ}$  and  $325^{\circ}$ - $335^{\circ}$ . The gap between the two peaks covers a range of  $20^{\circ}$ - $30^{\circ}$ . This spread corresponds with the distribution of fault-plane dip azimuths in Fig. 4.11 B and supports the observation of a fault plane/riedel shear-plane relationship. Only 10% of all data were interpreted as reverse faulting kinematic indicators. Figure 4.12 D shows 112 data sets with a weakly pronounced maximum in the third quadrant. This shows that the majority of reverse slips occurred on roughly SW-dipping fault planes. A minor peak is found at  $175^{\circ}$  azimuth, which refers to the only two thrust faults found in the Cenozoic basin (site 16/00 in Fig. 4.10 and site 39/99).

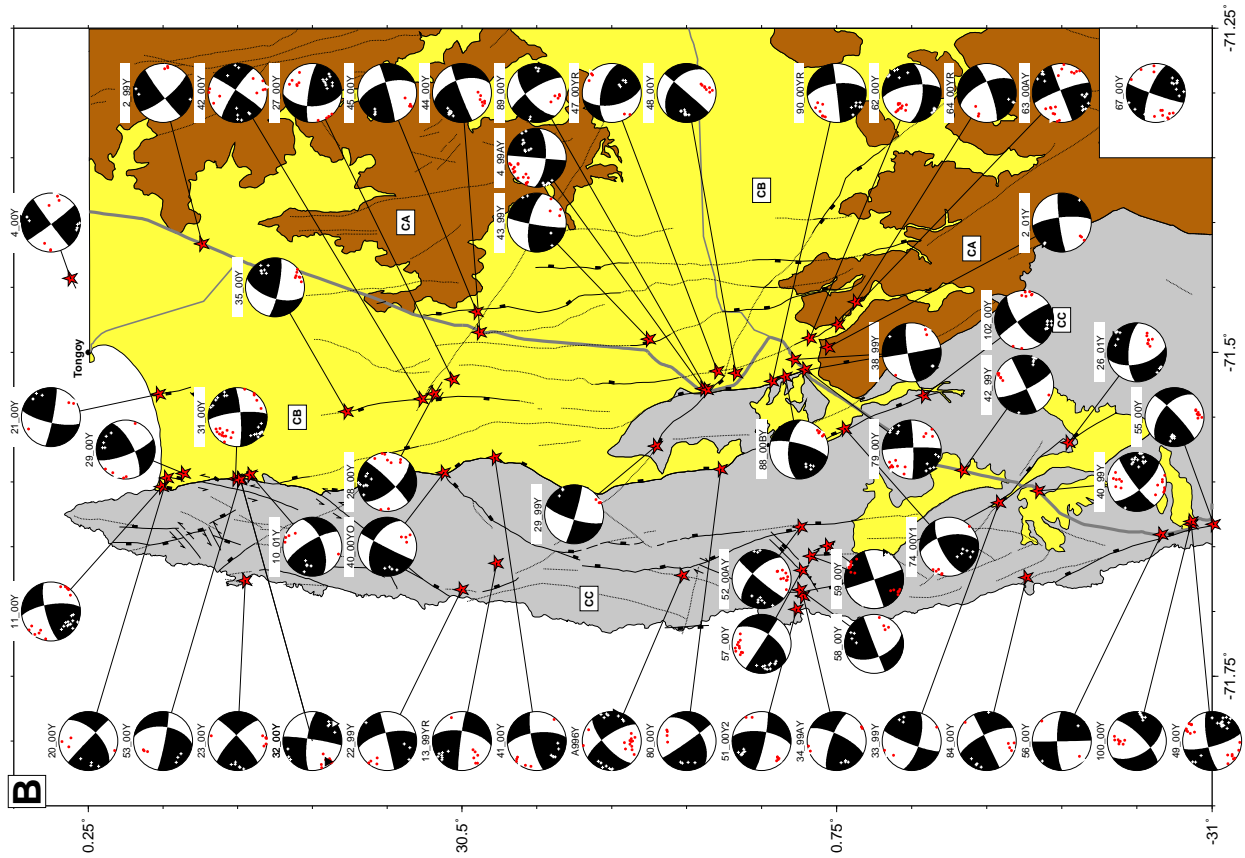
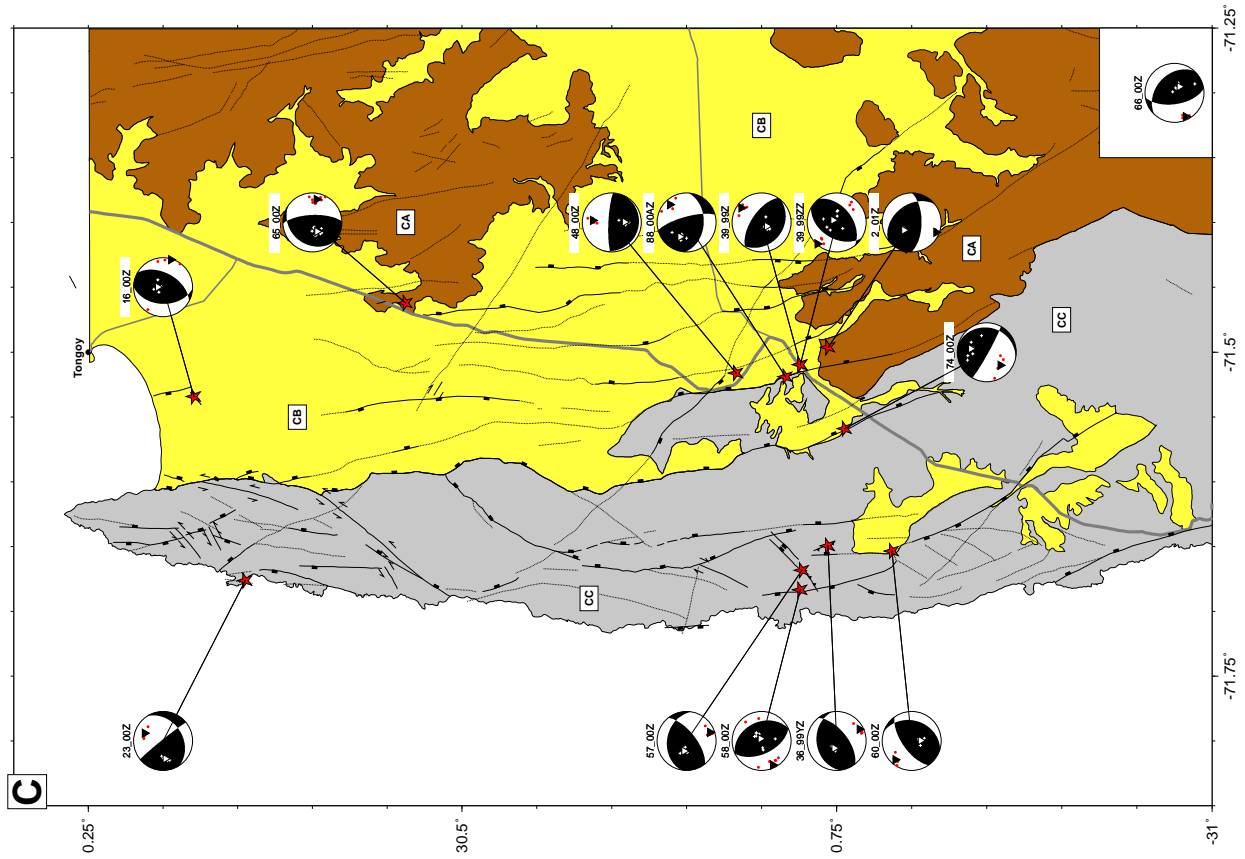
### 4.2.3 Fault Plane Solutions

For all outcrops that either bear sufficient fault-slip data or, if only few data sets are available, show significant macroscopic evidence for the sense of slip, the principal strain axes were calculated following the routine described in Chapter 3.2.2. In Figs. 4.13 A-C the results of the fault-slip data analysis are plotted as *hypothetical focal mechanisms*. The white sectors of the focal mechanisms denote the extensive quadrants, whereas the black sectors indicate compressive quadrants according to the convention of Aki and Richards [1980].

---

Figure 4.13: (See next page) Fault-plane solutions inferred from 1513 neotectonic fault-slip data sets presented as focal mechanisms at individual outcrops. A – Extensional faulting; B – Strike-slip faulting; C – Reverse faulting; White sectors – extensive quadrants; Black sectors – compressive quadrants; Borderlines between quadrants show dip and azimuth of fault planes and auxiliary planes in the lower half sphere. Filled circles and white crosses show individual P- and T-axes orientations as derived from fault-slip data analysis at individual outcrops, respectively. Outcrop identifier above focal mechanism corresponds to name given in Appx. 6). Stars – location of outcrops. Thick gray line – Pan American Highway. Fault pattern as in Fig. 4.1; CA – Cretaceous Arc; CB – Cenozoic Basin; CC – Coastal Cordillera.





A total of 84 outcrops were analyzed within the framework of this thesis, 67 out of which show evidence of extensional deformation. In addition, strike-slip deformation was observed at 56 sites. Consequently ~60% of all outcrops experienced two deformations with at least two distinct senses of slip. The normal faulting fault-plane solutions presented in Fig. 4.13 show that E-W to NE-SW extension is the predominant type of deformation throughout the entire study area. Due to the discovery of numerous extraordinarily well preserved faults (Figs. 4.2-4.6) within the Cenozoic sedimentary record along the eastern flank of the Coastal Cordillera, the northern segment of the PAF can be traced with great accuracy between sites 11/00 and 17/01 (Fig. 4.1). The fault-plane solutions along this segment of the PAF predominantly show ENE-WSW to NE-SW extension. Only three examples for N-S extension were found in the immediate study area. These outcrops have fresh fault-gouges in Pliocene and Mid-Miocene sediments with normal displacements ranging between 0.8 – 3 m. A fourth outcrop showing N-S extension is located 15 km east of the study area (see inset Fig. 4.13 A). The highest concentration of outcrops found in the field is located in the central eastern parts of the study area, where scarplike landforms are more frequently observed than elsewhere in the study area. Based on these observations it is assumed that the highest present-day crustal faulting activity is located in the eastern central sections of the Cenozoic basin. However, extensional deformation is not restricted to the limits of the study area. Two outcrops, located ~50 km east of the PanAm show significant amounts of normal faulting in young river terraces (33/00) and Cretaceous volcanic rocks (67/00) (see inset Fig. 4.13 A).

The distribution of strike-slip deformations in the study area is shown in Fig. 4.13 B. Due to the fact that many outcrops at the same time reveal strike-slip and normal faulting kinematic indicators, a great number of sites is present in both, Figs. 4.13 A and 4.13 B. Throughout the study area the ratio between left-lateral and right-lateral deformations remains roughly equal with a slight dominance of sinistral shearing. However, the predominant orientation of P-axes is N-S to NW-SE, indicating a shortening direction subperpendicular to the plate convergence vector ( $67^\circ$  E). In addition, the T-axes of the strike-slip events commonly exhibit azimuths and plunges similar to the T-axes obtained for the normal faulting solutions in Fig. 4.13. The highest concentration of fault-plane solutions indicating right-lateral movement is found in the southwest near Qbd. Teniente (56/00, 49/00 and 100/00). In turn, the PAF can be traced as a left-lateral structural element from its northern tip near Tongoy Bay (11/00) down to its southern termination near the PanAm (102/00). The highest concentration of fault-plane solutions indicating left-lateral strike slip is found in the eastern central parts, where the most recent and most frequent intraplate activity is assumed to be localized according to Fig. 4.13.

The distribution of focal mechanisms that indicate reverse faulting (Fig. 4.13 C) creates a quite contrasting picture compared to the distribution for normal and/or strike-slip faulting Fig. 4.13 A & B. Only 14 sites reveal compressional fault-plane solutions, most of which belong to outcrops with up to three different types of kinematic indicators on older rock surfaces with average dip angles of  $65^\circ$ . This angle is relatively uncommon for thrust planes and implies subsequent rotation of the fault planes rather than high angle thrust faulting. The only two outcrops exhibiting shallow dipping thrust-planes are located in Cenozoic soft rocks (39/99; 16/00 – see also Fig. 4.10). The P-axes at these sites trend N-S to NW-SE, subperpendicular to the plate convergence direction. All other reverse faulting solutions were exclusively found in basement-type rocks. Their data show a trend towards NE-SW shortening directions, in line with the plate convergence. In addition most of these

fault-plane solutions show slight rotations of the P-axes out of their horizontal position and a tilt of the T-axes away from their vertical orientation, creating a number of oblique focal mechanism plots.

#### 4.2.4 Deformation of the Cenozoic Basin

In order to reveal the most recent type of deformation in the forearc it was necessary to extract those fault-plane solutions from the data, that were obtained along fault planes within the Cenozoic sedimentary record, hereafter termed as category A outcrops (for definition see Tab. 3.1). Category A fault planes are predominantly made up of fresh clay-gouges with broad striations showing plunge and azimuth of the fault slip. In addition to this, most of these outcrops exhibit displaced or tilted marker horizons that allow for the determination of the sense of slip and the amount of displacement. In Fig. 4.13 only fault-plane solutions derived from category A outcrops are plotted making sure that the most recent deformation is displayed. The composite equal area, lower hemisphere plots show the resulting P- and T-axis solutions for normal, strike-slip and reverse faulting events, respectively. For each diagram an *eigenvector analysis* was conducted in order to reveal the length and orientation of the principal axes of the reduced stress tensor. For each of the six diagrams, the longest eigenvector  $\lambda_3$  either represents the P- or T-axis. The resolving P-T-axes for 441 fault-slip data sets of normal faulting character reveal ENE-WSW extension with a trend/plunge for  $P = 295^\circ/83^\circ \pm 2.6^\circ$  and  $T = 70^\circ/3^\circ \pm 3.6^\circ$ . The composite result for 222 strike-slip faulting solutions clearly shows NW-SE shortening with  $P = 318^\circ/11^\circ \pm 9.4^\circ$  and  $T = 227^\circ/6^\circ \pm 8.1^\circ$ . Astonishingly the T-axes orientations resolving from both, the normal and strike-slip fault-plane solutions, predominantly fall into the NE quadrant of the stereogram. The orientation of the principal planes as demonstrated in the stereographic projections (dashed lines in Fig. 4.13) is also similar. Only 11 data sets indicating reverse faulting were obtained in the Cenozoic sediments. Here the composite P-axis orientation ( $P = 123^\circ/0^\circ \pm 14.0^\circ$ ) clearly reveals NW-SE shortening. The resolving T-axis in this case is oriented subvertical ( $T = 20^\circ/78^\circ \pm 14.5^\circ$ ). Taking into account the principal planes of all three types of deformation as shown in Fig. 4.13, the resulting P-axes are arranged on a NNW-SSE to NW-SE oriented great circle, with the T-axis being arranged on a great circle perpendicular to this. The fact that these data were exclusively obtained from the youngest geological units leaves a time span of no more than 5 Ma for the observed deformations. Altogether this suggests, that the different deformation types can be attributed to a single transtensional paleostress regime rather than distinct tectonic phases.

### 4.3 Tectonic Geomorphology

#### 4.3.1 Range Front Geometry

According to Bull and McFadden [1977] the geometric inventory of a range front reflects its relative tectonic activity. In the study area the Coastal Cordillera forms a prominent fault related range front along its eastern margin, which borders on the Cenozoic Basin. In order to analyze the geometry of this range front the piedmont and mountain-block landforms as well as the sinuosity and valley depth/valley width ratio were studied according to Bull and McFadden [1977] and Bull [1984; 1987] (see also Tab. 3.3). The range front largely falls in place with the trace of the PAF, which has been

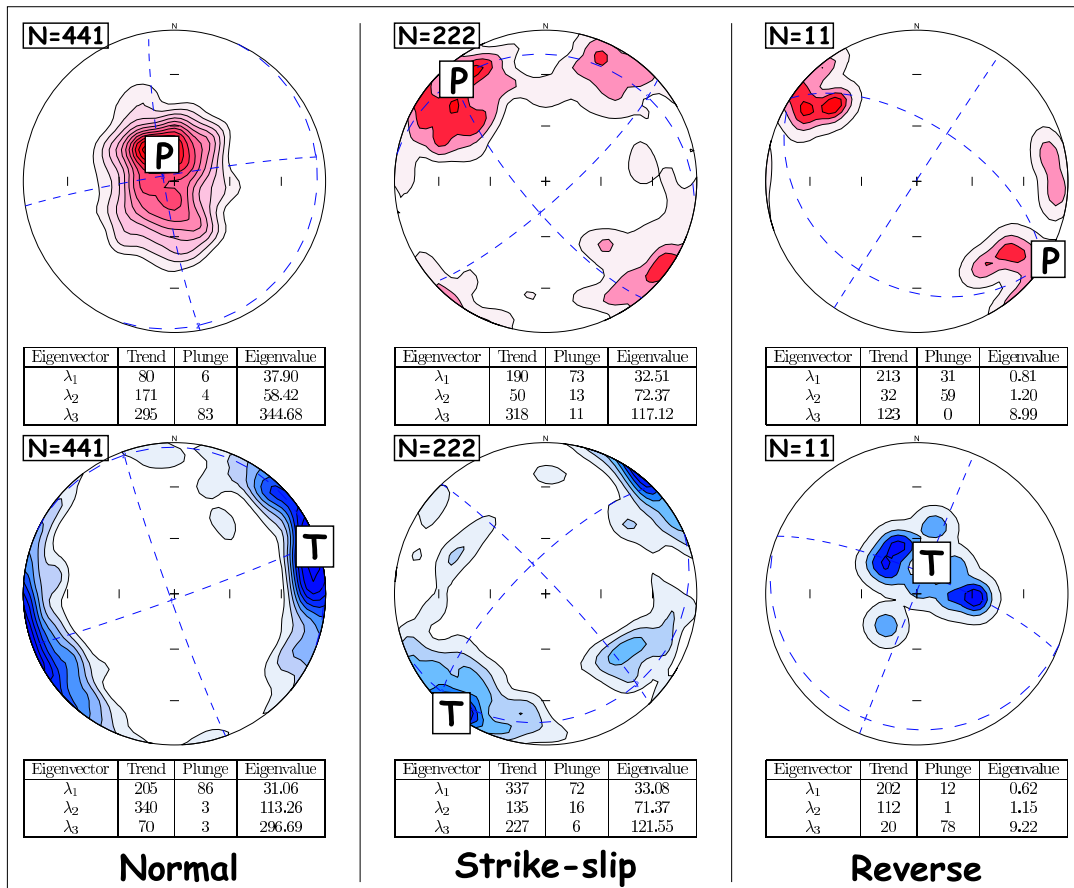


Figure 4.13: Equal area lower hemisphere plots showing composite P- and T-axis solutions for all normal, strike-slip and reverse deformations detected within the Cenozoic sedimentary record (outcrops of category A as described in Tab. 3.1);  $N$  gives number of fault-slip data sets; Dashed lines indicate principal planes; Intersections of principal planes denote orientations of eigenvectors  $\lambda_{1-3}$ , with  $\lambda_3$  as the longest eigenvector revealing the P- or T-axis orientations, respectively; Contours delineate density levels as calculated using a Gaussian bell-shaped weighting function. dark shading – higher densities.

studied intensively along its northern segment. The piedmont landforms on the hanging wall side are characterized by strongly entrenched alluvial fans as seen in a number of outcrops (i.e. 31/00, 13/01 and 17/01). The mountain-block landforms on the footwall side are marked by V-shaped valleys in the basement rock and triangular facets, so called "flat-irons", aligned with the trace of the range front. The occurrence of V-shaped rather than U-shaped valleys indicates that the mountain-block was not yet subject to long-lasting erosional processes. This is also expressed in the sinuosity (sinuous length/straight length) of the range front. The longer a mountain-block is exposed to weathering processes, the higher will be the curvature of the range front. This happens because of erosional processes regressively carving into the mountain-block over time. The sinuosity resulting for the range front between the Coastal Cordillera and the Cenozoic basin is 1.07-1.08. the results are stable for its entire length ( $\sim 60$  km) and subsegments of it ( $\sim 20$  km). This shows that the real length of the range front is only  $< 10\%$  longer than its straight line length. Only recent and significant tectonic uplift is capable of preserving a relatively straight fault-trace like this. If the uplift was very slow or

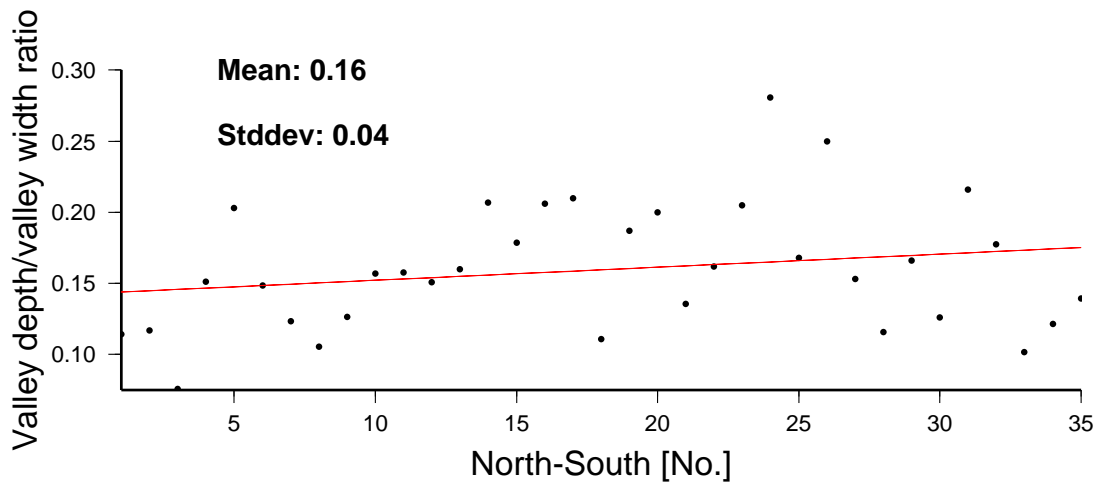


Figure 4.14: North-South variation of *valley depth/valley width* ratio along strike of the PAF. Measurements are based on topographic map (1:50 000). Width/Depth ratio is specified 500 m up-valley from the range front. X-axis – numbering from north to south, no scale along strike.

inactive it would soon be outpaced by erosional processes and a strongly embayed mountain-front would develop instead. Hence the uplift along the PAF must be considered active.

The valley depth/valley width ratio was calculated for 35 valleys along the PAF using georeferenced topographic maps (1:50 000). The individual ratios and the resulting trend are plotted in Fig. 4.14. The average valley depth/valley width ratio is  $0.16 \pm 0.04$ , with a slight increase from north to south. The average valley depth/valley width ratio as much as the range-front sinuosity perfectly match the values ascribed to *rapid tectonic uplift* by Bull and McFadden [1977] and Bull [1984; 1987]. Since geomorphic aspects like V-shaped valleys within the mountain-block and entrenched alluvial fans also match with the requirements for a rapid activity along the range front (Tab. 3.3), a tectonic uplift rate in the order of 0.5 m/ka can be deduced for the PAF.

### 4.3.2 Fault-scarp Degradation

The occurrence of fault-scarps is an important indicator for recent crustal faulting activity and the release of seismic energy at the surface. The state of degradation of a surface scarp due to weathering processes provides a measure for the age of faulting. As described in Chapter 3.3.3 a simple diffusion model can be applied to reproduce the present-day curvature of a scarplike landform. The best-fit model curve reveals a morphologic age ( $\kappa t$ ), which consists of the diffusivity constant ( $\kappa$ ) and the time ( $t$ ). Provided the diffusivity constant at the location of the scarp is well-known, the elapsed time since the formation of the scarp can easily be determined. The diffusivity constant is strongly dependent on two factors, the paleo-climatic conditions and the composition of sediments.

As shown in Figs. 4.1 and 4.13 the central and eastern parts of the study area bear the highest concentration of surface scarps associated with crustal faulting. While along the PAF most of these formerly existing scarps have already been degraded and vanished from the actual land surface, the topography in the central eastern parts is dissected by numerous scarplike landforms. Three of these scarps located in Plio-Pleistocene sediments of the Cenozoic Basin were studied in greater detail. The

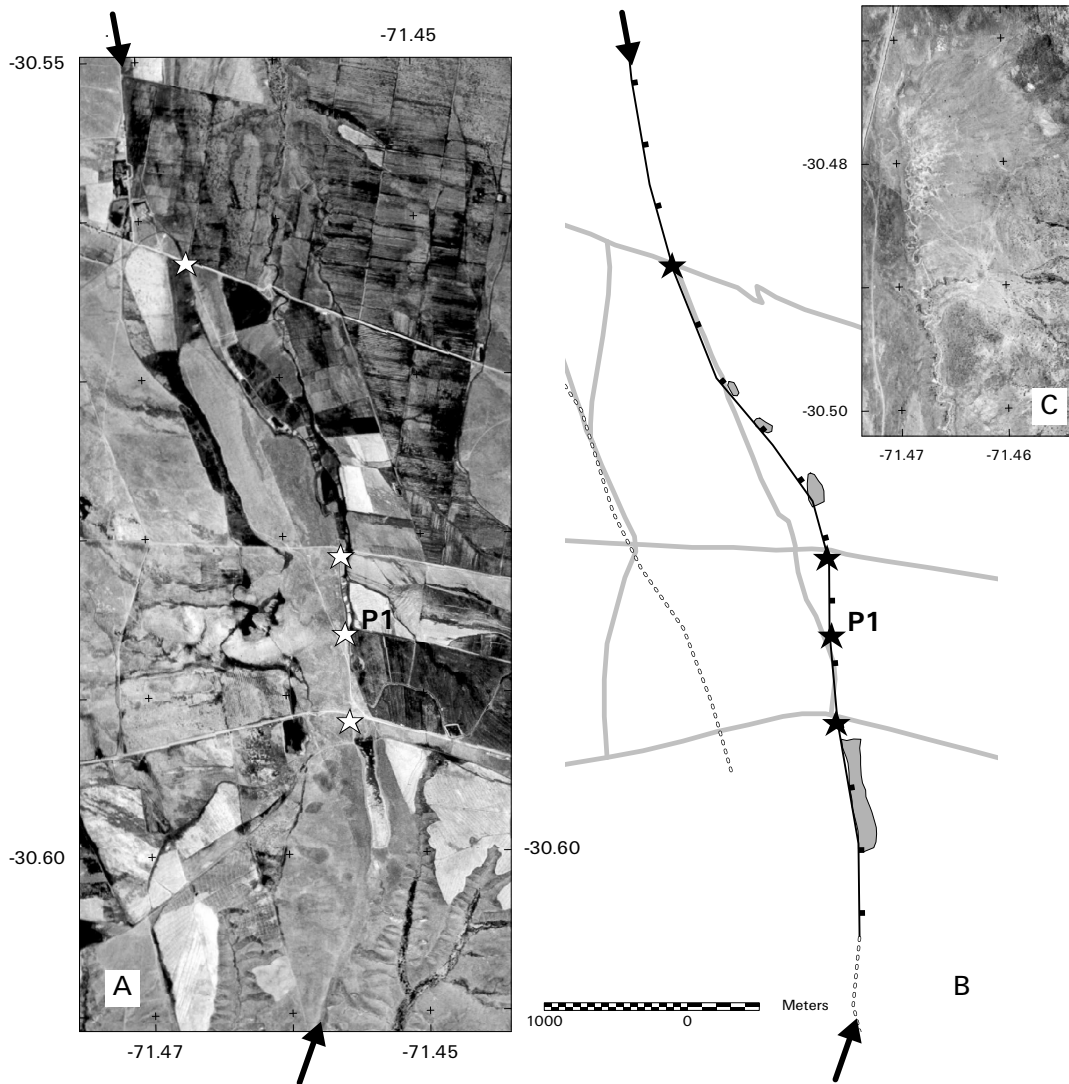


Figure 4.15: A – Aerial view of the scarp around location P1 (Fig. 4.16). Note the footwall side (light gray) with drainage system subperpendicular to the fault trace opposed to the hanging wall side (dark gray) with imprint of NNW oriented paleo-drainage network under heavily farmed area. Also note *left-stepping* of the fault-trace along the northern segment; B – Sketch map of A, showing the trace and dip direction of the scarp (boxed line); Polygons – Closed basins; Light gray lines – Roads; Stars – Location of scarps detected in the field; C – Northern termination of scarp-like landform. Note that drainage network splays into a *horse-tail* structure.

scarps truncate the extremely flat terrace surface of the Great Plain, which extends up to 35 km inland from the coast. The scarps were first identified as N-S striking linear features on aerial views and later verified during field investigation. The most striking example of the three scarps is presented in Fig. 4.15. Along strike several closed basins are aligned with the trace of the photolineament. At present these basins are used by the local farmers for irrigation purposes, however, they most probably originate from natural depressions that were formed due to intraplate normal faulting events. This interpretation is strengthened by a number of other observations, e.g. the presumed hanging wall

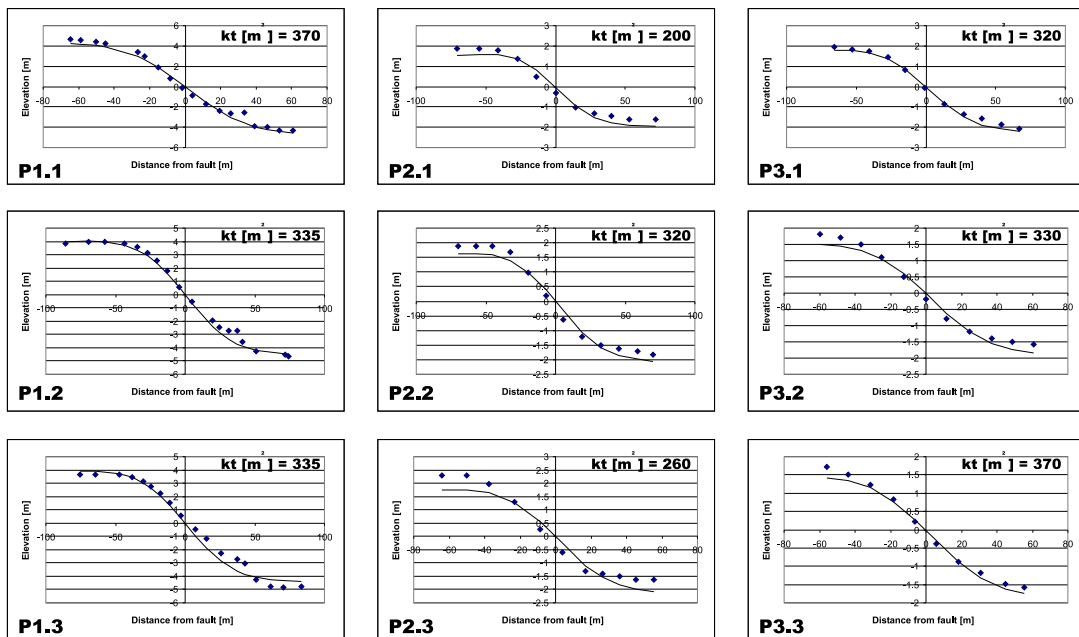


Figure 4.16: Dating of three morphologic scarps using diffusion equation modeling; Diamonds – Scarp morphology; Line – Diffusion model (large misfit between data points and model at the foot of the scarp in P1.1-P1.3 due to irrigation conduit parallel to the scarp).  $\kappa t [m^2 ka^{-1}]$  – Morphologic age; Far-field slope-angle –  $0.17^\circ$ .

side shows imprints of a paleo braided-river drainage network, while the footwall side is almost free from recent or paleo-drainages. Braided river-systems coalescing in a fault-parallel stream channel commonly develop on the hanging wall sides of tilted fault blocks. Slickenside kinematic indicators showing E-W extension were found on shear-planes at several sites along the trace of the scarp. The southern prolongation of the scarp leads into an area where numerous outcrops proved large-scale normal faulting activity. The magnitude of these displacements ranges between 10 – 40 m, suggesting the existence of prominent crustal faults of several kilometers length. The trace of the scarp in Fig. 4.15 also shows typical left-stepping as observed along many intraplate faults in the study area (Fig. 4.1). In addition, the northern termination of the scarp clearly resembles a fault-related feature, with the drainage network splaying into a "horse-tail" structure (see Fig. 4.15 C). Fault-splays arranged in a horse-tail fashion are commonly observed at the terminations of normal faults.

For location P1 (Fig. 4.15) and two similar sites (P2, P3), leveling profiles were mapped across the apparent fault-scarps (Fig. 4.16). All scarps are located on top of terrace surfaces in the central eastern part of the study area. According to the digital elevation model the far-field slope-angle of the terrace averages at  $0.17^\circ$ . The observed vertical displacements of the scarps range between 8.3 – 9.0 m for P1 and 3.3 – 4.0 m for P2 and P3. Using a simple diffusion equation that assumes a vertical initial scarp, the best-fit model curves for location P1 reveal morphologic ages ( $\kappa t$ ) between 335 – 370  $m^2$ . For P2 and P3 morphologic ages in the range of 200 – 370  $m^2$  were obtained. A robust value for the mass diffusivity constant ( $\kappa$ ) based on absolute age determinations (i.e. Radiocarbon datings) is not available for the study area. However, morphologic dating of similar materials (fluvial/alluvial gravels and sands) in other semiarid zones (i.e. Western United States) revealed mass diffusivity

constants ( $\kappa$ ) ranging between  $4.4 - 20 \text{ m}^2 \text{ ka}^{-1}$  [Nash 1980; Hanks 1984; Nash 1984; Arrowsmith 1995; Arrowsmith et al. 1995]. Provided the applicability of these diffusivity constants to the scarps observed in the study area, the age of faulting for P1 ranges from 17 – 84 ka BP. For P2 and P3 faulting ages of 10 – 84 ka BP have to be considered.

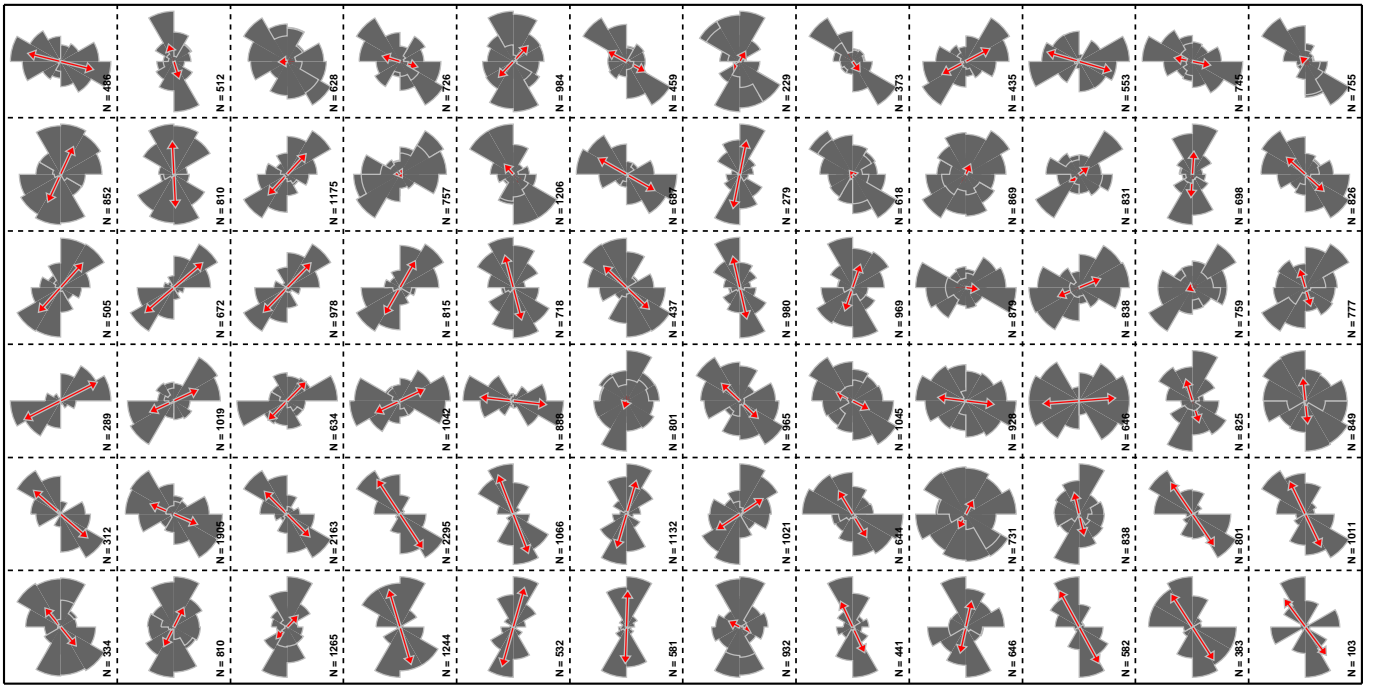
### 4.3.3 Drainage Network Analysis

In general continental drainage networks are highly sensitive towards crustal faulting activity. Due to earthquake induced surface rupture and/or tilting of fault blocks, drainages eventually change their course and adjust themselves to the newly formed relief. This causes the drainage network of a tectonically highly active region to develop preferred trends in the orientation of stream channels. The type of drainage pattern that will develop, largely depends on its position with respect to the fault-trace. Along the northern segment of the Coastal Cordillera (footwall block, CC in Fig. 4.17 A) the drainage system is predominantly oriented subperpendicular to the trace of the PAF. Along the southern segment of the Coastal Cordillera the drainage network still exhibits a preferred E-W trend but tends to become more dendritic, which itself is indicative for minor tectonic activity. Subparallel to the northern segment of the PAF the Cenozoic Basin (hanging wall block) developed a relatively linear drainage network. The corresponding rose diagrams in Fig. 4.17 B show a dominant N-S fault parallel trend. The neighboring rose diagrams to the east show a NW-SE trend, indicating a composition out of fault parallel flow and gentle sloping towards the range front due to the westward tilt of the hanging wall block. South of the *Río Limarí* the PAF rapidly tapers out into the Cretaceous arc and the drainage network becomes more dendritic, though a number of tributaries still strike NNW-SSE. The turning towards a more dendritic drainage system in this area, again indicates minor tectonic activity. The same accounts for the zones covered by the Cretaceous arc in the NE parts of the study area.

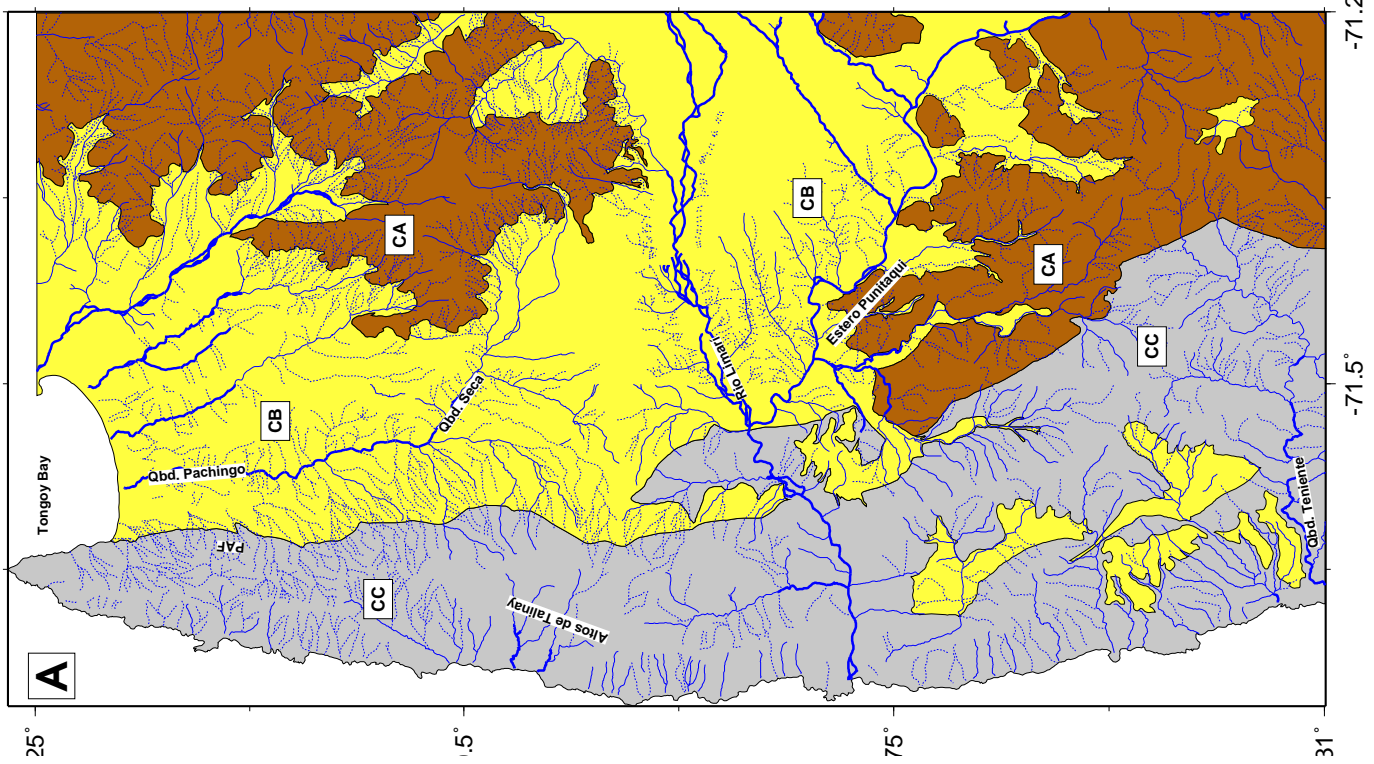
The *Río Limarí* is the only major river in the whole study area and it seems to be largely unimpressed by the apparent uplift of the Coastal Cordillera. It crosses the Coastal Cordillera subperpendicular to its strike, deeply cutting into the basement rocks. However, the confluence of the Limarí river with the Estero Punitaqui obviously falls in place with the easternmost range-front fault of the Coastal Cordillera. At this point the rose diagrams in Fig. 4.17 B show a radial pattern, indicating confluence into a local depression probably due to subsidence associated with recurrent faulting along the PAF. The formation of the Limarí valley in the Coastal Cordillera most probably predates its uplift, thus suggesting that river incision went on simultaneously with emergence of the basement, creating a so called *antecedent valley*. This is evidenced by apparently uplifted fluvial conglomerates ( $\sim 200 \text{ m a.s.l.}$ ) covering the flanks of the Limarí valley.

---

Figure 4.17: A – Drainage pattern adopted from topographic maps (1:50 000; [IGM 1968]); Dashed lines – Dry stream channels; Continuous lines – Intermediary stream valleys (occasional river discharge); Thick continuous lines – Major drainages (seasonal and/or year-round river discharge); B – Drainage pattern analysis. Rose diagrams show azimuths of river segments, weighted for stream order (see *Strahler's stream ordering*; chapter 3.3.2); Boxes delineate subareas of  $\sim 8 \times 8 \text{ km}$ .



**B**



**A**

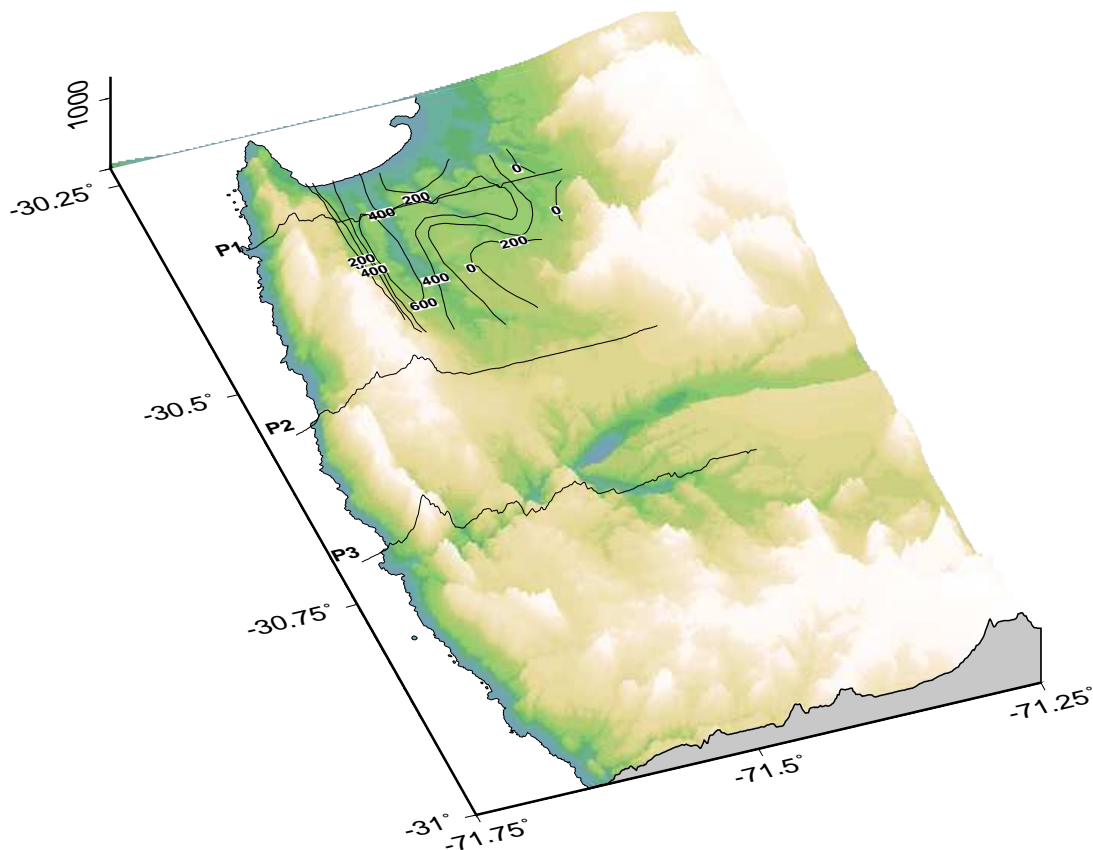


Figure 4.18: Digital elevation model (DEM) of the study area showing the location of E-W-profiles (P1-P3) as applied for the estimation of geological strain rates (Chapter 4.4.1); Contours – Depth of basement in meters below sea level [m b.s.l.]

## 4.4 Geologic Strains/Strain Rates

### 4.4.1 E-W Neotectonic Cross-sections – Recent Topography

The observed intraplate faulting processes, as presented in the previous sections, provide a useful basis for the calculation of geological strains/strain rates. The forearc deformation is closely linked to uplift processes in the Coastal Cordillera. The crucial aspects for the estimation of strain rates are the timing and the amount of deformation. The time span coming into consideration for the deformation observed in the study area was contained on the basis of published data specifying uplift rates for marine terraces and abrasion platforms along the SA forearc. Uplift rates presented by several authors range between  $0.1 - 0.8 \text{ m ka}^{-1}$  (Tab. 2.1). For the study area uplift rates of  $0.2 - 0.5 \text{ m ka}^{-1}$  are stated [Ota and Paskoff 1993; Ota et al. 1995], which coincides with uplift rates determined in Chapter 4.3.1. Maximum elevations of marine terraces in the study area and structurally similar regions along the Chilean coast (e.g. Mejillones peninsula, Fig. 2.3) range between  $600 - 700 \text{ m a.s.l.}$ . On the other hand, geophysical records from the Cenozoic Basin and modeling results from North Chile [Pelz 2000] show that the depth of the basement underlying the Cenozoic Basin is  $\sim 600 \text{ m b.s.l.}$ . The subsidence occurred along E-dipping normal faults (e.g. PAF) parallel to the range front of the Coastal Cordillera. Consequently, a cumulative vertical displacements of  $600 - 1300 \text{ m}$  has to be

Table 4.1: Minimum and maximum time span necessary to accomplish the observed uplifts, in dependence of minimum/maximum coastal uplift rates and vertical displacements, as obtained from Chapter 4.3.1 and previous studies.

	<b>Uplift</b> [m]	<b>Uplift rate</b> [ $m ka^{-1}$ ]	<b>Time</b> [Ma]
Min	600	0.5	1.2
Max	1300	0.2	6.5

considered for the range-front fault. Applying the above stated uplift rates to the maximum and minimum vertical displacements, the period necessary to accomplish the observed deformations reduces to 1.2 – 6.5 Ma (Tab. 4.1).

In order to infer E-W strains/strain rates for the study area, three cross-sections (P1-P3) subperpendicular to the NNW-SSE striking fault-traces (Fig. 4.18) were selected. Along these cross-sections the amount of vertical displacement at the particular intraplate faults was studied. Where traces of known or presumed faults coincide with noticeable free faces in the DEM, the vertical displacement was approximated geometrically, given a default dip angle of  $65^\circ$  as indicated by the fault-slip data analysis. An example for the validity of this approach is given by Fig. 4.19. The scarp-height approximated from the DEM ( $\sim 40$  m) is roughly equal to that measured at the same location in the field (35 m) by previous authors [Ota et al. 1995]. The vertical offsets were converted into horizontal displacements neglecting the fact that oblique dip slip may have occurred along the faults. All cross-sections are roughly equal in length ( $\sim 25$  km). The E-W *baselines* of cross-sections P1-P3 roughly equals the width of the fault zone as inferred from field and remote sensing data. The E-W-strains were approximated dividing the cumulative horizontal displacement for each profile by the length of the baseline. The resulting strains are presented as minimum and maximum values (Tab. 4.2) for

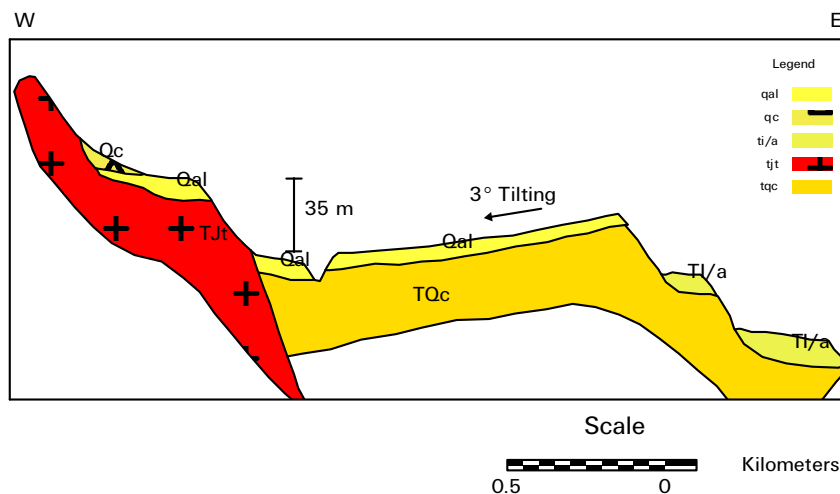


Figure 4.19: Rollover structure in Plio-Pleistocene sediments of the Cenozoic Basin. Adopted from Ota et al. [1995]; Qal/Qc – Quaternary alluvial/fan; TQc – Coquimbo Formation (Mid-Miocene-Pleistocene); TI/a – Limarí Formation (Plio-Pleistocene); TJt – Talinay Unit (U. Triassic - L. Jurassic).

<b>Profile</b>	<b>Horizontal displacement [m]</b>	<b>Strain</b>	<b>Time [Ma]</b>	<b>Strain rate [<math>\mu strain</math>]</b>
P1	369/435	0.015/0.017	6.5/1.2	0.002/0.014
P2	140/411	0.006/0.016	6.5/1.2	0.001/0.013
P3	386/487	0.015/0.019	6.5/1.2	0.002/0.016

Table 4.2: Min/Max E-W horizontal displacements, strains and strain rates for cross-sections P1-P3 in the study area (Fig. 4.20). Note that for calculation of strain rates the minimum and maximum available time span, as presented in Tab. 4.1, was taken into account. Average dip angle for all considered fault planes is  $65^\circ$ . Baseline length of  $\sim 25$  km) equal for all cross-sections (Fig. 4.20).

each cross-section. The maximum values include all displacements, also those purely inferred from remote sensing analysis and topographic signals. The minimum values account for offsets exclusively associated with faults mapped in the field.

All cross-sections in Fig. 4.20 (P1-P3) clearly show a prominent topographic scarp separating the basement of the Coastal Cordillera in the west from the deposits of the Cenozoic basin in the east. Flat topped units along the seaward portions of the Coastal Cordillera indicate uplifted abrasion platforms (P3 in Fig. 4.20). The well developed planation surface shown in cross-section P1 marks the marine transgression associated with the Last Interglacial Temperature Maximum (LGTm). The surface is covered with the Pleistocene *losa* deposits, that are attributed to Isotope stage 5e, corresponding to  $\sim 125$  ka BP (Fig. 2.7). The planation surface (Great Plain) is present in all cross-sections, gently sloping towards the NW with altitudes increasing from  $\sim 25$  m at the coast to  $\sim 200$  m further inland. From profile P1 to P3 the amount of internal deformation of the Cenozoic deposits increases significantly. Rollover structures tilting the Cenozoic deposits towards the west can be identified from the DEM. For comparison, the location of the rollover structure in Fig. 4.19 is well represented in cross-section P1 (indicated by dashed frame). The existence of rollover structures is supported by field evidence and proves that significant faulting occurred subsequent to the formation of the Pleistocene planation surface. The magnitude of subsurface offsets along the PAF ranges between 145 m in the south to 600 m in the north. The subsurface displacements are either based on geophysical results (P1 & P2) or inferred from the geometry of rollover structures (P3). It is quite contrasting that the decrease of subsurface displacement towards the south is accompanied by an increase of internal deformation. This misfit mainly arises from the lack of geophysical data for the southern cross-section.

The resulting E-W strains and strain rates for each individual cross-section are presented in Tab. 4.2. The cumulative lengthening of the 25 km long profiles ranges from 140 – 487 m, producing an extension of 0.6-1.9% over the length of the baselines. The average resolving strain amounts to  $0.014 \pm 0.0045$  corresponding to  $1.4 \pm 0.45\%$  extension in the forearc. The calculation of strain rates takes into account the minimum and maximum time spans as presented in Tab. 4.1. The resolving strain rates range from 0.001 –  $0.016 \mu strain a^{-1}$ . The lower strain rate of ( $0.001 \mu strain a^{-1}$ ) is obtained assuming that the minimum strain of 0.6% acted over the maximum time span of 6.5 Ma. The highest strain rate of  $0.016 \mu strain a^{-1}$  is based on the assumption that the maximum strain of 1.9% is distributed over the last 1.2 Ma. Because of this wide range, the average strain rate

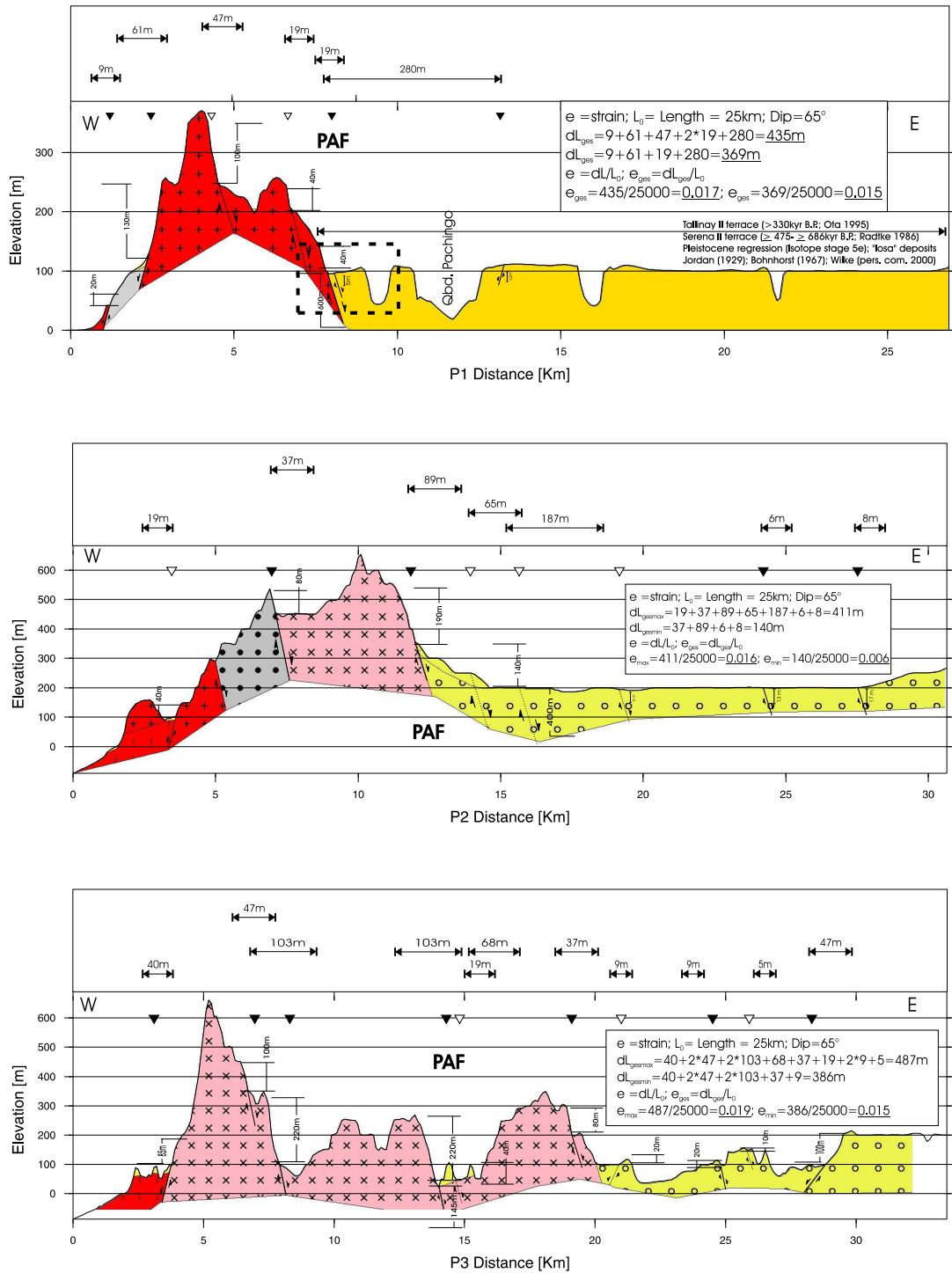


Figure 4.20: E-W cross-sections showing vertical and associated horizontal displacements inferred from field observations and topographic relief. Topographic relief (DEM) and location of cross-sections see Fig. 4.18. Closed triangle – Known fault-trace; Open triangle – Presumed fault-trace; PAF – Location of Puerto Aldea Fault.

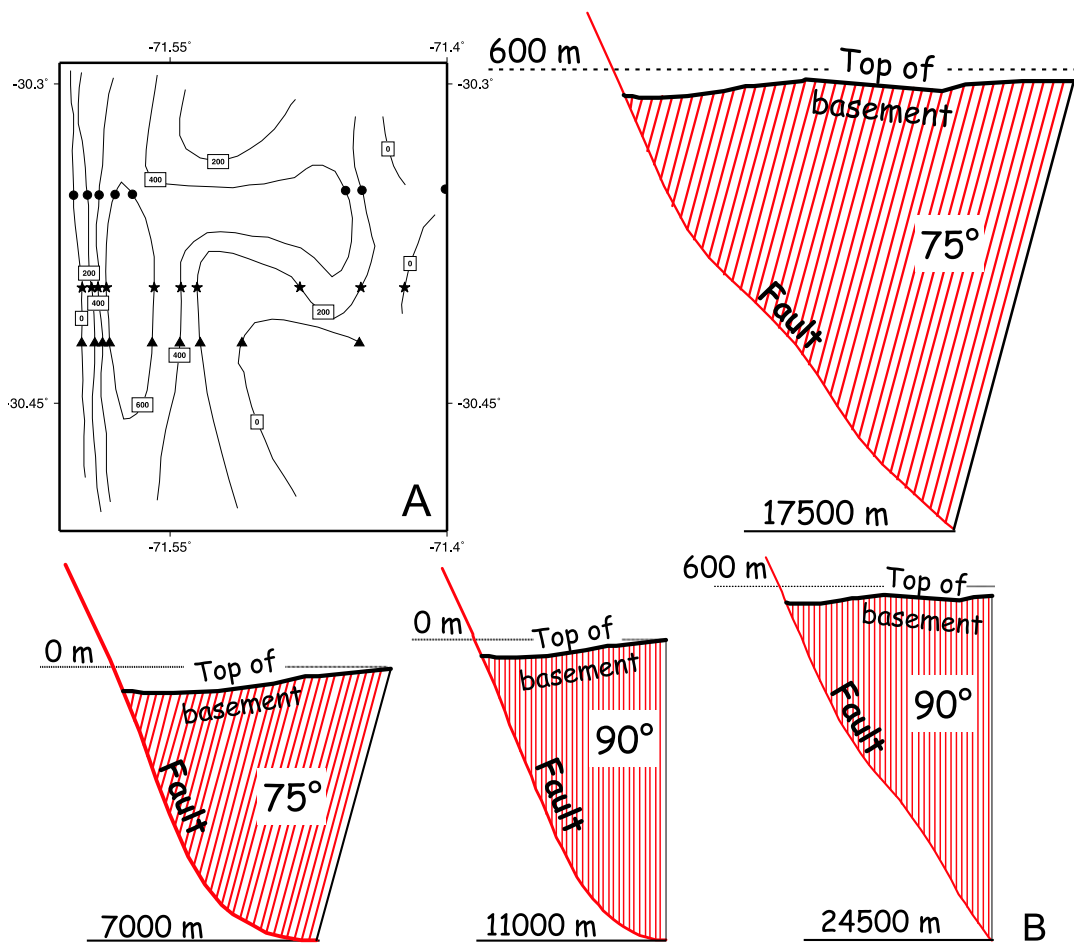


Figure 4.21: Depth of basement inferred from geophysical data [Meinardus 1961; Rocroi 1964] and examples for balanced cross-sections. A – Isolines delineating depth of basement on the hanging wall side along the northern segment of the PAF (see also Fig. 4.18); Circles, stars and triangles – different cross-sections from which a composite E-W profile as input for the inclined shear method is produced; B – balanced composite E-W cross-section applying the inclined shear method [White et al. 1986] using different shear angles and restoration levels; Shear angles – 75° and 90°. Original beds – 0 m a.s.l. and 600 m a.s.l..

( $0.008 \pm 0.007 \mu \text{ strain a}^{-1}$ ) shows an error in the same order as the mean value. Despite these uncertainties an 0.5-2.0% extension during Plio-Pleistocene times has to be considered as a realistic approximation for the deformation rate within this part of the continental forearc.

#### 4.4.2 E-W Balanced Cross-section – Basement Geometry

With the help of a balanced cross-section parallel to P1 (Fig. 4.20) the depth of the detachment and the amount of dilatation to be expected in the forearc can further be constrained. The initial shape of the cross-section is inferred from reflection-seismic data [Meinardus 1961; Rocroi 1964], as presented in Fig. 4.21 A, which shows the depth distribution for the *top of basement* (TOB) on the hanging wall side of the PAF. Provided the authors determined a velocity model for the Cenozoic Basin with an accuracy of  $\pm 0.2 \text{ km/s}$ , a maximum vertical error for the depth of TOB is expected to be around

Shear angle	Original bed	Detachment	Heave	Strain	Time	Strain rate
[°]	[m a.s.l.]	[m b.s.l.]	[m]		[Ma]	[ $\mu strain a^{-1}$ ]
75	0	7000	425	0.017	6.5/1.2	0.003/0.014
75	600	17500	825	0.033	6.5/1.2	0.005/0.028
90	0	11000	260	0.010	6.5/1.2	0.002/0.008
90	600	24500	525	0.021	6.5/1.2	0.003/0.018

Table 4.3: Fault plane geometries and E-W horizontal strains resulting from restorations of the basement geometry to original beds on sea level and 600 m altitude, respectively. Results are tested for shear angles of 75° and 90° as shown in Fig. 4.21.

80 – 90 m. Since the isolines for the TOB are inhomogeneously distributed over a relatively small area, a composite solution of three possible geometries was constructed in order to represent the TOB in the initial E-W cross-section. This geometry was restored to two possible paleoelevations, sea level and 600 m above sea level. The range in altitude roughly corresponds to the minimum and maximum vertical displacement (600 – 1200 m) as shown in Tab. 4.1. For the actual restoration process, the *inclined shear* method [White et al. 1986] was applied, as described in Chapter 3.4. After the construction of the fault-plane geometries, two different shear angles (75° and 90°) were tested for their potential to reconstruct the assumed paleotopographies at sea level and 600 m a.s.l., respectively. In order to reveal the E-W horizontal strains, the resulting heave for each restoration process was related to a 25 km long baseline. The length of the baseline was chosen in accordance with the width of the fault zone and the length of the cross-sections in Fig. 4.20. The point of intersection between the fault plane and the TOB was chosen to be two kilometers east of the apparent trace of the range-front fault. This assumption is supported by the drainage network analysis, which shows that the major drainage, the Quebrada Pachingo, turns into range front parallel flow 2 – 3 km east of the range-front fault (Fig. 4.1). The center of strike-parallel flow at the surface probably indicates the position of the present-day active fault at depth.

The resulting fault geometries and the associated detachment depths are strongly dependent on the specified elevation to which the TOB on the hanging wall side is restored. Applying shear angles of 75° and 90° for the restoration of the TOB to sea level reveals detachment depths ranging at 7 and 11 km, respectively (Tab. 4.3). The detachment depths inferred for the restorations of the TOB to 600 m a.s.l. range between 17.5 – 24.5 km, using shear angles of 75° and 90°, respectively. The heave obtained for the different reconstructions varies between 260 – 825 m. Related to the length of the baseline (25 km), the heave indicates strains ranging from 0.010-0.033, which corresponds to 1.0-3.3% extension over the length of the chosen baseline. These results mostly agree with the strains obtained from the neotectonic cross-sections in Chapter 4.4.1. According to the time span shown in Tab. 4.1, the resolving strain rates range between 0.002 – 0.028  $\mu strain a^{-1}$ .

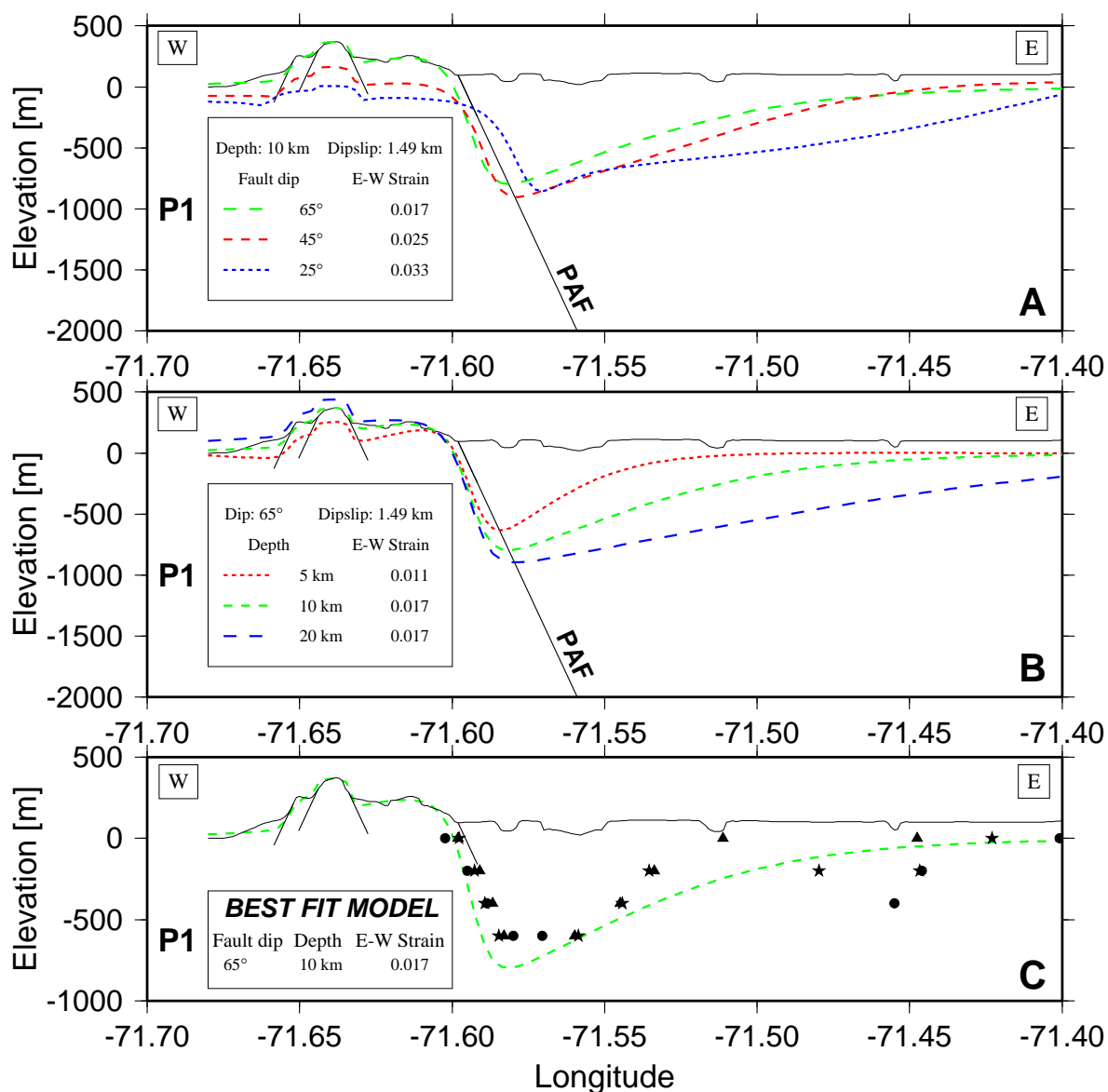


Figure 4.22: Dislocation modeling of topographic cross-section P1 (Fig. 4.20) tested for different model fault geometries; A – Effects of changing fault-dip angle; B – Effects of changing down-dip extension of fault; C – Correlation between best-fit dislocation curve and basement geometry as inferred from geophysical record [Meinardus 1961; Rocroi 1964]; PAF – Puerto Aldea Fault Stars, Circles and Triangles denote three different solutions for the basement geometry as shown in Fig. 4.21; Black lines – Location and dip of normal faults.

## 4.5 Elastic Half-Space Modeling

### 4.5.1 Intraplate Fault Geometries

The neotectonic analysis showed that the uplift of the Coastal Cordillera is closely associated with crustal faulting along major NNW-SSE striking intraplate normal faults, e.g. the PAF. Consequently, the deformation along these intraplate faults is assumed to be responsible for the build-up of the to-

pography of the Coastal Cordillera. Dislocation modeling provides an excellent tool for the study of interrelationships between fault geometries at depth and surface offsets. Assuming that the topography of the Coastal Cordillera represents the surface expression of cumulative intraplate faulting activity along the NNW-SSE striking normal faults, a simple dislocation model can be applied in order to constrain the geometries of these faults as described in Chapter 3.5.2. In the following the results for three best-fit models reproducing the topographies of the E-W neotectonic cross-sections P1-P3 (Fig. 4.20) are presented. The locations and orientations of faults introduced to the model correspond to the observed and inferred fault-traces and -strikes as shown in Fig. 4.1. In a first step, dip angles are tested for their applicability to sufficiently reconstruct the topography of the northern profile (P1). The dip slip along the model equivalent of the range-front fault was set to  $\sim 1.5$  km. This equals the amount of slip necessary to accomplish a 1350 m vertical uplift of the hanging wall block along a  $65^\circ$  dipping fault plane. As shown in Fig. 4.22 A, a best-fit solution is obtained for  $65^\circ$  dipping model faults. Shallower dips ( $45^\circ$  or  $25^\circ$ ) are insufficient to reconstruct the topographic heights accurately. The best-fitting dip angle of  $65^\circ$  corresponds to the average fault dip resulting from the fault-slip data analysis (Chapter 4.2).

Looking at the downdip extensions necessary to reproduce the topographic cross-sections shown in Fig. 4.22 B, a fault depth of 10 km provides the *best-fit* dislocation curve for cross-section P1. Given the same amount of dip slip and a  $65^\circ$  dip angle, faults extending down to 20 km depth produce dislocation curves that tend to over-represent the existing topography. In turn, fault depths of 5 km produce dislocation curves that are insufficient to explain the observed topographic heights. In Fig. 4.22 C, the best-fit dislocation curve for P1 (dip:  $65^\circ$ , depth: 10 km, dip slip: 1.5 km) is tested for its potential to reproduce the geometry of the TOB as presented in Fig. 4.21 A. Between longitudes  $71.6^\circ$ -  $71.55^\circ$  W a basic correspondence of both curves is observed. This shows that the dislocation model is capable to reconstruct realistic geometries for both, the footwall and the hanging wall block. Consequently, the uplift of the Coastal Cordillera and the tilting of the basement underlying the Cenozoic Basin is likely to be caused by intraplate normal faulting along the range-front fault.

In a next step, the dislocation model is tested for its potential to match the topographies of cross-sections P2 and P3 (Fig. 4.23). In the first case (Fig. 4.23 A) the topography is matched by introducing a higher dip angle ( $75^\circ$ - $80^\circ$ ) to the model of the range-front fault (PAF). The amount of dip slip on this fault necessary to reproduce the cross-section has to be increased by 0.8 – 1 km to about 2.3 – 2.6 km. A dip slip of  $\sim 2.3$  – 2.6 km along a  $75$ - $80^\circ$  dipping fault produces a  $\sim 1.6$  km vertical displacement in the dislocation model. For cross-section P3 the modeling results are presented in Fig. 4.23 B. The amount of dip slip necessary to sufficiently model the topography, again has to be increased by 1.4 – 1.7 km to almost 4 km. In addition to this, the best-fit dip angle for the model range-front fault has to be fixed to  $80^\circ$ . A  $\sim 4$  km dip slip along an  $80^\circ$  dipping fault produces almost 2 km vertical offset in the dislocation curve. Comparing this displacement with the vertical offsets obtained for cross-sections P1 and P2, an increasing subsidence of the Cenozoic Basin towards the south can be inferred. This result corresponds to neotectonic field observations, such as a higher concentration of intraplate faulting in the eastern and central parts of the study area (Chapter 4.2.3). The thickness of Plio-Pleistocene fluvial deposits in this area (Fig. 2.6) and the existence of a local depression in the drainage network (Fig. 4.17) provide additional support to this interpretation.

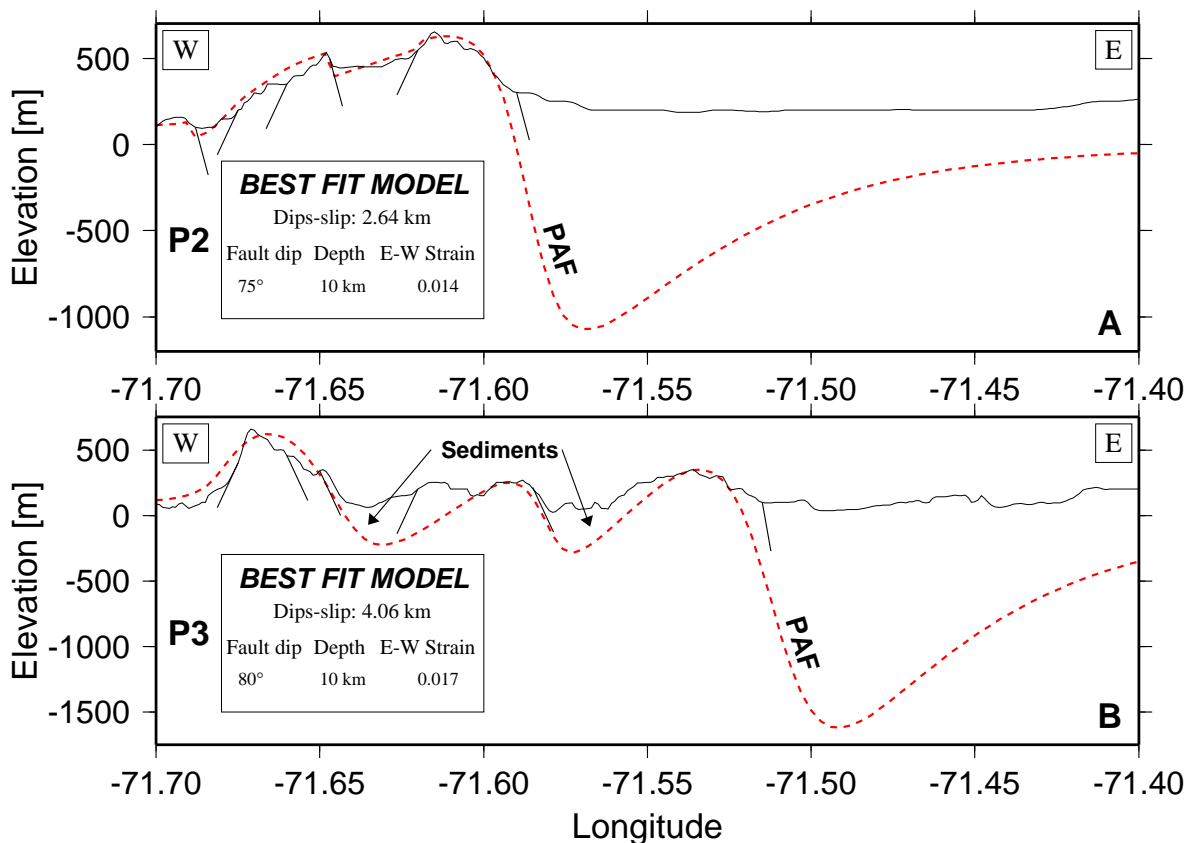


Figure 4.23: Dislocation modeling of topographic cross-section P2-P3 (Fig. 4.20); Thin solid line – Topographic cross-sections; Thick solid line – Location, dip-angle and dip-direction of model faults; Dashed line – Dislocation curve.

The E-W horizontal strains, calculated for all dislocation models on the basis of line length changes of the 25 km long baseline, fall within the same order of magnitude as the strains resulting from the neotectonic and balanced cross-sections. Strains resulting from best-fit dislocation models range from 0.014-0.017, which corresponds to 1.4-1.7% extension over the length of the considered baseline or a strain rate of  $0.002 - 0.015 \mu \text{ strain a}^{-1}$ .

Cross-section P3 exhibits significant mismatches between the dislocation curve and the topographic signal. However, where the dislocation curve apparently underestimates the topography, the missing volume is usually filled with sedimentary deposits in nature. This indicates that the apparent mismatches between the existing and the modeled topography do not represent inaccuracies of the model, but reflect the present geological settings in the study area. Consequently, the results from elastic dislocation modeling strongly correlate with both the field observations and the results from the neotectonic analysis and thus support the interpretation of the Coastal Cordillera to have formed due to repeated earthquakes along the range-front fault (PAF).

#### 4.5.2 Forearc Deformation due to Large Subduction Earthquakes

Large subduction earthquakes, hereafter termed as *interplate events*, periodically rupture segments of the plate interface, which connects the subducting slab with the overriding crust along the Nazca-

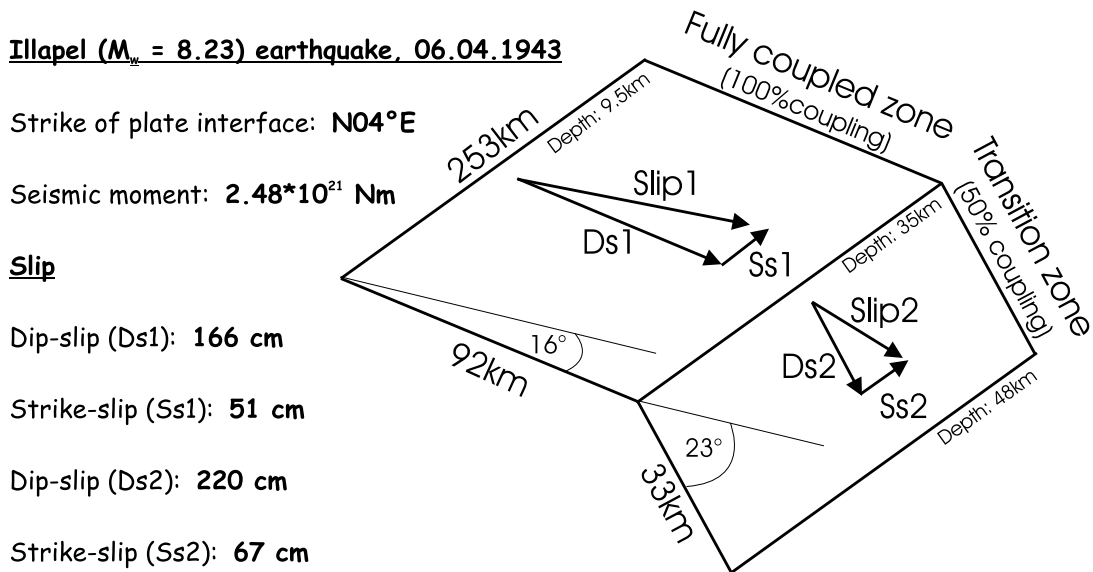
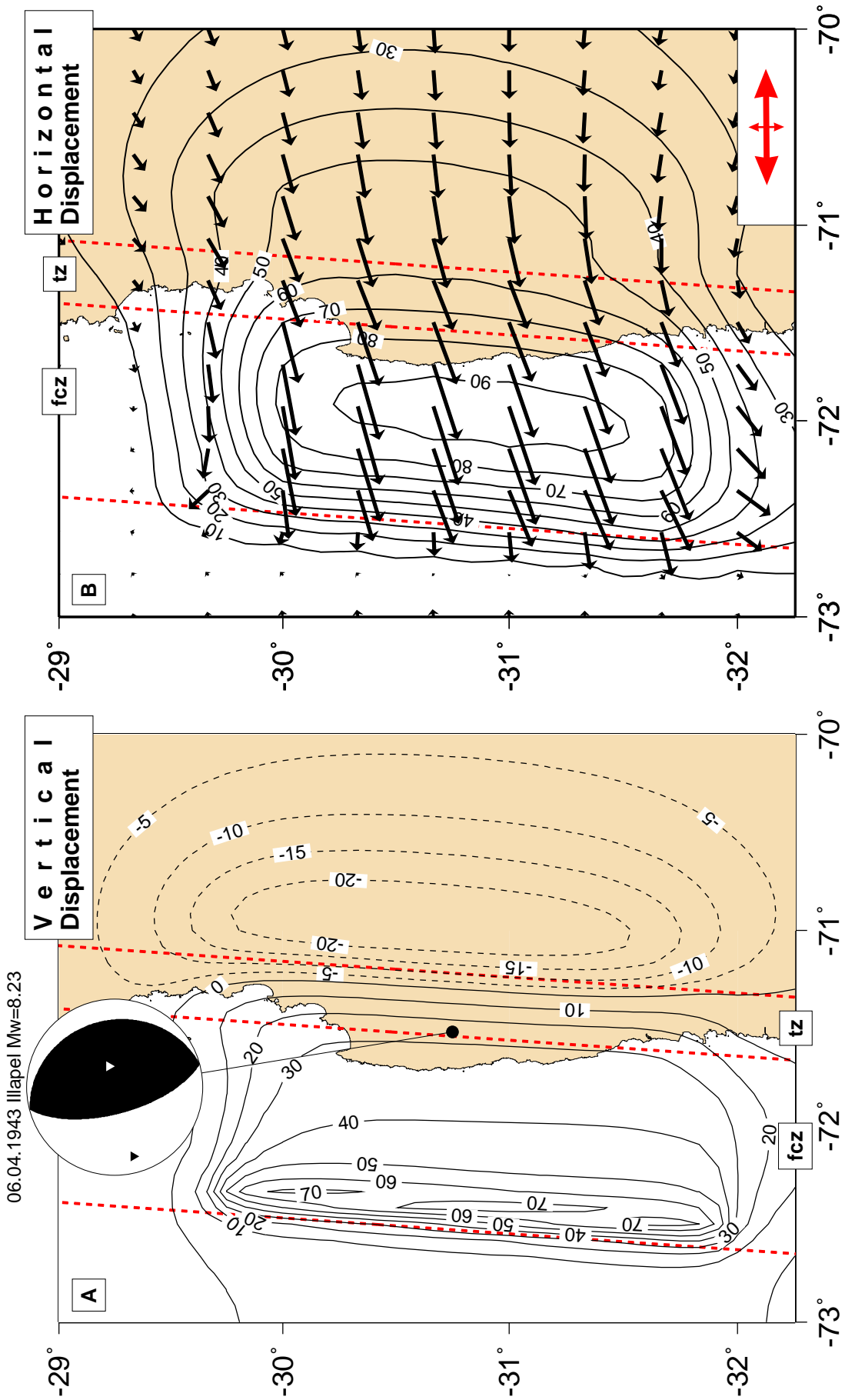


Figure 4.24: Model interface and faulting parameters for the 1943 Illapel  $M_w$ 8.2 interplate event. Vectors show movement of the subducting slab, subdivided into dip-slip and strike-slip components. Total seismic moment for all slip components (Ds1+Ss1+Ds2+Ss2) equals  $2.24 \times 10^{21}$  Nm.

SA plate boundary. During these earthquakes significant uplift or subsidence of coastal segments and/or activation of crustal faults is observed. For instance, during the 1995 Antofagasta  $M_w$ 8.0 interplate event, coastal uplift in the order of 0.1 – 0.4 m [Ortlieb et al. 1996a] and normal offset along an intraplate fault bordering the Coastal Cordillera to the east were observed (Gonzalez, 2002 pers. comm.). This suggests a close interaction between the processes in the subduction zone and the continental forearc. Thus, modeling the displacement field in the continental forearc generated due to large interplate events provides a key for the understanding of the intraplate deformation observed in the study area. The last significant interplate event ( $M_w$ 8.2), rupturing the segment of the plate interface adjacent to the study area, occurred on April 6<sup>th</sup>, 1943. For this event the dislocation model described in Fig. 4.24 was used to approximate coastal uplifts and horizontal displacements in the continental forearc between latitudes 29°–32° S. According to the AEDM [Khazaradze et al. 1999], the applied model interface is subdivided into a *fully coupled zone* (100% coupling) between 8 – 35 km depth and a *transition zone* (50% coupling) between 35 – 48 km depth. The dip of the fully coupled and the transition zone is 16° and 23°, respectively. This provides a width of 92 km for the updip zone of the interface, and a width of 33 km for its downdip extension (Fig. 4.24). According to scaling laws by Wells and Coppersmith [1994], the length of the model interface was set to 253 km. The slip for each zone was subdivided into dip-slip and strike-slip components under conservation of

Figure 4.25: (next page) Vertical (A) and horizontal (B) displacements predicted by dislocation model for the 1943 Illapel  $M_w$ 8.2 earthquake. Faulting parameters are given in Fig. 4.24. Magnitude of displacements given in [cm]. Inset in B shows principal strain axes orientations in the center of the study area at 0 km depth; straight dashed lines – projection of updip and/or downdip edges of the model interface; fcz – fully coupled zone; tz – transition zone.



the total seismic moment of  $2.24 \times 10^{21}$  Nm. In correspondence with the average nucleation depth of large interplate earthquakes along the Chilean subduction zone [Tichelaar and Ruff 1991], the larger amount of dip slip (220 cm) is accomplished between 35 – 48 km depth. Between 8 – 35 km depth the amount of dip slip is smaller, but due to its larger area, the total seismic moment produced by this portion of the model interface is twice as high as the seismic moment exerted by the downdip transition zone.

The modeled coseismic uplift and horizontal displacement fields are plotted in Fig. 4.25. The horizontal displacement field shows a WSW directed coseismic motion of the continental forearc in the order of 80 – 90 cm. These results correspond well with the observations made for the 1995 Antofagasta  $M_w$  8.0 interplate event, where up to 90 cm horizontal displacement could be detected by means of resurveying several GPS monuments shortly after the earthquake [Klotz et al. 1999]. For the center of the study area the modeled coseismic displacement field predicts an E-W oriented maximum extension direction, normal to the trench (see inset Fig. 4.25 B), and a maximum shortening direction oriented N-S, parallel to the trench. These strain orientations largely coincide with the principal strain axes orientations inferred from neotectonic fault-slip data. Hence, the model described above shows, that the intraplate deformation observed in the continental forearc is most likely to be influenced, if not even controlled, by large interplate earthquakes rupturing the subduction zone.

The hypocenter of the 1943 Illapel earthquake as specified by the South American historical seismicity catalogue [USGS 2001] is located immediately beneath the continental forearc. According to the model described above, uplift within the continental forearc occurs up to 40 km landward from the coast. The study area with its seaward-protruding coastline lies well within this zone of coseismic uplift. Due to their greater distances to the trench, the adjacent coastal areas in the north and in the south of the study area either lie outside the uplift zone or within zones of less pronounced uplift. Within the study area, coseismic uplifts of up to 35 cm are predicted by the dislocation model (Fig. 4.25 A). These results compare well with the observations made for the 1995 Antofagasta event in North Chile [Delouis et al. 1998]. The hinge line between uplift and subsidence roughly falls in place with the downdip edge of the transition zone. This suggests that the commonly observed uplift of Coastal Cordilleran blocks along the Nazca-SA plate boundary is closely associated with the latitudinal position of the junction between the continental and oceanic crusts and the *asthenospheric wedge* (Fig. 2.2). This is supported by Ruff and Tichelaar [1996] who reported a general correlation between the location of the coastline and the downdip edge of the plate interface for the whole circum-Pacific region. Thus, a possible cause for the strong uplift of coastal areas during large subduction earthquakes is the updip translation of forearc slivers along the plate interface.

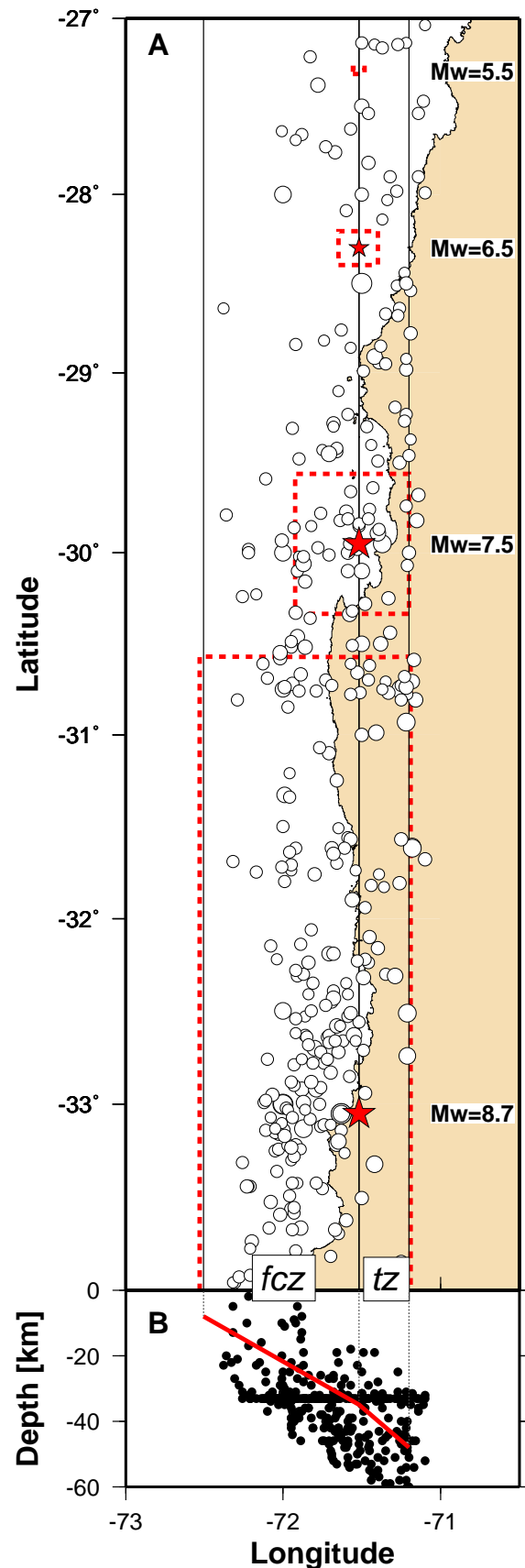
---

Figure 4.26: (See next page) Location of 339 interplate events with  $M_s > 5$  selected from NEIC catalogue [2001]. Epicenter locations for selected events are shown as white circles. Considered time span covers the last 350 years, starting with the 1647 megathrust [Beck et al. 1998]; A: Thin black lines – Outline of the model plate interface; fcz: fully coupled zone tz: transition zone; Dashed frames – Exemplary rupture areas for earthquakes of different magnitudes. B: E-W Cross-section with locations of selected earthquakes (black dots) relative to the model plate interface. Selected events plot within +/- 20 km vertical distance to the thrust interface. The horizontal alignment of hypocenters near 33 km depth represents earthquakes that were assigned the default depth in the NEIC catalogue [2001].

### 4.5.3 Strain Redistribution due to Large Subduction Earthquakes

In order to quantify the amount of strain redistributed during large subduction earthquakes along intraplate faults in the continental forearc, 339 events with magnitudes 5 ( $M_s$ ) or higher were selected from the NEIC [2001] or the USGS [2001] seismic catalogues and modeled using a simple dislocation model of the plate interface. The selected interplate earthquakes occurred during the last 350 years, starting with the 1647 megathrust [Beck et al. 1998] near  $33^\circ$  S. The selected events lie within  $\pm 20$  km vertical distance to the model plate interface as shown in Fig. 4.26 B. A high concentration of earthquakes can be observed for the area between  $32^\circ$ - $34^\circ$  S. At least three megathrusts (1647, 1730 & 1906; see Chapter 2.3.3) ruptured this segment of the plate interface, and due to their size possibly propagated northward into the study area [Beck et al. 1998]. The possible rupture area for the 1730 ( $M_s$ 8.7) subduction earthquake and the average rupture areas of a number of smaller interplate events are indicated in Fig. 4.26 A. The rupture area for all 339 earthquakes were estimated using scaling laws published by Wells and Coppersmith [1994]. The geometry of the applied model interface is nearly identical to the geometry presented in Fig. 4.24, apart from the strike of the interface, which was chosen to be due N-S.

Fig. 4.27 shows estimates for cumulative strains redistributed along major crustal faults due to 339 interplate earthquakes, which ruptured the north-central Chilean segment during the last 350 years. For three selected sites within in the study area moment rates and hypothetical focal mechanisms were calculated in order to quantify the coseismic strain redistribution along major intraplate or crustal fault planes.



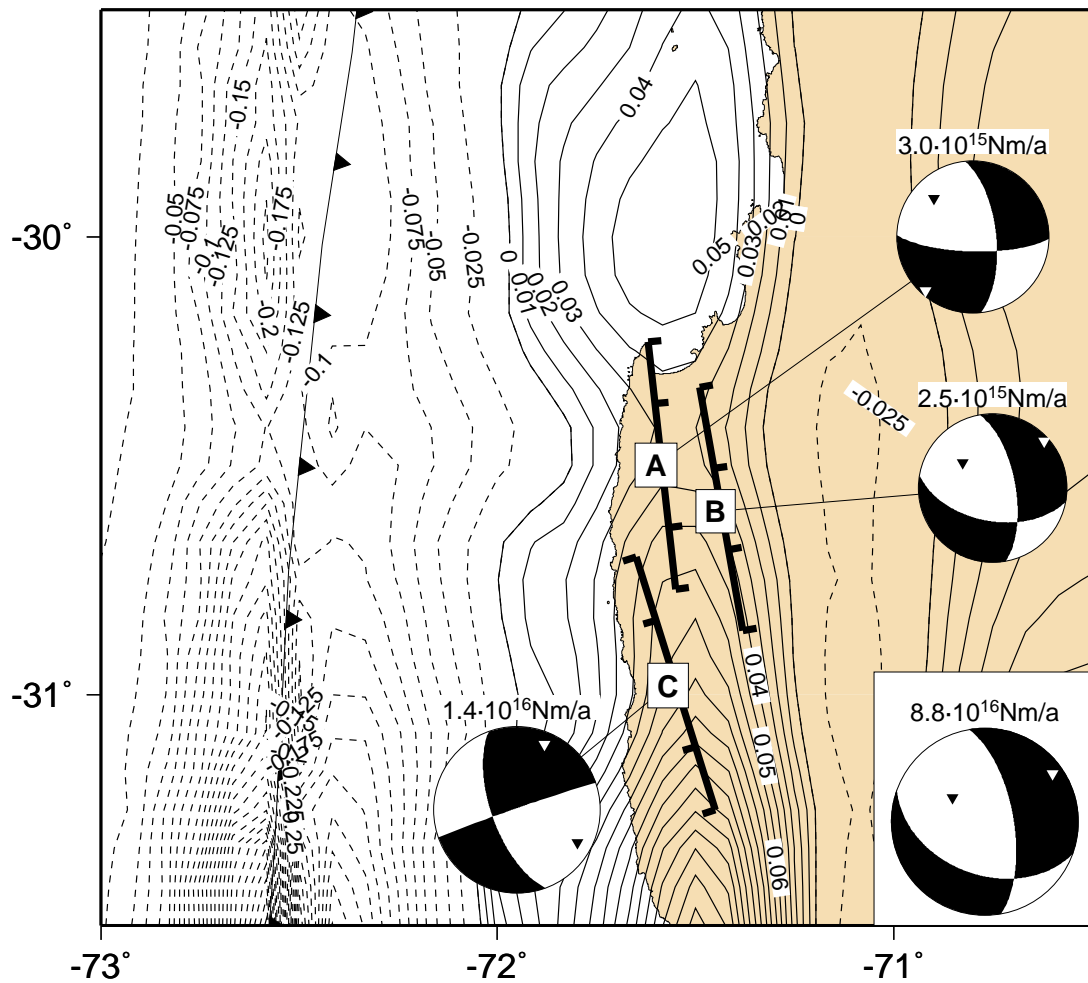


Figure 4.27: Strain rate inferred from dislocation modeling of 339 interplate events of magnitude  $M_w$  5 or higher since 1647. Solid contour lines show positive (extensional), dashed lines show negative (contractional) strain rates in  $\mu$  strain  $a^{-1}$ . A, B and C represent model intraplate faults of 60 km length, 11 km width and 65° dip. Focal mechanisms depict movement along fault and moment rate inferred from strain redistribution due to successive rupture of the subduction zone. Rake and slip were calculated from strain components parallel to the strike and dip of the individual fault planes. Inset shows focal mechanism and moment rate inferred from GPS-residuals.

The moment rates and focal mechanisms are calculated on the basis of two components of the modeled strain tensor ( $T_{xx}$ ,  $T_{yy}$ ), which is rotated into the planes of 65° E- or W-dipping model intraplate faults (A-C in Fig. 4.27), as described in Chapter 3.5.3. The contour lines in Fig. 4.27 show that the maximum E-W extensional strain rate at the surface falls in place with the major intraplate fault zone as observed in the study area. The magnitude of these E-W horizontal strain rates range between  $0.04 \mu$  strain  $a^{-1}$  in the center of the study area to  $0.08 \mu$  strain  $a^{-1}$  at its southern tip near Qbd. Teniente (C in Fig. 4.27). The higher strain rates in the south refer to the higher concentration of large subduction earthquakes between 32°- 35° S. Interestingly, the focal mechanisms inferred for the model intraplate fault planes show both, left oblique extensional faulting (B in Fig. 4.27) and left-lateral strike slip (A and C in Fig. 4.27). These results correlate with the focal mechanisms inferred from neotectonic fault-slip data obtained in the field (Fig. 4.13).

The moment rates obtained from strain redistribution modeling along major intraplate faults range from  $2.5 \times 10^{15} \text{ Nm a}^{-1}$  to  $1.4 \times 10^{16} \text{ Nm a}^{-1}$ , which is equivalent to moment magnitudes of  $M_w$ 4.2-4.7. The average magnitude of intraplate earthquakes (depth < 30 km) as provided by seismic catalogues [ISC 2001; NEIC 2001; USGS 2001] falls in the same order of magnitude. According to these catalogues, approximately one earthquake of magnitude  $M_w$ 4.1 per year occurred in the study area during the last decade. In contrast to this, the moment rate inferred from GPS residual velocities (see inset in Fig. 4.27) is much higher, ranging from  $8.8 \times 10^{16} \pm 4.1 \times 10^{16} \text{ Nm a}^{-1}$ . The most striking result of modeling the strain redistribution is that the model predictions largely correspond to the observations made in the field. On the one hand this shows, that simple dislocation models are capable to realistically image existing deformation processes, on the other hand it suggests that interplate and intraplate deformation processes in the forearc are closely associated to one another. This interpretation is strongly supported by eyewitnesses reporting the (re)activation of the *Salar del Carmen Fault* during the 1995 Antofagasta ( $M_w$ 8.0) earthquake. The Salar del Carmen Fault, which is located  $\sim 15$  km inland from the coast, suffered a left-oblique normal faulting offset cutting an agricultural fence line [Gonzalez et al. 2002].

## 4.6 Space Geodetic Observations

Based on observations from four GPS-campaigns conducted in 1994-1997 the contemporary crustal deformation field along the central and southern Andes ( $17^\circ$ - $42^\circ$  S) was analyzed [Khazaradze and Klotz 2002]. For this study, GPS data from the continental forearc were selected between  $28^\circ$ - $34^\circ$  S, in order to study the long-term intraplate deformation rates and to compare these with the field observations in the study area. As described in Chapter 3.6, the observed displacement vectors mainly reflect the interseismic elastic strain accumulation due to the locking of the subduction interface. The interseismic strain accumulation simply represents a dominant short-term signal which has to be removed in order to picture the long-term intraplate deformation rates. This is accomplished by estimating the interseismic deformation at the observation points using a three-dimensional elastic dislocation model (AEDM) of the seismogenic interface [Klotz et al. 2001]. Subtracting the modeled short-term deformation rates from the observed present-day deformation rates reveals a residual displacement field which can be interpreted as the long-term intraplate deformation of the overriding plate (Fig. 4.28).

### 4.6.1 GPS Strain Rates and Differential Motions

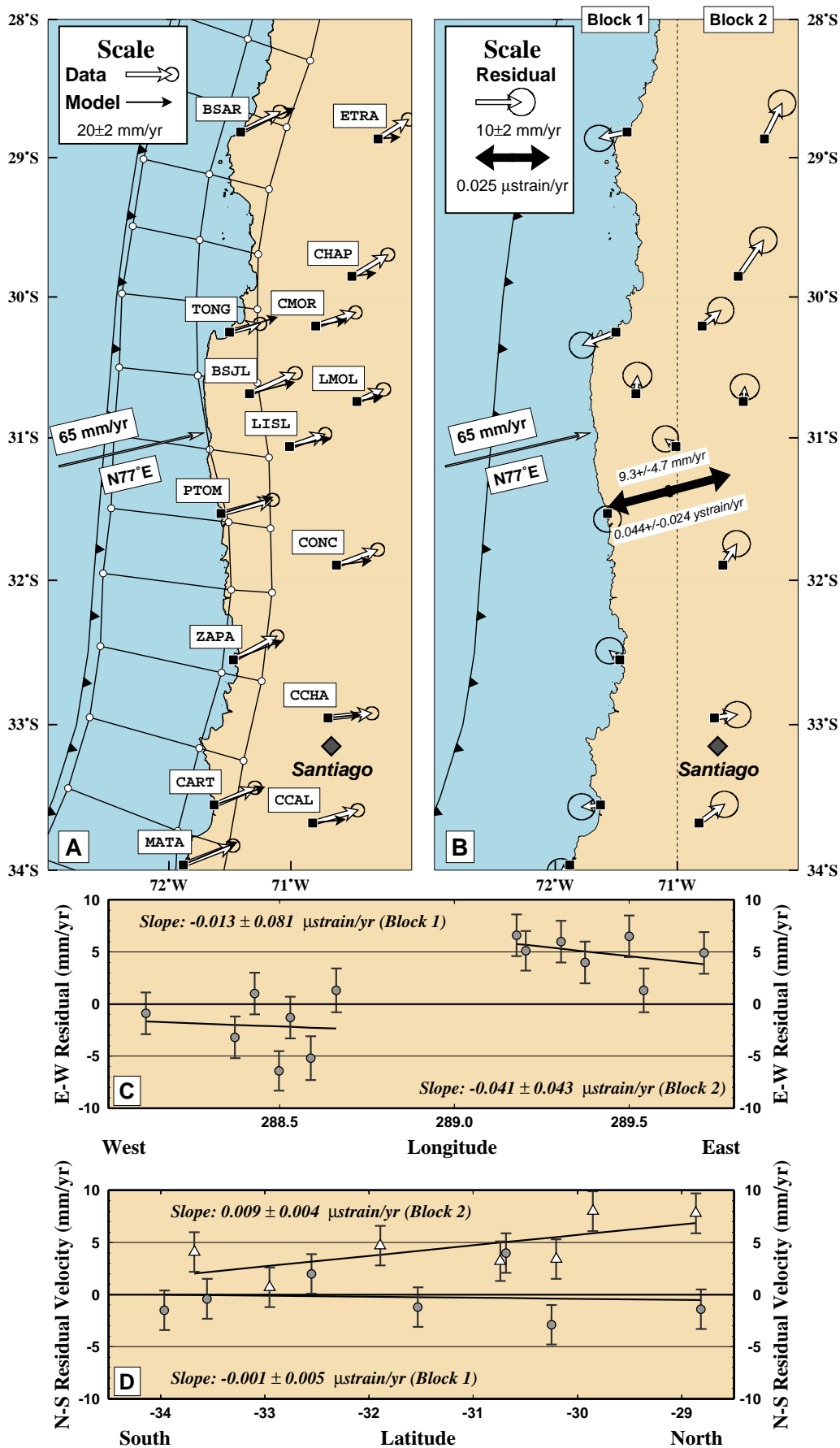
Observed and modeled velocities in the forearc of North-Central Chile are plotted in Fig. 4.28 A. The observed velocity field is relatively homogeneous and oriented subparallel to the Nazca-SA plate convergence direction [Angermann et al. 1999]. The length of the observed displacement vectors ranges between  $24 \pm 1.5 \text{ mm a}^{-1}$  at the coast and  $13 \pm 2 \text{ mm a}^{-1}$  in the Precordillera. Thus, the length of the displacement vectors generally decreases away from the Peru-Chile Trench leaving a pattern which could easily be interpreted as forearc shortening. However, as stated above, the observation data needs to be reduced by the dominant short-term signal. This is done by subtracting the AEDM model vectors from the observed data. Along the coastline the model vectors best fit

or even overcompensate the observed displacements. However, further inland the capability of the AEDM to predict the observations decreases rapidly and the length of the residual vectors (observed - modeled) increases substantially. Hence, the resolving residual velocity field presents a completely different pattern compared to that generated by the observed velocities (Fig. 4.28 B). The residual vectors along the coast are predominantly directed seaward while the residuals further inland indicate east or northeast motion. In the center of the considered area residual velocities are close to zero (stations: BSJL and LISL).

The horizontal strain rate at the center of the residual velocity field is determined according to the method described in Chapter 3.6. Length and azimuth of the resulting maximum extensional and contractional strains are shown by the black double arrow in Fig. 4.28 B. In correspondence with the neotectonic field studies and the modeling results, the two-dimensional strain tensor inferred from the residual velocity field resolves ENE-WSW oriented extension and NNW-SSE directed contraction. The maximum extensional strain rate is as large as  $0.044 \pm 0.013 \mu\text{strain a}^{-1}$  trending ENE, while the maximum contractional strain rate is by an order of magnitude smaller, ranging between  $0.003 \pm 0.01 \mu\text{strain a}^{-1}$ . Due to its large error, this component has to be considered insignificant. In Fig. 4.28 C the E-W component of residual velocities between  $70^\circ\text{-}72^\circ\text{ W}$  is displayed in a cross-sectional view. In the western half of the plot data points cluster around zero or slightly below which indicates stagnation or seaward residual motion. In the eastern half of the diagram data clearly plot above zero, indicating eastward residual motion. The internal strain for each cluster is expressed by the regression lines in Fig. 4.28 C. However, strains of  $-0.013 \pm 0.081 \mu\text{strain a}^{-1}$  (Block 1) and  $-0.041 \pm 0.043 \mu\text{strain a}^{-1}$  (Block 2) have to be considered insignificant due to their large errors. This indicates that no internal deformation takes place in E-W direction, thus allowing for the interpretation that each cluster represents a rigid, uniformly moving block. Based on this assumption, the residual velocities between  $28^\circ\text{S} - 34^\circ\text{ S}$  can be used to approximate a differential motion between the two blocks representing the Forearc (Block 1) and the Precordillera (Block 2), respectively. Residuals from 5 stations were attributed to Block 1 while residuals from 7 stations could be attributed to Block 2. Two stations (BSJL;LISL) were omitted during the calculation because of their vicinity to the block boundaries. The width of each block is  $\sim 100$  km. Converting the residual velocity field into a differential motion between the assumed blocks, a velocity of  $9.3 \pm 4.7 \text{ mm a}^{-1}$  distributed over a  $\sim 200$  km distance is achieved. The E-W component of the differential motion is  $7.6 \pm 3.6 \text{ mm a}^{-1}$ , while the N-S component amounts to  $5.5 \pm 3.1 \text{ mm a}^{-1}$ . The azimuth and direction of the differential motion ( $\text{N}54^\circ\text{ E}$ ) is roughly parallel to the orientation of the principal extensional strains inferred from the majority of neotectonic fault-slip data (NE-SW to ENE-WSW).

---

Figure 4.28: (See next page) GPS data from SAGA network [Klotz et al. 2001] between  $28^\circ\text{-}34^\circ\text{ S}$  latitude; A – Observed (white) and *best-fit* model velocities (black) at selected stations. Slab geometry is outlined by frames. Convergence rate is  $65 \text{ mm a}^{-1}$  [Angermann et al. 1999] oriented at  $\text{N}77^\circ\text{ E}$  azimuth; B – White arrows show length and azimuth of GPS residual velocities and the corresponding 95% confidence limits. Black double arrow (strain cross) shows length and azimuth of maximum extensional and compressional strain inferred from the residual velocities; C – E-W residual velocities for Coastal block (Block 1) and Precordilleran block (Block 2); D – N-S residual velocities for Coastal (circles) and Precordilleran (triangles) blocks. Error-bars delineate 95% confidence limits.



<b>GPS observed and residual velocities for North Central Chile (SAGA 1994-1997)</b>						
Station name	Longitude [°]	Latitude [°]	E-Observed [mm/a]	N-Observed [mm/a]	E-Residual [mm/a]	N-Residual [mm/a]
MATA	288.12	-33.96	23.8	10	-1.9	-1.5
CART	288.37	-33.55	22.1	8.0	-4.2	-0.4
PTOM	288.43	-31.53	22.6	7.2	0.0	-1.2
TONG	288.50	-30.25	20.8	6.5	-7.4	-2.9
ZAPA	288.53	-32.55	21.4	8.3	-2.3	2.0
BSAR	288.59	-28.82	23.6	10.3	-6.2	-1.4
BSJL*	288.66	-30.69	19.7	5.0	0.3	4.0
LISL*	288.99	-31.06	18.0	3.8	-2.3	1.7
CCAL	289.18	-33.68	14.2	1.5	5.6	4.1
CMOR	289.20	-30.21	13.4	2.5	4.1	3.4
CCHA	289.31	-32.95	14.2	1.3	5.0	0.7
CONC	289.37	-31.89	15.1	2.1	3.0	4.7
CHAP	289.50	-29.85	10.3	1.6	5.5	8.0
LMOL	289.54	-30.74	11.3	2.1	0.3	3.2
ETRA	289.71	-28.87	9.6	0.7	3.9	7.8

Table 4.4: Selected GPS residual velocities for North Central Chile. Based on these velocities, geodetic strain rates and differential motion between the Coastal and Precordilleran blocks are approximated. Upper section of the table, stations MATA-LISL, are attributed to the Forearc or Coastal block (Block 1 in Fig. 4.28); Lower section of the table, stations CCAL-ETRA, are attributed to the assumed Precordilleran block (Block 2); \* – Stations not included into calculation of differential motion due to their vicinity to the block boundaries.

The N-S residual velocities presented in Fig. 4.28 D show a clear trend within the data of Block 1, indicating N-S extension. Together with the eastward component of this block a northeastward motion is resolved. The coastal block shows no N-S trend at all, thus a predominantly westward motion results for this block. Provided the motions of Block 1 and 2 are indicative for the intraplate deformation in the continental forearc, a potential fault-plane solution would show left oblique normal dip slip or left-lateral strike slip for N-S striking intraplate faults. A potential fault-plane solution for the PAF is presented in Fig. 4.27. This fault-plane solution corresponds well to the fault-plane solutions presented in Chapter 4.2.3, which were inferred from neotectonic fault-slip data. Since the 1943 Illapel  $M_w$  8.23 interplate event, no large subduction earthquake ruptured the plate interface of North Central Chile. Consequently, the observed GPS-signal represents a purely interseismic state of deformation without any contributions from coseismic and/or postseismic effects, as reported for the rupture areas of the 1995 Antofagasta and 1960 Valdivia events [Klotz et al. 1999; Klotz et al. 2001]. In the light of the overall correlation between principal strain axes inferred from neotectonic fault-slip data, strain redistribution modeling, and GPS-residual field analysis, space geodetic techniques seem to be applicable to correctly image intraplate deformation processes along the North Central Chilean forearc.

### 4.6.2 Recurrence Intervals for Intraplate Earthquakes

Recurrence intervals for intraplate normal faulting events are approximated on the basis of the differential motion estimates as presented in Chapter 4.6. In addition, the moment rates resolving from the redistribution of strains during large subduction earthquakes (Chapter 4.5.3) are added to the GPS-derived moment rates. The calculation of recurrence intervals was conducted according to two model approaches:

1. a *characteristic earthquake model*, assuming that 100% of the accumulated intraplate strains is removed by characteristic  $M_w7$  crustal events
2. a *truncated Gutenberg-Richter relationship*, assuming that only  $\sim 30\%$  characteristic earthquakes occur [Schwartz and Coppersmith 1984] while the remaining intraplate strains are removed by numerous smaller crustal events

Both approaches are based on moment-rate estimates for a potential intraplate fault with the subsurface dimensions of the Puerto Aldea Fault (PAF) as shown in Chapter 4.5.1. The moment rates were calculated applying the horizontal differential motion to the PAF as described in Chapter 3.6. The differential motion inferred from GPS residual velocities ( $9.3 \pm 4.7 \text{ mm a}^{-1}$ ) converts to a dip-slip rate of  $2.9 \pm 1.4 \text{ mm a}^{-1}$  and a strike-slip rate of  $3.3 \pm 1.6 \text{ mm a}^{-1}$  on the  $65^\circ$  E dipping and  $N170^\circ$  E striking fault (Tab. 4.5). Using Kostrov's formulation (3.5), and assuming a 60 km long and 11 km wide fault plane (PAF), a moment rate of  $8.8 \times 10^{16} \pm 4.1 \times 10^{16} \text{ Nm a}^{-1}$  is achieved. Compared to this, the average moment rate of  $6.3 \times 10^{15} \pm 4.8 \times 10^{15} \text{ Nm a}^{-1}$  redistributed along equivalent fault geometries (Fig. 4.27) during large subduction earthquakes is by an order of magnitude smaller than the moment rate derived from the GPS differential motion. Slip rates inferred from seismic moment redistribution range between  $0.05 \pm 0.02 \text{ mm a}^{-1}$  in dip-slip and  $0.30 \pm 0.25 \text{ mm a}^{-1}$  in strike-slip direction.

Scaling laws [Wells and Coppersmith 1994] show that the fault dimensions (length, width) of the PAF and the average displacement observed at several outcrops along its trace (Figs. 4.3-4.6) correspond to  $M_w7$  events. This suggests that the characteristic earthquake along the PAF has a moment release of approximately  $3.55 \times 10^{19} \text{ Nm}$ . Recurrence intervals for intraplate earthquakes were approximated relating the moment rates as shown in Tab. 4.5 to the moment release of the characteristic earthquake. For the purely characteristic approach conservation of the apparent geodetic rates is invoked and the occurrence of smaller earthquakes was taken as insignificant for the release of intraplate deformation. For the truncated Gutenberg-Richter distribution the b-value was set to 0.95 and the frequency-magnitude distribution was sharply bounded at the  $M_w7$  earthquake (cut-off model). The purely characteristic approach results in a minimum recurrence time of  $480 \pm 190 \text{ a}$  for characteristic  $M_w7$  earthquakes. Applying the truncated Gutenberg-Richter relationship resolves a recurrence time of  $1185 \pm 525 \text{ a}$  (Tab. 4.5). Following these results, significant crustal faulting induced by interseismic strain accumulation along the Chilean forearc is to be expected at 500 – 1500 a intervals.

<b>GPS/Modeled slip rates &amp; recurrence times/reduction for <math>M_w7</math> intraplate earthquakes</b>					
<b>Type</b>	<b>Dip-slip</b>	<b>Strike-slip</b>	<b>Moment rate</b>	<b>100% charact.</b>	<b>30% charact.</b>
	[ <i>mm/a</i> ]	[ <i>mm/a</i> ]	[ <i>Nm/a</i> ]	<i>time</i> [ <i>a</i> ]	<i>time</i> [ <i>a</i> ]
GPS	2.9±1.4	3.3±1.6	$8.8 \times 10^{16} \pm 4.1 \times 10^{16}$	480±190	1185±525
DISL	0.05±0.02	0.30±0.25	$6.3 \times 10^{15} \pm 4.8 \times 10^{15}$	-35±14	-85±38

Table 4.5: Intraplate fault-slip rates derived from GPS differential motion or elastic dislocation modeling (DISL). Moment rates are estimated assuming a NNW-SSE striking  $65^\circ$  E dipping normal fault (e.g. PAF). Recurrence times for  $M_w7$  intraplate earthquakes are given for GPS derived moment rates applying 1.) a *purely characteristic* model and 2.) a *truncated Gutenberg-Richter frequency relationship* assuming 30% characteristic earthquakes. DISL derived data gives reduction to GPS-derived recurrence intervals; Seismic moment for characteristic earthquake =  $3.55 \times 10^{19}$  Nm; Applied fault dimensions – 60 km length, 11 km width. Thickness of seismogenic zone set to 3 – 13 km.

Due to large subduction earthquakes, as shown in Fig. 4.27, an additional load caused by strain redistribution is imposed on intraplate faults. This additional load causes a reduction of the above stated recurrence times in the order of 20 – 50 a for the purely characteristic approach, or 40 – 120 a for the cut-off model (Tab. 4.5). Thus, compared to the interseismic strain accumulation as inferred from GPS residual velocities, the seismic moment redistribution only contributes a subordinate amount of strain accumulation to the intraplate faults. This result shows that the extensional crustal strains required to produce the observed intraplate normal faults are predominantly accumulated during the interseismic period, when the interface between the continental crust and the subducting slab is assumed to be locked. Hence, strain accumulation during times of interseismic locking plays a much more significant role with respect to crustal extension and the formation of intraplate normal faults, than the redistribution of stresses and strains along intraplate faults during large subduction earthquakes. However, the redistribution of seismic moment along these faults may eventually lead to their (re)activation at earlier stages in the (intraplate) seismic cycle due to a momentary exceedance of the peak shear strength of the fault plane during large subduction earthquakes, which was possibly the case along the Salar del Carmen Fault during the 1995 Antofagasta earthquake in Northern Chile.

## 5 Discussion

Within the framework of this study intraplate as well as interplate faulting processes were analyzed for their potential to control the pattern of brittle deformation as observed in a fraction of the continental forearc of Chile (30°-31° S). The analysis is based on three main approaches - (1) *Neotectonic Field Investigation*, (2) *Elastic Dislocation Modeling*, and (3) *Space Geodetic Observation*. Since each approach provides a limited scope for further interpretations and bears significant sources of error, none of these alone suffices to explain the observed deformation pattern. But altogether the individual results provide complementary information for the understanding of forearc deformation processes as a whole. Their contributions as much as their limitations will be discussed in the following paragraphs.

### 5.1 Active Intraplate Faulting

The remote sensing analysis and the field investigations in the study area clearly showed that E-W to ENE-WSW extension along N-S to NNW-SSE striking normal faults provides the ruling deformation mechanism within the study area. According to previous authors, the extension is closely connected to the uplift of the Coastal Cordillera, which is evidenced by the occurrence of widespread abrasion platforms along its western margin [Herm et al. 1967; Paskoff 1970; Ota et al. 1995]. In addition, ongoing uplift of the coastline is indicated by the present-day closing of the Río Limarí estuary by laterally shifting coastal sand bars and the formation of longitudinal dunes, the latter of which suggest exposure of beach ridges to subaerial conditions due to a relative rise of land. The recent nature of uplift is also evidenced by the observation that Plio-Pleistocene alluvial/fluvial sediments deposited by the Río Limarí are found as high as 300 m a.s.l. within the Coastal Cordillera opposed to 100 – 200 m a.s.l. in the Cenozoic basin. In addition to this, the drainage pattern analysis proves that the present day river network is tectonically controlled in major parts of the Cenozoic basin, which indicates ongoing intraplate faulting activity in the study area.

The occurrence of uplifted Pleistocene *losa* deposits [Jordan 1929; Bohnhorst 1967] overlying the Great Plain as much as radiocarbon datings at the southern beaches of Tongoy Bay [Ota and Paskoff 1993] suggest that the Cenozoic Basin itself is currently uplifting as well. The satellite image (Fig. 2.7) shows that the *losa* deposits cover the Great Plain between 25 – 125 m a.s.l., fringing the southern shores of Tongoy Bay in a semicircular fashion parallel to the coastline. They consist of calcareous muds and shelly horizons, presumably representing regression cycles of the Pleistocene transgression at ~ 125 ka BP (isotope stage 5e in Fig. 2.7). Similar observation on Pleistocene marine shelly horizons are known from Mejillones Peninsula (Wilke, 2001 pers. comm.), roughly 1000 km

north of the study area. The Holocene uplift rate inferred from radiocarbon datings for the Cenozoic Basin is  $0.2 - 0.3 \text{ m ka}^{-1}$  [Ota and Paskoff 1993], opposed to  $0.4 - 0.5 \text{ m ka}^{-1}$  for the Altos de Talinay [Ota et al. 1995]. The uplift rate for the Talinay region is supported by the results of the range-front analysis in Chapter 4.3.1, which reveals vertical displacement in the order of  $0.5 \text{ m ka}^{-1}$  between the Coastal Cordillera and the Cenozoic Basin. Altogether this means that both morphostructural units are currently uplifting, with the Coastal Cordillera rising at least  $0.1 - 0.3 \text{ m ka}^{-1}$  faster than the neighboring Cenozoic basin. Consequently, the apparent normal faulting activity as observed along the range-front fault (PAF) in particular and in other parts of the study area, needs to be interpreted as due to *differential uplift* associated with the *extrusion* of the SA forearc.

Brittle deformation as observed at numerous outcrops in the study area (e.g. Figs. 4.2-4.9) is largely controlled by *crustal faulting* events rather than *aseismic slip* along the mapped fault planes. This is strongly supported by the occurrence of *crushed cobbles* within the trace of fault planes and the observation of *colluvial wedges*, *fault-scarps*, *landslides*, and *tension gashes*. Crushed cobbles within the fault plane are unlikely to be produced by aseismic slip because of the stress shadows along the free surfaces at the cobble margins. In order to overcome the stress shadow at the free surface, very high strains need to be applied [Fisher et al. 1995; Becker and Gross 1996; Engelder and Fisher 1996]. The amount of energy necessary to build up very high strains is generally associated with earthquake rupture. To avoid confusion with the effects of weathering processes which are capable of creating fractures in rocks as well, the author specifically examined those cobbles that are obviously truncated by the fault plane. Hence, the numerous examples of crushed cobbles provide evidence for seismically induced crustal faulting.

The formation of colluvial wedges and fault-scarps is a strong indication for surface rupture due to crustal faulting. In the study area three examples for the development of colluvial wedges were found along the PAF (Sites 17/01-19/01; Appx. A.12). Site 17/01 (Fig. 4.6) exhibits a clear example for the development of a colluvial wedge on the top of the hanging-wall block. It consists of an extremely heterogeneous matrix, ranging from silts to coarse sand, and rests against the footwall block. Sites 18/01 and 19/01 show less well developed colluvial wedges but site 19/01 is associated with the outlet of a spring at the contact between the footwall and the hanging wall. Despite the development of colluvial wedges, which give a clear sign for surface rupture, fault-scarps are generally absent along the PAF. Instead, the uppermost 0.5 m commonly consist of red, coarse-clastic alluvial fan deposits showing weakly developed soil formation. The coarse-clastic character of the alluvial fan deposits indicates that fault-scarp degradation was possibly increased due to mass flux from the nearby range front during times of heavy rains. The limited amount of red soil formation in turn suggests that no more than a few thousand years have passed since the activation of the alluvial fans. This corresponds with thoughts on the climatic evolution of North Central Chile (Chapter 2.4), which was characterized by heavy rains and the activation of alluvial fans during Late-Pleistocene to Mid-Holocene times (Tab. 2.3). The present-day semiarid climate developed only some 3000 years ago. The occurrence of heavy rains and the activation of alluvial fans as stated for the Early Holocene is closely related to the northward shift of the Southern Westerlies [Veit 1996], which might have contributed significantly to the degradation of fault-scarps. In addition to this, the relatively young age of the faulted sediments (Plio-Pleistocene), their very low degree of cementation, and the fact that most of these faults almost reach the surface (max 0.5 m below surface), shows that no significant amount of time has elapsed

since the formation of these structures. Thus, faulting along the range-front fault must have occurred during Late Pleistocene to Early Holocene times.

Looking at the central eastern parts of the Cenozoic Basin, the occurrence of fault-related topographic features and presumed fault scarps increases significantly compared to the western domains. This observation is supported by the higher concentration of fault planes observed in this part of the study area (Fig. 4.13). In addition, a number of seasonal springs in the Cenozoic Basin and the *hot-spring* at Termas Socos provide evidence for the existence of open connected fractures in close association with the observed fault planes. Three scarps in the central eastern part of the study area were mapped and analyzed morphologically in order to approximate the age of faulting. Assuming semiarid conditions throughout the entire degradation process, the determined faulting ages fall well within the Upper-Pleistocene period (10 – 84 ka BP). The climatic evolution during this time, however, has changed towards more humid conditions repeatedly, suggesting higher diffusivity constants than those applied to the diffusion equation ( $4.4 - 20 \text{ m}^2\text{ka}^{-1}$ ) in Chapter 3.3. Assuming higher diffusivity constants ( $\sim 100 \text{ m}^2\text{ka}^{-1}$ ) as stated for other semiarid climate zones in the world, e.g. the Mediterranean [Fernandes and Dietrich 1997], the calculated faulting ages would decrease by a factor of 5-20, or to 0.5 – 17 ka BP. Based on this assumption the occurrence of crustal earthquakes would shift much closer towards historical times with respect to the human occupation of this part of SA.

## 5.2 Fault-Slip Data Analysis

The paleokinematic analysis largely confirms the results derived from the remote sensing studies and the macroscopic findings along numerous fault planes. Since fault-slip data at individual outcrops do not necessarily represent the regional deformation pattern [Marrett and Allmendinger 1990; Twiss and Unruh 1998], a full coverage of the study area with observation sites and the collection of statistically relevant amounts of fault-slip data were aspired in order to compensate for these limitations. The principal strain directions inferred from the fault-slip data analysis show predominantly E-W to NE-SW extension (T) and N-S to NW-SE shortening (P). In addition to this, the most striking examples for intraplate faulting (Figs. 4.2-4.6) found along the PAF, show left-lateral strike-slip deformation. These findings contrast the overall plate tectonic situation in a way that crustal shortening occurs perpendicular to the NNW-SSE directed plate convergence, instead of parallel to it. These observations are confirmed by previous authors who studied neotectonics along the Chilean coasts (Fig. 2.3; [Armijo and Thiele 1990; Delouis et al. 1998; Lavenu and Cembrano 1999; Marquardt and Lavenu 1999]). A coexistence of margin normal extension and margin parallel shortening is also well known from the Cascadia and Nankai subduction zones [Wang 2000]. Here, the *stress-strain paradox* between the maximum compressive stresses (margin normal plate convergence) and the maximum compressive strain (margin parallel shortening) was inferred from P-T-axes distributions of recent crustal seismicity in the continental forearc.

Taking into account the obliquity of the plate convergence, a dextral strike-slip regime has to be expected for N-S striking faults in the continental forearc [Yu et al. 1993]. Based on modeling results [Chemenda et al. 2000], this holds true for the case that the forearc is subject to long-term compression. However, as observed for the study area, the forearc is predominantly under extension

and consequently exhibits left-lateral deformation along N-S striking faults instead of dextral strike slip. On the basis of geodetic triangulation data, Plafker and Savage [1970] also showed that coseismic and postseismic deformations associated with the 1960 Valdivia earthquake cause sinistral strike slip and E-W extension along N-S striking intraplate faults. The youngest deformation in the study area is defined as brittle faulting located within the Mid-Miocene to Plio-Pleistocene sedimentary record of the Cenozoic Basin. Looking at the distribution of P- and T-axes of the youngest normal faulting events (Fig. 4.13), a relatively tight clustering of the P-axes and a fanning-out for the T-axes can be observed. This is usually associated with *radial extension* [Meschede 1994] and commonly termed as gravitational collapse. However, assuming that the active uplift of the Coastal Cordillera is produced by a lag faulting process as stated above, this would also cause the  $\sigma_1$ -axes to be oriented vertically. This setting would reveal a similar type of stereogram, with the P-axes vertical and the T-axes horizontal, as obtained for the case of true gravitational collapse. Based on the assumption that differential uplift rather than gravitational collapse is the driving force for intraplate faulting, the P-T-axes distribution most likely represents the effects of forearc *extrusion* due to the collision of the subducting slab with the continent.

Along the northern segment of the PAF several offset drainages clearly indicate left-lateral strike slip. Spatially, these offsets are closely connected to the occurrence of outstanding outcrops showing dip-slip faulting (Fig. 4.5) along this segment of the PAF. From a geomorphological point of view, the horizontal displacements seem to postdate the vertical offsets in this part of the study area. The strike-slip deformation reveals P-axes striking roughly perpendicular to the plate convergence direction. Plotting these together with the P-axes distribution for the normal faulting events, which itself is slightly elongated in NNW-SSE (Fig. 4.13) direction, the total of all P-axes could be considered to be lying on a NW-SE trending great circle, while the associated T-axes predominantly fall into the NE and SW quadrants. This suggests that both, dip slip and strike slip along the fault planes can be attributed to a single stress regime causing *transtensional* deformation. A transtensional regime is supported by the fact that even the youngest fault planes, truncating Plio-Pleistocene sediments, exhibit two sets of cross-cutting kinematic indicators – oblique dip slip and strike-slip lineations (Fig. 4.13). Since the age of the sediments does not allow for faulting ages older than 2 – 3 Ma, major changes within the plate convergent setting have to be excluded as the driving mechanism for changes in the deformation regime. Neither the *convergence rate* nor the *convergence obliquity* underwent significant changes during the last 5 Ma [Fig. 2.1 Somoza 1998]. Instead, recent crustal seismicity from Nankai and Cascadia [Wang 2000] shows that the coexistence of dip-slip and strike-slip faulting is quite common in the continental forearc of an active plate margin. At Nankai and Cascadia the occurrence of thrust and strike-slip events in the forearc is explained by changes of the margin normal stresses due to an increase of locking in the subduction interface shortly before and after large interplate earthquakes [Wang 2000]. The change of one component of the reduced stress tensor may cause a swap of its principal axes, thus initiating a different deformation regime. The switching between deformation regimes in conjunction with the seismic cycle of the subduction zone could be the reason for a transtensional deformation pattern to be developed in the study area.

In general fault-slip data taken at the near surface in relatively young sediments may not represent the deformation regime at depth. Therefore not only outcrops within the Cenozoic sedimentary record were studied, but also shear planes, cleavages and joints within the basement rocks of the Coastal Cordillera (Fig. 4.13). Here, similar P-T-axes distributions were obtained as compared to the results derived from fault-slip data analysis in the Cenozoic Basin. On shear planes and cleavages within the basement rocks fibre growth commonly served as kinematic indicator for dip-slip normal faulting. Fibre growth itself occurs at greater depth where abundant fluids and crack sealing mechanisms under higher temperature and pressure conditions are active [Meschede 1994]. Since the same extensional deformation regime as shown for the Plio-Pleistocene sedimentary cover can be resolved from these fault planes it is most likely that both groups of fault-slip data (A & C in Tab. 3.1) reflect the type of brittle deformation that governs the continental forearc at depth as much as at the surface. This interpretation is supported by the observation that fresh fault gouges in sedimentary deposits parallel shear planes and cleavages in basement rocks where both are juxtaposed to one another in the same outcrop.

While the fault planes within the sedimentary cover usually do not show more than two different types of lineations, the cleavages and shear planes within the basement rocks exhibit up to four cross-cutting slickenside kinematic indicators. This shows that the study area has experienced multiple deformation, including reverse faulting throughout its geological history. In the southwestern corner of the study area evidence for reverse faulting and folding of basement rocks is observed [Irwin et al. 1988]. These deformations took place during Upper-Jurassic to Lower Cretaceous times and prove that the study area once has been subject to the full compressive stresses exerted by the plate convergence. The intrusion of alkaline - sub-alkaline dikes (Fig. 2.5) during this period [Irwin 1989] indicates that the study area might have been located within an *intraarc* or *backarc* extensional environment [Allen 1986], far away from the present day coastline. This implies that the study area must have shifted from a position much farther inland from the coast towards its present location in the forearc. This shift of the position relative to the trenchline would agree with modern concepts of tectonic erosion and eastward trench migration in the order of  $1 - 2 \text{ km Ma}^{-1}$  with respect to the SA continent [von Huene et al. 1999]. This concept is generally supported by the observation of reverse faulting indicators on older rock surfaces. These indicators are usually rotated which shows that they predate the normal and strike-slip deformation which are commonly found on the same surfaces. However, the proposal of a constant trenchward migration and erosion of the continent stated above is contrasted by Hervé [1974] and Forsythe [1982] who consider the coastal region of Central Chile a *Paleozoic forearc province*. This interpretation is based on the occurrence of Late Paleozoic blueschist containing mélanges and high grade metamorphic rocks along the coast of Central Chile [Irwin et al. 1988] and implies that the forearc remained stable for hundreds of millions of years. Ramos [1988] however, concluded that due to an important period of continental accretion the Paleozoic subduction zone between  $30^\circ - 33^\circ \text{ S}$  shifted westward over a distance of  $\sim 300 \text{ km}$ .

### 5.3 Intraplate Fault Geometries and Plio-Pleistocene Strain Rates

The E-W extension in the continental forearc was quantified using three different approaches, a *neotectonic-geomorphologic* analysis based on field evidence in conjunction with a DEM of the study area (Figs. 4.18-4.20), the *balancing of crustal profiles* (Fig. 4.21), and *elastic dislocation modeling* (Figs. 4.22-4.23). The neotectonic-geomorphologic analysis is based on the assumption that over-steepened hillslopes, as inferred from the topographic profiles P1-P3 in Fig. 4.20, represent exhumed fault planes. This rather simplistic approach reveals vertical offsets comparable to those observed by previous authors in the field (Fig. 4.19). Free faces in the topography without any indication for faulting from remote sensing data or field studies were not considered here. Subsurface information about the depth of the basement (Fig. 2.4) were included to profiles P1 and P2. For profile P3 no subsurface information is available. Profile P3 however shows the highest number of intraplate faults and a strong fragmentation of the Great Plain into several horst and graben structures. The higher density of intraplate faults and a local drainage pattern (Fig. 4.17) showing radial confluence, suggest higher amounts of vertical offsets and the formation of a depression at depth along this part of the range-front fault (PAF). This is supported by the results derived from dislocation modeling, which indicate that increasing amounts of dip slip are required from north (P1) to south (P3) in order to sufficiently reproduce the topography of the DEM.

Elastic dislocation modeling of profiles P1-P3 shows that model faults of  $\sim 10$  km depth range have to be assumed in order to reproduce the observed topographies and the basement geometry in P1. These results were obtained without taking into account viscoelastic relaxation effects of the crust. However, King et al. [1988] show that flexural rigidities or the apparent elastic thicknesses of the crust provide the main control on the width of geological structures. Effective elastic thicknesses of 2 – 4 km are sufficient to produce structures of 22 – 30 km wavelength, respectively. An effective elastic thicknesses of 8 km, i.e. would require a structural wavelength of 65 km, which is truly not the case for the study area. The Coastal Cordillera and the Cenozoic Basin together exhibit a wavelength of  $\sim 25$  km, indicating a very small effective elastic thickness in the order of 2 km.

The loading due to erosion and deposition of sediment determines the ratio of uplift and subsidence between the two sides of the fault [King et al. 1988]. Erosion would create an asymmetric structure, with the hanging wall side showing much greater subsidence than uplift could be observed on the footwall side. However, the relatively well-balanced symmetry between subsidence ( $\sim -600$  m) and uplift ( $\sim +400$  m) in the study area, as inferred from the geophysical record [Meinardus 1961; Rocroi 1964] and the DEM respectively (Fig. 4.22), shows that erosion can also be neglected as a major factor for the formation of the Basin and Range structure. In turn, assuming that the Coastal Cordillera suffered higher erosion rates than the ones known from the climatic evolution of the study area (Tab. 2.3), significantly deeper rooted intraplate faults would have to be introduced to the model. As shown in Fig. 4.22 B, a 20 km deep normal fault produces a dislocation curve that overestimates the topographic profile, which in turn could be used to model the missing volume between the initial and the weathered topography.

Balancing of a basement cross-section (Fig. 4.21) through the northern part of the study area shows that the required fault geometry reaches down to 7.0 – 17.5 km depth for shear angles of  $75^\circ$ . Applying a vertical shear angle instead, produces detachment horizons between 11.0 – 24.5 km

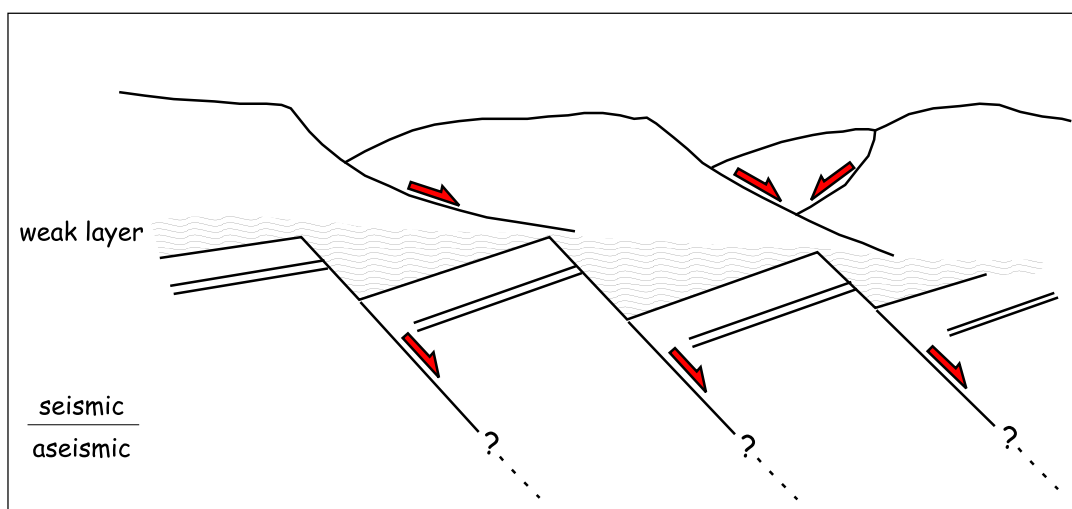


Figure 5.1: Schematic cross-section showing how a lithological weak layer (e.g. overpressured shale or salt) may allow the extension in the sedimentary cover to be decoupled from the fault-bounded tilted blocks in the basement below; adopted from Jackson and White [1989].

depth, which would fall in place with the lower-bound depth range commonly associated with crustal faults. However, since a  $75^\circ$  shear angle is supported by the abundance of  $65\text{--}80^\circ$  W-dipping antithetic fault planes within the Cenozoic Basin, detachment depths of  $7.0 - 17.5$  km are to be preferred. The balancing of crustal profiles as performed in this study leaves room for two sources of error, the accuracy to which the depth of the TOB was determined from reflection seismic data [Meinardus 1961; Rocroi 1964], and the fact that the actual line of tectonic transport is slightly out of the E-W plane used for construction and restoration. For the latter source of error no major discrepancies ( $>15\%$ ) are to be expected, as long as the deviation from the line of tectonic transport does not exceed  $30^\circ$  [Price 1981; Woodward et al. 1989]. Since this is truly not the case in the study area, where the direction of tectonic transport (see average dip of the fault plane in Fig. 4.11) deviates only  $10^\circ\text{--}15^\circ$  from the E-W plane used for the balanced profile, the error arising from the obliquity factor can be neglected here. Considering the error coming along with the depth migration of the reflection seismic data, it has to be assumed that the authors [Meinardus 1961; Rocroi 1964], thanks to the excellent outcrop conditions in the study area, were capable to determine a velocity model within an accuracy of  $\pm 0.2$  km/s. This would leave a maximum vertical error of  $80 - 90$  m or less than 30% deviation from the approximated depth of the TOB at around 600 m. In addition to this, it has been observed that tilted marine terraces along the northern segment of the PAF, dipping  $30^\circ$  towards the west, come to rest in a subhorizontal position at a distance of about 1.5 km perpendicular to the fault trace. Applying simple trigonometric laws and assuming an average dip angle of  $20^\circ$  holding true for the full wavelength, a vertical offset of  $\sim 550$  m is to be expected along the fault, which corresponds well with the TOB depth predicted by reflection seismic data.

In contrast to this, the rollover structures that characterize the surface of the Cenozoic Basin in the vicinity of the range-front fault would usually indicate a listric fault geometry with a detachment horizon at  $3 - 4$  km depth for a shear angle of  $75^\circ$ . This result was derived from crustal balancing on Mejillones Peninsula [Pelz 2000], where stratigraphically equivalent marine deposits [Martinez 1979;

	<b>Neotectonic Profiles</b>	<b>Balanced Cross-Sections</b>	<b>Elastic Half- Space Modeling</b>	<b>GPS-Residuals Velocities</b>
Strain [%]	0.6-1.9	1.0-3.3	1.4-1.7	–
Strain rate [ $\mu strain a^{-1}$ ]	0.001-0.016	0.002-0.028	0.002-0.015	0.038 $\pm$ 0.018

Table 5.1: E-W strain rates approximated using geologic (Neotectonic profiles, Balanced cross-sections) and geodetic (Elastic half-space modeling, GPS-residual velocities) techniques.

Martinez and Perez 1980] and near identical tectonic settings as in the study area prevail. Hence, similar fault geometries are to be expected for the rollover structures in the Altos de Talinay region, which contrasts the above stated results obtained from crustal balancing. In turn, shallow crustal depths like these do not allow for the generation of intraplate earthquakes [Maggi et al. 2000], which according to the field investigations frequently occurred in the study area. This contradiction can only be solved by a mechanical decoupling between a lithologically weak layer (e.g. overpressured shale or salt) at the base of the Cenozoic Basin from the underlying basement rocks [Fig. 5.1 Jackson and White 1989].

The amount of E-W extension in the forearc, as inferred from neotectonic profiles, crustal balancing and elastic dislocation modeling ranges between 0.6-3.3% for Plio-Pleistocene times (Tab. 5.1). All three approaches focus on the E-W extension, neglecting the obliqueness of the dip-slip component as much as the N-S displacements, both of which are relatively small and therefore only interpretable in a qualitative manner. Strains derived from elastic dislocation modeling were calculated by relating the modeled E-W displacement of the end points of the 25 km long baseline to its initial length. Therefore the modeling results do not represent infinitesimal strains, but line-length changes due to horizontal displacements and thus provide a proper means to further constrain the geologically derived deformation. For the 25 km wide forearc, strain rates resolving from all three approaches vary between 0.001 – 0.028  $\mu strain a^{-1}$  (Tab. 5.1). The wide range between minimum and maximum strain rates mainly refers to the weakly constrained timing of the deformation in the forearc (1.2 – 6.5 Ma). To set further constraints on this issue, future investigations involving absolute dating techniques are required.

In order to compare the geologic and modeled E-W strain rates with those derived from the GPS residual velocity field, the differential motion between the coastal and the precordilleran blocks (Fig. 4.28) has to be calculated. Relating the E-W component of the differential motion as shown in Chapter 4.6 ( $7.6 \pm 3.6 mm a^{-1}$ ) to the roughly 200 km long baseline between the stations, reveals an E-W strain rate of ( $0.038 \pm 0.018 \mu strain a^{-1}$ ). Due to the mode of calculation, the obtained strain rates do not reflect infinitesimal strains, and thus can be compared to those derived by the geologic and modeling approaches. The comparison shows that the geodetic strain rates tend to exceed the mean geologic/modeled strain rates by a factor of 1.5-3. A possible cause for this discrepancy could be related to the fact that the residual velocities still reflect a certain amount of elastic deformation [Liu et al. 2000], which has not been accounted for by the AEDM yet [Khazaradze et al. 1999], as shown in the following paragraph. A more common assumption is that the geological record is incomplete and thereby underestimates the amount of deformation.

The residual velocities are calculated subtracting the modeled GPS vectors from the observed displacement vectors. The resolving residual field is thought to represent the intraplate deformation, because of the elastic part of the deformation having been subtracted by the model velocities. The AEDM itself only is an approximation of the real plate interface and therefore bears a significant source of error. However, the fact that the model already reflects the upper limits of the relatively well known geometry of the plate interface and accounts for 100% of the plate convergence rate, the residual velocity field represents a maximum approach. A smaller plate interface or the introduction of aseismic slip would increase the length of the residual vectors without changing much of their relative motions, thus revealing results almost similar as those discussed above within the relevant center of the investigation area. The introduction of a time-dependent rheology and a viscoelastic layer below the elastic layer is expected to alter the surface results to a certain degree [King et al. 1988 among others]. This has not been further investigated herein

Further potential for the overestimation of long-term strain rates inferred from GPS residual velocities is provided by coseismic and or postseismic deformations which have occurred shortly before or after the deployment of the network. However, only subduction earthquakes of magnitudes  $M_s > 7$  are capable to produce detectable variations in the GPS displacement field. In addition to this, even larger events like the 1995 Antofagasta  $M_w$ 8.2 earthquake, do not influence the displacement vectors for more than 2-3 years [Khazaradze and Klotz 2002]. For the immediate study area no major underthrust events ( $M_s > 7$ ) were recorded during the last 50 years. Based on this fact, the GPS data obtained for this stretch of the forearc are considered to be free of coseismic and/or postseismic effects and therefore most likely represent purely *interseismic deformation*, unlike it is the case for southern Chile, where up to the present date deformations associated with the very large ( $M_L > 9$ ) 1960 Valdivia earthquake influence the space geodetic observations [Khazaradze and Klotz 2002].

## Interactions of Interplate and Intraplate Deformation

Forearc deformation due to large subduction earthquakes has been studied using a simplified dislocation model for the subduction interface as inferred from the AEDM ([Khazaradze et al. 1999]). Modeling the surface deformation due to the 1943 Illapel  $M_w$ 8.2 earthquake, the last significant interplate event in this segment of the Nazca-SA plate boundary, resolves a coseismic displacement field which nicely coincides with the results obtained from the fault-slip data analysis. Both approaches not only show that extension is the predominant type of forearc deformation but also reveal almost identical azimuths for the orientation of the principal strain axes. This is supported by a resurvey of the GPS network in Northern Chile a few months after the 1995 Antofagasta  $M_w$ 8.2 earthquake, which revealed displacement vectors [Klotz et al. 1999] almost identical to those inferred from dislocation modeling [Delouis et al. 1998]. Together, this allows the interpretation that intraplate faulting is, within certain limits, controlled by deformation processes in the plate interface.

Dislocation modeling of large interplate events also shows significant amounts of coseismic uplift (30 – 40 cm) of the onshore forearc. Coseismic uplift is a well known phenomenon along the Chilean plate margin and has already been observed as early as the middle of the 19<sup>th</sup> century [Darwin 1846]. Since then, various techniques have been applied to quantify coastal uplift associated with subduction

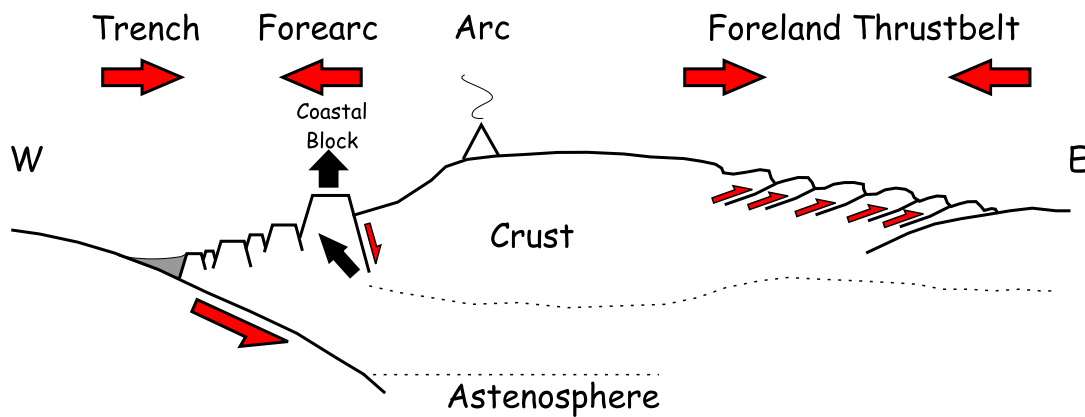


Figure 5.2: Schematic cross-section showing possible interaction between updip translation of the continental forearc, uplift of the coastal block, and normal faulting along predominantly E-dipping faults on the eastern range front of the Coastal Cordillera; modified after Dewey and Lamb [1992].

earthquakes [e.g. Ortlieb et al. 1996a], which coincide well with the amount of uplift predicted by dislocation modeling. However, significant uplift seems to be restricted to coastal areas that protrude westward from the present-day coastline, as was shown for both the 1995 Antofagasta and the 1960 Valdivia earthquakes. During these events, uplift was predominantly observed on the Mejillones and Arauco peninsulas, respectively [Delouis et al. 1998], whereas most of the coastal areas adjacent to the peninsulas remained relatively stable or underwent up to 2 m of subsidence as was the case during the 1960 Valdivia event [Plafker and Savage 1970]. This is due to the fact that for both earthquakes the hinge line between uplift and subsidence in the dislocation field matches the trace of the coastlines, leaving only westward-protruding coastal areas within the zone of coseismic uplift. For the study area, an almost identical vertical displacement field is suggested, with the Talinay peninsula being exposed to significant coseismic uplift while the coastlines to the north and south largely coincide with the hinge line between uplift and subsidence. In addition, significant interaction of interplate and intraplate deformation is suggested by the observation that a lateral correlation between the downdip edge of the subduction zone and the coastline exists in the entire circum-Pacific region.

Despite the fact that elastic dislocation theory seems to be applicable to model coseismic coastal uplift phenomena, it simply describes the exact reversal of stresses and strains which have accumulated due to interseismic loading processes prior to subduction earthquakes (Fig. 3.4). This means that elastic rebound alone cannot explain permanent uplift as observed along the coast of the study area and structurally similar regions (e.g. Mejillones, Caldera, Arauco). However, if the elastic rebound is related to *updip translation* [Dewey and Lamb 1992] along the plate interface due to shortening of the distance between the SA continent and the trench, a sustained uplift of the forearc block and normal faulting along its eastern border can be achieved (Fig. 5.2). Updip translation as a driving mechanism for the rapid uplift in the forearc is strongly supported by 3D density modeling of the Central Andean gravity field, which reveals an overall *mass surplus* (relatively high densities in the upper lithosphere; crust  $\rho = 2.7 \text{ Mg m}^{-3}$ , mantle  $\rho = 3.3 \text{ Mg m}^{-3}$ ) along the Coastal Cordillera with respect to normal isostatic conditions [Kirchner et al. 1996]. Assuming  $10 \text{ mm a}^{-1}$  of shortening and taking partial isostatic compensation into account, Dewey [1992] calculates an uplift rate of

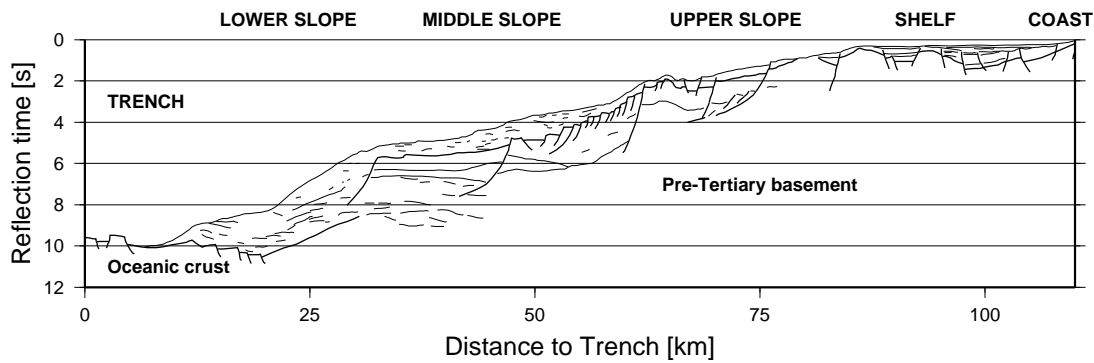


Figure 5.3: Structural interpretation of E-W seismic profile (CINCA Experiment) showing the Nazca-SA plate boundary from the trench to the coastline at 21° S latitude [Pelz 2000]. Heavy lines - Fault blocks, Thin lines - Sedimentary structure.

$1 \text{ m ka}^{-1}$  for a  $20^\circ$  dipping plate interface. Considering the long-term continental slope retreat rate of  $1 - 2 \text{ km Ma}^{-1}$  presented by von Huene et al. [1999], and using a purely geometric approach, similar uplift rates ( $0.25 - 0.95 \text{ m ka}^{-1}$ ) would result for the study area with its  $15\text{-}25^\circ$  dipping plate interface. In turn, these uplift rates coincide well with those stated by numerous authors [Radtko 1987; Leonard et al. 1988; Hsu et al. 1989; Leonard and Wehmler 1992; Nelson and Manley 1992; Ota and Paskoff 1993; Leonard et al. 1994; Ota et al. 1995] who studied the emergence of marine terraces along the Chilean coasts, applying different dating techniques such as Radiocarbon, Aminostratigraphy, and Electron Spin Resonance.

Updip translation as the controlling process for uplift along the coast agrees well with the results from neotectonic field studies and the fault-slip data analysis, both of which suggest that the forearc is actively uplifted and extruded. This assumption is based on the observation that the apparent normal faulting pattern on the landward side of the Coastal Cordillera is most likely to be caused by *differential uplift* along the PAF. Differential uplift between the Coastal Cordillera and the Cenozoic Basin has to be assumed because both blocks are currently emerging. This phenomenon has been observed by means of lateral terrace correlations in the study area [Ota et al. 1995] and on Mejillones peninsula (Gonzalez 2002, pers. comm.). Due to updip translation of the forearc block and simultaneous tectonic erosion at its base the continental slope constantly oversteepens, forming a *critical taper* geometry [Davis et al. 1983; Dahlen et al. 1984]. A critical taper geometry infers destabilization of the continental slope and extension in the forearc wedge. Indeed, the offshore forearc of Northern and southern Chile is predominantly under extension, due to which the middle slope of the offshore forearc is partitioned into basement blocks separated by shallow listric normal faults as shown from seismic records near Antofagasta (Fig. 5.3). The listric, shallowly rooted geometry of the normal faults in the lower slope suggests that extension in this part is largely controlled by gravitational forces. Thrust planes are virtually absent within the continental slope, and only occur superficially in trench-fill sediments off Southern Chile, e.g.  $36^\circ - 40^\circ \text{ S}$  (Reichert 2002, pers. comm.).

In order to quantify the amount of deformation exerted on the continental forearc during large subduction earthquakes, 339 historical and teleseismically recorded earthquakes of magnitudes  $M_s > 5$  were applied to a dislocation model. Based on this model the strain redistribution along intraplate normal faults was approximated. For the study area, the maximum E-W extensional strains are centered

over the observed intraplate fault (Fig. 4.27), whereas north of 30° S the zero trace of the E-W strains roughly falls in place with the coastline and therefore probably with the downdip edge of the plate interface [Ruff and Tichelaar 1996]. Since the strain rates are averaged over 350 years they can be considered to represent the long-term deformation caused by the interplate-intraplate interaction. If this is the case, it appears that all coastal areas with a maximum distance to the trench of 70 – 80 km, experience long-lasting extension and uplift. In the long run the straining of these westward-protruding segments of the forearc will cause their collapse until the regular distance (100 – 110 km) between the trench and the coastline is restored. Once the distance between the trench and the coast is set back to its regular range, it seems that little or no E-W straining occurs, leaving the coastline in a relatively stable position.

The resolving moment rates along intraplate normal faults range in the order of  $M_w$ 4.2-4.7 which roughly corresponds to the average size and recurrence of crustal seismicity in the study area inferred from seismic catalogues of the last decade [NEIC 2001]. The focal mechanisms that can be inferred from the strain tensors rotated into the model fault planes largely correspond to the fault-plane solutions obtained from the paleokinematic analysis (Fig. 4.13). The prediction of normal and/or left-lateral strike-slip faulting events in the overriding plate as inferred from modeling results and field investigations is strongly supported by observations of crustal seismicity in the continental forearc near Antofagasta (23.60° S; Fig. 2.3) and Copiapó (27.35° S) [Comte et al. 1992; Comte et al. 2002]. Focal mechanisms of crustal seismicity in these areas reveal predominantly normal faulting along N-S striking and E-dipping fault planes. In addition, eyewitness accounts from the 1995 Antofagasta interplate event state that intraplate normal faulting occurred along the Salar del Carmen fault, ~ 20 km east of Antofagasta (Gonzalez, 2002 pers. comm.).

## 5.4 Recurrence Times for Significant Intraplate Earthquakes

The potential for intraplate earthquakes is of great importance for the hazard assessment along the Chilean coast. Due to their shallow focal depth, even moderate size earthquakes ( $M_L$ 5.0-5.9) are capable of causing severe damage to housing and property. In contrast to this, large subduction earthquakes like the 1995 Antofagasta  $M_w$ 8.2 event do not necessarily cause significant destruction within the overriding plate. The most damaging earthquake in south Central Chile during the 20<sup>th</sup> century, the 1939 Chillan  $M_s$ 7.8 event, which caused 28 000 deaths was caused by intraplate normal faulting, either in the subducting slab or within the continental crust [Beck et al. 1998]. Though Beck et al. [1998] favor a hypocenter location at 80 – 100 km, their results do also suggest a possible rupture plane at 10 km depth. The long duration of this event, the unclear first arrivals of P-waves, and the large extend of the area which suffered intensities of MMI = 9 (Fig. 2.3) suggest shallow crustal depths for the hypocenter location rather than a position at greater depth within the subducting plate. In addition to this, the strike (N320°-350° E), the dip angle (60°-80°) and the dip azimuth (N90°-130° E) of the focal plane coincide well with the fault-plane geometries as inferred from fault-slip data analysis and dislocation modeling between 30°-31° S. Present-day recordings of crustal seismicity also support the existence of intraplate normal faulting [Comte et al. 1992; Comte et al. 2002].

For the study area, the approximation of recurrence times of intraplate earthquakes relies on two major results, the detailed study of Plio-Pleistocene displacements and fault geometries, and

the geodetic strain rates. Using geodetic data for the approximation of recurrence times requires the assumption that the inferred strain rates are conserved along intraplate faults, such that strain accumulates linearly along their planes with time. For this study we assumed that the full strain rate is accommodated along one intraplate fault plane with a geometry corresponding to field evidence and modeling results. For the reason that significant amounts of elastic deformation haven't been accounted for yet, the GPS derived residual velocities might overestimate the long-term strain rates in the study area. Taking into account a reduction of the strain rate to 1/10th of its size, would result in ten times higher recurrence intervals. Consequently, the recurrence times within the study area for characteristic earthquakes ( $M_w 7$ ) would increase from 500 – 1500 years to 5000 – 15000 years. Despite this increase of the recurrence interval, significant intraplate faulting would still have to be considered active during Late-Quaternary times, thus leaving a high potential for intraplate faulting up to the present date. This interpretation is strongly supported by numerous field evidence from faulted Plio-Pleistocene sediments and the results from diffusion equation modeling.

Previous authors considered the range-front fault (PAF) to be active until Late Pliocene - Early Pleistocene times and attribute later changes in elevation of the Coastal Cordillera and the Cenozoic Basin to regional updoming [Ota et al. 1995]. The fact that colluvial wedges along the trace of the PAF are already eroded and partly overlain by unfaulted Quaternary alluvial fans supports this interpretation. However, a few kilometers east of the range front, the Cenozoic Basin is strongly affected by recent intraplate faulting, with numerous faults-scarps and landslides forming the landscape. This indicates that deformation is still active but that the actual deformation front probably moved further inland from the coast. The present-day deformation front seems to be centered over the down-dip edge of the plate interface (Fig. 4.25). Thus its present location is much closer to highly populated areas like the city of Ovalle than during the geologic past. This is supported by the epicenter location of the 1997 Punitaqui  $M_w 7.1$  *intraslab* event [Pardo et al. 2002] which occurred 40 – 45 km inland from the coast. Despite its focal depth (68 km) the earthquake caused severe damage to the cities of Punitaqui and Ovalle.

## 5.5 Implications for the Nazca-SA Plate Boundary

The applicability of the results towards the SA plate convergent margin as a whole, as discussed in the preceding sections of this thesis, is suggested by the observation that the study area by no means represents an exceptional case with respect to forearc deformation, but fits well within a row of structurally and geomorphologically similar regions found along the Chilean coast, i.e. Mejillones, Caldera and Arauco peninsulas. The most obvious similarities between all peninsulas refer to geomorphological aspects, such as the presence of broad abrasion platforms deeply cut into the basement rocks of the Coastal Cordillera, and the shape of the coastline, showing forms of *lee erosion*, thus indicating an exposition of these areas towards the open sea. The seaward protruding nature of these coastal stretches puts them closer towards the trench. In turn, the closer the forearc moves towards the trench the more likely updip translation along the plate interface comes into play (Fig. 5.2).

The structural content of the study area, with the Cenozoic Basin on the eastern side of the Coastal Cordillera being truncated by prominent N-S striking, E-dipping normal faults, is very similar to its

northern [Mejillones and Caldera: Armijo et al. 1993; Delouis et al. 1998; Marquardt and Lavenu 1999; Marquardt et al. 1999; Marquardt 2000] and southern [Arauco: Lavenu and Cembrano 1999] analogies. Additionally, the Cenozoic Basins of all four peninsulas exhibit almost identical stratigraphic records, which can be correlated on the basis of foraminiferous and diatomitic deposits of Mid-Miocene age [Martinez 1979; Martinez and Perez 1980]. Martinez [1980] even correlates diatomites from the Pisco and Zapayal formations in Peru with those exposed in the study area. On Arauco peninsula subbituminous coals of Eocene-Miocene age from Lebu [Concepción-Arauco basin: Helle et al. 2000] provide further evidence for the presence of a Cenozoic Basin east of the Coastal Cordillera. Finally, Mejillones peninsula (Gonzalez, 2002 pers. comm.) and the study area [Ota and Paskoff 1993] both have in common that at the same time the Coastal Cordillera and the Cenozoic Basin are uplifting, but with different velocities, suggesting that this rather uncommon situation is more frequently to be found along the Chilean coasts. In addition to this, the offshore forearc of northern [von Huene et al. 1999; Pelz 2000; von Huene and Ranero 2002] and southern (Reichert, 2002 pers. comm.) Chile exhibits the same extensional deformation pattern with horst and graben structures between its upper and middle slope as observed for the aforementioned peninsulas. This suggests that the considered peninsulas merely represent onshore relics of a forearc, which has elsewhere already collapsed due to basal erosion at its lower slope and the effects of repeated seismic loading and unloading processes along the Nazca-SA plate interface.

The consistency of the geomorphological, structural and stratigraphical aspects of Mejillones, Caldera, Talinay, and Arauco peninsulas, which are hundreds of kilometers apart from each other, suggests that all of them are subject to identical deformation processes associated with the plate convergence as a whole. Selective processes like the subduction of aseismic ridges [Machare and Ortlieb 1992; Hartley and Jolley 1995] or the underplating of large amounts of sediments are unlikely to be responsible for the uplift of all four considered regions. Aseismic ridge subduction is currently acting on none of the Chilean areas under consideration and can at present only be associated with the uplift of the Ica peninsula in southern Peru, where the Nazca Ridge subducts beneath the SA continent [Machare and Ortlieb 1992]. Between 30°-31° S, the subduction of the aseismic Juan-Fernandez-Ridge occurred during 5 – 7 Ma BP [Yanez et al. 2001] and therefore cannot be made responsible for most of the deformations in the study area which clearly postdate this process. Tectonic underplating of thick sedimentary packages is unlikely to happen in areas of no or limited trench fill, thus, apart from Arauco the uplift of Mejillones, Caldera and Talinay peninsulas cannot be explained by this model, because of the general absence of sediments in the trench. In turn, updip translation of the forearc along the plate interface, pinpointed as shortening of the distance between the trench and the coastline, provides an overall active process along the SA plate margin, and reveals uplift rates for the forearc that are consistent with uplift rates inferred from fossil records of marine terraces. Updip translation as a possible mechanism for the uplift of the continental forearc is strongly supported by the fact that the Chilean Coastal Cordillera north of 39°S exhibits a mass surplus with respect to normal isostatic conditions [Kirchner et al. 1996].

## 6 Conclusions

The structural characteristics of the continental forearc between 30°-31° S and its potential to represent the forearc deformation along the SA plate convergent margin as a whole can be comprised as follows:

- Since Plio-Pleistocene times, the forearc between 30°-31° S is dissected by numerous N-S to NNW-SSE striking, predominantly 65-80° E-dipping intraplate normal faults of up to 60 km length.
- The fault-slip data analysis indicates that, in contrast to the overall plate-convergent setting, the continental forearc is dominated by E-W to NE-SW extension (trench-normal), and to a limited extent, by N-S to NW-SE contraction (trench-parallel).
- Long-term geologic deformation rates derived from the analysis of neotectonic cross-sections, the balancing of crustal profiles, and the elastic half-space modeling of intraplate normal faults all show that the continental forearc underwent 0.6-3.3% E-W extension during Plio-Pleistocene times, revealing E-W strain rates of  $0.001 - 0.028 \mu \text{ strain a}^{-1}$ .
- The orientations of the maximum extension and the maximum shortening directions, as inferred from GPS-residual velocities, convincingly match the principal strain directions inferred from the fault-slip data analysis. The geodetic E-W strain rates ( $0.038 \pm 0.018 \mu \text{ strain a}^{-1}$ ) exceed the mean geologic deformation rates by a factor of 1.5-3.
- It is apparent from paleoseismological observations and elastic dislocation modeling of topographic cross-sections that extension in the forearc is generally associated with seismogenic ruptures along prominent, deeply rooted (10 – 20 km) intraplate normal faults. The inferred intraplate fault dimensions and observed offsets suggest that characteristic intraplate earthquakes with magnitudes as large as  $M_w=7$  have occurred in the recent geologic past.
- Based on complementary information deduced from geologic, geodetic, and modeling results, intraplate faulting has to be considered active up to the present, leaving a high potential for the occurrence of large intraplate earthquakes in the near future.
- Elastic dislocation modeling of large subduction earthquakes shows that the tectonic setting of the continental forearc is strongly influenced by deformation processes within the plate interface, depending on the position of the coastline with respect to the trench.

- 
- Evidence for thrusting and folding of Paleozoic and Mesozoic rocks, as documented by previous authors, and the current position of the intraplate deformation front at about 40 – 50 km inland from the coast, as inferred from topographic signals, suggest that the present forearc has shifted through time from an intraarc/backarc environment into its present location and will in the future be consumed by the subduction process.
  - The shift of the deformation front is accompanied by extrusion and differential uplift of the forearc block. Extrusion itself is produced by updip translation of the continental forearc along the plate interface.
  - The correlation of specific coastal morphologies and tectonic settings with significantly uplifted marine terraces and abrasion platforms requires the existence of an overall deformation mechanism independent from topographic features within the subducting slab (aseismic ridges) or from the thickness of the trench fill. Updip translation of the forearc in association with tectonic erosion at the base of the forearc wedge not only provides an independent deformation mechanism but also fits the concept of continental slope retreat followed by its gravitational collapse due to oversteepening.

## References

- Adam, J., and Kukowski, N., 1999, Erosive Mass Transfer at Convergent Margins; Constraints and Application of Coulomb Wedge Analysis to Fore-Arc Systems: European Union of Geosciences conference abstracts, v. 4, p. 611.
- Aki, K., and Richards, P. G., 1980, Quantitative Seismology; Theory and Methods: A Series of Books in Geology, v. 1: San Francisco, Calif., United States, W. H. Freeman and Company, 932 p.
- Allen, J. F., 1986, Geology of the Northern Colima and Zocoalco Grabens, Southwest Mexico: Bulletin of the Geological Society of America, v. 97, p. 473-485.
- Allmendinger, R. W., Figuero, D., Snyder, D., Beer, J., Mpodozis, C., and Isacks, B. L., 1990, Foreland Shortening and Crustal Balancing in the Andes at 30° S Latitude.: Tectonics, v. 9, p. 789-809.
- Anderson, E. M., 1951, The Dynamics of Faulting and Dyke Formation with Applications to Britain: Edinburgh, Oliver and Boyd, 260 p.
- Angelier, J., 1989, From Orientation to Magnitudes in Paleostress Determinations Using Fault Slip Data: Journal of Structural Geology, v. 11, p. 37-50.
- Angelier, J., 1994, Fault Slip Analysis and Paleostress Reconstruction, in Hancock, P. L., ed., Continental Deformation, Oxford, Pergamon Press, p. 53-100.
- Angermann, D., Klotz, J., Reigber, C., Reinking, J., and Wilson, P., 1996, Active Deformation Derived from Large Scale GPS Networks: Eos, Transactions, American Geophysical Union, v. 77, p. 144.
- Angermann, D., Baustert, G., Galas, R., and Zhu, S. Y., 1997, Epos.P.V3 (Earth Parameter & Orbit System) : Software User Manual for GPS Data Processing, Scientific Technical Report, STR97/14, Potsdam, Germany, GeoForschungsZentrum, 52 p.
- Angermann, D., Klotz, J., and Reigber, C., 1999, Space-Geodetic Estimation of the Nazca-South America Euler Vector: Earth and Planetary Science Letters, v. 171, p. 329-334.
- Armijo, R., and Thiele, R., 1990, Active Faulting in Northern Chile; Ramp Stacking and Lateral Decoupling Along a Subduction Plate Boundary?: Earth and Planetary Science Letters, v. 98, p. 40-61.
- Armijo, R., Ruegg, J. C., Briole, P., Lyon, C. H., Barrientos, S. E., Thiele, R., Banchero, L., and Arancibia, M., 1993, Crustal Deformations and Seismic Cycle in Northern Chile: Seismological Research Letters, v. 64, p. 24.
- Arrowsmith, J. R., 1995, Coupled Tectonic Deformation and Geomorphic Degradation Along the San Andreas Fault System: Unpub. Ph.D. Thesis, Stanford University, 346 p.
- Arrowsmith, J. R., Pollard, D. D., Hilley, G., and Rhodes, D. D., 1995, Morphologic Dating of Scarps Along the San Andreas Fault, Carrizo Plain, California, and Progressive Deformation Along the Big Bend: Eos, Transactions, American Geophysical Union, v. 76, p. 575.
- Arrowsmith, J. R., Pollard, D. D., and Rhodes, D. D., 1996, Hillslope Development in Areas of Active Tectonics: Journal of Geophysical Research, B, Solid Earth and Planets, v. 101, p. 6255-6275.

- Atwater, B. F., Jimenez, N. H., and Vita, F. C., 1992a, New Late Holocene Emergence Despite Earthquake-Induced Submergence, South-Central Chile: *Quaternary International*, v. 15-16, p. 77-85.
- Atwater, B. F., Nunez, H. J., and Vita-Finzi, C., 1992b, Net Late Holocene Emergence Despite Earthquake-Induced Submergence, South-Central Chile: *Quaternary International*, v. 15-16, p. 77-85.
- Barazangi, M., and Isacks, B. L., 1976, Spatial Distribution of Earthquakes and Subduction of the Nazca Plate beneath South America: *Geology*, v. 4, p. 686-692.
- Beck, S., Barrientos, S., Kausel, E., and Reyes, M., 1998, Source Characteristics of Historic Earthquakes Along the Central Chile Subduction Zone: *Journal of South American Earth Sciences*, v. 11, p. 115-129.
- Becker, A., and Gross, M. R., 1996, Mechanism for Joint Saturation in Mechanically Layered Rocks: An Example from the Southern Israel: *Tectonophysics*, v. 257, p. 223-237.
- Bohnhorst, T. H., 1967, *Geología De La Hoja Ovalle, Provincia De Coquimbo*: Instituto de Investigaciones Geológicas, Santiago, Chile, 63 p.
- Bott, M. H. P., 1959, The Mechanics of Oblique Slip Faulting: *Geological Magazine*, v. 96, p. 109-117.
- Brüggen, J., 1929, *Texto De Geología.: Primera Parte.:* Santiago, Imprenta "El Globo", 450 p.
- Brüggen, J., 1950, *Fundamentos De La Geología De Chile*: Santiago.
- Bucknam, R. C., and Anderson, R. E., 1979, Estimation of Fault-Scarp Ages from a Scarp-Height-Slopeangle Relationship: *Geology*, v. 7, p. 11-14.
- Bull, W. B., and McFadden, L. D., 1977, Tectonic Geomorphology, North and South of the Garlock Fault, California, in Doehring, D. O., ed., *Geomorphology in Arid Regions: Annular Binghampton Geomorphological Symposium*, London, Allen and Unwin, p. 115-138.
- Bull, W. B., 1984, Tectonic Geomorphology: *Journal of Geological Education*, v. 32, p. 310-324.
- Bull, W. B., 1987, Relative Rates of Long-Term Uplift of Mountain Fronts: *Proceedings of Conference XXXIX; directions in paleoseismology*, Open-File Report, U.S. Geological Survey, p. 192-202.
- Cahill, T., and Isacks, B. L., 1992, Seismicity and Shape of the Subducted Nazca Plate: *Journal of Geophysical Research*, v. 97, p. 17503-17529.
- Chemenda, A. I., Lallemand, S., and Bokun, A., 2000, Strain Partitioning and Interplate Friction in Oblique Subduction Zones: Constraints Provided by Experimental Modeling: *Journal of Geophysical Research*, v. 105, p. 5567-5581.
- Chinnery, M. A., 1961, The Deformation of the Ground around Surface Faults: *Bulletin of the Seismological Society of America*, v. 51, p. 355-372.
- Comte, D., Pardo, M., Dorbath, L., Dorbath, C., Haessler, H., Rivera, L., Cisternas, A., and Ponce, L., 1992, Crustal Seismicity and Subduction Morphology around Antofagasta, Chile; Preliminary Results from a Microearthquake Survey: *Tectonophysics*, v. 205, p. 13-22.
- Comte, D., Haessler, H., Dorbath, L., Pardo, M., Monfret, T., Lavenu, A., Pontoise, B., and Hello, Y., 2002, Seismicity and Stress Distribution in the Copiapó, Northern Chile Subduction Zone Using Combined on- and Off-Shore Seismic Observations: *Physics of the Earth and Planetary Interiors*, v. 132, p. 197-217.
- Creager, K. C., Ling Yun, C., Winchester, J. P., and Engdahl, E. R., 1995, Membrane Strain Rates in the Subducting Plate beneath South America: *Geophysical Research Letters*, v. 22, p. 2321-2324.
- Dahlen, F. A., Suppe, J., and Davis, D., 1984, Mechanics of Fold-and-Thrust Belts and Accretionary Wedges; Cohesive Coulomb Theory: *Journal of Geophysical Research. B.*, v. 89, p. 10.
- Dahlstrom, C. D. A., 1969, Balanced Cross Sections: *Canadian Journal of Earth Sciences*, v. 6, p. 743-757.

- Darwin, C., 1846, *Geological Observations on South America*: London, Smith Elder and Co., 279 p.
- Darwin, C., 1891, *Geological Observations on the Volcanic Islands and Parts of South America Visited During the Voyage of H.M.S. "Beagle"*: London, Smith, Elder, 648 p.
- Davis, D., Suppe, J., and Dahlen, F. A., 1983, *Mechanics of Fold-and-Thrust Belts and Accretionary Wedges*: JGR. *Journal of Geophysical Research*. B., v. 88, p. 1153-1172.
- Delouis, B., Philip, H., Dorbath, L., and Cisternas, A., 1998, *Recent Crustal Deformation in the Antofagasta Region (Northern Chile) and the Subduction Process*: *Geophysical Journal International*, v. 132, p. 302-338.
- Dewey, J. F., and Lamb, S. H., 1992, *Active Tectonics of the Andes*: *Tectonophysics*, v. 205, p. 79-95.
- Doblas, M., 1998, *Slickenside Kinematic Indicators*: *Tectonophysics*, v. 295, p. 187-197.
- Domeyko, I., 1848, *Mémoire sur le Terrain Tertiaire et les Lignes d'ancien Niveau de l'Océan du sud, aux Environs de Coquimbo (Chili)*: *Annales des Mines*, v. 14, p. 153-162.
- Dziewonski, A. M., Ekström, G., Woodhouse, J. H., and Zwart, G., 1990, *Centroid-Moment Tensor Solutions for January-March 1989*: *Physics of the Earth and Planetary Interiors*, v. 59, p. 233-242.
- Engelder, T., and Fisher, M. P., 1996, *Loading Configurations and Driving Mechanisms for Joints Based on the Griffith Energy-Balanced Concept*: *Tectonophysics*, v. 256, p. 253-277.
- Etchecopar, A., Vasseur, G., and Daignieres, M., 1981, *An Inverse Problem in Microtectonics for the Determination of Stress Tensors from Fault Striation Analysis*: *Journal of Structural Geology*, v. 3, p. 51-65.
- Ewing, T., 1990, *Australian Earthquake; Twelve Dead after Earthquake*: *Nature*, v. 343, p. 105.
- Farrar, E., Clark, A. H., Haynes, S. J., Quirt, S. J., Conne, H., and Zentilli, M., 1970, *K-Ar Evidence for the Post-Paleozoic Migration of Granitic Intrusion Foci in the Andes of Northern Chile*: *Earth and Planetary Science Letters*, v. 10, p. 60-66.
- Fedotov, S. A., 1968, *The Seismic Cycle, Quantitative Seismic Zoning, and Long-Term Seismic Forecasting*, in Medvedev, S. V., ed., *Seismic Zoning in the USSR*, Moscow, Izdatel'stvo Nauka, p. 133-166.
- Fernandes, N. F., and Dietrich, W. E., 1997, *Hillslope Evolution by Diffusive Processes: The Timescale for Equilibrium Adjustments*: *Water Resources Research*, v. 33, p. 1307-1318.
- Fisher, M. P., Gross, M. R., Engelder, T., and Greenfield, R. J., 1995, *Finite-Element Analysis of the Stress Distribution around Pressurized Cracks in a Layered Elastic Medium: Implication for the Spacing of Fluid-Driven Joints in Bedded Sedimentary Rock*: *Tectonophysics*, v. 247, p. 49-64.
- Flueh, E. R., Vidal, N., Ranero, C. R., Hojka, A., Von Huene, R., Bialas, J., Hinz, K., Cordoba, D., Danobeitia, J. J., and Zelt, C., 1998, *Seismic Investigation of the Continental Margin Off- and Onshore Valparaiso, Chile*: *Tectonophysics*, v. 288, p. 251-263.
- Forsythe, R., 1982, *The Late Paleozoic to Early Mesozoic Evolution of Southern South America: A Plate Tectonic Interpretation*: *Journal of the Geological Society, London*, v. 139, p. 671-682.
- Fuenzalida, A., Sandoval, A., Cisternas, A., and Dorbath, L., 1993, *Crustal Microseismicity in Central Chile; Evidence of Active Faulting?*: ISAG 93; *International Symposium on Andean Geodynamics*, p. 93-94.
- Gana, P., 1991, *Mapa Geologico De La Cordillera De La Costa Entre La Serena Y Quebrada Del Teniente*: Servicio Nacional de Geología y Minería, Santiago, Chile.
- Gonzalez, G., Cembrano, J., Carrizo, D., Macci, A., and Schneider, H., 2002, *Link between Forearc Tectonics and Pliocene-Quaternary Deformation of the Coastal Cordillera, Northern Chile*: *Journal of South American Earth Sciences*, submitted.
- Gutscher, M.-A., Spakman, W., Bijwaard, H., and Engdahl, E. R., 2000, *Geodynamics of Flat Subduction: Seismicity and Tomographic Constraints from the Andean Margin*: *Tectonics*, v. 19, p. 814-833.

- Hanks, T. C., 1984, Modification of Wave-Cut and Faulting-Controlled Landforms: *Journal of Geophysical Research*, v. 89, p. 5771-5790.
- Hanks, T. C., 2000, The Age of Scarplike Landforms from Diffusion-Equation Analysis, in Noller, J. S., Sowers, J. M., and Lettis, W. R., eds., *Quaternary Geochronology; Methods and Applications*, Washington, DC, United States, p. 313-338.
- Hartley, A. J., and Jolley, E. J., 1995, Tectonic Implications of Late Cenozoic Sedimentation from Coastal Cordillera of Northern Chile (22-24°S): *Journal of Geological Society*, v. 152, p. 51-63.
- Helle, S., Alfaro, G., Kelm, U., and Tascon, J. M. D., 2000, Mineralogical and Chemical Characterisation of Coals from Southern Chile.: *International Journal of Coal Geology*, v. 44, p. 85-94.
- Heredia, N., Rodríguez Fernández, L. R., Gallastegui, G., Busquets, P., and Colombo, F., 2002, Geological Setting of the Argentine Frontal Cordillera in the Flat-Slab Segment (30° 00' -31° 30' S): *Journal of South American Earth Sciences*, v. 15, p. 79-99.
- Herm, D., Paskoff, R., and Stiefel, J., 1967, Premieres Observations Sur Les Alentours De La Baie De Tongoy (Chili). *Bulletin de la Societé Geologique de France*, v. 8, p. 21-24.
- Hervé, F. A., Munizaga, F., Godoy, E., and Aguirre, L., 1974, Late Paleozoic K/Ar Ages of Blueschists from Pichilemú, Central Chile: *Earth and Planetary Science Letters*, v. 23, p. 261-264.
- Hossack, J. R., 1979, The Use of Balanced Cross-Sections in the Calculation of Orogenic Contraction: A Review: *Journal of the Geological Society*, v. 136, p. 705-711.
- Hsu, J. T., Leonard, E. M., and Wehmiller, J. F., 1989, Aminostratigraphy of Peruvian and Chilean Quaternary Marine Terraces: *Quaternary Science Reviews*, v. 8, p. 255-262.
- Hyndman, R. D., and Wang, K., 1993, Thermal Constraints on the Zone of Major Thrust Earthquake Failure: The Cascadia Subduction Zone: *Journal of Geophysical Research*, v. 98, p. 2039-2060.
- IGM, 1955, *Fotografias Aereas*: Instituto Geografico Militar, Santiago, Chile, 1:70 000.
- IGM, 1968, *Mapa Topografica De Chile*: Instituto Geografico Militar, Santiago, Chile, 1:50 000.
- Irwin, J. J., Garcia, C., Herve, F., and Brook, M., 1988, Geology of Part of a Long-Lived Dynamic Plate Margin; the Coastal Cordillera of North-Central Chile, Latitude 30° 51' -31° S: *Canadian Journal of Earth Sciences = Journal Canadien des Sciences de la Terre*, v. 25, p. 603-624.
- Irwin, J. J., 1989, A Note on Jurassic and Early Cretaceous Alkaline Magmatism in the Coastal Cordillera of Central Chile (30° 30' -34° S): *Journal of South American Earth Sciences*, v. 2, p. 305-309.
- ISC, 2001, *On-Line Bulletin*, International Seismological Centre, Thatcham, United Kingdom.
- Jackson, J. A., and White, N. J., 1989, Normal Faulting in the Upper Continental Crust: Observations from Regions of Active Extension: *Journal of Structural Geology*, v. 11, p. 15-36.
- Jaeger, J. C., and Cook, N. G. W., 1979, *Fundamentals of Rock Mechanics*: London, United Kingdom, Chapman and Hall, 593 p.
- Jordan, E., 1929, Report on Fossils from Coquimbo, in Willis and Bailey, eds., *Earthquake Conditions in Chile*, Washington, Carnegie Institution, p. 117-119.
- Kanamori, H., and Anderson, D. L., 1975, Theoretical Basis of Some Empirical Relations in Seismology: *Bulletin of the Seismological Society of America*, v. 65, p. 1073-1095.
- Katz, H. R., 1971, Continental Margin in Chile: Is the Tectonic Style Compressional or Extensional?: *American Association of Petroleum Geologists Bulletin*, v. 10, p. 1753-1758.
- Kelleher, J. A., 1972, Rupture Zones of Large South American Earthquakes and Some Predictions: *Journal of Geophysical Research*, v. 77, p. 2087-2103.

- Khazaradze, G., 1999, Tectonic Deformation in Western Washington State from Global Positioning System Measurements: Unpub. Ph.D. thesis, University of Washington 159 p.
- Khazaradze, G., Klotz, J., Angermann, D., Michel, G. W., and Reigber, C., 1999, 3D Modeling of Inter-Seismic Strain Accumulation in the Central and Southern Andes Based on GPS Measurements: *Eos, Transactions, American Geophysical Union*, v. 80, p. F270.
- Khazaradze, G., and Klotz, J., 2002, Short and Long-Term Effects of GPS Measured Crustal Deformation Rates Along the South-Central Andes: *Journal of Geophysical Research*, v. in Review.
- King, G. C. P., Stein, R. S., and Rundle, J. B., 1988, The Growth of Geological Structures by Repeated Earthquakes, 1, Conceptual Framework: *Journal of Geophysical Research*, v. 93, p. 13,307-13,318.
- Kirchner, A., Goetze, H. J., and Schmitz, M., 1996, 3-D Density Modelling with Seismic Constraints in the Central Andes: *Physics and Chemistry of the Earth*, v. 21, p. 289-293.
- Kley, J., Monaldi, C. R., and Salfity, J. A., 1999, Along-Strike Segmentation of the Andean Foreland: Causes and Consequences: *Tectonophysics*, v. 301, p. 75-94.
- Klotz, J., Angermann, D., Michel, G. W., Porth, R., Reigber, C., Reinking, J., Viramonte, J., Perdomo, R., Rios, V. H., Barrientos, S., Barriga, R., and Cifuentes, O., 1999, GPS-Derived Deformation of the Central Andes Including the 1995 Antofagasta M (Sub W) = 8.0 Earthquake: *Pure and Applied Geophysics*, v. 154, p. 3709-3730.
- Klotz, J., Khazaradze, G., and Reigber, C., 2000, New GPS Results Along the Andean Subduction Zone: *EGS 25th General Assembly, Geophysical Research Abstracts*, v. 2.
- Klotz, J., Khazaradze, G., Angermann, D., Reigber, C., Perdomo, R., and Cifuentes, O., 2001, Earthquake Cycle Dominates Contemporary Crustal Deformation in Central and Southern Andes: *Earth and Planetary Science Letters*, v. 193, p. 437-446.
- Kostrov, V. V., 1974, Seismic Moment and Energy of Earthquakes, and Seismic Flow of Rock: *Izv. Acad. Sci. USSR Phys. Solid Earth*, v. 1, p. 13-21.
- Lamy, F., Hebbeln, D., and Wefer, G., 1998, Late Quaternary Precessional Cycles of Terrigenous Sediment Input Off the Norte Chico, Chile (27.5 Degrees S) and Palaeoclimatic Implications: *Palaeogeography, Palaeoclimatology, Palaeoecology*, v. 141, p. 233-251.
- Lamy, F., Hebbeln, D., and Wefer, G., 1999, High-Resolution Marine Record of Climatic Change in Mid-Latitude Chile During the Last 28,000 Years Based on Terrigenous Sediment Parameters: *Quaternary Research*, v. 51, p. 83-93.
- Larsen, S., and Reilinger, R., 1992, Global Positioning System Measurements of Strain Accumulation across the Imperial Valley, California 1986-1989: *Journal of Geophysical Research*, v. 97, p. 8865-8876.
- Larsen, S., Reilinger, R., Neugebauer, H., and Strange, W., 1992, Global Positioning System Measurements of Deformations Associated with the 1987 Superstition Hills Earthquake; Evidence for Conjugate Faulting: *Journal of Geophysical Research*, v. 97, p. 4885-4902.
- Lavenu, A., and Cembrano, J., 1999, Compressional- and Transpressional-Stress Pattern for Pliocene and Quaternary Brittle Deformation in Fore Arc and Intra-Arc Zones (Andes of Central and Southern Chile): *Journal of Structural Geology*, v. 21, p. 1669-1691.
- Lavenu, A., Marquardt, C., Comte, D., Pardo, M., Ortlieb, L., and Monfret, T., 1999, Quaternary Extensional Deformation and Recent Vertical Motion Along the Chilean Coast (between 23° S and 47° S): *Fourth International Symposium on Andean Geodynamics*, p. 424-427.
- Leonard, E., Wehmiller, J., and Fergusson, D., 1988, Rates of Quaternary Uplift Along the North-Central Coast of Chile; Results of Amino Acid Dating of Marine Terrace Fauna: *Serie Comunicaciones Departamento de Geologia, Facultad de Ciencias Fisicas y Matematicas, Universidad de Chile*, v. 39., 21 p.

- Leonard, E. M., and Wehmiller, J. F., 1992, Low Uplift Rates and Terrace Reoccupation Inferred from Mollusk Aminostratigraphy, Coquimbo Bay Area, Chile: *Quaternary Research*, v. 38, p. 246-259.
- Leonard, E. M., Muhs, D. R., Ludwig, K. R., and Wehmiller, J. F., 1994, Coral Uranium-Series Ages and Mollusc Amino-Acid Ratios from Uplifted Marine Terrace Deposits, Morro De Copiapo, North-Central Chile: Program and Abstracts, American Quaternary Association, v. 13, 223 p.
- Liu, M., Yang, Y., Stein, S., Zhu, Y., and Engeln, J., 2000, Crustal Shortening in the Andes: Why Do GPS Rates Differ from Geological Rates?: *Geophysical Research Letters*, v. 27, p. 3005-3008.
- Lomnitz, C., 1970, Major Earthquakes and Tsunamis in Chile During the Period 1535 to 1955: *Geologische Rundschau*, v. 59, p. 938-960.
- Lynch, T. F., 1990, Quaternary Climate, Environment, and the Human Occupation of the South-Central Andes: *Geoarcheology*, v. 5, p. 199-228.
- Machare, J., and Ortlieb, L., 1992, Plio-Quaternary Vertical Motions and the Subduction of the Nazca Ridge, Central Coast of Peru: *Tectonophysics*, v. 205, p. 97-108.
- Maggi, A., Jackson, J. A., McKenzie, D., and Priestley, K., 2000, Earthquake Focal Depths, Effective Elastic Thickness, and the Strength of the Continental Lithosphere: *Geology*, v. 28, p. 495-498.
- Mansinha, L., and Smylie, D. E., 1967, Effect of Earthquakes on the Chandler Wobble and the Secular Polar Shift: *Journal of Geophysical Research*, v. 72, p. 4731-4743.
- Mansinha, L., Smylie, D. E., and Orphal, D. L., 1971, The Displacement Fields of Inclined Faults: *Bulletin of the Seismological Society of America*, v. 61, p. 1433-1440.
- Marquardt, C., and Lavenu, A., 1999, Quaternary Brittle Deformation in the Caldera Area, Northern Chile (27° S): Fourth International Symposium on Andean Geodynamics, p. 476-481.
- Marquardt, C., Ortlieb, L., Lavenu, A., and Guzman, N., 1999, Recent Vertical Motion and Quaternary Marine Terraces in the Caldera Area, Northern Chile: Fourth International Symposium on Andean Geodynamics, p. 482-487.
- Marquardt, C., 2000, Analyse Des Deformations Cassantes Dans La Peninsule De Mejlliones (23° S), Ses Relations Avec La Subduction Nord Chili: Unpub. Master thesis, Université Montpellier II, 69 p.
- Marrett, R., and Allmendinger, R. W., 1990, Kinematic Analysis of Fault-Slip Data: *Journal of Structural Geology*, v. 12, p. 973-986.
- Marrett, R., and Peacock, D. C. P., 1999, Strain and Stress: *Journal of Structural Geology*, v. 21, p. 1057-1063.
- Marrett, R., and Strecker, M. R., 2000, Response of Intracontinental Deformation in the Central Andes to Late Cenozoic Reorganization of South American Plate Motions: *Tectonics*, v. 19, p. 452-467.
- Martinez, P. R., 1979, Hallazgo De Foraminiferos Miocenicos Cerca De Puerto Aldea, Bahia De Tongoy, Provincia De Coquimbo, Chile: *Revista Geologica de Chile*, v. 8, p. 65-78.
- Martinez, P. R., and Perez, R. C., 1980, Microfosiles Siliceos De Las Diatomitas De Tongoy, Provincia De Coquimbo, Chile: Su Significado Biocronoestratigrafico, Biocronogeologico, Paleoecologico Y Paleogeografico: *Revista Geologica de Chile*, v. 10, p. 33-53.
- McCalpin, J. P., 1996, Paleoseismology in Extensional Tectonic Environments, in McCalpin, J. P., ed., *Paleoseismology*, New York, United States, Academic Press, p. 85-146.
- Meinardus, H., 1961, Exploraciones Geofisicas En El Área De Tongoy: *Annales de Facultad de Ciencias Fisicas y Matematicas*, Universidad de Chile, Santiago, Chile, v. 18, p. 206-215.
- Meschede, M., 1994, *Methoden Der Strukturgeologie*: Stuttgart, Ferdinand Enke Verlag, 169 p.

- Michel, G., 1994, Neo-Kinematics Along the North-Anatolian Fault (Turkey): *Tübinger Geowissenschaftliche Abhandlungen, Reihe A*, v. 16, p. 248.
- Michel, G. W., 1993, Modeling Fault-Slip Data Sets: A Key for Approximating Stretching Ratios?: *Zeitschrift der Deutschen Geologischen Gesellschaft*, v. 144, p. 150-158.
- Nash, D. B., 1980, Forms of Bluffs Degraded for Different Lengths of Time in Emmet County, Michigan, U.S.A.: *Earth Surface Processes*, v. 5, p. 331-345.
- Nash, D. B., 1984, Morphologic Dating of Fluvial Terrace Scarps and Fault Scarps near West Yellowstone, Montana: *Geological Society of America Bulletin*, v. 95, p. 1413-1424.
- NEIC, 2001, USGS/NEIC (PDE) 1973 - Present, USGS, National Earthquake Information Center, World Data Center for Seismology.
- Nelson, A. R., and Manley, W. F., 1992, Holocene Coseismic and Aseismic Uplift of Isla Mocha, South-Central Chile: *Quaternary International*, v. 15-16, p. 61-76.
- Okada, A., 1971, On the Neotectonics of the Atacama Fault Zone Region. Preliminary Notes on Late Cenozoic Faulting and Geomorphic Development of the Coast Range of Northern Chile: *Bulletin of the Department of Geography, University of Tokyo*, v. 3, p. 47-65.
- Okada, Y., 1985, Surface Deformation Due to Shear and Tensile Faults in a Half-Space: *Bulletin of the Seismological Society of America*, v. 75, p. 1135-1154.
- Oleskevich, D. A., Hyndman, R. D., and Wang, K., 1999, The Updip and Downdip Limits to Great Subduction Earthquakes: Thermal and Structural Models of Cascadia, South Alaska, SW Japan, and Chile: *Journal of Geophysical Research*, v. 104, p. 14965-14992.
- Orife, T., Arlegui, L., and Lisle, R. J., 2002, Dipslip: A Quickbasic Stress Inversion Program for Analysing Sets of Faults without Slip Lineations: *Computer and Geosciences*, v. 28, p. 775-781.
- Ortlieb, L., Barrientos, S., and Guzman, N., 1996a, Coseismic Coastal Uplift and Coralline Algae Record in Northern Chile; the 1995 Antofagasta Earthquake Case: *Quaternary Science Reviews*, v. 15, p. 949-960.
- Ortlieb, L., Zazo, C., Goy, J. L., Hillaire-Marcel, C., Ghaleb, B., and Cournoyer, L., 1996b, Coastal Deformation and Sea-Level Changes in the Northern Chile Subduction Area (23° S) During the Last 330 Ky: *Quaternary Science Reviews*, v. 15, p. 8-9.
- Ota, Y., and Paskoff, R., 1993, Holocene Deposits on the Coast of North-Central Chile; Radiocarbon Ages and Implications for Coastal Changes: *Revista Geologica de Chile*, v. 20, p. 25-32.
- Ota, Y., Miyauchi, T., Paskoff, R., and Koba, M., 1995, Plio-Quaternary Terraces and Their Deformation Along the Altos De Talinay, North-Central Chile: *Revista Geologica de Chile*, v. 22, p. 89-102.
- Pacheco, J. F., and Sykes, L. R., 1992, Seismic Moment Catalog of Large Shallow Earthquakes, 1900 to 1989: *Bulletin of the Seismological Society of America*, v. 82, p. 1306-1349.
- Pardo, M., Comte, D., Monfret, T., Boroschek, R., and Astroza, M., 2002, The October 15, 1997 Punitaqui Earthquake (Mw = 7.1); a Destructive Event within the Subducting Nazca Plate in Central Chile: *Tectonophysics*, v. 345, p. 199-210.
- Paskoff, R., 1970, *Recherches Geomorphologiques Dans Le Chili Semi-Aride*: Bordeaux, Biscaye Freres, 420 p.
- Paskoff, R., 1973, Radiocarbon Dating of Marine Shells Taken from the North and Central Coast of Chile: *International Geological Congress*, p. 281-282.
- Paskoff, R., 1977, Quaternary of Chile: The State of Research: *Quaternary Research*, v. 8, p. 2-31.

- Paskoff, R., 1996, Atlas De Las Formas De Relieve De Chile: Santiago de Chile, Instituto Geográfico Militar de Chile, 288 p.
- Pelz, K., 2000, Tektonische Erosion Am Zentralandinen Forearc (20-24° S): Scientific Technical Report - Geoforschungszentrum Potsdam, v. 00-20, p. 118.
- Petit, J. P., 1987, Criteria for the Sense of Movement on Fault Surfaces in Brittle Rocks: *Journal of Structural Geology*, v. 9, p. 5-6.
- Pinter, N., 1996, Fault-Scarp Degradation, Exercises in Active Tectonics - an Introduction to Earthquakes and Tectonic Geomorphology, Upper Saddle River, Prentice-Hall, p. 99-110.
- Plafker, G., and Savage, J. C., 1970, Mechanism of the Chilean Earthquakes of May 21 and 22, 1960: *Geological Society of America Bulletin*, v. 81, p. 1001-1030.
- Price, R. A., 1981, The Cordilleran Foreland Thrust and Fold Belt in the Southern Canadian Rocky Mountains, in McClay, K. R., and Price, N. J., eds., *Thrust and Nappe Tectonics*, Geological Society of London Special Publications, p. 427-448.
- Radtke, U., 1987, Marine Terraces in Chile (22° -32° S) - Geomorphology, Chronostratigraphy, and Neotectonics: *Congress of the International Union for Quaternary Research*, v. 12, 247 p.
- Ramos, V. A., 1988, The Tectonics of the Central Andes; 30° to 33° S Latitude: *Geological Society of America; Special Paper*, v. 218, p. 31-54.
- Ramos, V. A., Cegarra, M., and Cristallini, E., 1996, Cenozoic Tectonics of the High Andes of West-Central Argentina (30-36° S Latitude), in Dewey, J. F., and Lamb, S. H., eds., *Geodynamics of the Andes: Tectonophysics*, Amsterdam, Netherlands, Elsevier, p. 185-200.
- Riquelme, R., Martinod, J., Hérail, G., Darrozes, J., and Charrier, R., 2003, A Geomorphological Approach to Determining the Neogene to Recent Tectonic Deformation in the Coastal Cordillera of Northern Chile (Atacama): *Tectonophysics*, v. 361, p. 255-275.
- Rocroi, J. P., 1964, Geophysical Survey at Tongoy (Coquimbo), Santiago de Chile, United Nations Special Fund Mineral Survey, p. 36.
- Ruff, L. J., and Tichelaar, B. W., 1996, What Controls the Seismogenic Plate Interface in Subduction Zones?, in Bebout, G. E., Scholl, D. W., Kirby, S. H., and Platt, J. P., eds., *Subduction Top to Bottom*, Washington, DC, United States, American Geophysical Union, p. 105-111.
- Savage, J. C., and Hastie, L. M., 1966, Surface Deformation Associated with Dip-Slip Faulting: *Journal of Geophysical Research*, v. 71, p. 4897-4904.
- Schwartz, D. P., and Coppersmith, K. J., 1984, Fault Behavior and Characteristic Earthquakes: Examples from the Wasatch and San Andreas Fault Zones ( USA): *Journal of Geophysical Research*, v. 89, p. 5681-5698.
- Schweller, W. J., Kulm, L. D., and Prince, R. A., 1981, Tectonics, Structure, and Sedimentary Framework of the Peru-Chile Trench, in Kulm, L. D., Dymond, J., Dasch, E. J., Hussong, D. M., and Roderick, R., eds., *Nazca Plate; Crustal Formation and Andean Convergence: Memoir Geological Society of America*, Boulder, CO, United States, Geological Society of America, p. 323-349.
- Segerstrom, K., 1964, Quaternary Geology of Chile: Brief Outline: *Geological Society of America*, v. 75, p. 157-170.
- Segerstrom, K., 1965, Dissected Gravels of the Río Copiapó Valley and Adjacent Coastal Area, Chile: *U.S. Geological Survey, Professional Paper*, v. 525B, p. B117-B121.
- Smith, W. H. F., and Sandwell, D. T., 1997, Global Sea Floor Topography from Satellite Altimetry and Ship Depth Soundings: *Science*, v. 277, p. 1956-1962.

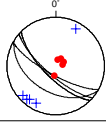
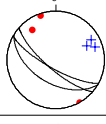
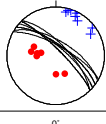
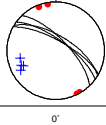
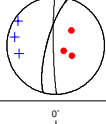
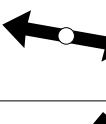
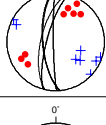
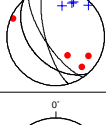
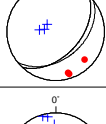
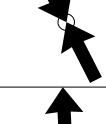
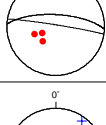
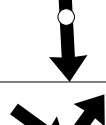
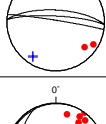
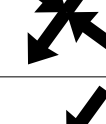
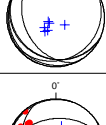
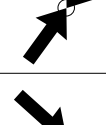
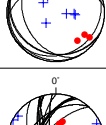
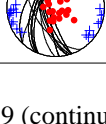
- Somoza, R., 1998, Updated Nazca (Farallon)-South America Relative Motions During the Last 40 My; Implications for Mountain Building in the Central Andean Region: *Journal of South American Earth Sciences*, v. 11, p. 211-215.
- Spang, J. H., 1972, Numerical Method for Dynamic Analysis of Calcite Twin Lamellae: *Geological Society of America Bulletin*, v. 83, p. 467-472.
- Sperner, B., Ratschbacher, L., and Ott, R., 1993, Fault-Striae Analysis; a Turbo Pascal Program Package for Graphical Presentation and Reduced Stress Tensor Calculation: *Computers and Geosciences*, v. 19, p. 1361-1388.
- Sperner, B., and Ratschbacher, L., 1996, Computer Programs for the Kinematic Analysis of Brittle Deformation Structures and the Tertiary Tectonic Evolution of the Western Carpathians (Slovakia): *Tübinger Geowissenschaftliche Arbeiten, Reihe A*, v. 27, p. 120.
- Steketee, J. A., 1958, On Volterra's Dislocations in a Semi-Infinite Medium: *Canadian Journal of Physics*, v. 36, p. 192-205.
- Strahler, A. N., 1952, Dynamic Basis of Geomorphology: *Geological Society of America Bulletin*, v. 63, p. 923-938.
- Tichelaar, B. W., and Ruff, L. J., 1991, Seismic Coupling Along the Chilean Subduction Zone: *Journal of Geophysical Research*, v. 96, p. 11,997-12,022.
- Tichelaar, B. W., and Ruff, L. J., 1993, Depth of Seismic Coupling Along Subduction Zones: *Journal of Geophysical Research*, v. 98, p. 2017-2037.
- Turner, F. J., 1953, Nature and Dynamic Interpretation of Deformation Lamellae in Calcite of Three Marbles: *American Journal of Science*, v. 251, p. 276-298.
- Twiss, R. J., and Unruh, J. R., 1998, Analysis of Fault Slip Inversion: Do They Constrain Stress or Strain Rate?: *Journal of Geophysical Research*, v. 103, p. 12,205 - 12,222.
- USGS, 2001, South American Earthquakes between 1471 - 1981, USGS, National Earthquake Information Center, World Data Center for Seismology, <http://neic.usgs.gov/neis/epic/epic.html>.
- Veit, H., 1993a, Upper Quaternary Landscape and Climate Evolution in the Norte Chico (Northern Chile): An Overview: *Mountain Research and Development*, v. 13, p. 139-144.
- Veit, H., 1993b, Alter und Genese der Deckschichten im semiariden Abschnitt der Küstenkordillere Chiles: *Mitteilungen der Deutschen Geographischen Gesellschaft*, v. 72, p. 1085-1088.
- Veit, H., 1995, Jungquartäre Landschafts- und Klimaentwicklung der Zentralen Anden und ihres westlichen Vorlandes; Kenntnisstand und Probleme: *Geomethodica*, v. 20, p. 163-194.
- Veit, H., 1996, Southern Westerlies During the Holocene Deduced from Geomorphological and Pedological Studies in the Norte Chico, Northern Chile (27-33° S): *Palaeogeography, Palaeoclimatology, Palaeoecology*, v. 123, p. 107-119.
- von Huene, R., Corvalan, J., Flueh, E. R., Hinz, K., Korstgard, J., Ranero, C. R., and Weinrebe, W., 1997, Tectonic Control of the Subducting Juan Fernandez Ridge on the Andean Margin near Valparaiso, Chile: *Tectonics*, v. 16, p. 474-488.
- von Huene, R., Weinrebe, W., and Heeren, F., 1999, Subduction Erosion Along the North Chile Margin: *Journal of Geodynamics*, v. 27, p. 345-358.
- von Huene, R., and Ranero, C. R., 2002, Subduction Erosion and Basal Friction Along the Sediment Starved Convergent Margin Off Antofagasta: *Journal of Geophysical Research*. B., v. in press.
- Wang, K., and Dragert, H., 1998, Strain\_M: Computer Program to Calculate Average Strain Tensor, Pacific Geoscience Centre, Geological Survey of Canada.

- Wang, K., 2000, Stress-Strain 'Paradox', Plate Coupling, and Forearc Seismicity at the Cascadia and Nankai Subduction Zones: *Tectonophysics*, v. 319, p. 321-338.
- Wells, D. L., and Coppersmith, K. J., 1994, New Empirical Relationships among Magnitude, Rupture Length, Rupture Width, Rupture Area, and Surface Displacements: *Bulletin of the Seismological Society of America*, v. 84, p. 974-1002.
- White, N., Jackson, J., and McKenzie, D., 1986, The Relationship between the Geometry of Normal Faults and That of Sedimentary Layers in Their Hanging Walls: *Journal of Structural Geology*, v. 8, p. 897-909.
- Woodward, N. B., Boyer, S. E., and Suppe, J., 1989, *Balanced Geological Cross-Sections: An Essential Technique in Geological Research and Exploration: Short Course in Geology*: Washington DC, United States, American Geophysical Union, 132 p.
- Yanez, G. A., Ranero, C. R., von Huene, R., and Diaz, J., 2001, Magnetic Anomaly Interpretation across the Southern Central Andes (32° -34° S); the Role of the Juan Fernandez Ridge in the Late Tertiary Evolution of the Margin: *Journal of Geophysical Research*, B, v. 106, p. 6325-6345.
- Yu, G., Wesnousky, S. G., and Ekstrom, G., 1993, Slip Partitioning Along Major Convergent Plate Boundaries: *Pure and Applied Geophysics*, v. 140, p. 183-210.

# Appendix

No.	Name	Geology	Deformation	Fault Slip Data	Stress Tensor	Comments
1	1_99X; PanAm - Puente Camarones 71.411°W / 30.317°S	Mid-Miocene - Pleistocene marine terraces - Quart. alluvial fan (TQc-Qal)	A - fault gouge; Normal faulting; offset ca. 3 m; crushed cobbles!			$\sigma_1 = 120/81$ $\sigma_2 = 254/6$ $\sigma_3 = 345/6$ $n = 26; R = 0.48; F = 15^\circ$
2	2_99X; PanAm - Puente Camarones 71.416°W / 30.326°S	Mid-Miocene - Pleistocene marine terraces - Quart. alluvial fan (TQc-Qal)	A - fault gouge; Normal faulting; offset 0.8 m			$\sigma_1 = 128/88$ $\sigma_2 = 297/2$ $\sigma_3 = 28/5$ $n = 9; R = 0.44; F = 21^\circ$
	2_99Y; PanAm - Puente Camarones 71.416°W / 30.326°S	Mid-Miocene - Pleistocene marine terraces - Quart. alluvial fan (TQc-Qal)	A - fault gouge; Strike-slip faulting			$\sigma_1 = 98/14$ $\sigma_2 = 251/74$ $\sigma_3 = 6/7$ $n = 3; R = 0.47; F = 8^\circ$
3	4_99AY; PanAm - Puente Limari 71.528°W / 30.661°S	Plio-Pleistocene fluvial conglomerates and sands & Mid-Jurassic Monzodiorites (TLa & JPo)	A - fault gouge; Strike-slip faulting			$\sigma_1 = 320/18$ $\sigma_2 = 190/63$ $\sigma_3 = 58/18$ $n = 15; R = 0.39; F = 16^\circ$
4	11_99X; Coastal Cordillera - Qbd. Arrayán 71.640°W / 30.540°S	Mid-Jurassic monzodiorites (JPo)	B - fault gouge; Normal faulting			$\sigma_1 = 97/73$ $\sigma_2 = 190/1$ $\sigma_3 = 281/18$ $n = 13; R = 0.57; F = 13^\circ$
5	13_99X; Coastal Cordillera - Qbd. Arrayán 71.663°W / 30.523°S	Upper Triassic - Lower Jurassic monzodiorites and gabbros (TJtm)	B - fault gouge; Normal faulting			$\sigma_1 = 11/79$ $\sigma_2 = 203/11$ $\sigma_3 = 112/2$ $n = 3; R = 0.50; F = 3^\circ$
	13_99YR; Coastal Cordillera - Qbd. Arrayán 71.663°W / 30.523°S	Upper Triassic - Lower Jurassic monzodiorites and gabbros (TJtm)	B - fault gouge; Strike-slip faulting			$\sigma_1 = 232/23$ $\sigma_2 = 89/61$ $\sigma_3 = 325/17$ $n = 7; R = 0.58; F = 16^\circ$
6	16_99X; Coastal Cordillera - Ctas. Tomatiaco 71.684°W / 30.456°S	Upper Triassic - Lower Jurassic monzodiorites and gabbros (TJtm)	B - fault gouge; Normal faulting			$\sigma_1 = 1/81$ $\sigma_2 = 166/9$ $\sigma_3 = 256/3$ $n = 5; R = 0.52; F = 10^\circ$
7	22_99X; Coastal Cordillera - Los Morillos 71.683°W / 30.500°S	Upper Triassic - Lower Jurassic monzodiorites and gabbros (TJtm)	C - shear plane/cleavage; Normal faulting			$\sigma_1 = 208/81$ $\sigma_2 = 333/5$ $\sigma_3 = 64/7$ $n = 9; R = 0.50; F = 10^\circ$
	22_99Y; Coastal Cordillera - Los Morillos 71.683°W / 30.500°S	Upper Triassic - Lower Jurassic monzodiorites and gabbros (TJtm)	C - shear plane/cleavage; Strike-slip faulting			$\sigma_1 = 304/17$ $\sigma_2 = 80/67$ $\sigma_3 = 208/15$ $n = 4; R = 0.41; F = 12^\circ$
8	29_99BX; Coastal Cordillera - Los Hornitos 71.572°W / 30.630°S	Mid-Jurassic monzodiorites (JPo)	B - fault gouge; Normal faulting			$\sigma_1 = 207/80$ $\sigma_2 = 18/10$ $\sigma_3 = 109/1$ $n = 3; R = 0.45; F = 12^\circ$
	29_99Y; Coastal Cordillera - Los Hornitos 71.572°W / 30.630°S	Mid-Jurassic monzodiorites (JPo)	B - fault gouge; Strike-slip faulting			$\sigma_1 = 152/8$ $\sigma_2 = 273/75$ $\sigma_3 = 61/13$ $n = 3; R = 0.49; F = 6^\circ$
9	30_99X; Coastal Cordillera - Los Hornitos 71.566°W / 30.631°S	Mid-Jurassic monzodiorites (JPo)	B - fault gouge; Normal faulting			$\sigma_1 = 336/84$ $\sigma_2 = 138/6$ $\sigma_3 = 228/1$ $n = 8; R = 0.43; F = 16^\circ$

Appx. A.1: Data 1999 (+ - T-axes; • - P-axes).

No.	Name	Geology	Deformation	Fault Slip Data	Stress Tensor	Comments
10	33_99X; Coastal Cordillera - Cerro Talinay 71.616°W / 30.858°S	Mid-Jurassic Monzodiorites (JPo)	C – shear plane/cleavage; Normal faulting			$\sigma_1 = 64/82$ $\sigma_2 = 307/3$ $\sigma_3 = 217/7$ $n = 5; R = 0.49; F = 5^\circ$
	33_99Y; Coastal Cordillera - Cerro Talinay 71.616°W / 30.858°S	Mid-Jurassic Monzodiorites (JPo)	C – shear plane/cleavage; Strike-slip faulting			$\sigma_1 = 332/9$ $\sigma_2 = 220/66$ $\sigma_3 = 66/22$ $n = 3; R = 0.52; F = 1^\circ$
11	34_99AX; Coastal Cordillera - Pta. Limarí Sur 71.688°W / 30.728°S	Upper Triassic - Lower Jurassic monzodiorites and gabbros (TJtm)	C – shear plane/cleavage; Normal faulting			$\sigma_1 = 261/66$ $\sigma_2 = 123/18$ $\sigma_3 = 30/9$ $n = 8; R = 0.56; F = 20^\circ$
	34_99AY; Coastal Cordillera - Pta. Limarí Sur 71.688°W / 30.728°S	Upper Triassic - Lower Jurassic monzodiorites and gabbros (TJtm)	C – shear plane/cleavage; Strike-slip faulting			$\sigma_1 = 338/2$ $\sigma_2 = 72/66$ $\sigma_3 = 248/24$ $n = 4; R = 0.51; F = 3^\circ$
	34_99BX; Coastal Cordillera - Pta. Limarí Sur 71.688°W / 30.728°S	Upper Triassic - Lower Jurassic monzodiorites and gabbros (TJtm)	C – shear plane/cleavage; Normal faulting			$\sigma_1 = 91/67$ $\sigma_2 = 190/4$ $\sigma_3 = 282/17$ $n = 3; R = 0.50; F = 22^\circ$
	34_99BY; Coastal Cordillera - Pta. Limarí Sur 71.688°W / 30.728°S	Upper Triassic - Lower Jurassic monzodiorites and gabbros (TJtm)	C – shear plane/cleavage; Strike-slip faulting			$\sigma_1 = 40/8$ $\sigma_2 = 284/73$ $\sigma_3 = 119/16$ $n = 8; R = 0.62; F = 31^\circ$
	36_99Y; Coastal Cordillera - Qbd. de la Leña 71.649°W / 30.744°S	Mid-Jurassic monzodiorites (JPo)	B – fault gouge; Strike-slip faulting			$\sigma_1 = 128/23$ $\sigma_2 = 259/57$ $\sigma_3 = 28/22$ $n = 4; R = 0.58; F = 14^\circ$
36_99YZ; Coastal Cordillera - Qbd. de la Leña 71.649°W / 30.744°S	Mid-Jurassic monzodiorites (JPo)	B – fault gouge; Reverse faulting			$\sigma_1 = 153/14$ $\sigma_2 = 60/14$ $\sigma_3 = 288/69$ $n = 3; R = 0.53; F = 11^\circ$	
13	38_99X; PanAm - Estero Monumento 71.505°W / 30.722°S	Plio-Pleistocene fluvial conglomerates and sands (TI/a)	A – fault gouge; Normal faulting; crushed cobbles!			$\sigma_1 = 239/59$ $\sigma_2 = 87/28$ $\sigma_3 = 350/12$ $n = 3; R = 0.49; F = 9^\circ$
	38_99Y; PanAm - Estero Monumento 71.505°W / 30.722°S	Plio-Pleistocene fluvial conglomerates and sands (TI/a)	A – fault gouge; Strike-slip faulting; crushed cobbles!			$\sigma_1 = 126/9$ $\sigma_2 = 343/78$ $\sigma_3 = 214/7$ $n = 3; R = 0.50; F = 14^\circ$
14	39_99Z; PanAm - Estero Monumento 71.510°W / 30.726°S	Plio-Pleistocene fluvial conglomerates and sands (TI/a)	B – fault gouge; Reverse faulting; offset: 3.5 m			$\sigma_1 = 36/17$ $\sigma_2 = 306/0$ $\sigma_3 = 215/72$ $n = 6; R = 0.50; F = 4^\circ$
	39_99ZZ; PanAm - Estero Monumento 71.510°W / 30.726°S	Plio-Pleistocene fluvial conglomerates and sands (TI/a)	A – fault gouge; Reverse faulting			$\sigma_1 = 312/0$ $\sigma_2 = 221/11$ $\sigma_3 = 36/79$ $n = 7; R = 0.44; F = 9^\circ$
15	40_99X; PanAm - Qbd. Talinay 71.607°W / 30.884°S	Upper Triassic - Lower Jurassic monzodiorites and gabbros (TJtm)	C – shear plane/cleavage; Normal faulting			$\sigma_1 = 81/87$ $\sigma_2 = 185/1$ $\sigma_3 = 275/2$ $n = 23; R = 0.46; F = 16^\circ$

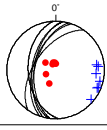
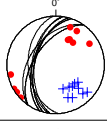
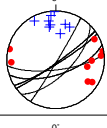
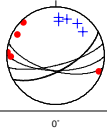
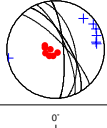
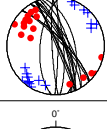
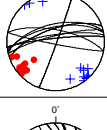
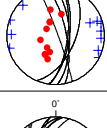
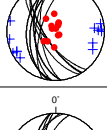
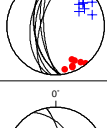
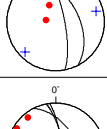
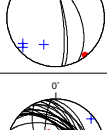
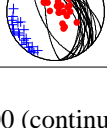
Appx. A.2: Data 1999 (continued).

No.	Name	Geology	Deformation	Fault Slip Data	Stress Tensor	Comments
	40_99Y; PanAm - Qbd. Talinay 71.607°W / 30.884°S	Upper Triassic - Lower Jurassic monzodiorites and gabbros (TJtm)	C - shear plane/cleavage; Strike-slip faulting			$\sigma_1 = 6/9$ $\sigma_2 = 255/67$ $\sigma_3 = 96/22$ $n = 15; R = 0.61; F = 16^\circ$
<b>16</b>	42_99X; PanAm - Qbd. de los Ciénagos 71.591°W / 30.834°S	Cretaceous Lamprophyric dyke	C - shear plane/cleavage; Normal faulting			$\sigma_1 = 56/67$ $\sigma_2 = 172/10$ $\sigma_3 = 265/18$ $n = 12; R = 0.53; F = 12^\circ$
	42_99Y; PanAm - Qbd. de los Ciénagos 71.591°W / 30.834°S	Cretaceous Lamprophyric dyke	C - shear plane/cleavage; Strike-slip faulting			$\sigma_1 = 19/10$ $\sigma_2 = 241/76$ $\sigma_3 = 110/9$ $n = 7; R = 0.51; F = 11^\circ$
<b>17</b>	43_99X; Puente Limarí - Qbd. de los Chiripies 71.490°W / 30.625°S	Plio-Pleistocene fluvial conglomerates and sands (TL/a)	A - fault gouge; Normal faulting; offset: > 1 m			$\sigma_1 = 255/71$ $\sigma_2 = 132/11$ $\sigma_3 = 39/13$ $n = 7; R = 0.52; F = 14^\circ$
	43_99Y; Puente Limarí - Qbd. de los Chiripies 71.490°W / 30.625°S	Plio-Pleistocene fluvial conglomerates and sands (TL/a)	A - fault gouge; Strike-slip faulting			$\sigma_1 = 144/19$ $\sigma_2 = 354/68$ $\sigma_3 = 237/10$ $n = 4; R = 0.49; F = 14^\circ$
<b>18</b>	A 9910J; Coastal Cordillera - Qbd. de Talca 71.655°W / 30.902°S	Upper Triassic - Lower Jurassic monzodiorites and gabbros (TJtm)	C - shear plane/cleavage; Normal faulting			$\sigma_1 = 267/74$ $\sigma_2 = 152/7$ $\sigma_3 = 60/14$ $n = 8; R = 0.18; F = 12^\circ$
<b>19</b>	A 996Y; Coastal Cordillera - Parque Nacional "Frey Jorge" 71.672°W / 30.647°S	Lower Paleozoic ortho- and paragneisses (Pzt)	C - shear plane/cleavage; Strike-slip faulting			$\sigma_1 = 187/28$ $\sigma_2 = 5/62$ $\sigma_3 = 97/1$ $n = 14; R = 0.50; F = 14^\circ$
<b>20</b>	M11_99X; Coastal Cordillera - Cerro Talinay 71.609°W / 30.863°S	Mid-Jurassic monzodiorites (JPo)	C - shear plane/cleavage; Normal faulting			$\sigma_1 = 294/62$ $\sigma_2 = 147/24$ $\sigma_3 = 50/15$ $n = 10; R = 0.48; F = 12^\circ$

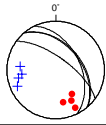
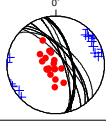
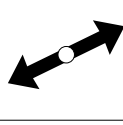
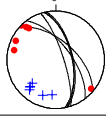
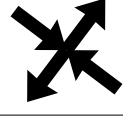
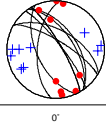
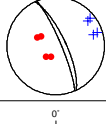
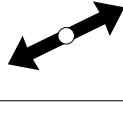
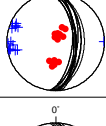
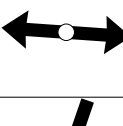
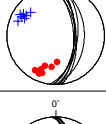
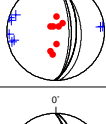
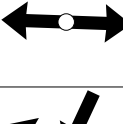
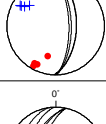
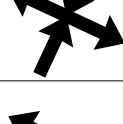
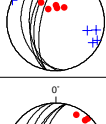
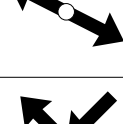
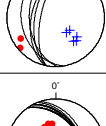
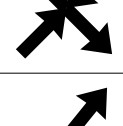
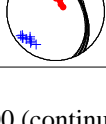
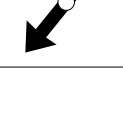
Appx. A.3: Data 1999 (continued).

No.	Name	Geology	Deformation	Fault Slip Data	Stress Tensor	Comments
1	4_00X; Tongoy - chalk-pit 71.443°W / 30.238°S	Mid-Miocene - Pleistocene marine terraces (TQc)	A - fault gouge; Normal faulting; offset: 0.9 m			$\sigma_1 = 315/80$ $\sigma_2 = 68/4$ $\sigma_3 = 158/6$ $n = 6; R = 0.51; F = 14^\circ$
	4_00Y; Tongoy - chalk-pit 71.443°W / 30.238°S	Mid-Miocene - Pleistocene marine terraces (TQc)	A - fault gouge; Strike-slip faulting			$\sigma_1 = 98/4$ $\sigma_2 = 261/85$ $\sigma_3 = 8/1$ $n = 6; R = 0.56; F = 15^\circ$
2	11_00X; Tongoy Bay - El Rincon 71.604°W / 30.299°S	Mid-Miocene - Pleistocene marine terraces - Quart. alluvial fan (TQc-Qal)	A - fault gouge; Normal faulting; offset: ca. 600 m			$\sigma_1 = 279/83$ $\sigma_2 = 145/5$ $\sigma_3 = 235/0$ $n = 23; R = 0.58; F = 21^\circ$
	11_00Y; Tongoy Bay - El Rincon 71.604°W / 30.299°S	Mid-Miocene - Pleistocene marine terraces - Quart. alluvial fan (TQc-Qal)	A - fault gouge; Strike-slip faulting			$\sigma_1 = 305/3$ $\sigma_2 = 41/64$ $\sigma_3 = 212/25$ $n = 12; R = 0.51; F = 7^\circ$
3	16_00Z; Tongoy Bay - Qbd. Los Litres 71.534°W / 30.321°S	Mid-Miocene - Pleistocene marine terraces - Quart. alluvial fan (TQc-Qal)	A - fault gouge; Reverse faulting; offset: 0.9 m			$\sigma_1 = 106/3$ $\sigma_2 = 197/14$ $\sigma_3 = 2/76$ $n = 4; R = 0.56; F = 15^\circ$
	20_00X; Tongoy Bay - El Rincon 71.597°W / 30.303°S	Mid-Miocene - Pleistocene marine terraces (TQc)	A - fault gouge; Normal faulting; offset: 1.5 m			$\sigma_1 = 38/61$ $\sigma_2 = 207/29$ $\sigma_3 = 299/4$ $n = 13; R = 0.47; F = 9^\circ$
4	20_00Y; Tongoy Bay - El Rincon 71.597°W / 30.303°S	Mid-Miocene - Pleistocene marine terraces (TQc)	A - fault gouge; Strike-slip faulting			$\sigma_1 = 3/20$ $\sigma_2 = 131/59$ $\sigma_3 = 266/23$ $n = 4; R = 0.55; F = 10^\circ$
	21_00X; Tongoy Bay - Qbd. Los Litres 71.532°W / 30.297°S	Mid-Miocene - Pleistocene marine terraces (TQc)	A - fault gouge; Normal faulting; offset: 0.5 m			$\sigma_1 = 45/71$ $\sigma_2 = 181/14$ $\sigma_3 = 275/13$ $n = 3; R = 0.51; F = 3^\circ$
5	21_00Y; Tongoy Bay - Qbd. Los Litres 71.532°W / 30.297°S	Mid-Miocene - Pleistocene marine terraces (TQc)	A - fault gouge; Strike-slip faulting			$\sigma_1 = 147/7$ $\sigma_2 = 263/74$ $\sigma_3 = 57/15$ $n = 3; R = 0.55; F = 10^\circ$
	201_00X; Tongoy Bay - El Rincon 71.596°W / 30.305°S	Mid-Miocene - Pleistocene marine terraces (TQc)	A - fault gouge; Normal faulting; offset: 0.3m			$\sigma_1 = 68/76$ $\sigma_2 = 175/4$ $\sigma_3 = 266/13$ $n = 1; R = 0.50; F = 0^\circ$
7	23_00X; Coastal Cordillera - Cta. Totoral (Recinto Militar) 71.676°W / 30.355°S	Upper Triassic - Lower Jurassic Monzogranites (TJ)	C - shear plane/cleavage; Normal faulting			$\sigma_1 = 198/83$ $\sigma_2 = 350/7$ $\sigma_3 = 81/9$ $n = 10; R = 0.59; F = 19^\circ$
	23_00Y; Coastal Cordillera - Cta. Totoral (Recinto Militar) 71.676°W / 30.355°S	Upper Triassic - Lower Jurassic Monzogranites (TJ)	C - shear plane/cleavage; Strike-slip faulting			$\sigma_1 = 181/4$ $\sigma_2 = 78/73$ $\sigma_3 = 271/16$ $n = 6; R = 0.50; F = 10^\circ$
	23_00Z; Coastal Cordillera - Cta. Totoral (Recinto Militar) 71.676°W / 30.355°S	Upper Triassic - Lower Jurassic Monzogranites (TJ)	C - shear plane/cleavage; Reverse faulting			$\sigma_1 = 23/33$ $\sigma_2 = 139/34$ $\sigma_3 = 262/39$ $n = 4; R = 0.52; F = 3^\circ$

Appx. A.4: Data 2000 (+ - T-axes; • - P-axes).

No.	Name	Geology	Deformation	Fault Slip Data	Stress Tensor	Comments
<b>8</b>	27_00X; Qbd. Seca - Los Molles 71.521°W / 30.494°S	Mid-Miocene - Pleistocene marine terraces (TQc)	A – fault gouge; Normal faulting; offset: 0.8 m			$\sigma_1 = 297/81$ $\sigma_2 = 194/2$ $\sigma_3 = 103/11$ $n = 7; R = 0.48; F = 15^\circ$
	27_00Y; Qbd. Seca - Los Molles 71.521°W / 30.494°S	Mid-Miocene - Pleistocene marine terraces (TQc)	A – fault gouge; Strike-slip faulting			$\sigma_1 = 46/18$ $\sigma_2 = 293/51$ $\sigma_3 = 143/35$ $n = 10; R = 0.59; F = 16^\circ$
<b>9</b>	28_00Y; Qbd. Seca/Pachingo 71.532°W / 30.481°S	Plio-Pleistocene fluvial conglomerates and sands - Quaternary alluvial (Tl/a - Qal)	D – topographic feature & shear plane; Strike-slip faulting; offset drainage (3*10 m)			$\sigma_1 = 95/12$ $\sigma_2 = 209/63$ $\sigma_3 = 357/23$ $n = 9; R = 0.54; F = 12^\circ$
	29_00Y; Tongoy bay - El Rincon 71.594°W / 30.314°S	Plio-Pleistocene fluvial conglomerates and sands - Quaternary alluvial (Tl/a - Qal)	D – topographic feature & shear plane; Strike-slip faulting; offset drainage (2*25 m)			$\sigma_1 = 290/4$ $\sigma_2 = 191/64$ $\sigma_3 = 22/26$ $n = 5; R = 0.52; F = 4^\circ$
<b>11</b>	31_00X; Propiedad El Tanguo - Qbd. Estero Seco 71.598°W / 30.349°S	Plio-Pleistocene fluvial conglomerates and sands - Quaternary alluvial (Tl/a - Qal)	A – fault gouge; Normal faulting; offset 5.2 m; crushed cobbles!			$\sigma_1 = 253/79$ $\sigma_2 = 158/1$ $\sigma_3 = 68/11$ $n = 7; R = 0.47; F = 10^\circ$
	31_00Y; Propiedad El Tanguo - Qbd. Estero Seco 71.598°W / 30.349°S	Plio-Pleistocene fluvial conglomerates and sands - Quaternary alluvial (Tl/a - Qal)	A – fault gouge; Strike-slip faulting; crushed cobbles!			$\sigma_1 = 310/15$ $\sigma_2 = 117/75$ $\sigma_3 = 220/3$ $n = 17; R = 0.53; F = 11^\circ$
<b>12</b>	32_00Y; Propiedad El Tanguo - Qbd. Estero Seco 71.598°W / 30.352°S	Upper Triassic - Lower Jurassic Monzogranites (TJ)	C – shear plane/cleavage; Strike-slip faulting			$\sigma_1 = 234/14$ $\sigma_2 = 26/74$ $\sigma_3 = 142/7$ $n = 12; R = 0.49; F = 10^\circ$
	33_00X; Precordillera - Road to Samo Alto 70.984°W / 30.432°S	Fluvial terraces	A – fault gouge; Normal faulting; offset > 10 m			$\sigma_1 = 262/77$ $\sigma_2 = 3/3$ $\sigma_3 = 93/4$ $n = 11; R = 0.60; F = 30^\circ$
<b>14</b>	35_00X; Propiedad Huayanay - Qbd. Pachingo 71.546°W / 30.423°S	Mid-Miocene - Pleistocene marine terraces (TQc)	A – fault gouge; Normal faulting; offset: 2 m			$\sigma_1 = 315/85$ $\sigma_2 = 173/4$ $\sigma_3 = 83/4$ $n = 13; R = 0.48; F = 18^\circ$
	35_00Y; Propiedad Huayanay - Qbd. Pachingo 71.546°W / 30.423°S	Mid-Miocene - Pleistocene marine terraces (TQc)	A – fault gouge; Strike-slip faulting			$\sigma_1 = 153/13$ $\sigma_2 = 265/58$ $\sigma_3 = 56/29$ $n = 7; R = 0.49; F = 8^\circ$
<b>15</b>	40_00XY; Propiedad Buenos Aires - Qbd. Baroa 71.593°W / 30.488°S	Plio-Pleistocene fluvial conglomerates and sands - Quaternary regolith (Tl/a - Qr)	A – fault gouge; Normal faulting; offset: 2.9 m			$\sigma_1 = 319/69$ $\sigma_2 = 151/20$ $\sigma_3 = 60/1$ $n = 2; R = 0.44; F = 18^\circ$
	40_00YY; Propiedad Buenos Aires - Qbd. Baroa 71.593°W / 30.488°S	Plio-Pleistocene fluvial conglomerates and sands - Quaternary regolith (Tl/a - Qr)	A – fault gouge; Strike-slip faulting			$\sigma_1 = 315/5$ $\sigma_2 = 57/67$ $\sigma_3 = 223/22$ $n = 3; R = 0.46; F = 11^\circ$
	40_00XO; Propiedad Buenos Aires - Qbd. Baroa 71.593°W / 30.488°S	Upper Triassic - Lower Jurassic Monzogranites (TJ)	C – shear plane/cleavage; Normal faulting			$\sigma_1 = 57/83$ $\sigma_2 = 325/0$ $\sigma_3 = 235/11$ $n = 23; R = 0.50; F = 17^\circ$

Appx. A.5: Data 2000 (continued).

No.	Name	Geology	Deformation	Fault Slip Data	Stress Tensor	Comments
	40_00Y; Propiedad Buenos Aires - Qbd. Baroa 71.593°W / 30.488°S	Upper Triassic - Lower Jurassic Monzogranites (TJ)	C – shear plane/cleavage; Strike-slip faulting			$\sigma_1 = 155/30$ $\sigma_2 = 23/49$ $\sigma_3 = 261/25$ $n = 4; R = 0.50; F = 6^\circ$
16	41_00X; Propiedad Buenos Aires - Qbd. La Punta 71.581°W / 30.522°S	Upper Triassic - Lower Jurassic Monzogranites (TJ)	C – shear plane/cleavage; Normal faulting			$\sigma_1 = 262/82$ $\sigma_2 = 154/3$ $\sigma_3 = 64/5$ $n = 18; R = 0.54; F = 17^\circ$
	41_00Y; Propiedad Buenos Aires - Qbd. La Punta 71.581°W / 30.522°S	Upper Triassic - Lower Jurassic Monzogranites (TJ)	C – shear plane/cleavage; Strike-slip faulting			$\sigma_1 = 307/7$ $\sigma_2 = 51/63$ $\sigma_3 = 213/26$ $n = 6; R = 0.51; F = 6^\circ$
17	42_00X; Qbd. Pachingo/Qbd. Seca 71.536°W / 30.473°S	Mid-Miocene - Pleistocene marine terraces (TQc)	D – topographic feature & shear plane; Normal faulting			$\sigma_1 = 167/78$ $\sigma_2 = 325/11$ $\sigma_3 = 56/5$ $n = 16; R = 0.52; F = 11^\circ$
	42_00Y; Qbd. Pachingo/Qbd. Seca 71.536°W / 30.473°S	Mid-Miocene - Pleistocene marine terraces (TQc)	D – topographic feature & shear plane; Strike-slip faulting			$\sigma_1 = 168/4$ $\sigma_2 = 56/79$ $\sigma_3 = 259/10$ $n = 9; R = 0.48; F = 20^\circ$
18	43_00X; Qbd. Seca/Qbd. Socotoco 71.492°W / 30.511°S	Plio-Pleistocene fluvial conglomerates and sands - Quaternary alluvial (TI/a - Qal)	A – fault gouge; Normal faulting; offset: 0.3 m			$\sigma_1 = 266/70$ $\sigma_2 = 154/8$ $\sigma_3 = 62/15$ $n = 4; R = 0.55; F = 18^\circ$
19	44_00X; PaAm/Qbd. Seca 71.485°W / 30.512°S	Plio-Pleistocene fluvial conglomerates and sands - Quaternary alluvial (TI/a - Qal)	D – topographic feature & shear plane; Normal faulting; topographic offset: 12.2 m			$\sigma_1 = 157/84$ $\sigma_2 = 4/5$ $\sigma_3 = 274/9$ $n = 16; R = 0.59; F = 22^\circ$
	44_00Y; PanAm/Qbd. Seca 71.485°W / 30.512°S	Plio-Pleistocene fluvial conglomerates and sands - Quaternary alluvial (TI/a - Qal)	D – topographic feature & shear plane; Strike-slip faulting			$\sigma_1 = 199/29$ $\sigma_2 = 65/52$ $\sigma_3 = 301/23$ $n = 7; R = 0.53; F = 9^\circ$
20	45_00X; Qbd. Seca/Qbd. Churaué 71.469°W / 30.510°S	Plio-Pleistocene fluvial conglomerates and sands - Quaternary alluvial (TI/a - Qal)	D – topographic feature & shear plane; Normal faulting; topographic offset: max. 25 m			$\sigma_1 = 198/87$ $\sigma_2 = 2/3$ $\sigma_3 = 272/4$ $n = 8; R = 0.58; F = 21^\circ$
	45_00Y; Qbd. Seca/Qbd. Churaué 71.469°W / 30.510°S	Plio-Pleistocene fluvial conglomerates and sands - Quaternary alluvial (TI/a - Qal)	D – topographic feature & shear plane; Strike-slip faulting			$\sigma_1 = 205/18$ $\sigma_2 = 82/60$ $\sigma_3 = 302/24$ $n = 4; R = 0.53; F = 10^\circ$
21	47_00X; Rio Limari/Estero Punitaqui (Salala) 71.515°W / 30.670°S	Plio-Pleistocene fluvial conglomerates and sands (TI/a)	A – fault gouge; Normal faulting; offset: ca. 2 m			$\sigma_1 = 351/63$ $\sigma_2 = 207/22$ $\sigma_3 = 111/14$ $n = 5; R = 0.50; F = 5^\circ$
	47_00Y; Rio Limari/Estero Punitaqui (Salala) 71.515°W / 30.670°S	Plio-Pleistocene fluvial conglomerates and sands (TI/a)	A – fault gouge; Strike-slip faulting			$\sigma_1 = 45/2$ $\sigma_2 = 313/42$ $\sigma_3 = 138/48$ $n = 5; R = 0.53; F = 10^\circ$
22	48_00X; In Salala - ford through Estero Punitaqui 71.516°W / 30.683°S	Mid-Jurassic Monzodiorites (JPo)	C – shear plane/cleavage; Normal faulting			$\sigma_1 = 354/63$ $\sigma_2 = 129/20$ $\sigma_3 = 226/20$ $n = 10; R = 0.53; F = 12^\circ$

Appx. A.6: Data 2000 (continued).

No.	Name	Geology	Deformation	Fault Slip Data	Stress Tensor	Comments
	48_00Y; In Salala - ford through Estero Punitaqui 71.516°W / 30.683°S	Mid-Jurassic Monzodiorites (JPo)	C – shear plane/cleavage; Strike-slip faulting			$\sigma_1 = 165/31$ $\sigma_2 = 42/42$ $\sigma_3 = 276/33$ $n = 8; R = 0.52; F = 11^\circ$
	48_00Z; In Salala - ford through Estero Punitaqui 71.516°W / 30.683°S	Mid-Jurassic Monzodiorites (JPo)	C – shear plane/cleavage; Reverse faulting			$\sigma_1 = 6/36$ $\sigma_2 = 273/4$ $\sigma_3 = 178/54$ $n = 4; R = 0.50; F = 6^\circ$
<b>23</b>	49_00X; PanAm - Qbd. Teniente 71.633°W / 30.986°S	Plio-Pleistocene fluvial conglomerates and sands - Quaternary alluvial (TI/a - Qal)	A – fault gouge; Normal faulting; offset: > 29 m; crushed cobbles!			$\sigma_1 = 256/85$ $\sigma_2 = 5/2$ $\sigma_3 = 95/7$ $n = 82; R = 0.49; F = 21^\circ$
	49_00Y; PanAm - Qbd. Teniente 71.633°W / 30.986°S	Plio-Pleistocene fluvial conglomerates and sands - Quaternary alluvial (TI/a - Qal)	A – fault gouge; Strike-slip faulting; crushed cobbles!			$\sigma_1 = 31/0$ $\sigma_2 = 300/70$ $\sigma_3 = 122/20$ $n = 17; R = 0.47; F = 14^\circ$
<b>24</b>	51_00Y1; Coastal Cordillera - Pta. Limari Norte 71.698°W / 30.723°S	Upper Triassic - Lower Jurassic monzodiorites and gabbros (TJm)	C – shear plane/cleavage; Strike-slip faulting			$\sigma_1 = 293/7$ $\sigma_2 = 157/80$ $\sigma_3 = 24/7$ $n = 3; R = 0.51; F = 4^\circ$
	51_00Y2; Coastal Cordillera - Pta. Limari Norte 71.698°W / 30.723°S	Upper Triassic - Lower Jurassic monzodiorites and gabbros (TJm)	C – shear plane/cleavage; Strike-slip faulting			$\sigma_1 = 232/12$ $\sigma_2 = 118/62$ $\sigma_3 = 329/24$ $n = 7; R = 0.55; F = 10^\circ$
<b>25</b>	52_00AY; Coastal Cordillera - Rio Limari/Qbd. Las Vacas 71.635°W / 30.726°S	Mid-Jurassic Monzodiorites (JPo)	C – shear plane/cleavage; Strike-slip faulting			$\sigma_1 = 174/24$ $\sigma_2 = 29/61$ $\sigma_3 = 269/16$ $n = 10; R = 0.45; F = 17^\circ$
	52_00X; Coastal Cordillera - Rio Limari/Qbd. Las Vacas 71.635°W / 30.726°S	Mid-Jurassic Monzodiorites (JPo)	C – shear plane/cleavage; Normal faulting			$\sigma_1 = 265/80$ $\sigma_2 = 146/5$ $\sigma_3 = 56/4$ $n = 22; R = 0.55; F = 20^\circ$
	52_00Y; Coastal Cordillera - Rio Limari/Qbd. Las Vacas 71.635°W / 30.726°S	Mid-Jurassic Monzodiorites (JPo)	C – shear plane/cleavage; Strike-slip faulting			$\sigma_1 = 299/17$ $\sigma_2 = 62/61$ $\sigma_3 = 202/23$ $n = 6; R = 0.45; F = 11^\circ$
<b>26</b>	53_00X; Propiedad El Tangué - Qbd. Estero Seco 71.599°W / 30.352°S	Plio-Pleistocene fluvial conglomerates and sands - Quaternary alluvial (TI/a - Qal)	A – fault gouge; Normal faulting; offset: > 2 m			$\sigma_1 = 59/70$ $\sigma_2 = 155/2$ $\sigma_3 = 246/21$ $n = 15; R = 0.52; F = 11^\circ$
	53_00Y; Propiedad El Tangué - Qbd. Estero Seco 71.599°W / 30.352°S	Plio-Pleistocene fluvial conglomerates and sands - Quaternary alluvial (TI/a - Qal)	A – fault gouge; Strike-slip faulting			$\sigma_1 = 332/31$ $\sigma_2 = 108/50$ $\sigma_3 = 227/23$ $n = 3; R = 0.48; F = 6^\circ$
<b>27</b>	55_00X; Qbd. Teniente - La Loma 71.633°W / 31.001°S	Lower Paleozoic metabasites and gneisses (Pzch/a)	C – shear plane/cleavage; Normal faulting			$\sigma_1 = 340/67$ $\sigma_2 = 134/21$ $\sigma_3 = 228/9$ $n = 5; R = 0.49; F = 7^\circ$
	55_00Y; Qbd. Teniente - La Loma 71.633°W / 31.001°S	Lower Paleozoic metabasites and gneisses (Pzch/a)	C – shear plane/cleavage; Strike-slip faulting			$\sigma_1 = 173/20$ $\sigma_2 = 55/51$ $\sigma_3 = 276/32$ $n = 9; R = 0.51; F = 5^\circ$

Appx. A.7: Data 2000 (continued).

No.	Name	Geology	Deformation	Fault Slip Data	Stress Tensor	Comments
28	56_00Y; PanAm - exit La Cebada 71.641°W / 30.966°S	Plio-Pleistocene fluvial conglomerates and sands - Quaternary alluvial (TI/a - Qal)	A - fault gouge; Strike-slip faulting; offset: 1.1 m			$\sigma_1 = 223/9$ $\sigma_2 = 354/77$ $\sigma_3 = 135/10$ $n = 2; R = 0.48; F = 6^\circ$
29	57_00Y; Rio Limarí - Loma de los Loros 71.668°W / 30.727°S	Mid-Jurassic Monzodiorites (JPo)	B - fault gouge; Strike-slip faulting			$\sigma_1 = 353/23$ $\sigma_2 = 124/58$ $\sigma_3 = 253/22$ $n = 11; R = 0.51; F = 7^\circ$
	57_00Z; Rio Limarí - Loma de los Loros 71.668°W / 30.727°S	Mid-Jurassic Monzodiorites (JPo)	B - fault gouge; Reverse faulting			$\sigma_1 = 160/17$ $\sigma_2 = 62/23$ $\sigma_3 = 283/61$ $n = 6; R = 0.51; F = 4^\circ$
30	58_00Y; Rio Limarí - Loma de los Loros 71.683°W / 30.726°S	Mid-Jurassic Monzodiorites (JPo)	C - shear plane/cleavage; Strike-slip faulting			$\sigma_1 = 119/27$ $\sigma_2 = 250/52$ $\sigma_3 = 18/26$ $n = 4; R = 0.51; F = 14^\circ$
	58_00Z; Rio Limarí - Loma de los Loros 71.683°W / 30.726°S	Mid-Jurassic Monzodiorites (JPo)	C - shear plane/cleavage; Reverse faulting			$\sigma_1 = 245/11$ $\sigma_2 = 155/0$ $\sigma_3 = 64/83$ $n = 8; R = 0.52; F = 11^\circ$
31	59_00Y; Rio Limarí - Loma de los Loros 71.657°W / 30.733°S	Mid-Jurassic Monzodiorites & Quaternary alluvial (JPo & Qal)	B - fault gouge; Strike-slip faulting			$\sigma_1 = 29/1$ $\sigma_2 = 252/89$ $\sigma_3 = 113/1$ $n = 14; R = 0.43; F = 20^\circ$
32	60_00X; Coastal Cordillera - Qbd. de los Loros 71.654°W / 30.787°S	Lower Paleozoic paragneisses (Pzt)	C - shear plane/cleavage; (cataclastic zone) Strike-slip faulting			$\sigma_1 = 79/82$ $\sigma_2 = 301/6$ $\sigma_3 = 211/2$ $n = 6; R = 0.52; F = 16^\circ$
	60_00Z; Coastal Cordillera - Qbd. de los Loros 71.654°W / 30.787°S	Lower Paleozoic paragneisses (Pzt)	C - shear plane/cleavage; (cataclastic zone) Reverse faulting			$\sigma_1 = 311/17$ $\sigma_2 = 46/17$ $\sigma_3 = 178/65$ $n = 4; R = 0.52; F = 8^\circ$
33	62_00X; Baños del Soco - Estero Soco 71.489°W / 30.732°S	Plio-Pleistocene fluvial conglomerates and sands (TI/a)	A - fault gouge; Normal faulting; offset: > 8 m; Thermal spring connected to fault!			$\sigma_1 = 187/59$ $\sigma_2 = 344/29$ $\sigma_3 = 79/9$ $n = 3; R = 0.52; F = 11^\circ$
	62_00Y; Baños del Soco - Estero Soco 71.489°W / 30.732°S	Plio-Pleistocene fluvial conglomerates and sands (TI/a)	A - fault gouge; Strike-slip faulting; Thermal spring connected to fault!			$\sigma_1 = 308/38$ $\sigma_2 = 142/51$ $\sigma_3 = 45/5$ $n = 11; R = 0.45; F = 14^\circ$
34	63_00AY; Baños del Soco - Qbd. del Gigante 71.479°W / 30.751°S	Cretaceous monzodiorites and granodiorites & Plio-Pleistocene fluvial conglomerates and sands (kg3 & TI/a)	C - shear plane/cleavage; Strike-slip faulting			$\sigma_1 = 291/6$ $\sigma_2 = 65/82$ $\sigma_3 = 207/7$ $n = 15; R = 0.60; F = 22^\circ$
	63_00BY; Baños del Soco - Qbd. del Gigante 71.479°W / 30.751°S	Cretaceous monzodiorites and granodiorites & Plio-Pleistocene fluvial conglomerates and sands (kg3 & TI/a)	C - shear plane/cleavage; Strike-slip faulting			$\sigma_1 = 23/27$ $\sigma_2 = 217/63$ $\sigma_3 = 116/6$ $n = 3; R = 0.53; F = 11^\circ$
	63_00X; Baños del Soco - Qbd. del Gigante 71.479°W / 30.751°S	Cretaceous monzodiorites and granodiorites & Plio-Pleistocene fluvial conglomerates and sands (kg3 & TI/a)	A - fault gouge; Normal faulting; offset in Plio-Pleistocene strata: 0.7 m			$\sigma_1 = 227/81$ $\sigma_2 = 337/3$ $\sigma_3 = 68/7$ $n = 11; R = 0.45; F = 17^\circ$

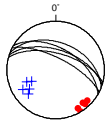
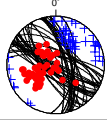
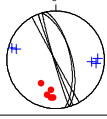
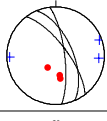
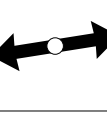
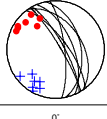
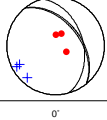
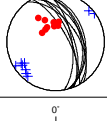
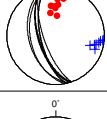
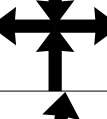
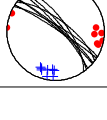
Appx. A.8: Data 2000 (continued).

No.	Name	Geology	Deformation	Fault Slip Data	Stress Tensor	Comments
35	64_00XR; Loma Uvilla - Qbd. Gigante 71.461° W / 30.763°S	Plio-Pleistocene fluvial conglomerates and sands - Quaternary alluvial (Tl/a - Qal)	A - fault gouge; Normal faulting; offset > 15 m			$\sigma_1 = 285/78$ $\sigma_2 = 132/11$ $\sigma_3 = 41/5$ $n = 3; R = 0.50; F = 2^\circ$
	64_00YR; Loma Uvilla - Qbd. Gigante 71.461° W / 30.763°S	Plio-Pleistocene fluvial conglomerates and sands - Quaternary alluvial (Tl/a - Qal)	A - fault gouge; Strike-slip faulting			$\sigma_1 = 296/29$ $\sigma_2 = 89/59$ $\sigma_3 = 198/11$ $n = 3; R = 0.51; F = 3^\circ$
36	65_00X; PanAm - Cerro Pachingo 71.462° W / 30.462°S	Cretaceous monzonites and tonalites (kg2)	C - shear plane/cleavage; Normal faulting			$\sigma_1 = 338/82$ $\sigma_2 = 160/8$ $\sigma_3 = 250/3$ $n = 13; R = 0.53; F = 15^\circ$
	65_00Z; PanAm - Cerro Pachingo 71.462° W / 30.462°S	Cretaceous monzonites and tonalites (kg2)	C - shear plane/cleavage; Reverse faulting			$\sigma_1 = 100/22$ $\sigma_2 = 4/15$ $\sigma_3 = 243/62$ $n = 8; R = 0.51; F = 10^\circ$
37	66_00X; Embalse La Paloma - road cut 71.012°W / 30.699°S	Lower Cretaceous granites ? (Kg?)	B - fault gouge; Normal faulting			$\sigma_1 = 324/60$ $\sigma_2 = 149/30$ $\sigma_3 = 57/2$ $n = 15; R = 0.50; F = 14^\circ$
	66_00Z; Embalse La Paloma - road cut 71.012°W / 30.699°S	Lower Cretaceous granites ? (Kg?)	B - fault gouge; Reverse faulting			$\sigma_1 = 245/12$ $\sigma_2 = 339/19$ $\sigma_3 = 129/68$ $n = 5; R = 0.39; F = 10^\circ$
38	67_00X; Ovalle - Mina El Dorado 71.224°W / 30.555°S	Lower Cretaceous granites ? (Kg?)	C - shear plane/cleavage; Normal faulting			$\sigma_1 = 253/77$ $\sigma_2 = 81/13$ $\sigma_3 = 351/2$ $n = 11; R = 0.53; F = 11^\circ$
	67_00Y; Ovalle - Mina El Dorado 71.224°W / 30.555°S	Lower Cretaceous granites ? (Kg?)	C - shear plane/cleavage; Strike-slip faulting			$\sigma_1 = 246/9$ $\sigma_2 = 6/72$ $\sigma_3 = 154/16$ $n = 12; R = 0.53; F = 13^\circ$
39	74_00X1; Alcones - Qbd. Angostura 71.559°W / 30.756°S	Mid-Jurassic Monzodiorites & Quaternary alluvial (JPo & Qal)	B - fault gouge; Normal faulting			$\sigma_1 = 273/78$ $\sigma_2 = 138/9$ $\sigma_3 = 47/2$ $n = 5; R = 0.44; F = 15^\circ$
	74_00X2; Alcones - Qbd. Angostura 71.559°W / 30.756°S	Mid-Jurassic Monzodiorites & Quaternary alluvial (JPo & Qal)	B - fault gouge; Normal faulting			$\sigma_1 = 84/74$ $\sigma_2 = 216/11$ $\sigma_3 = 309/14$ $n = 6; R = 0.53; F = 22^\circ$
	74_00Y1; Alcones - Qbd. Angostura 71.559°W / 30.756°S	Mid-Jurassic Monzodiorites & Quaternary alluvial (JPo & Qal)	B - fault gouge; Strike-slip faulting			$\sigma_1 = 297/6$ $\sigma_2 = 34/50$ $\sigma_3 = 202/40$ $n = 6; R = 0.46; F = 11^\circ$
	74_00Y2; Alcones - Qbd. Angostura 71.559°W / 30.756°S	Mid-Jurassic Monzodiorites & Quaternary alluvial (JPo & Qal)	B - fault gouge; Strike-slip faulting			$\sigma_1 = 210/31$ $\sigma_2 = 348/51$ $\sigma_3 = 104/20$ $n = 3; R = 0.56; F = 7^\circ$
	74_00Z; Alcones - Qbd. Angostura 71.559°W / 30.756°S	Mid-Jurassic Monzodiorites & Quaternary alluvial (JPo & Qal)	B - fault gouge; Reverse faulting			$\sigma_1 = 224/36$ $\sigma_2 = 120/17$ $\sigma_3 = 12/45$ $n = 6; R = 0.46; F = 21^\circ$

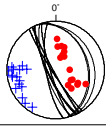
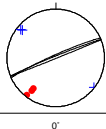
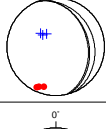
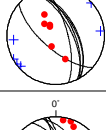
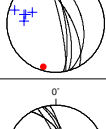
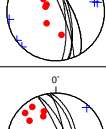
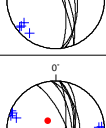
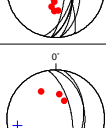
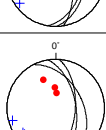
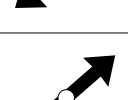
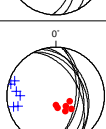
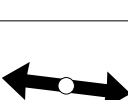
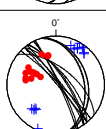
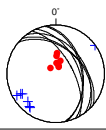
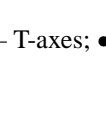
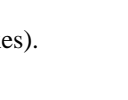
Appx. A.9: Data 2000 (continued).

No.	Name	Geology	Deformation	Fault Slip Data	Stress Tensor	Comments
40	75_00X; Alcones - Qbd. Angostura 71.562 °W / 30.751°S	Quaternary alluvial (Qal)	A – fault gouge; Normal faulting; offset: > 0.25 m			$\sigma_1 = 286/57$ $\sigma_2 = 123/31$ $\sigma_3 = 28/8$ $n = 4; R = 0.50; F = 4^\circ$
41	78_00X; Alcones - Qbd. Rancho Grande 71.567°W / 30.736°S	Quaternary alluvial (Qal)	A – fault gouge; Normal faulting; offset: > 1.5 m			$\sigma_1 = 340/62$ $\sigma_2 = 161/28$ $\sigma_3 = 71/0$ $n = 4; R = 0.49; F = 5^\circ$
42	79_00X; PanAm - Lomas del Soco 71.513 °W / 30.729°S	Mid-Jurassic Monzodiorites & Plio-Pleistocene fluvial conglomerates and sands (JPo & TI/a)	A – fault gouge; Normal faulting; offset: 4.2 m; crushed cobbles!			$\sigma_1 = 285/87$ $\sigma_2 = 158/2$ $\sigma_3 = 248/0$ $n = 44; R = 0.45; F = 17^\circ$
	79_00Y; PanAm - Lomas del Soco 71.513 °W / 30.729°S	Mid-Jurassic Monzodiorites & Plio-Pleistocene fluvial conglomerates and sands (JPo & TI/a)	A – fault gouge; Strike-slip faulting; crushed cobbles!			$\sigma_1 = 315/7$ $\sigma_2 = 129/83$ $\sigma_3 = 222/0$ $n = 12; R = 0.56; F = 18^\circ$
43	80_00AX; Fray Jorge - Qbd. Las Minas 71.590 °W / 30.673°S	Mid-Jurassic Monzodiorites & Plio-Pleistocene lacustrine deposits (JPo & TI/b)	B – fault gouge; Normal faulting			$\sigma_1 = 356/66$ $\sigma_2 = 168/24$ $\sigma_3 = 259/1$ $n = 3; R = 0.50; F = 5^\circ$
	80_00X; Fray Jorge - Qbd. Las Minas 71.590 °W / 30.673°S	Mid-Jurassic Monzodiorites & Plio-Pleistocene lacustrine deposits (JPo & TI/b)	B – fault gouge; Normal faulting			$\sigma_1 = 209/67$ $\sigma_2 = 51/21$ $\sigma_3 = 318/8$ $n = 8; R = 0.50; F = 9^\circ$
	80_00Y; Fray Jorge - Qbd. Las Minas 71.590 °W / 30.673°S	Mid-Jurassic Monzodiorites & Plio-Pleistocene lacustrine deposits (JPo & TI/b)	B – fault gouge; Strike-slip faulting			$\sigma_1 = 18/31$ $\sigma_2 = 148/47$ $\sigma_3 = 270/26$ $n = 4; R = 0.49; F = 5^\circ$
44	84_00X; Coastal Cordillera - Qbd. Talinay 71.674°W / 30.877°S	Upper Triassic - Lower Jurassic monzodiorites and gabbros (TI/m)	B – fault gouge; Normal faulting			$\sigma_1 = 265/85$ $\sigma_2 = 167/1$ $\sigma_3 = 77/5$ $n = 2; R = 0.53; F = 7^\circ$
	84_00Y; Coastal Cordillera - Qbd. Talinay 71.674°W / 30.877°S	Upper Triassic - Lower Jurassic monzodiorites and gabbros (TI/m)	B – fault gouge; Strike-slip faulting			$\sigma_1 = 198/13$ $\sigma_2 = 63/71$ $\sigma_3 = 290/13$ $n = 5; R = 0.51; F = 7^\circ$
45	85_00X; Puente Limarí - Qbd. El Romero 71.536°W / 30.637°S	Mid-Jurassic Monzodiorites & Quaternary alluvial (JPo & Qal)	B – fault gouge; Normal faulting			$\sigma_1 = 57/85$ $\sigma_2 = 306/2$ $\sigma_3 = 215/3$ $n = 5; R = 0.52; F = 13^\circ$
46	86_00X; Puente Limarí - Qbd. Agua de los Pajaritos 71.523°W / 30.629°S	Plio-Pleistocene fluvial conglomerates and sands - Quaternary alluvial (TI/a - Qal)	A – fault gouge; Normal faulting; offset: 1.8 m			$\sigma_1 = 344/61$ $\sigma_2 = 135/26$ $\sigma_3 = 232/13$ $n = 2; R = 0.52; F = 6^\circ$
47	88_00AX; Loma Monumento - Qbd. La Poza 71.519°W / 30.716°S	Mid-Jurassic Monzodiorites & Plio-Pleistocene fluvial conglomerates (JPo & TI/a)	B – fault gouge; Normal faulting			$\sigma_1 = 175/73$ $\sigma_2 = 12/16$ $\sigma_3 = 281/3$ $n = 2; R = 0.43; F = 9^\circ$
	88_00AZ; Loma Monumento - Qbd. La Poza 71.519°W / 30.716°S	Mid-Jurassic Monzodiorites & Plio-Pleistocene fluvial conglomerates (JPo & TI/a)	B – fault gouge; Reverse faulting			$\sigma_1 = 47/19$ $\sigma_2 = 152/37$ $\sigma_3 = 294/46$ $n = 4; R = 0.52; F = 14^\circ$

Appx. A.10: Data 2000 (continued).

No.	Name	Geology	Deformation	Fault Slip Data	Stress Tensor	Comments
	88_00BY; Loma Monumento - Qbd. La Poza 71.519°W / 30.716°S	Mid-Jurassic Monzodiorites & Plio-Pleistocene fluvial conglomerates (JPo & TI/a)	A – fault gouge; Strike-slip faulting; offset > 0.25 m			$\sigma_1 = 142/9$ $\sigma_2 = 39/55$ $\sigma_3 = 239/33$ $n = 5; R = 0.49; F = 6^\circ$
48	89_00X; PanAm - Puente Limari 71.529°W / 30.663°S	Mid-Jurassic Monzodiorites & Plio-Pleistocene fluvial conglomerates and sands (JPo & TI/a)	A – fault gouge; Normal faulting subsequently rotated or reverse faulting (backthrust); offset: 15; crushed cobbles!			$\sigma_1 = 253/65$ $\sigma_2 = 139/11$ $\sigma_3 = 44/23$ $n = 46; R = 0.44; F = 16^\circ$
	89_00Y; PanAm - Puente Limari 71.529°W / 30.663°S	Mid-Jurassic Monzodiorites & Plio-Pleistocene fluvial conglomerates and sands (JPo & TI/a)	A – fault gouge; Strike-slip faulting; crushed cobbles!			$\sigma_1 = 192/31$ $\sigma_2 = 356/58$ $\sigma_3 = 97/7$ $n = 5; R = 0.45; F = 12^\circ$
49	90_00X; Barraza - Qbd. La Peña 71.522°W / 30.707°S	Mid-Jurassic Monzodiorites & Plio-Pleistocene fluvial conglomerates (JPo & TI/a)	A – fault gouge; Normal faulting			$\sigma_1 = 180/59$ $\sigma_2 = 351/30$ $\sigma_3 = 84/4$ $n = 3; R = 0.50; F = 7^\circ$
	90_00YR; Barraza - Qbd. La Peña 71.522°W / 30.707°S	Mid-Jurassic Monzodiorites & Plio-Pleistocene fluvial conglomerates (JPo & TI/b)	A – fault gouge; Strike-slip faulting			$\sigma_1 = 312/19$ $\sigma_2 = 86/63$ $\sigma_3 = 214/17$ $n = 7; R = 0.52; F = 5^\circ$
50	92_00X; Estero Punitaqui - El Durazno 71.429°W / 30.704°S	Plio-Pleistocene fluvial conglomerates and sands (TI/a)	D – topographic feature & shear plane; Normal faulting; offset: ca. 50 m			$\sigma_1 = 41/76$ $\sigma_2 = 145/3$ $\sigma_3 = 236/15$ $n = 3; R = 0.53; F = 10^\circ$
51	95_00X; Termas Socos - Qbd. Aguita de los Burros 71.454°W / 30.733°S	Plio-Pleistocene lacustrine deposits (TI/b)	A – fault gouge; Normal faulting; offset: 2 m			$\sigma_1 = 339/59$ $\sigma_2 = 135/29$ $\sigma_3 = 231/11$ $n = 9; R = 0.51; F = 6^\circ$
52	100_00Y; PanAm - Qbd. Teniente 71.631°W / 30.986°S	Plio-Pleistocene fluvial conglomerates and sand (TI/a)	A – fault gouge; Strike-slip faulting; spring 5 m E of fault trace!; crushed cobbles!			$\sigma_1 = 0/39$ $\sigma_2 = 206/48$ $\sigma_3 = 101/13$ $n = 8; R = 0.51; F = 9^\circ$
53	102_00Y; Qbd. Alcones/Qbd. Las Torcazas 71.533°W / 30.808°S	Mid-Jurassic Monzodiorites (JPo)	B – fault gouge; Strike-slip faulting			$\sigma_1 = 99/9$ $\sigma_2 = 345/70$ $\sigma_3 = 192/18$ $n = 8; R = 0.51; F = 6^\circ$

Appx. A.11: Data 2000 (continued).

No.	Name	Geology	Deformation	Fault Slip Data	Stress Tensor	Comments
1	2_01X; Lomas del Soco - Estero Soco 71.496°W / 30.745°S	Cretaceous monzogranites and granodiorites (kg3)	C – shear plane/cleavage; Normal faulting; spring 300 m N of outcrop - in prolongation of major fault!			$\sigma_1 = 71/66$ $\sigma_2 = 164/1$ $\sigma_3 = 254/18$ $n = 16; R = 0.64; F = 27^\circ$
	2_01Y; Lomas del Soco - Estero Soco 71.496°W / 30.745°S	Cretaceous monzonites and tonalites (kg2)	C – shear plane/cleavage; Strike-slip faulting; spring 300 m N of outcrop - in prolongation of major fault!			$\sigma_1 = 217/15$ $\sigma_2 = 61/73$ $\sigma_3 = 309/6$ $n = 3; R = 0.51; F = 8^\circ$
	2_01Z; Lomas del Soco - Estero Soco 71.496°W / 30.745°S	Cretaceous monzonites and tonalites (kg2)	C – shear plane/cleavage; Reverse faulting; spring 300 m N of outcrop - in prolongation of major fault!			$\sigma_1 = 202/12$ $\sigma_2 = 106/26$ $\sigma_3 = 315/60$ $n = 3; R = 0.50; F = 2^\circ$
2	5_01X; Baños del Soco - Estero Soco 71.491°W / 30.741°S	Cretaceous monzonites and tonalites & Plio-Pleistocene fluvial conglomerates and sands (kg2 & TI/a)	A – fault gouge; Normal faulting			$\sigma_1 = 303/80$ $\sigma_2 = 153/9$ $\sigma_3 = 243/2$ $n = 6; R = 0.61; F = 22^\circ$
3	10_01Y; Propiedad El Tangué - Qbd. Estero Seco 71.595°W / 30.359°S	Mid-Miocene - Pleistocene marine terraces - Quart. alluvial fan (TQc-Qal)	A – fault gouge; Strike-slip/reverse faulting; offset: 0.85 m			$\sigma_1 = 21/9$ $\sigma_2 = 124/56$ $\sigma_3 = 286/33$ $n = 5; R = 0.52; F = 9^\circ$
4	13_01X; Propiedad El Tangué - Qbd. Estero Seco 71.595°W / 30.358°S	Plio-Pleistocene fluvial conglomerates and sands - Quaternary alluvial (TI/a - Qal)	A – fault gouge; Normal faulting; offset: 4.5 m; crushed cobbles!			$\sigma_1 = 284/74$ $\sigma_2 = 157/10$ $\sigma_3 = 66/6$ $n = 6; R = 0.61; F = 21^\circ$
	13_01Y; Propiedad El Tangué - Qbd. Estero Seco 71.595°W / 30.358°S	Plio-Pleistocene fluvial conglomerates and sands - Quaternary alluvial (TI/a - Qal)	A – fault gouge; Strike-slip faulting			$\sigma_1 = 324/27$ $\sigma_2 = 120/60$ $\sigma_3 = 228/10$ $n = 5; R = 0.52; F = 8^\circ$
5	15_01X; Propiedad El Tangué - Qbd. Estero Seco 71.599°W / 30.374°S	Plio-Pleistocene fluvial conglomerates and sands - Quaternary alluvial (TI/a - Qal)	B – fault gouge; Normal faulting; offset: 0.9 m; fault gouge cemented with carbonate (caliche)			$\sigma_1 = 192/69$ $\sigma_2 = 11/21$ $\sigma_3 = 281/1$ $n = 7; R = 0.52; F = 12^\circ$
6	17_01X; Propiedad El Tangué - Ramadilla 71.598°W / 30.387°S	Plio-Pleistocene fluvial conglomerates and sands - Quaternary alluvial (TI/a - Qal)	A – fault gouge; Normal faulting; offset: > 2 m; Colluvial wedge! Spring at 200 m W of fault!			$\sigma_1 = 359/50$ $\sigma_2 = 142/34$ $\sigma_3 = 246/20$ $n = 3; R = 0.54; F = 8^\circ$
7	18_01X; Propiedad Pachingo - Ramadilla 71.572°W / 30.462°S	Plio-Pleistocene fluvial conglomerates and sands - Quaternary alluvial (TI/a - Qal)	(A – fault gouge;?) Normal faulting; colluvial wedge?			$\sigma_1 = 349/53$ $\sigma_2 = 139/33$ $\sigma_3 = 239/15$ $n = 3; R = 0.52; F = 10^\circ$
8	19_01X; Propiedad Pachingo - Ramadilla 71.585°W / 30.468°S	Plio-Pleistocene fluvial conglomerates and sands - Quaternary alluvial (TI/a - Qal)	(A – fault gouge;?) Normal faulting; colluvial wedge?; spring 0.5 m from possible fault trace			$\sigma_1 = 142/67$ $\sigma_2 = 7/17$ $\sigma_3 = 272/17$ $n = 6; R = 0.47; F = 11^\circ$
9	20_01X; Chalinga - Estero Punitaqui 71.397°W / 30.740°S	Plio-Pleistocene fluvial conglomerates and sands - Quaternary alluvial (TI/a - Qal)	A – fault gouge; Normal faulting; offset: 3.5 m			$\sigma_1 = 308/45$ $\sigma_2 = 122/45$ $\sigma_3 = 214/2$ $n = 14; R = 0.47; F = 7^\circ$
10	25_01X; Estero Punitaqui - El Durazno 71.447°W / 30.704°S	Cretaceous monzogranites and granodiorites & Plio-Pleistocene fluvial conglomerates and sands (kg3 - TI/a)	A – fault gouge; Normal faulting; offset in Plio-Pleistocene sands: 0.1m			$\sigma_1 = 5/70$ $\sigma_2 = 137/14$ $\sigma_3 = 231/14$ $n = 7; R = 0.49; F = 7^\circ$

Appx. A.12: Data 2001 (+ – T-axes; • – P-axes).



## Acknowledgements

The present study was conducted within the framework of the interdisciplinary research project “SFB 267 – Deformation Processes in den Andes“, funded by the Deutsche Forschungsgemeinschaft (DFG). These investigations would not have been possible without financial support from the Geo-ForschungsZentrum Potsdam.

Sincere thanks go to Prof. O. Oncken for assistance and encouragement throughout the scientific discourse, which greatly inspired me to study the subject of this thesis from various aspects.

I feel much obliged to Prof. Ch. Reigber for giving me the opportunity to rely on the excellent research facilities provided by the division “Kinematics & Dynamics of the Earth“ of the Geo-ForschungsZentrum Potsdam and for outstanding support of field my studies.

I wish to thank Dr. G. W. Michel for providing me with an interesting research topic and for advice throughout the course of the investigation. I also thank Dr. J. Klotz and Dr. G. Khazaradze for the provision of extensive geodetic databases and for fruitful discussions on the interdisciplinary aspects of this study.

The cooperation with the Universidad Católica del Norte in Antofagasta, Chile, and the help from various official and private institutions in and around La Serena and Ovalle contributed to the successful conclusion of the scientific field work. Dr. H. Wilke from the Departamento de Ciencias Geológicas in Antofagasta provided great logistical support for the field campaigns. The Corporación Nacional Forestal (IV Region - Coquimbo) and the Armada de Chile are thanked for special permissions to enter restricted areas in the Altos de Talinay region. Many thanks go to the owners and executives of the estates of El Tangué, Huayanay and Pachingo for providing access to private property, which made the discovery of outstanding paleoseismological outcrops along the Puerto Aldea Fault possible. My special thanks are given to Rodney and Alberto for assistance in the field and insights in the cultural life of the city of Ovalle.

For invaluable advice and support which contributed to the successful solution of the many challenges that crossed my path throughout this study, I am very thankful to (without precedence) K. Elger, A. Hoffmann-Rothe, Th. Nischan, K. Munier, R. Hinsch, J. Lohrmann, S. Mannheim, U. Wetzel, M. Nitschke, M. Ge, S. Goebell, D. Stromeyer, M. Menning, F. Lorenzo, D. Marchenko, and U. Meyer.

Many thanks to Dr. J. Adam, Dr. D. Tanner, Dr. G. Hilley, and Dr. A. Abolghasem who volunteered to read and correct parts of this thesis.

# Curriculum Vitae

Name: Bertram Heinze  
Date of Birth: 14. 04. 1971  
Place of Birth: Ratzeburg  
Marital Status: unmarried, 1 child  
Citizenship: German

## School

08/1977–06/1981 Elementary school in Mölln  
08/1981–06/1990 Grammar school in Ratzeburg

## University Education

10/1991–12/1994 University of Kiel, Geology (Marine geosciences)  
01/1995–07/1995 University of Bergen, Norway, ERASMUS-Program (Petroleum geology)  
10/1995–12/1998 Freiberg University of Mining and Technology, Diploma (Coal petrography)  
Diploma Thesis: “Lagerungsverhältnisse und fazieller Aufbau des 2. Lausitzer Flözes im Südteil des Tagebaues Welzow-Süd, Lausitzer Braunkohle AG“

## Employment History

04/1999–05/1999 KUM – Umwelt- und Meerestechnik Kiel GmbH; Expedition to Laptev Sea, Russia (Ice coring, Core documentation)  
06/1999–12/2002 GFZ – GeoForschungsZentrum Potsdam; Scientific employee, Division “Kinematics & Dynamics of the Earth“, PhD. Thesis within the framework of the Sonderforschungsbereich 267 “Deformation Processes in the Andes“, financed by the Deutsche Forschungsgemeinschaft (DFG)